Dr-358

LA-6245-PR
PROGRESS REPORT

9-23-76

UC-21
Issued: July 1976

Laser Fusion Program

COMPILED BY
F. SKOBERNE

July 1—December 31, 1975

los alamos
scientific laboratory
of the University of California
LOS ALAMOS, NEW MEXICO 87545

MASTER

UNITED STATES
ENERGY RESEARCH AND DEVELOPMENT ADMINISTRATION
CONTRACT W-7405-ENG. 36

The four most recent reports in this series, unclassified, are LA-5542-PR, LA-5739-PR, LA-5919-PR, and LA-6050-PR.

Printed in the United States of America. Available from
National Technical Information Service
U.S. Department of Commerce
5285 Port Royal Road
Springfield, VA 22161
Price: Printed Copy $5.50 Microfiche $2.25

CONTENTS

Progress Report on

LASER-FUSION PROGRAM AT LASL

July 1 – December 31, 1975

ABSTRACT

Progress in the development of high-energy short-pulse CO_2 lasers for fusion research is reported. The Single-Beam System, which continues to be used in target experiments at a power level of 0.2 TW, has been improved. The status of the Dual-Beam System, which has produced a single-beam output of ~ 0.7 TW and a total output of ~ 1.4 TW, is described. Installation of the Eight-Beam System, which will produce outputs in the 5- to 20-TW range, is continuing. The reference design for the High-Energy Gas Laser Facility and results of preliminary design tradeoff studies are discussed, based on a design goal of 200 TW in a 200-ps pulse.

Research into new lasers for fusion application emphasized the rare-gas oxides and molecular mercury. Experimental kinetics studies, damage threshold measurements, and the theoretical support are described. Final results are given for the HF chemical laser program, which has been discontinued.

Target experiments conducted with a 150-J, 1-ns CO_2 laser pulse and a 10-J, 50-ps Nd:glass laser pulse are described. Use of data from a new charged-particle detector to deduce target compression is discussed. Spectra of emitted electrons and low-energy x rays are presented. Developments in automated data acquisition and reduction, and imaging of subkilovolt x rays are discussed. Improved methods of screening, fabricating, and characterizing hollow and cryogenic DT-filled microballoons are described. Studies of laser-target interaction physics and its effect on target design are discussed.

New results on feasibility and system studies are presented, including the fusion-fission hybrid, the magnetically protected reactor concept, and studies of alternative applications of laser fusion to the generation of process heat.

SUMMARY

CO_2 Laser Development

Four major laser systems are either in operation or under development in the CO_2 laser program: (a) the Single-Beam System (SBS), now being used in target work at 0.2 TW; (b) the Dual-Beam Module (DBM), a prototype system intended to produce ~ 2 TW; (c) the Eight-Beam System (EBS), consisting of four DBMs; and (d) the 200-TW High-Energy Gas Laser Facility (HEGLF). Significant progress was made on each of these systems; advances were made in CO_2 laser excitation methods, and new techniques for system isolation and short-pulse generation were developed.

Despite a heavy schedule of target-irradiation experiments, we installed in the SBS a master-oscillator system with a tenfold increase in output intensity over the previous system, increased the background extinction ratio of the single-pulse selector to 4.5×10^5 with two tandem electro-optic switches, and reduced the prepulse energy on target to 50 μJ by a combination of saturable absorber cells. This level of prepulse energy is the threshold for target surface melting, but constitutes only 5% of the energy required for plasma formation. After completion of these and other improvements, the SBS delivered a target irradiance of 3.4×10^{14} W/cm^2.

Many goals for the DBM prototype were attained. One chamber was operated at 90% of its electrical design level, delivering 600-J, 1.4-ns pulses after its triple-pass optics had been installed. This output was achieved at the point of marginal stability against self-oscillation without the use of gain suppression. The module was operated at a fill pressure of 1300 torr and a discharge voltage of 200 kV, yielding a center-line gain coefficient of 0.027 cm^{-1}. Operation of the cold-cathode electron gun was characterized, revealing that emission starts at 10 to 20 isolated points on the cathode foil before spreading laterally, giving the observed temporal behavior of the emission current. Theoretical studies indicated that absorption by inverse bremsstrahlung in a preionized laser medium should adequately protect the triple-pass optics from target reflections while providing good transmission of the outgoing beam.

Beneficial occupancy of Bldg. TSL-86, which will house the EBS, was essentially complete in October 1975. Procurement and installation of components for the various subsystems are proceeding according to plan. All components for the vacuum, control, and pulse-forming-network subsystems have been delivered and are being installed, except for the safety-control system, which is being designed. The electron-beam pulsers have been delivered, and their assembly and testing are well under way. About 80% of the hardware for the four DBMs has been designed and procured, and a request for proposal for the target-area subsystem has been issued. The first pulse-forming network (PFN) to be delivered has been partially characterized with a simulated load.

We completed a reference design for the HEGLF, based on an output intensity of 200 TW in a 200-ps pulse with a three-line, single-band spectrum. Each of the six final amplifier modules will require an 8.3-J optical input, which will be produced by a master oscillator and a series of double-discharge amplifiers operating at 1900 torr. In the reference design, double-pass amplification is specified in the final power amplifiers, but three versions of a single-pass design are being evaluated to avoid the isolation problems of double-pass amplification. Two types of pulse-forming network are being evaluated for the final amplifiers, generating the high-voltage driver pulse with a pulse transformer or a Marx circuit. The HEGLF control system will consist of several microprocessor-based control centers located near the controlled equipment, with communication to the central command center via fiber-optic bundles.

In the supporting research program, two methods of generating subnanosecond pulses of CO_2 radiation were reduced to practice. Free-induction decay (FID) in hot CO_2 has been used to generate pulses of 80-ps duration, and 300-ps pulses have been generated electro-optically. The latter approach will be used in the 250-ps oscillator being designed for the SBS. Extensive measurements were made on solid-state (p-type germanium), and on gaseous (SF_6, NH_2D, and C_2H_4) saturable absorbers. The solid-state device is a reliable interstage isolator for beam fluxes up to 0.5 GW/cm^2. Tests on the gases showed only partial bleaching and the ability to withstand larger optical fluxes. Helium-free laser-gas mixtures were studied experimentally and theoretically, showing greater pumping efficiency, greater energy storage, and faster rotational relaxation than the standard helium-rich mixtures. However, the higher operating voltages required by these mixtures may pose difficult engineering problems. Small-signal gain of up to 0.07 cm^{-1} was achieved in an electron-beam-preionized, self-sustained discharge in a helium-free mixture at 900 torr.

Advanced Laser Research

Research is continuing on potential high-energy, short-wavelength lasers for fusion. This investigation has been directed mainly toward the kinetics and excitation physics of rare-gas oxides ($\lambda \approx 557$ nm) and molecular mercury ($\lambda = 335$ nm). Kinetics studies of Xe_2 and ArO have been carried out with relativistic electron beams. Electrical discharge initiation has been achieved in Hg_2 above atmospheric pressure.

The physics of several possible new laser systems has been studied. These systems include the rare-gas excimers, rare-gas oxides, molecular mercury, and rare-gas dimers. Theoretical studies on the effect of electron collisions on excited-state kinetics have been initiated. Ab initio calculations have been performed to describe quantitatively the excited-state potential energy curves and transition matrix elements for the rare-gas oxides and Hg_2. The Hg_2 system was simulated by the analogous Zn_2 system; ArO was chosen for the initial studies of the rare-gas oxides. The calculated transition lifetime of 3 μs in ArO is considered to be in good agreement with the measured value of 10 μs. Calculations keyed to understanding the electronic structure of the excited states of F_2 and its ions have been completed.

Optical-damage studies of sputtered dielectric coatings are continuing, in an attempt to find damage-resistant materials for use in laser-fusion research. A breakdown fluence of 11 J/cm^2 has been achieved with 30-ps pulses at 1.06 μm.

The HF chemical laser program at LASL was discontinued in January 1976. In the final phase of this program, we defined and tested the components and techniques that would be needed in an HF oscillator/amplifier system designed to produce 10-J, 1-ns pulses that would meet the criteria on laser energy and low prepulse energy for flat-target irradiation experiments. The oscillator pulse would be linearly polarized and passed through an electro-optic crystal which would rotate the plane of polarization by 90° in a 1-ns portion of the oscillator pulse. After amplification, the pulse would pass through a Brewster-angle polarizer, oriented to reflect only the polarization of the 1-ns portion. Any prepulse energy would be caused by polarization impurity of the oscillator pulse, but it would see only saturated gain rather than the large unsaturated gain. Thus, the contrast ratio of pulse-to-prepulse energy would be the same after amplification as before. The F_2-H_2 amplifier would be activated by an axially propagated 2-MV electron beam, producing gain for ~20 ns.

Experiments were completed with a three-stage HF oscillator/amplifier system, using SF_6 and C_2H_6, which demonstrated for the first time the virtually complete extraction of the energy developed in an electron-beam-energized HF amplifier by an externally generated oscillator pulse. Gated rotation of the oscillator pulse produced a 4-ns pulse from this system, thus demonstrating the above pulse-generation scheme. We made progress in optimizing the performance and control of our electron-beam sources and in understanding electron-beam-energized F_2-H_2 amplifier media.

Target Experiments

Several advances were made in the diagnostics and understanding of target-interaction experiments with a CO_2 laser system delivering 150-J, 1-ns pulses and with a Nd:glass laser system delivering 10-J, 50-ps pulses.

A new charged-particle detector was used to observe d-d protons and d-t α-particles at KMSF, and d-d protons from a CO_2 target illuminated by our glass laser system. With these data, we calculated values of ρR (density x radius) for glass microballoons filled with D_2/T_2 and illuminated by two beams. Theoretical calculations were made on the α-particle spectra from microballoon targets and on the use of these spectra to deduce target compression.

Time-integrated data on the spectra and angular distribution of emitted electrons were taken in target experiments at 10.6 and 1.06 μm. The spectra could be fit by summing a set of single-temperature spectra.

We measured low-energy x rays from flat polyethylene targets; the cold K-lines of silicon, aluminum, and magnesium observed in 10.6-μm target work were identified as possible means of diagnosing target preheat by suprathermal electrons. Measurement of soft x-ray fluxes by a pinhole camera was begun in the CO_2 target-irradiation experiments.

Laser and Target Diagnostics

Automated data acquisition and reduction, calorimetry, and the spatial and temporal imaging of subkilovolt x rays were the major goals of our diagnostics development effort.

The Nd:glass laser-target system was improved significantly by using the minicomputer which runs the system for automatic data acqusition and reduction. Our analysis indicates that further automation will be cost- and manpower-effective.

We completed the designs for a proximity-focused streak tube with a predicted spatial resolution of 10 μm and a temporal resolution of < 2 ps. A contract was let for the production of visible and x-ray versions of the streak tube. Experimental results with a prototype tube were very encouraging.

Advances were made in calorimetry, ion-current detectors, and x-ray diagnostics. In diagnostic support of the glass-laser system, we developed a reliable pulse-selection system using a Pockels cell driven by a laser-induced krytron-switched Blumlein.

Target Design and Fabrication

We have continued our development of techniques to separate and characterize glass microballoons (GMBs). A quantitative evaluation of the "crunch" test showed that the GMB quality was substantially improved by our processing.

For evaluating the quality and measuring GMBs we have switched largely to optical interferometry because it offers higher resolution and is faster than microradiography. However, the development of microradiography is continuing to improve its resolution so that a proven technique will be available when needed for use with opaque microballoons.

Work on the deposition of high-strength metal shells has continued. We have determined that our chemical-vapor-deposited (CVD) molybdenum coatings [from $Mo(CO)_6$] are actually dimolybdenum carbide (Mo_2C) and we are now in the process of characterizing these carbide shells. Our control of the CVD process has been improved considerably by changes in equipment design.

We have continued our development of the electroless and the electroplating techniques by using the new apparatus that we developed, and a complete description of this apparatus is given.

Our cryogenic-target effort received considerable emphasis, and substantial progress has been made toward our first goal of providing uniform layers of DT ice frozen onto the inside surface of a microballoon container. Two techniques are being employed, either immersing the gas-filled microballoon in a low-pressure heat-exchange gas inside a cryostat or letting a jet of cold helium impinge directly onto the microballoon surface. Very encouraging results have been obtained with both techniques.

To attain an adequate two-dimensional target-design capability, LASNEX, a two-dimensional Lagrangian laser-fusion design code, was acquired from Lawrence Livermore Laboratory. In addition, we have selected for support and development one of the several two-dimensional codes under consideration at LASL. One-dimensional design studies, stability calculations, and hydrodynamic modeling of laser targets have continued.

Laser-target experiments continue to show evidence of anomalous behavior. Efforts to identify qualitatively the relevant plasma phenomena have been reasonably successful; however, efforts to identify these phenomena quantitatively have met extreme difficulties. The major difficulty lies in the complicated hydrodynamic behavior of the pellet, which is strongly dependent on the nonlinear plasma behavior. For example, the character of the plasma ablation can change the absorption from very large values to very small. We have continued to develop advanced hybrid and plasma codes which contain self-consistently some of these hydrodynamic effects.

In light of recent CO_2 experimental data suggesting low absorption, we are studying the important effect of self-consistent flow on stimulated scattering instabilities. Efforts to understand mechanisms that could limit electron-heat conduction have continued with the examination of several possibilities.

Applications of Laser Fusion -- Feasibility and Systems Studies

The major efforts of our recent feasibility and systems studies of commercial applications of laser fusion have included:

- Extensions of the computer program for simulation of fusion-pellet microexplosions in magnetic fields,
- Studies of reactor blanket designs with enhanced tritium breeding ratios,
- Systems studies of laser-fusion generating stations based on the magnetically protected reactor concept, and
- Studies of alternative applications of laser fusion.

The computer program for simulation of fusion-pellet microexplosions in magnetic fields is one of the principal investigative tools for use in engineering studies of the magnetically protected laser-fusion reactor concept. The capabilities of this code are being expanded to permit calculations for fusion pellets of arbitrary composition and to provide detailed information necessary for the design of the solenoids and energy-sink regions.

It may be advantageous to restrict tritium breeding to as few reactors as possible in multireactor generating stations or energy parks, permitting alternative designs of the remaining reactors that may not be compatible with the inclusion of lithium blankets around the reactor cavities. We have studied the effects on the tritium breeding ratio of the wetted-wall reactor concept if different structural materials are used, the use of beryllium as a neutron-moderating and multiplying material, and the possibility of enriching the lithium in the ^{6}Li isotope. The results indicate that adequate tritium breeding ratios can probably be obtained to permit freeing about half the reactors in a large installation from the necessity of breeding tritium.

Our previous detailed studies of electric generating stations based on the wetted-wall reactor design have indicated that the power level of magnetically protected reactors will be about ten times higher than that of wetted-wall reactors and will result in significantly different electric generating station concepts. We have completed the specification of components for a generating station that includes four magnetically protected reactors. The laser type is optional and may be CO_2, chemical HF, or some other type of high-efficiency gas laser. The power-conversion system is also optional, and the electric power output is in the range of 1100 to 1900 MW depending on the efficiencies of the selected conversion cycle and laser type.

Our investigation of the ^{239}Pu burner-^{233}U breeder laser-fusion/fission hybrid concept is continuing. We have completed an initial optimization of the blanket design for optimum ^{233}U breeding rate and power output. The present design, based on the wetted-wall reactor concept, would produce ~1000 MW of electric power, and the ^{233}U production rate would be $\sim$ 2 kg per day.

We have begun an investigation of the use of laser-fusion reactors as sources of process heat. The reactor blanket of our initial concept is replaced by a refractory material in which neutron and x-ray energy is deposited, and energy transfer from this region to an adjacent region of process fluid or chemical reactants is accomplished by radiation. The results of preliminary analyses indicate that the use of graphite and boron carbide as the energy deposition materials will permit operation of the radiating surface at temperatures exceeding 2000 K.

Resources, Facilities, and Operational Safety

There are 223 employees directly involved in the Laser-Fusion Program. Two of the three buildings in the new Laser-Fusion Laboratory complex are complete. The CO_2 Laser Laboratory has been occupied and the Eight-Beam System is being assembled. The Chemical Laser Building has been reassigned to CO_2 and advanced laser development, and occupancy has begun.

Installation of the target chamber and of the associated screen room in the Dual-Beam System is nearly complete. A reference design has been completed for the High-Energy Gas Laser Facility, and design tradeoff studies have been initiated. This facility is designed to produce a total intensity on target of 200 TW in a 200-ps pulse in six annular beams.

Safety policies and procedures continue to be applied successfully, with no lost-time accidents.

51,131

I. CO_2 LASER DEVELOPMENT

The research and development programs on high-energy, short-pulse CO_2 lasers were begun at LASL in 1969. Three large systems are now either operating or are being installed. The Single-Beam System (SBS), a four-stage prototype, was designed in 1971 and has been in operation since 1973 with an output energy of 250 J in a 1-ns pulse with an on-target intensity of 3.5 x 10^{14} W/cm². The Dual-Beam System (DBS), now in the final stages of electrical and optical checkout, will provide about ten times more power for two-beam target irradiation experiments. Four such dual-beam modules are being installed in the Laser-Fusion Laboratory to provide an Eight-Beam System (EBS) scheduled for operation at the 5- to 10-TW level in 1977. A fourth system, a 100- to 200-TW CO_2 laser, is being designed for the High-Energy Gas Laser Facility (HEGLF) program.

SINGLE-BEAM SYSTEM (SBS)

Introduction

Effort with the single-beam CO_2 system has been directed mainly toward target experiments and laser operation. After several modifications, the oscillator output was increased about tenfold in a 1-ns pulse. Much effort was also devoted to measuring the output extinction ratio and the oscillation threshold. These topics are discussed in detail in subsequent paragraphs.

Oscillator Improvement

The oscillator of this system was modified extensively. We added an improved ultraviolet (uv) preionized discharge and optimized the gas mixture. Mirrors of larger focal length were installed to increase the mode volume. These two changes increased the energy output about tenfold. A second electro-optic shutter was added to improve the contrast ratio of the pulse switchout.

The new oscillator is shown schematically in Fig. 1. Part of the output transmitted through the

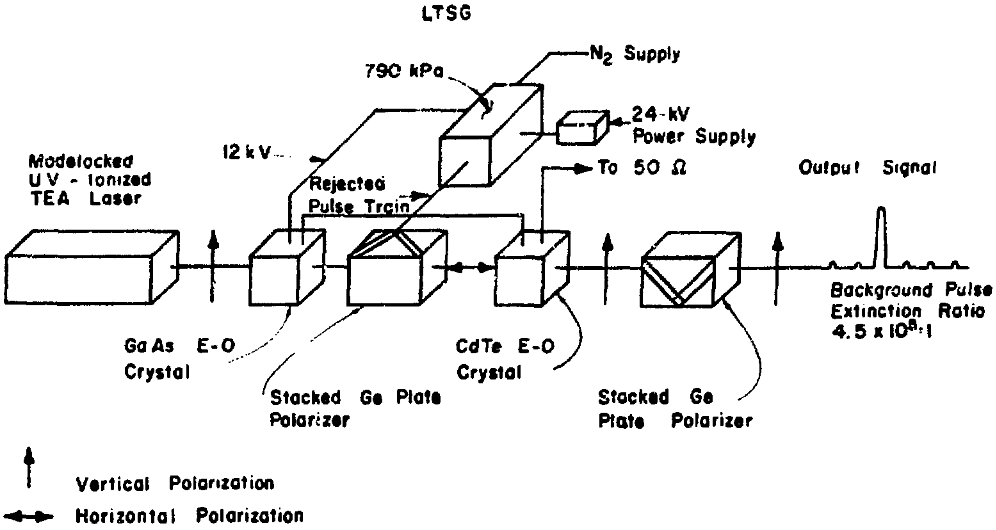

Fig. 1. Schematic of oscillator modifications in single-beam CO_2 laser system.

7-43

first electro-optic crystal was used to fire the laser-triggered spark gap (LTSG), which operated the two switches. Transmission lines and crystal holders were matched to 50 Ω.

We measured the extinction ratio of the double electro-optic switch with a Santa Barbara Research LHe-cooled Ge:Hg detector (risetime, 400 ps) and calibrated attenuators. The observed prepulse-intensity extinction ratio was 4.5×10^5, and the oscillator output energy was 2 mJ in a single nanosecond pulse.

With the improved oscillator, the first two preamplifiers of the SBS now produce a 2-J pulse having an integrated background energy of 30 μJ. Previously, the pulse energy at this location was ~ 20% of that observed with the new configuration.

Self-Oscillation and Extinction Measurements

Interpretation of target experiments has been complicated by the presence of prepulses arising either from self-oscillation of the amplifier chain or from inadequate energy extinction in the oscillator Pockels cells. Such energy may cause either the disintegration of the target or plasma formation before the amplified laser pulse arrives. Obviously, self-lasing is more serious for targets oriented normal to the beam path, and some experiments have required this orientation.

We have made some measurements to determine the threshold for melting caused by 10-μm laser light focused on 1000-Å-thick plastic films under vacuum. This threshold was 50 μJ for a 1.5-ns FWHM pulse. Experiments also demonstrated that the integrated prepulse energy could be reduced to this threshold with the addition of two absorption cells containing mixtures of SF_6 at 3 and 8 torr-cm, respectively, and helium at a partial pressure of 200 torr. The effective absorption coefficient for the P(20) line (10-μm band) was higher with the SF_6:He mixture than with pure SF_6.

In a subsequent experiment we determined that the threshold energy for plasma formation with a 1000-Å-thick plastic film target is ~ 1 mJ for a 1.5-ns FWHM pulse; this level is at least 20 times higher than the melting threshold for the film. The plasma shortened the risetime of the pulse transmitted by the plastic target.

Self-oscillation of the amplifier chain lasted for ~ 1 μs. Typically, this signal arrived at the target later than the main laser pulse, although the time of arrival of the self-oscillation signal depended on both the system operating parameters and the target configuration employed.

Beam Quality Measurements

With the existing beam line and improved optical components, we determined the target irradiance delivered by the SBS to be 3.4×10^{14} W/cm^2 for the 100-J nanosecond pulse. These measurements were made by using a transmission grating and Kalvar film.

DUAL-BEAM SYSTEM (DBS)

Introduction

The main goals of the two-beam laser program are to verify the performance of the laser module for the eight-beam, 10-TW laser system and to serve as a short-pulse laser system for the irradiation of targets at the 1- to 5-TW level. Many performance objectives of the prototype system have been attained. We operated the south chamber of the DBS reliably at 90% of its electrical design level, installed the triple-pass optical system in the north chamber of the DBS, yielding 600-J, 1.4-ns pulses, and concluded our studies on the use of NH_2D as a saturable gain suppressor. The facility is being prepared for target experiments by the installation of the target-area screen room and of a diagnostics trailer outside the facility.

Oscillator-Preamplifier System

To perform energy-extraction experiments on the north pumping chamber, we modified the oscillator to operate at 10-μm-band wavelengths other than the P(20) line. The P(16), P(20), and P(22) lines were obtained by inserting a NH_2D saturable absorber cell in the cavity. With an 8-cm-long cell filled with NH_2D to 107 torr, we extracted 0.85 J from the second preamplifier. An SF_6 cell was also employed between the first two preamplifiers (PA-1 and PA-2) to improve the prepulse contrast ratio.

We installed an optical system after the second preamplifier to provide two input beams for the

DBS. This system consisted of a one-dimensional Galilean beam expander to elongate the beam cross section in a 2:1 aspect ratio, followed by a 90°-wedged copper beam-splitting mirror. Two concave cylindrical mirrors, with radii of 250 and 500 cm, respectively, were used in the expander. The line focus produced between the mirrors was employed as a one-dimensional beam spatial filter, providing some geometrical isolation against optical feedback from the DBS.

To avoid breakdown at the cylindrical focus, we reduced the input energy to ~ 1 J by inserting 14-torr SF_6 into the gas cell between PA-1 and PA-2. The net result of the splitter-isolator optics was an output of ~ 200 mJ per beam in a spatially clean 1-ns pulse characterized by a nearly square cross section and a somewhat asymmetrical energy distribution. This duration represents some pulse-shortening.

A sensitive, LHe, mercury-doped germanium detector was used to examine the oscillator output. Preliminary results indicate that some radiation around 5 μm (presumably due to frequency doubling in the GaAs switchout crystal) is present early in the pulse train. The prepulse energy we observed is less than 1 μJ at the output of the second preamplifier. Thus, the use of pure SF_6 in the cell between PA-1 and PA-2 increased the prepulse contrast ratio to ~ 10^9.

Dual-Beam System (DBS)

Electron-Gun Development -- We used electron radiography in the continuing study of our cold-cathode electron gun. The spatial distribution of the electron emission was observed at several stages during the development of the gun; we placed sealed x-ray film in nearly direct contact with the outside surface of the electron-beam window over its full area and obtained exposures for pulse durations of ~ 0.5, 2.0, and 5.0 μs. The emission process in the single-foil cold-cathode device may now be characterized as follows:

- Emission starts at a limited number of points, perhaps 10 to 20, separated by ~ 5 to 10 cm.
- The beam patterns at the window have rounded tops and sharp sides. Occasionally, the edges of two adjacent patterns overlap and produce a region of relatively high electron intensity.
- As the pulse duration increases, the number of emission sites increases slightly.
- The total electron-beam emission current increases with time, doubling or tripling (4000 to ~ 10 000 A) in ~ 5 μs. In the Child-Langmuir model of space-charge-limited emission, the current varies with the applied potential, V, according to a $V^{3/2}$ law, and inversely as the square of the effective anode-cathode spacing $(d-v_0t)$ where d is the gap spacing and v_0 the gap plasma closure velocity. The observed behavior is not consistent with this model. Instead,
- We believe that the observed time variation is consistent with a model in which the emission varies due to the transverse spread of plasma at velocities of ~ 1 cm/μs. In other words, the major source of emission increase is the increase of effective cathode area with time. In this model the expansion of the plasma towards the anode does not play the dominant role.
- The height of the electron beam at the beginning of the pulse is ~ 25 cm and increases to ~ 35 cm in ~ 3 μs. The top and bottom edges of the beam are sharply delineated, presumably due to the focusing action of the field-forming electrode. These observations are in agreement with the qualitative predictions of our electron ray-tracing program.
- It is tempting to think of the cold-cathode gun as a device that begins to emit a copious electron beam within a small fraction of a microsecond. Instead, it appears that the emission early in the pulse is spotty and irregular. Therefore, significant variations in the electric field of the gas discharge may exist during the first microsecond of its development.

A final feature of the cold-cathode operation deserves a more detailed discussion. Despite a two- to threefold rise in electron-beam current during the pulse, the measured gas-discharge current remains nearly constant, although one would expect the gas current to increase as the square root of the electron-beam current. However, this discrepancy is now understood to be due to the finite impedance of the power supply and to the electric-field dependence of the recombination coefficient.

The gas current is given by

$$I_g = n_e e v = \sqrt{\frac{J}{\alpha}}\,\mu\,\frac{V}{d} \times \text{const} , \qquad (1)$$

where n_e and v are the electron density and velocity, J is the electron-beam current, α is the recombination coefficient, V/d is the mean electric field, and μ is the electron mobility. In the V/d range of interest, $\alpha \sim (V/d)^{-2}$, so that

$$I_g = \text{const} \times \sqrt{J}\ V^2 . \qquad (2)$$

By computing $dI_g/dt = (\partial I_g/\partial J)(dJ/dt) + (\partial I_g/\partial V)(dV/dt)$ from these equations, one can show that $dI_g/dt = 0$ when

$$\frac{dJ}{dt} = \frac{4J}{R_g C_p} = 1.8 \times 10^9 \text{ A/s} \quad . \qquad (3)$$

In Eq. (3), R_g is the gas resistance and C_p the pulser capacitance. In other words, if J is increasing at a rate of 1.8×10^9 A/s, dI_g/dt will be nearly zero. The value of J is known to increase almost linearly with time, and near the middle of the pulse the observed value of dJ/dt is $\sim 1.4 \times 10^9$ A/s, sufficiently close to the computed value for us to expect that I_g is nearly independent of J over much of the pulse duration.

Late in 1975 we installed an improved cold cathode, which consists of two tantalum foils on each side of the cathode frame, offset from the center line and displaced toward the windows by 0.8 cm. X-ray pictures of the electron distribution after this change indicated that the electron beam more nearly filled the entire 35-cm by 200-cm window than with the single-foil cathode. Measurements of the gain in the north pumping chamber indicated slightly improved performance.

Small-Signal Gain Measurements -- We have measured the spatial variation of small-signal gain in the north pumping chamber at 10.59 μm. Operating conditions were 1300 torr of standard 3:1/4:1:: He:Ne:CO_2 laser gas mixture, a discharge voltage of $\sim$200 kV, and a discharge current of $\sim$10 A/cm^2. Main results of this work were

- The center-line gain was 0.028 cm^{-1}, in fair agreement with the predictions of our kinetic code.
- The gain is reduced to 0.023 cm^{-1} near the top of the gain medium, presumably because of electron-beam nonuniformity.
- The measured gain was 0.033 cm^{-1} in the region adjacent to the anode. While electric-field enhancement due to electron depletion should increase the gain in this region, our calculations predict a somewhat larger gain enhancement than we observed.

Triple-Pass System Optical Stability Studies-- The threshold for self-oscillation was determined for two configurations of the DBS optical system. First, we studied the round-trip stability of the module with the 40-cm-diam final collimating mirror installed. After we gained sufficient experience in optimizing the oscillation threshold with this arrangement, we repeated the study with both elements of the triple-pass optical train in place. We then completed our initial energy-extraction measurements in the triple-pass configuration.

A conservative analysis of the round-trip configuration shows that the threshold for oscillation will be exceeded if

$$r_d \geq L_0^2/Ae^{2g_0L} , \qquad (4)$$

where L_0 is the total chamber length, L is the length of the gain medium, r_d is the effective reflectivity, and A the area of the diffuse black plate opposite the collimating mirror in these tests. The operating point for marginal stability of the pumping chamber was 200 kV and a fill pressure of 1300 torr, corresponding to a center-line gain coefficient of 0.027% cm^{-1}. With A $\sim$ 1500 cm^2, Eq. (4) gives $r_d \sim 0.01$; this reflectivity value agrees with direct measurements of the interral diffuse reflectivity of the DBS cavity. The maximum center-line gain coefficient for marginal stability against self-oscillation was also 0.027 cm^{-1} when the triple-pass optics were installed.

Diffraction-coupling between the triple-pass mirrors has long been identified as a source of positive feedback in this design. It was this recognition that led to the adoption of the diagonal off-axis Cassegrain configuration to reduce diffraction feedback. Theoretical estimates of the round-trip gain needed to produce oscillation in this design suggest that the unstable resonator mode may become important for gain coefficients of the order 0.04 cm^{-1}. Thus, our measurements verify that diffraction is less important than diffuse reflection as a source of regeneration in our system.

Measurements of optimum energy extraction in the triple-pass system were made on the 1.2-ns preamplifier signal injected at the time of peak gain, while the DBS was operated below the observed instability threshold. In this measurement, 10.6 J was obtained with a 4.45-cm-diam sampling aperture. This energy corresponds to a beam flux of 680 mJ/cm^2, many times the saturation flux of the medium. Because heavy saturation will give a relatively flat transverse profile for the output beam, extrapolation of the measured output energy to the 34-cm design beam diameter gives an estimated short-pulse energy extraction of 620 J.

Gain Suppression Using NH_2D -- We made a series of measurements to determine whether the addition of deuterated ammonia to the pumping chamber would increase the extractable energies. The general conclusion reached was that it would not. The results of this gain-suppression study are:

- For the P(20) wavelength (10-μm band) the extractable energy is 10 to 20% less with the addition of deuterated ammonia, despite a much greater electrical input energy.
- For the P(22) wavelength (10-μm band) the addition of deuterated ammonia slightly increases the extractable energy, because the ammonia absorption coefficient at P(22) is 3.3 times smaller than at P(20).
- Deuterated ammonia interferes with the pumping kinetics to some extent, and is destroyed rapidly in the discharge.
- The saturation flux of deuterated ammonia on P(20) is at least 100 mJ/cm^2.
- The saturation flux on P(22) was much higher than 100 mJ/cm^2, and the saturation energy (product of small-signal absorption and saturation flux) is probably constant.

Reflected-Pulse Isolation by Inverse Bremsstrahlung -- A major concern in using the DBS for target experiments is damage to various optical components by laser energy reflected from the target. The 8-cm-diam input mirror is particularly vulnerable due to the large spatial compression of the reflected beam. Ignoring losses and assuming 1% residual gain in the medium, the flux on this mirror could reach 100 J/cm^2, well over damage threshold.

The actual flux reaching the mirror will be limited by optical breakdown of the laser medium. To evaluate this flux, we carried out numerical calculations of inverse-bremsstrahlung absorption in the region adjacent to the input mirror. The electron density, η_e, as a function of the intensity, I, is calculated in 0.75-mm zones, by using the relation

$$\eta_e(I+1) = \eta_e(I)\ (1 + \frac{\Delta t}{t_g})\ , \qquad (5)$$

where t_g is a function of optical intensity, pressure, and gas mixture. Experimental values of t_g for a 3:1:1::He:N_2:CO_2 mixture were used in the calculations.

For an initial electron density of 10^6 cm^{-3}, the maximum flux reaching the input mirror was 6.6 J/cm^2. The flux, which passed twice through the breakdown plasma and reached the input window, was 4.9 J/cm^2.

Greater mirror protection could be achieved by preionizing the gas adjacent to the input mirror. For example, if the initial electron density were 10^{12} cm^{-3}, the flux incident on the mirror would be reduced to 3.9 J/cm^2 and the reflected energy flux would decrease to 3.4 J/cm^2. Because electron densities of 10^{12} cm^{-3} and higher can be achieved with modest electron-beam currents, preionizing the gas may be a viable method of protection against reflected pulses.

Additional numerical calculations were made to determine the optical flux that can be transmitted without attenuation by optical breakdown. Table I summarizes the results for a pressure of 3600 torr with a 3:1:1::He:N_2:CO_2 mixture. It appears that a flux of 2 J/cm^2 is easily handled for all but the shortest pulse lengths and highest initial electron densities expected. In particular, it is anticipated that a 250-ps laser pulse having a flux of 2 J/cm^2 would suffer negligible loss in a helium-free mixture.

Status of Optical Components

NaCl Windows -- Fabrication of the 40-cm-diam, 7-cm-thick "Polytran" salt windows at Harshaw Chemical Co. is nearly complete; six have been forged, four of which have been polished and shipped. All seem to be of very good quality and one will be installed in the DBS soon. Delivery of the last two windows is expected in January 1976.

Y-12 Mirror Tests -- The large mirrors for the DBS facility have been evaluated optically. The surfaces have been examined visually for gross defects and the contour was evaluated interferometrically. The concave elements were evaluated from the center of curvature by using an unequal-path interferometer, whereas the flat elements were examined interferometrically in the Ritchey-Common Test with an excellent 30.5-cm-diam spherical mirror as the reference surface.

Tests were performed to determine the repeatability, drift rate, and stability of the motor-driven mirror mounts being fabricated for the triple-pass optical systems; results are shown in Table II.

Target Positioning Assembly -- The DBS target positioner and a prototype target pedestal have been fabricated. Tests were performed to determine the repeatability and stepping size of each actuator on the assembly. The results are presented in Table III.

TABLE I

*CALCULATED ENERGY FLUX FOR 0.01-cm^{-1} ABSORPTION, AS A FUNCTION OF PULSEWIDTH AND INITIAL ELECTRON DENSITY, η_{ei}.**

Pulsewidth (FWHM) (ns)	Energy Flux at Different Initial Electron Densities (Jcm^{-2}) $\eta_{ei} = 10^6$ cm^{-3}	 $\eta_{ei} = 10^{12}$ cm^{-3}
0.84	6.02	2.88
0.42	4.93	2.25
0.21	4.8	1.86

---

*3:1:1::He:N_2:CO_2 mixture at 3600 torr.

TABLE II

SUMMARY OF MIRROR MOUNT TESTS

Motion	Angular Step Size (μrad)	Drift Rate (μrad min^{-1})	Maximum Excursion (μrad)
Altitude	2	0.01 (< 3 h) 0.0021 (> 3 h)	3.0
Azimuth	2	0.008 (≤ 3 h) 0.0009 (> 3 h)	1.3
Rigid Mount Data (used for comparison)		0.01 (≤ 3 h) 0.0006 (> 3 h)	3.0

TABLE III

SUMMARY OF TARGET POSITIONER TESTS

Motion	Linear Step Size (μm)	Repeatability (μm)
Indexing	30.0	≤ 12
Vertical	0.63	<< 10
Lateral	2.9	<< 10
Focus	2.9	<< 10

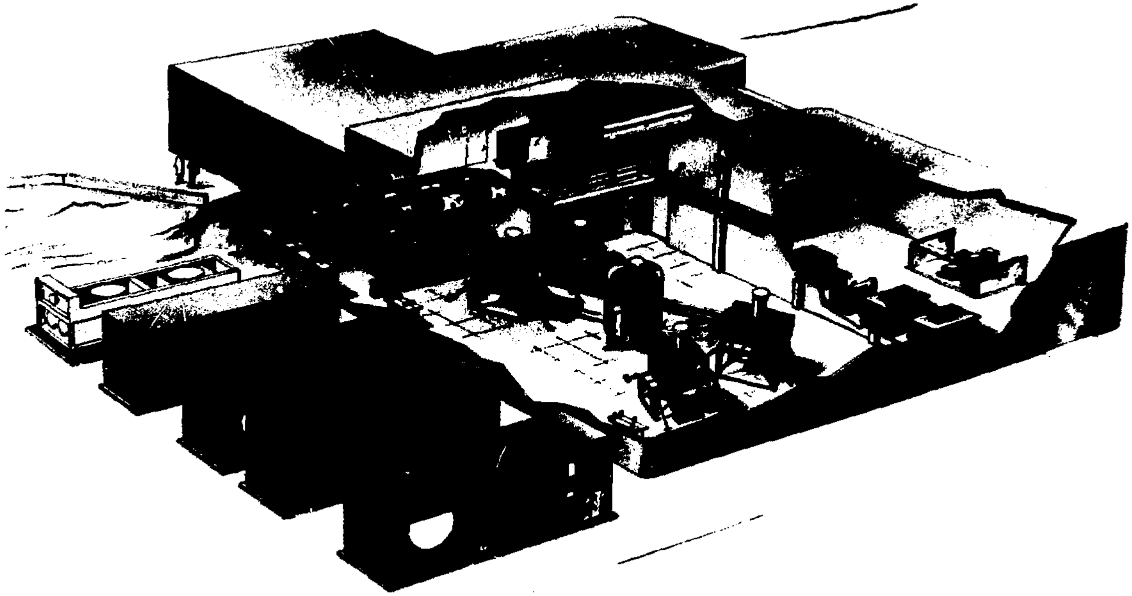

Fig. 2. Equipment layout for eight-beam CO_2 laser system.

EIGHT-BEAM CO_2 LASER SYSTEM

Introduction

In this section, we will discuss the current status of the design, procurement, fabrication, installation, and checkout of the various components and systems for the Eight-Beam CO_2 Laser System. Beneficial occupancy of a portion of the CO_2 Laser Building, TSL-86, which houses this laser, and of the outside pads for the pulse-forming networks took place on August 28, 1975 The remainder of the building with the exception of the building-equipment room, was turned over to us in October 1975. The layout of the principal equipment is shown in Fig. 2.

Master Oscillator and Preamplifiers

The base-line design for the Eight-Beam CO_2 Laser System was based on a pulse input of 1-ns duration. Higher target irradiances in the future will necessitate a phased upgrading of the oscillator/preamplifier systems. (Work on a 250-ps oscillator is discussed in a later section.) We will conduct a series of evaluations on the existing preamplifiers to determine whether they may be operated successfully at 1500 torr. If not, we will develop a new design to provide the necessary preamplification hardware.

Prior to installation of the 250-ps system, we will install a 1-ns system to permit integration of the front-end control systems and evaluation of the dual-beam power modules without interruption.

We investigated the parameters of the beam-transport system for the front end by using our pulse-propagation code. The results show that, in the absence of saturable absorber cells between the preamplifiers, a single-line pulse is broadened from an initial value of 1 ns (FWHM) to slightly over 2 ns (FWHM) if the preamplifiers are operated at 600 torr with a gain of 0.038 cm^{-1}. A parametric study is under way to identify means of minimizing temporal pulse broadening, and thus, to produce the required beam characteristics at the input to the dual beam-amplifier modules.

All optical supports have been procured and placed in position in TSL-86; final assembly of these supports has begun, and will be followed by the assembly and installation of the motor-driven mirror mounts.

Vacuum System

All components for the vacuum system have been delivered and the roughing-pump packages have been installed. These systems are being evaluated.

Control System

All vacuum-control systems chassis have been fabricated and are being installed. Evaluation of the digital ionization gauge-control system has been completed; this evaluation included successful tests in an RFI-EMI (electro-magnetic interference) environment simulating the environment anticipated for operations in TSL-86.

All spark-gap gas-control systems, with the exception of the SF_6 gas control, have been fabricated and are being installed, as are the laser gas-control systems. Some modifications of the latter will be required so that they may be used with the 250-ps front-end oscillator.

The high-voltage controllers and circuit breakers for the 50-kV supplies are complete and are being installed. Circuit boards for both the krytron pulsers and the pulsers for the oscillators and preamplifiers are also complete.

The safety-control system is being designed. Four areas of control are being provided, depending upon what equipment is being operated:

- Oscillator and preamplifiers only;
- Oscillator and preamplifiers with beams into the experimental area;
- Electron-beam pulsers and gas pulsers only;
- Entire system.

Computer System Status

The computer has been installed in TSL-86 and was used to check out the CAMAC modules, crates, and interconnecting cables. Several defective CAMAC modules were returned to the supplier. The first set of CAMAC channel-information cards, which describe the gas-pulser system, was successfully processed with the computer. In addition, certain operational functions of the PFN (pulse-forming network) control systems have been tied into, and checked out, with the computer.

Additional items have been ordered to increase the versatility and capability of the computer system.

Pulse-Forming Networks (PFNs)

Tests on the prototype unit have been completed successfully. All equipment for the eight PFNs, including controls for manual operation, has been procured, assembled, and installed on the pads next to TSL-86. The performance of the first unit is being characterized with an appropriate simulated load. All high-voltage-pulse coaxial cables have been run from the PFN tanks into the building and were terminated at the outside ends. The cables will be cut to correct length and terminated at the inside ends after assembly of the main power amplifiers.

Experiments are under way to develop an overvoltage protection switch for the PFNs capable of withstanding open-circuit load conditions. Presently, a point-plane gap design (Fig. 3) is being studied to determine its voltage hold-off characteristics and breakdown delay. The "point" is, in reality, a hollow, sharp-edged, stainless steel tube, whereas the "plane" is either a stainless steel plate or a 5-cm-diam brass ball. The latter was used in some experiments to increase the external stand-off capability of the test switch. The measured breakdown voltages versus pressure for various spacings and for positive or negative polarity are shown in Fig. 4. Our tests indicated that best operation was obtained with the point electrode at negative potential. This polarity of the gap results in more linear breakdown and shorter gap spacing. The long-term reliability and reproducibility of this switch, and its response to a slowly rising pulse, remain to be determined.

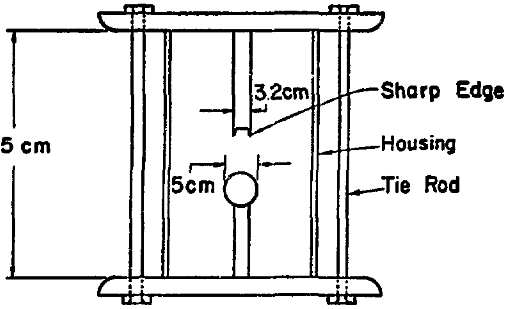

Fig. 3. Construction of point-plane spark gap.

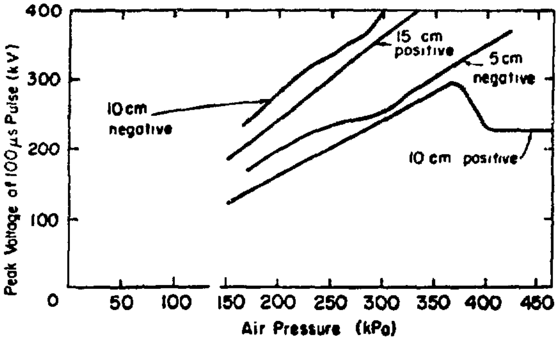

Fig. 4. Measured breakdown voltage vs pressure for several electrode spacings and alternate polarity in point-plane gap.

Main Power Amplifier Hardware

About 80% of the hardware for the four dual-beam modules has been designed and procured. Assembly and installation of the support stands is 70% complete, and assembly of the first dual-beam module is under way.

Optical Components

The final design and fabrication of the folding mirrors for the Eight-Beam CO_2 System will necessarily depend on results from the DBS. Because the folding optics are spherical, they should present no problem in procurement.

We have designed our large turning and focusing mirrors with handling problems in mind. We will use aluminum substrates with 0.381-mm (0.015-in.)-thick bonded copper surfaces. The required optical surface will be obtained by diamond-turning the copper surface.

The flat turning mirrors present no major problem in procurement; they can be fabricated with little difficulty either at Y-12 or in industry.

The purchase order for twenty 40.6-cm-diam NaCl windows has been written and is awaiting authorization before being placed with Harshaw Chemical Co.

Electron-Beam Pulsers

All electron-beam pulsers have been delivered, and assembly and testing are well under way. Initial tests will be made with a simulated load, prior to full-scale tests with an electron gun in the dual-beam module.

Target Optics

A request for proposal (RFP) for the target-area subsystem has been prepared and sent to nine companies. The RFP specifies four tasks:

- Conceptual design of the mirror mounts and mechanical control systems; of the optics mounting support structure, target chamber, and vacuum system; and of a pointing and tracking system;
- Hard design and fabrication drawings for all above items other than target chamber and vacuum system;
- Hard design and fabrication drawings for the target chamber along with the specifications for the vacuum system; and
- Fabrication of the necessary hardware.

HIGH-ENERGY GAS LASER FACILITY

Introduction

Reference design for the LASL's High-Energy Gas Laser System (HEGLF) specifies an output energy of 100 kJ delivered in a 1-ns pulse on one line in the 10-μm CO_2 band. Subsequent analysis indicates that other combinations of energy, power, and time are desirable and can be met within the original scope. Regardless of the energy-time specification the general concept is unchanged, and HEGLF is the next logical step beyond the eight-beam 5- to 10-TW system now under construction. Six annular power amplifiers will be used to generate energy for delivery to targets. An artist's rendering of a double-pass, annular power amplifier is shown in Fig. 5. The power amplifiers are driven by an optical front end that includes an oscillator, preamplifiers, and driver stages. The six high-energy beams propagate through evacuated lines to a target chamber housed in a separate building underground.

Comprehensive design studies now in progress are directed toward the objective of maximizing operational flexibility while meeting the performance

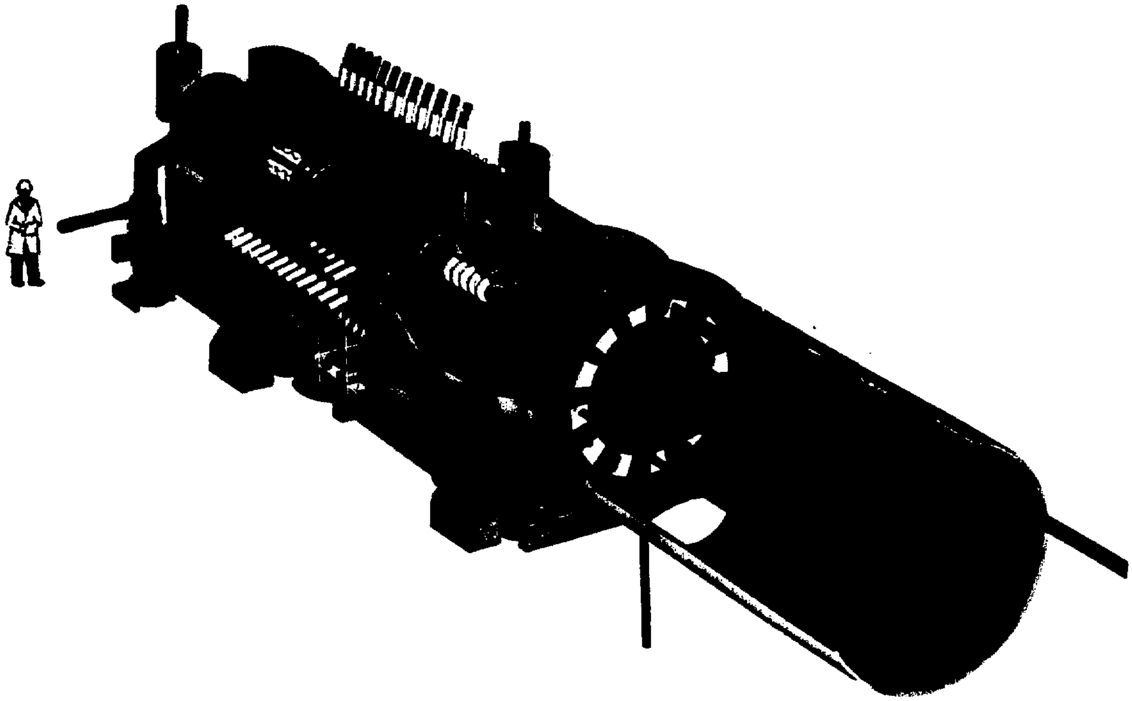

Fig. 5. HEGLF double-pass annular power amplifier.

specifications. These studies are not complete, so that the following presentation must be regarded as representative of the scope and breadth of the design tradeoffs, indicating trends rather than conclusions.

Front-End Reference Design

Introduction -- The particular front-end design chosen for the HEGLF depends critically on power-amplifier parameters, the operating design point, inefficiencies due to isolation devices, and the optical configuration. The following reference design criteria for 200-TW peak power should be considered preliminary, subject to further modification and improvement as the exact configuration of the HEGLF emerges:

Power, TW	200
Pulse, ps (FWHM)	250
Modules	six with an optical aperture of 8333 cm/ module
Operating press., torr	2400
Laser mixture	0:1/4:1::He:N_2:CO_2
Frequency	three-line operation, single-band, 10.6-μm wavelength
Configuration	double-pass power amplifier
Gain, %/cm	3.75
Length, m	2.4

The performance of a double-pass power-amplifier module complying with these specifications has been calculated. The results listed in Table IV show that the required driver energy is a sensitive function of both the required output and the frequency spectrum of the oscillator. At the

TABLE IV

HEGLF MODULE POWER OUTPUT AS A FUNCTION OF SPECTRAL CONTENT OF DRIVING PULSE. $E_{in} = 10^{-3}$ J/cm^2 (8.3 J/module)

Lines/Band		I_{out}
10 μm	9 μm	(GW/cm^2)
1	0	3.20
2	0	4.37
3	0	5.03
1	1	5.23
2	2	7.00

design point of 200 TW and an output window area of 50 000 cm the required flux is 4 GW/cm^2; however, when a 25% allowance is made for window and mirror losses and for design contingency, the effective flux required increases to 5 GW/cm^2. Such a performance can be attained with either multiband or single-band front-end operation. Our front-end reference design is based on the more conservative of these two approaches, namely, a single-band oscillator/preamplifier.

System -- A layout of the reference HEGLF front end is shown in Fig. 6. The modular system is based on a single short-pulse generator followed by two preamplifiers. The preamplifiers operate at 2.5 atm (abs) to allow adequate bandwidth for the 250-ps pulses. The beam is then split into six parts followed by two more preamplifiers for each beam. Isolation and beam-forming optics are indicated schematically. The modular laser elements are assumed to have the following characteristics:

Short-pulse generator	250-ps pulse duration; 3-line/single-band operation; 1 mJ/pulse; double discharge.
Preamp. 1	10-cm^2 area by 120 cm long; operating pressure, 2.5 atm; small-signal gain, 3%/cm; double discharge.
Preamp. 2	50-cm^2 area by 100 cm long; operating pressure, 2.5 atm; small-signal gain, 3%/cm; double discharge.

The calculated output from this system is ~ 15 J/beam. Additional driver amplifiers may be required depending upon the design of the power-amplifier module.

Figure 6 also shows the beam-forming optics for proper illumination of the preamplifier stages. These elements incorporate vacuum spatial filters in the telescope design and provide both spatial cleanup of the beam and isolation against retroreflected signals. Also indicated in the front-end layout are the isolation modules; by combining solid and gaseous saturable absorbers isolation is provided against oscillator precursors. An additional design requirement is fast-rising gain in the preamplifier and driver stages: if the gain

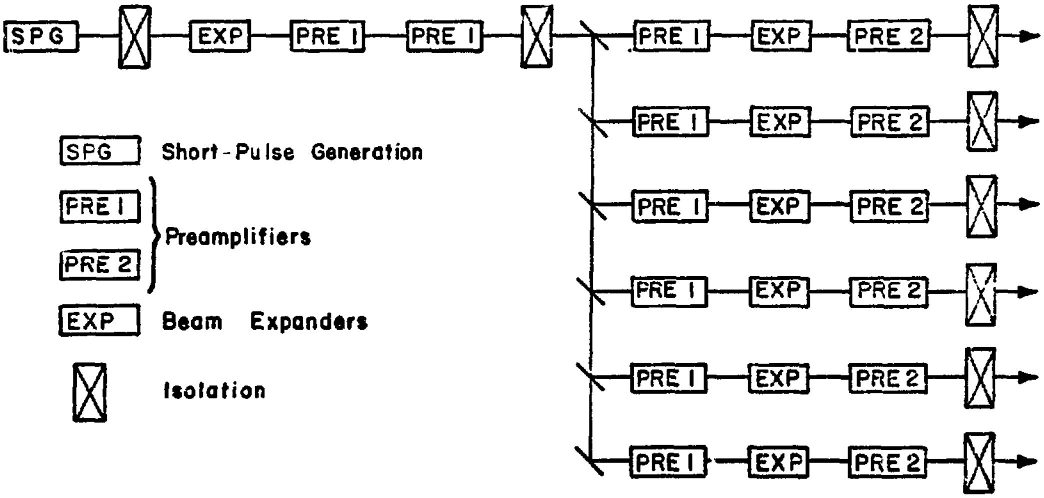

Fig. 6. Schematic of HEGLF front-end reference design.

risetime in these units is shorter than the oscillator-target transit time, lasing from the target is eliminated.

Power Amplifier Module

Experimental comparisons of helium-free and helium-rich CO_2 laser gas mixtures show that the helium-free mixtures are more efficient and store more energy for the same gain coefficient. In addition, the electrical impedance of the helium-free mixtures is greater than with helium. Consequently, a single axial, rather than multiple azimuthal, subdivision of the power amplifiers reduces the magnetic field associated with the gas current to a level that will not pinch the primary electron beam. As a result, both the mechanical and electrical design of the annular power amplifiers are considerably simplified and the power-supply impedance is increased about fourfold.

Data from gain standoff experiments with the DBS amplifiers indicate that a single-pass gain length product of 10 in some double-pass power amplifier designs will result in instability. We are investigating several alternative possibilities. They include interposing saturable absorbers within the amplifier and adoption of a single-pass design. An analysis of the single path amplifier is nearly complete.

Three versions of a single-pass power amplifier are being examined: (1) single-stage, constant area; (2) two-stage, constant area per stage (but different for each stage); and (3) two-stage, constant-area first stage and tapered second stage.

Certain basic assumptions are common to these studies:

- Allowable optical fluences for NaCl and metal mirrors are 2.2 and 6 J/cm^2, respectively;
- The gain coefficient varies as 1/r and, for a 20-cm-aperture, falls at the outer edge to 80% of the inner-edge value;
- About 80% of annular aperture area is available;
- The output with 1-ns, one-line operation is 17 kJ/module; and
- The gain lengths of the stages are chosen to be at a minimum consistent with the efficient use of stored energy.

Table V compares a variety of mechanical and electrical information for a two-stage single-pass power amplifier. Analysis shows that a constant area amplifier is quite inefficient in its use of stored energy. The two-stage amplifier with a tapered second stage is still being evaluated.

Pulse Power and High-Voltage Design

Conceptual Design Studies -- Preliminary conceptual studies for the electrical design identify the scope of requirements for the system. The basic specifications depend on electron-beam current density, gas mixture, gas energy density, voltages, impedances, and power-amplifier geometry.

The example summarized in Table V requires an operating voltage of 525 kV and delivered energy of ~520 kJ/module. The impedance is ~ 1.2 Ω.

If the annular anode is divided into 24 segments of 30 Ω each, impedance-matching requires 24 transmission lines (i.e., coaxial cables) of 30-Ω characteristic impedance. A mill run of 30-Ω polyethylene cable with a maximum stress of 960 V/mil and a diameter of ~ 3.5 cm is required.

The design of the pumping chamber is greatly simplified by virtue of axial rather than azimuthal subdivisions in the electrical circuit to reduce the magnetic fields. Capacitatively graded bushings for 500 kV are within the state of the art; uniform-field electrode profiles have been throughly studied and are described in the literature; and sufficient design information, as well as pressure and life-test data about the electron-beam window and window support structure, is available at LASL and elsewhere.

The energy can be stored in impedance-matched PFNs that are "Marxed" to the required voltage of 1080 kV. The use of cables as storage elements makes sense only for pulses shorter than 1 μs. Storage in water lines will lead to higher cost and does not seem warranted because of the requirement of a relatively slow risetime.

The selection of the optimum number of energy-storage modules for each power amplifier is a com-

TABLE V

PARAMETERS FOR A TWO-STAGE POWER AMPLIFIER

Assumptions:

80% of aperture optically available;

20% gain falloff with radius in Stage 2;

Stage 1 fast-pumped; and

Yield strength of polycrystalline salt is four times higher than single crystal value.

Parameters	Stage 1	Stage 2
g_o, small-signal gain (cm^{-1})	0.04	0.04
Length (cm)	175	225
g_oL, overall small-signal gain	7	9
Pressure for 0:1/4:1::He:N_2:CO_2 mix (torr)	2400	2400
E_{sat}, saturation energy (J/cm^2)	0.334	0.334
Gas voltage (kV)	250	525
Gas current density (A/cm^2)	20	5
Time to peak gain (μs)	0.5	2.0
Energy input (J/liter)	200	200
Stored energy, electrical, in optical aperture (kJ)	60	360
Interstage beam-expander magnification	$\sqrt{5}$	
Beam o.d. (cm)	89	198
Beam i.d. (cm)	69	158
Beam o.d. after output contractor (cm)	--	127
Beam i.d. after output contractor (cm)	--	101
Optical drive to Stage 1 (J)	2.0	--
Optical energy out, one line, 1 ns (J)	425	17,000
NaCl window thickness (cm)	3	6
Maximum flux density in beam (J/cm^2)	--	5.3

promise between considerations of economy, fault protection, and maintenance. The cost for storage and transmission is estimated at 35 to 40 ¢/J for a breakdown into four packages per module and at 50 to 55 ¢/J for twelve packages per module.

Reliability -- The most important aspect of all design considerations is reliability. We have made a preliminary examination of system reliability and of its impact on cost. Capacitors, spark-gap switches, high-voltage cables, and trigger generators have been singled out for closer inspection. Results are not yet available, but indications are that careful modeling and experimental design verification will be required to guarantee adequate reliability of vacuum and gas feedthrough insulators.

Pulse-Forming Networks

(1) Gas Insulation -- We have measured the optical absorption at 10 μm of several gases with high dielectric strength which are considered for PFN insulation. These gases were Freon-318, -114, -115, and -116. Of these, only Freon-116 did not have significant absorption with the 9- and 10-μm bands of CO_2. Freon-116 has a breakdown strength relative to air of 2 and is the least interesting of the dielectric gases. Previous data showed that Freon-12, and of course SF_6, absorb in this region of the spectrum. If a dielectric gas other than air or N_2 is to be used, special precautions will have to be taken to prevent gas leakage.

(2) PFN Circuit -- Two circuits are suitable for use in the high-voltage, high-power PFNs: the Guillemin Type-A and Type-C, shown in Fig. 7. The latter type is being installed in our Eight-Beam CO_2 Laser System.

Both networks have the advantage of requiring series inductance in the energy-storage capacitors. Because high-voltage capacitor systems have internal inductance, this inherent inductance is used for pulse-shaping.

The simplest technique to achieve high voltage is to use a Marx circuit (transformers may

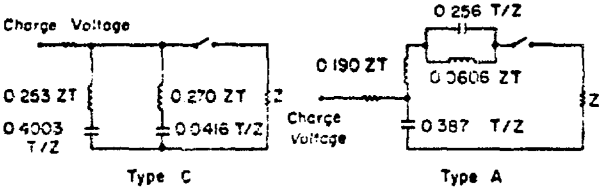

Fig. 7. Schematic of two-section Guillemin networks.

also be practical, see below) in which capacitors are charged in parallel and discharged in series. Looked at in this way, the Type-A network consists of a simple Marx generator with a series-resonant circuit, whereas Type-C consists of a Marx generator, each stage of which is a Guillemin network (see Fig. 8). Each stage of the Type-C PFN must be identical so that the stages generate pulses of equal length. Also, the geometry must be fairly simple and linear so as to control the inductance of the interconnections. The Type-A network allows more freedom in design, e.g., the current path may zigzag, to make the generator physically shorter.

The principal disadvantage of the Type-A network is the fact that the voltage at the terminal of the Marx generator is ~1.6 times the load voltage if all the inductance is internal to the Marx, and higher if some additional inductance is required. In the Type-C circuit, the highest voltage is the load voltage if the inductance is distributed through the stages.

The second, less serious, disadvantage of the Type-A network is the peculiar waveform of the pulse-shaping capacitors, C_2, which may adversely affect their life. The voltage waveform consists of one sinusoid, with a period somewhat longer than the effective pulse length. The peak voltage is 50% the load voltage and the reversal is 100% when operating into a matched impedance. When operating into a short circuit (electrical breakdown, or prefire into shorting relay), the peak voltage is somewhat less than the normal load voltage, with 100% reversal. There is little or no industrial experience with capacitors in this type of service. A testing and development program would be required to establish their lifetime under such operation.

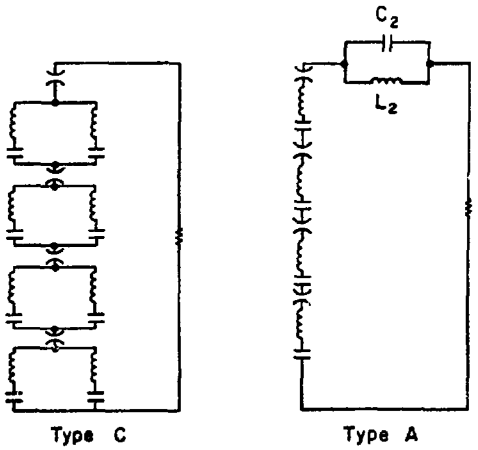

Fig. 8. Guillemin/Marx networks.

(3) Pulse Transformers -- One of the major energy-storage problems in the HEGLF is the availability of adequate high-voltage insulation. A step-up transformer would alleviate many of these problems. Of course, the secondary of the transformer would require insulation, but its volume would be much smaller than that of a PFN-Marx system. All capacitors would be run in parallel, with their cases at ground. The capacitors would be held in open racks, which would simplify both servicing and replacement.

A PFN pulse-transformer load system and its equivalent circuit are shown in Fig. 9. Clearly, the desirable features in a pulse transformer are low leakage inductance, L , and high primary inductance, L_p. Further analysis and some experiments are required to adequately evaluate transformers for HEGLF applications.

Large Optical Components

Diamond-Turned Mirrors -- The large mirrors for HEGLF must be lightweight copper-surfaced structures. Light weight may be achieved by cored aluminum structures, by honeycombed structures, or by welded aluminum structures. Copper surfaces are required because of the high reflectivity (~ 99%) and high damage threshold that are achieved with both diamond-tool finishing and conventional superpolishing.

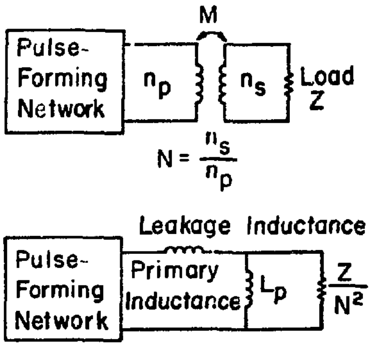

Fig. 9. Pulse-forming network with step-up transformer and equivalent circuit.

The large number of metal mirrors required may burden the conventional fabrication capability of the country when completion-time constraints are considered. Consequently, we have supported the diamond-tool turning program at the Y-12 plant at Oak Ridge. That plant has two machines capable of turning small and large mirrors: the Moore and Excello lathes. Their performance characteristics are listed below:

Moore Lathe (Actual)

Flats

Diameter (cm/in.)	Contour (μm)
Up to 15/6	0.3
Up to 63.5/25	1.2

Surface finish: 7.5×10^{-3} to 2.0×10^{-2} μm peak-to-valley.

Curves

Diameter (cm/in.)	Contour (μm)
Up to 15/6	0.45
Up to 63.5/25	1.9

Surface finish: 2.0×10^{-2} to 6.3×10^{-2} μm peak-to-valley.

Excello Lathe (Extrapolated)

Diameter (cm/in.)	Contour (μm)
Up to 203/80	~1.0

Surface finish: $\sim 7.5 \times 10^{-2}$ μm peak-to-valley.

Several mirrors have been fabricated for us with electroplated copper on aluminum substrates. Although satisfactory in regards to final-matching, electroplating produces an uncertain bond between the aluminum and the copper with a consequent high rate of rejection. We are investigating explosively bonded copper on aluminum, a process that may provide an alternative to electroplating.

NaCl Windows -- The production of NaCl windows is one of the critical items in the completion of the HEGLF system. Current production capability is one completed polycrystalline window per month; additional crystal-growing furnaces will therefore be required. Approaches to trebling the NaCl window production capacity are being examined.

Fresnel losses in the amplifier output NaCl windows are 10%. Considerable systems savings can be achieved if we develop damage-resistant antireflection coatings for the windows. The Naval Weapons Center and Optical Coatings Laboratory, Inc., (OCLI), are under contract to deposit coatings on NaCl. The Naval Weapons Center is developing polishing techniques to maintain both surface contour and finish and is evaluating antireflection coatings for these surfaces, whereas OCLI is investigating the application of these techniques for furnace-coating large (40-cm-diam) windows.

Optical Study -- Itek Corp. has completed a systems study on the HEGLF optical system. Details will be given in the next progress report. Itek has reviewed and evaluated the optical design with particular attention to the double-pass power amplifier, to diffraction effects, to the optical-error budget, and to manufacturing design and fabrications.

Instrumentation and Control

Control-System Policy -- Because of the large size of the facility and the large number of control functions, we have adopted an approach that calls for decentralized control. This control system is made up of separate Intelligent Control Centers (ICCs) located in small, shielded enclosures near the process being controlled.

Each ICC will incorporate several microprocessors, each of which will handle one or two specific tasks such as transmitting communications between the ICC and the supervisory computer, control of data-acquisition functions, and general control functions (e.g., beam alignment, sequence timing, and monitoring of system parameters).

Each ICC will communicate to a supervisory control computer over a fiber-optic high-speed serial data system. The operator issues commands to the ICCs through an interactive graphics terminal over the fiber-optics communication links. These links provide electrical isolation between the ICCs and the control room as well as immunity to the severe EMI environment of the laser-pulse power system.

Both the hardware and the software for the ICCs will be modular to provide flexibility in configuring the ICCs for a given control function.

Two supervisory minicomputers will be located in the control room: one for controlling and collecting data from the laser system; the other, to support the target experiments. Several ICCs will be associated with the target area. The target minicomputer will collect target data during a shot, display the data to the experimenters, and provide permanent records.

Fiber Optics -- The present state of the art of optical fibers, solid-state transmitters, and solid-state receivers recommends that a fiber-optic bundle of six to fifty fibers be adopted as the optical cable. Such a cable will provide reliability and mechanical integrity and is available at reasonable cost with losses of ~ 40 db/km.

The fiber-optic transmitter will require an infrared-light-emitting diode rather than laser diodes because the latter are not sufficiently reliable for this type of application.

The optical receiver will be a PIN photodiode-integrated amplifier detector. This device is well developed and does not require the special temperature-compensated high-voltage supplier needed by the high-gain avalanche photodetector.

With these components, available from several suppliers, data links ~ 50 m long, operating at 25 MHz with an error rate of less than one in 10^{12} bits, can be assembled. Components for such a link have been ordered for evaluation.

Microprocessors -- We conducted an extensive review of available microprocessors to determine which microprocessor would meet HEGLF requirements best for control, data acquisition, and data communication. Control functions demand a powerful input-output capability, whereas data acquisition requires efficient data handling in both the hardware and the instruction set. Motorola's M6800 miniprocessor was selected to meet the above requirements.

Shielding Calculations

In transport calculations performed to determine the nominal thickness of the biological shield for the HEGLF we assumed a point source of 14-MeV neutrons with a source strength of 4.5×10^{17} rem/pulse. The target building is a reinforced concrete shell with 0.61-m (2-ft)-thick walls and ceiling. Additional shielding is provided by surrounding the building with an earth berm. For 2.3 m (7 ft) or 3.05 m (10 ft) of additional earth (tuff) shielding, the dose rates near the outer surface of the shield are computed to be 5.2×10^{-3} and 1.9×10^{-4} rem/pulse, respectively. Based on 200 pulses/year, the latter figures convert to annual doses of 1.0 and 0.04 rem. The calculated annual dose at a radius of 33.5 m (110 ft) from the source, approximately the distance to the nearest uncontrolled area, is 0.07 and 0.002 rem for the 2.3- and 3.05-m-thick shields, respectively.

The transport calculations also yield information on neutron intensity and neutron spectrum in the target building. Reflection of the 14-MeV incident neutrons from the concrete walls produces a wealth of intermediate- and low-energy neutrons in the source enclosure, which can cause activation problems. The thermal and 14-MeV neutron fluences in the vicinity of the concrete walls were found to be comparable.

One of the locations for which a radiation-dose estimate is required is the control room. To make this estimate, we need to know the intensity and the spectrum of the neutrons emerging from the laser-beam lines into the laser building. As a first step, we set up a Monte Carlo calculation which includes the point neutron source, one of the six main laser-beam entrances and associated mirrors; and the floor, ceiling, and walls of the target building. Results of these initial calculations will provide the input for more detailed neutron tracking down the laser-beam lines.

PERT (Program Evaluation Review Technique)

Program control is by PERT. A preliminary network has been developed and the program is running. The eight major subnets are:

Building construction	Pulsed power
Prototype	Optics
Front end	Instrumentation
Power amplifier	Control.

About 1200 activities are tabulated, with an increase to 2000 anticipated.

SUPPORTING RESEARCH AND ANALYSIS

Introduction

The availability of subnanosecond CO_2 laser pulses is of increasing importance in experimental laser-fusion studies. Two methods of generating subnanosecond pulses of CO_2 radiation have been demonstrated successfully. One uses a free-induction-decay (FID) pulse generator, producing pulses of 80-ps duration with 50-ps risetimes, whereas the other employs a full-wave electro-optical switch to produce laser pulses of 300-ps (FWHM) duration. We have investigated several techniques of laser-target isolation. Doped germanium was shown to be a reliable laser isolator for beam fluxes up to 500 MW/cm^2; saturation measurements of SF_6 and NH_2D indicated that the absorption could not be entirely bleached in either gas for power levels up to 1 GW/cm^2; and high-power (400 MW/cm^2) transmission measurements in C_2H_4 showed that its absorption can be partially bleached, indicating potential utility of this gas for interstage isolation.

In a systematic experimental study we investigated the impact of helium-free laser-gas mixtures on the short-pulse performance of electron-beam-sustained CO_2 amplifiers. Performance was improved significantly, although higher operating voltages will be required.

We also studied the effect of laser-gas additives on gain suppression and improved pumping efficiency, as well as the use of radioactive additives to improve preionization. Exceptional performance was obtained from self-sustained (double-discharge) lasers with certain gas mixtures.

The effects of magnetic fields on the primary electron trajectories and in the main discharge have been analyzed. The use of gridded cold-cathode electron guns along with the use of higher impedance gas mixtures reduced the magnetic field effects to negligible levels.

In an analysis of the effects that the intensity-dependent index of refraction might have upon the optical quality of the output beam, we found that HEGLF operating intensities are far from the region of self-focusing damage; we also found that at intensities of $\sim 4 \times 10^9$ W/cm^2 in the NaCl window the focused intensities would be reduced by 20%.

Target-irradiation geometries for the Eight-Beam system have been analyzed for both two-sided symmetric illumination and isotropic illumination. These analyses and investigations are discussed below.

Subnanosecond Pulse Generation

Free-Induction Decay Pulse Generation -- We have utilized the optical analog of nuclear magnetic resonance (NMR) free-induction decay (FID) to generate ultrashort CO_2 laser pulses.[1] In this scheme, a temporally smoothed, long-duration CO_2 pulse is sharply terminated by optical breakdown in a gas.[2] The pulse then passes through a resonant gaseous absorber. Here, nearly total absorption occurs until input-pulse termination. If this termination is sufficiently rapid, the absorber reradiates the absorbed intensity by FID for a very brief interval, comparable to the molecular response time.

Additional understanding of this short-pulse-generation method may be gained by viewing it in the frequency domain. Here, abrupt truncation of the smoothed pulse causes a broadened spectrum to be superimposed on the original laser frequency. When this line-broadened pulse is passed through a narrow-band absorber, the carrier frequency is filtered out, leaving the broadened spectrum. The Fourier transform of this spectrally filtered pulse is a short pulse in time. The spectral content of the truncated pulse and the absorption linewidth of the absorber determine the pulse shape. Because the absorption linewidth is a function of pressure, the pulse shape can be varied by changing the pressure of the absorbing gas.

A simple analysis of the free-induction decay predicts an infinitely fast rise followed by an exponential decay, with the decay time τ_p, given by

$$\tau_p = \tau_2/\alpha L \; . \qquad (6)$$

Here τ_2 is the molecular dephasing time of the absorber and αL is the optical density of the hot CO_2 cell. At 30 torr and 725 K, we find $\alpha L \simeq 9.3$ and τ_2 = 64 ns-torr, so that the expected pulse duration is $\tau_p(\text{FW } 1/e^2) \simeq 230$ ps.

Figure 10 illustrates the experimental configuration. A standard TEA CO_2 uv- preionized laser

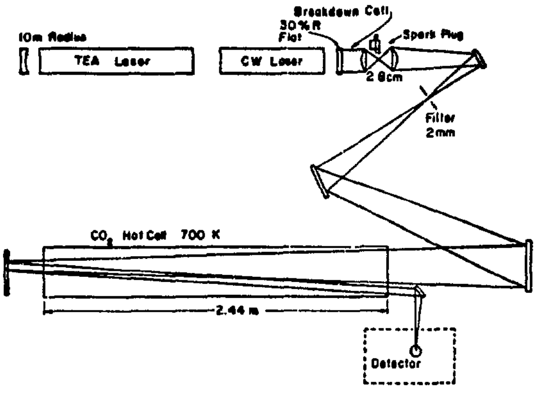

Fig. 10. Schematic of free-induction decay pulse generator.

chamber and a low-pressure cw CO_2 plasma tube were used for the oscillator gain medium. The combination of these two devices resulted in an output signal having a typical bandwidth of 50 to 100 MHz, sufficiently narrow to produce a smooth optical pulse of 50-ns duration.[3] This smoothed pulse was then admitted to the optical breakdown cell, recollimated, and transmitted to the resonant absorption cell.

The lens system focused the smoothed pulse to produce a controlled optical breakdown, abruptly truncating the pulse at peak intensity. The resulting signal was then passed through a spatial filter to prevent nonuniform bleaching of the absorber cell.

Finally, the beam was focused gently during two passes through the absorption cell, using an initial diameter of 45 mm to avoid absorber saturation.

The absorption cell was a 245-cm-long by 5-cm-diam pyrex tube, sealed at both ends with salt windows. The tube was heated to 725 K and filled with CO_2 to a pressure of 30 torr.

Figure 11 shows the observed pulse evolution. Figures 11a and 11b show the smoothed laser pulse before and after passing through the breakdown cell. The free-induction pulse from the absorber cell is shown in Fig. 11c as measured on a Tektronix 519 oscilloscope/Molectron P5-00 pyroelectric detector. The measured risetime is 300 ± 45 ps and the pulsewidth is 320 ps.

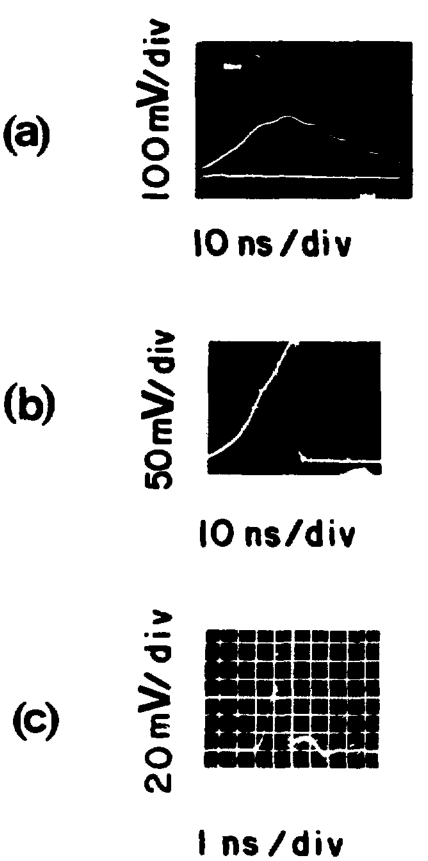

Fig. 11. Oscilloscope photos illustrating the process of free-inducation decay pulse generation. From top to bottom: (a) time-smoothed pulse as it enters the optical breakdown cell; (b) result of truncating this pulse in the breakdown cell; and (c) truncated pulse after hot CO_2 absorber.

By changing CO_2 pressure in the resonant absorber cell, pulses of varying duration can be generated. Figure 12 shows the pulse as measured with a Duguay shutter/streak camera system[4] for an absorber pressure of 200 torr. Pulses as short as 80 ps have been measured with this system, with detector-limited risetimes approaching 50 ps.

Electro-Optical Pulse Generation -- The transmission of a linearly polarized beam through a Pockels cell is directly dependent on the voltage applied to the crystal. In our earlier devices, the polarization was rotated 90° by a fast high-voltage pulse to permit maximum transmission through a Brewster-angle, stacked-plate polarizer. Conventional electronic circuitry permitted generation of a 1-ns pulse of CO_2 radiation. By doubling the applied voltage, the beam polarization is rotated 180°, giving maximum transmission through the Brewster-angle plates during the rise and fall of the applied electrical signal.[5] The result can be a much shorter optical pulse. A second Pockels cell is used to eliminate the second CO_2 pulse created by the fall of a high-voltage pulse and to improve the precursor extinction ratio.

This short-pulse-generation method is illustrated in Fig. 13. The oscillator produced a temporally smoothed, linearly polarized 100-ns laser pulse with ~ 5-MW peak power. The first Pockels cell selected a 3-ns section from the laser output, and the second further reduced the pulsewidth to 250 ps FWHM. For dependable synchronization, we used a laser-triggered spark gap to switch the second cell and to fire the electrically triggered spark gap which controlled the first cell. The smoothed oscillator and the second Pockels cell have been assembled with appropriate polarizers and tested.

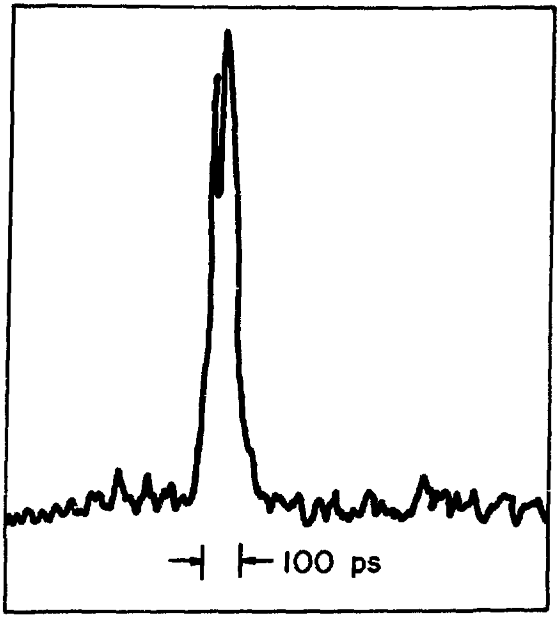

Fig. 12. Time history of free-induction decay pulse, as revealed by microdensitometer scan of Duguay shutter/streak camera system. Absorber pressure, 200 torr.

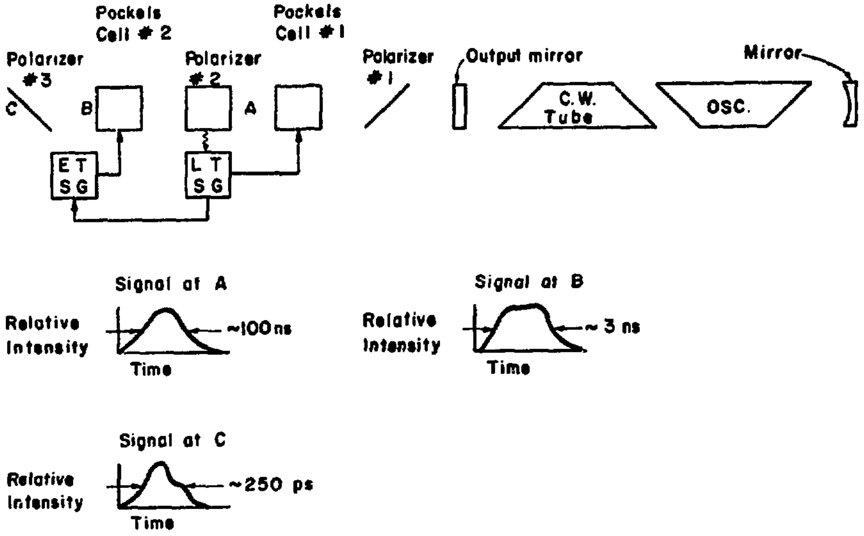

Fig. 13. Schematic of electro-optical short-pulse-generating system.

The output pulse measured with a Duguay shutter/streak camera system is shown in Fig. 14. The theoretically predicted pulse shape is superimposed on the observed pulse shape in Fig. 15. The measured duration is 325 ps FWHM, in excellent agreement with theoretical prediction. Modification of the high-voltage circuits is in progress to meet the 250-ps FWHM design goal.

250-ps CO_2 Oscillator System

We have initiated a development effort to build and install a 250-ps multiline oscillator system in our SBS laser-target facility. With present amplifiers, this oscillator will permit us to shorten the target-irradiation pulse duration to 400 ps FWHM. Our development program will utilize the best understood short-pulse-generation techniques developed in the research effort described earlier.

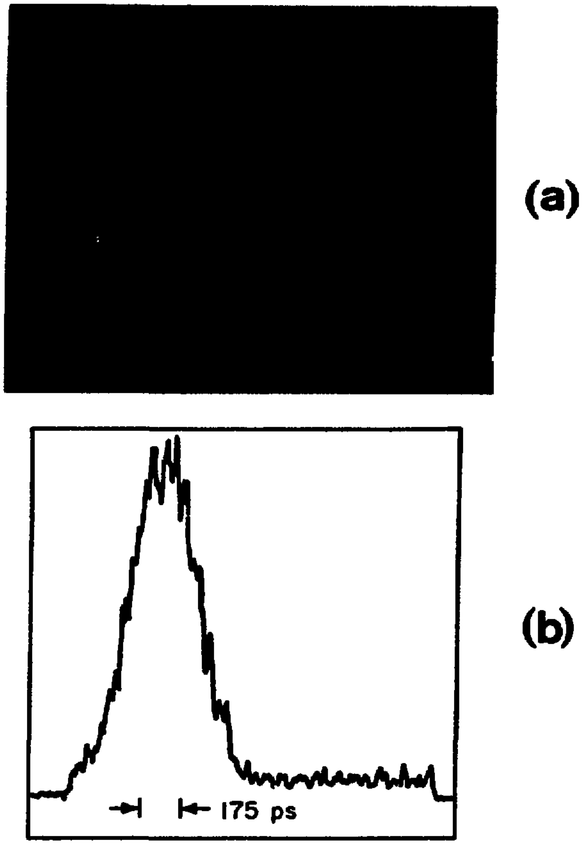

Fig. 14. Time history of electro-optically generated short pulse as revealed by (a) Duguay shutter/streak camera system; (b) microdensitometer scan.

System baseline performance specifications are:

Peak power, MW	4
Extinction ratio	10^8
Number of lines	3
Pulse duration, ps (FWHM)	250
Mode	TEM_{oon}
Repetition rate	10/min

A functional layout of the oscillator is shown in Fig. 16.

The oscillator cavity is bounded by elements M1 and M2 and comprises a conventional pulsed TEA gain medium for temporal smoothing and a gas-filled multiline cell. The latter is a selective absorber that provides simultaneous multiline operation of the laser.[6] The result will be a smooth, multiline infrared pulse of 50 ns duration and 4 MW peak power.

Tandem Pockels cells (S01 and S02) are used to select a 250-ps section from the 50-ns pulse at its peak-intensity point. Two cells are used to enhance the extinction of background intensity before and after the short pulse is switched out. For easier synchronization, S1 is a standard, 3-ns-duration optical gate, whereas S2 is a 250-ps gate of the type described earlier.

We chose this method of generating 250-ps CO_2 pulses over the more common mode-locking approach because it permits the use of an oscillator gain

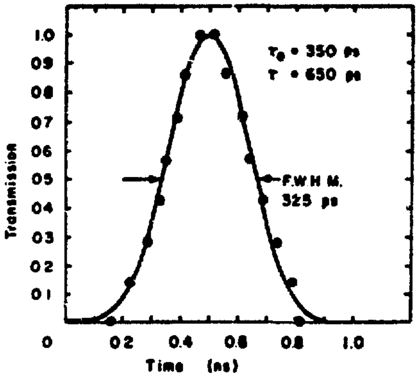

Fig. 15. Transmission vs time for 33-Ω fast Pockels cell. Solid lines: predicted response based on measured input voltage waveform; dots: measured transmission.

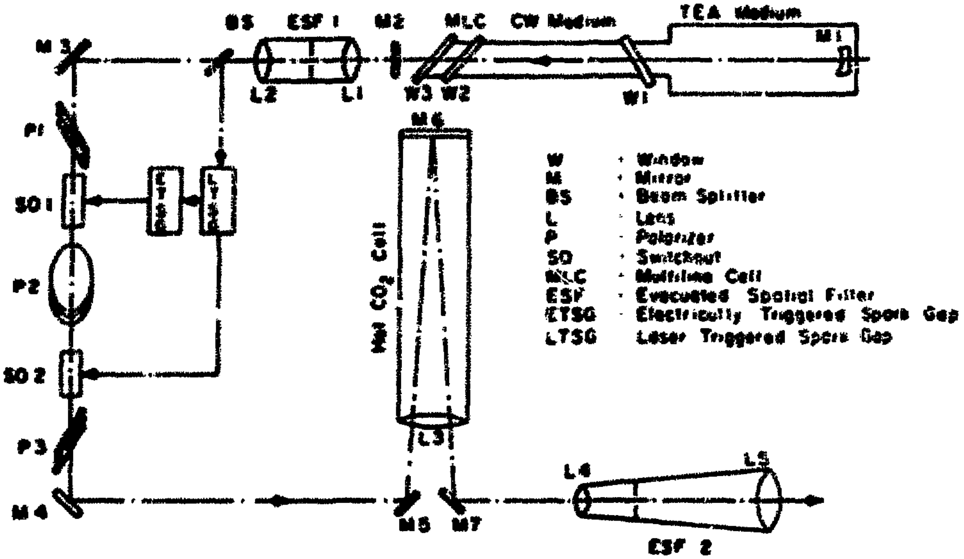

Fig. [illegible]. Schematic of [illegible] oscillator system.

medium at atmospheric pressure. In addition, it enables us to use a hot CO_2 absorption cell in a novel scheme for improving background extinction.

The behavior of such a cell has been described above in connection with our work on free-induction decay. Application of the cell is the same, except that no optical breakdown cell is used. The narrow bandwidth of the 30- to 60-torr, 725-K CO_2 absorber is chosen to match the spectrum of the 50-ns background intensity. The result is selective absorption of the background and transmission of the broadband 250-ps signal. A 4- to 6-m path length in the hot cell will provide sufficient additional background discrimination to meet the extinction-ratio design goal of 10^8 indicated in the tabulation above.

Two evacuated spatial filters (ESFs) are included in the system design to provide homogeneous beam spatial profiles: ESF1 is required to minimize damage to the electro-optic crystals used in Pockels Cells SO1 and SO2, whereas ESF2 provides final beam cleanup and expansion to the waist dimension required by the first amplifier stage of the SBS. This system will be installed in the summer of 1976.

Analyses of Magnetic Effects on Discharge

An electron beam from a cold-cathode gun provides the ionization in the gain medium of the CO_2 laser amplifiers. Kinetics calculations and experiments indicate that suitable gain can be provided by 0.2 to 0.8 A/cm^2 of primary electron-beam current for a $3:1/4:1::He:N_2:CO_2$ mixture. A much lower current density would be required for a new 0:1/4:1 mixture. Because of the coaxial geometry of the electron gun, the azimuthal magnetic field in the gun region, at large beam currents, can pinch the electron beam severely along the axial direction. This pinching reduces the axial length over which the electron beam can provide ionization in the gain medium and contributes to nonuniform ionization that can result in a nonuniform optical-gain profile. The effect of a magnetic field on the electron trajectories in the gun region can be minimized by operating either at low electron-beam current densities or with an axially short electron gun. However, a low electron-beam current would demand a longer optical pumping time, which may be undesirable, whereas a shorter individual electron gun would suggest that a greater number of electron guns be used to obtain the same total optical-gain length, but would increase capital cost significantly. Because of these undesirable aspects, we have carefully studied the effect of a magnetic field on the electron trajectories in the gun region with a numerical electron-ray-tracing code. We have also obtained a scaling law for the incidence angle of the electron beam entering the gain medium.

An iterative perturbation calculation of the two-dimensional electron flow equations with P_z/P_r as expansion parameter yielded the following scaling law for the electron incidence angle at the anode of the gun.

$$\cos\theta = P_z/(P_z^2 + P_r^2)^{1/2} = \frac{4\pi e\, J_A r_A\, \ln(r_A/r_C)}{c[(e\phi)^2 + 2\, e\phi\, m\, c^2]^{1/2}} ,$$

where P_z, P_r, e, m, J_A, r_A, r_C, Z, c, and ϕ are, respectively, the z-component of electron momentum, the r-component of electron momentum, the electron charge, electron rest mass, current density at the anode of the electron gun, radius of the anode, radius of the cathode, the axial distance, the speed of light, and the potential difference between the gun anode and cathode. Figure 17 shows good agreement between the analytical result and that obtained from a numerical electron-ray-tracing code developed at the Stanford Linear Accelerator Center. The calculations were made for electron incidence angles 45° < θ < 90° and

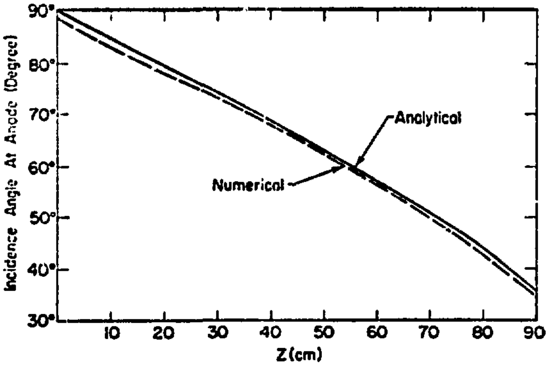

Fig. 17. Comparison of numerical and analytical calculations on spatial variation in angle of incidence of electrons at anode of electron gun.

$$0 < Z < \frac{2.65[(e\phi)^2 + 1024\,(e\phi)]^{1/2}}{J_A r_A\, \ln(r_A/r_C)} , \qquad (7)$$

where $e\phi$ is expressed in kV, J_A in A/cm^2, and r_A, r_C, and z in cm.

By adding a grid between the cathode and the anode and by varying the grid potential the electron-beam current can be varied independently of potential differences between the cathode and the anode. This approach is much more desirable than varying the beam current via variation of the spacing between the cathode and the anode. When a grid is inserted between the cathode and the anode, the above equation can be used to calculate the electron trajectories between the cathode and the grid. Because $J_g r_g = J_A r_A$, it is only necessary to replace $\ln(r_A/r_C)$ with $\ln(r_g/r_C)$. Table VI gives the characteristics of an electron gun with a cathode radius of 50 cm, an anode radius of 70 cm, a grid radius of 60 cm, a potential at the anode of 300 keV, and for four different grid potentials. Allowing for the expansion of the cathode plasma toward the grid at a speed of 2 x 10^6 cm/s, the corresponding discharge times to achieve 150 J/liter for the 3:1/4:1 mixture are given by Row 3. The discharge times are calculated by assuming that the current density varies as $(\frac{\Delta r}{\Delta r - ut})$, where Δr is the 10-cm separation between the grid and the cathode and u = 2 x 10^6 cm/s. The anode current density at the end of the discharge time is given by Row 2. The total length at the grid for which the electron incidence angle is greater than 45° is given for the initial and final current densities by Rows 4 and 5. At the anode, the corresponding lengths are given by Rows 6 and 7. The lengths would be halved if the electron gun were fed from one end only. The longer section at the anode in comparison to that at the grid indicates that the electron trajectories improve between the grid and anode because of the large electric field in that region.

Table VI clearly indicates that a grid between the anode and the cathode permits us to operate the gun at lower current density, which clearly improves the electron trajectories in the gun region. In addition, with a further decrease in required electron-gun current density for the 0:1/4:1 mix-

TABLE VI

ELECTRON-GUN CHARACTERISTICS

Cathode radius - 50 cm
Anode radius - 70 cm
Grid radius - 60 cm
Potential at anode - 300 keV

Characteristic	Grid Voltage (keV)			
	121	48	19	7.6
1. Initial J_A (A/cm^2)	0.641	0.204	0.051	0.013
2. Final J_A (A/cm^2)	0.993	0.303	0.113	0.063
3. Discharge time (μs)	0.46	0.906	1.05	2.75
4. Initial (2xZ) at grid (cm)	134	326	816	1493
5. Final (2xZ) at grid (cm)	123	273	563	901
6. Initial (2xZ) at anode (cm)	123	492	1966	7714
7. Final (2xZ) at anode (cm)	101	330	887	1474

tures, the magnetic field from the feed current appears not to have any significant effect on the operation of a single-section 280-cm-long coaxial electron gun, especially if operated at a discharge time exceeding 1.5 μs.

We have employed Monte Carlo electron-beam transport codes to analyze the electric discharge in the final HEGLF amplifiers. We have shown that, in this system, the magnetic fields are particularly critical in determining the distribution of ionization produced by the primary electron beam in the discharge region.

As discussed above, the first magnetic effect occurs in the diode region, where the primary beam current is pinched by self-fields; this pinching distorts the trajectories of the electrons entering the discharge. Our simulations show, however, that subsequent scattering (in the foil and discharge gas) will largely mask the fact that the electrons are not impinging normally on the foil (for a diode voltage of ~ 300 kV, titanium foil thickness of 30 μm, and a CO_2 gas pressure of ~ 3 atm). Therefore, the most serious consequence of diode pinching in this system is the fact that parts of the discharge region may receive very little primary current.

Magnetic fields are also generated in the power amplifier by the discharge current; these amplifiers require ~ 10^5 A, with resultant fields of 10^2 to 10^3 G. Such fields can dominate the electron scattering in the primary electron beam, leading to highly nonuniform ionization and, ultimately, to nonuniform optical-gain distributions. Our simulations have modeled this effect in the annular laser amplifier, both for a 30° sector (where the magnetic fields pinch in the θ-direction) and for an unsectored annulus. In this latter case, the system is approximately symmetrical in θ, but major variations in ionization can occur along $\underline{z}$ (the optical propagation path), and along $\underline{r}$. Figure 18 shows examples of ionization distributions produced by the Monte Carlo code for such a discharge chamber. The CO_2 gas at 3 atm extends for 140 cm in $\underline{z}$, between cylinders at r = 75 cm (the foil position) and r = 100 cm; the primary electrons have an energy of 500 keV, and the discharge voltage is 500 kV. The magnetic field is approximated by a field caused by a uniform radial discharge current; in Case (a), this current is 3 A/cm^2 (at the foil), and for Case (b), the current is 10 A/cm^2. Although this model is not entirely self-consistent

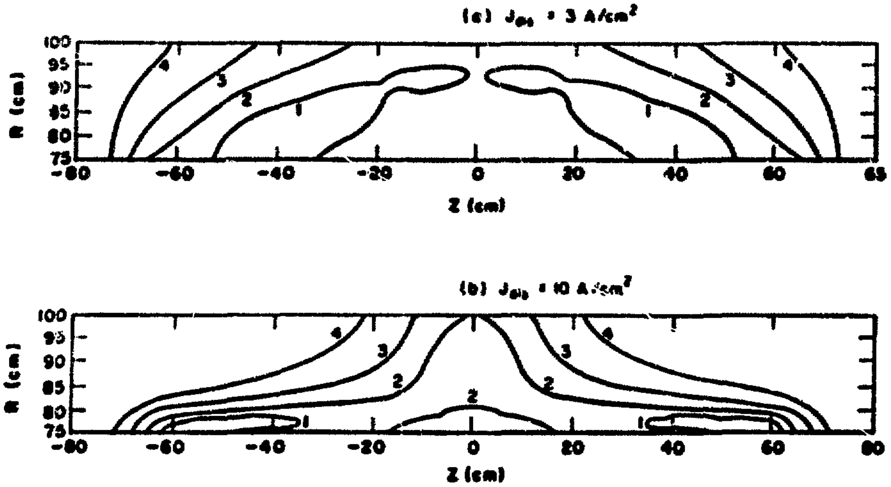

Fig. 18. Contours of equal ionization density produced by 500-keV primary beam entering a 3-atm CO_2 discharge gas (3:1/4:1::He:N_2:CO_2): (a) discharge current, 3 A/cm²; (b) discharge current, 10 A/cm². Contours, 1 through 4, respectively, are 90, 70, 40 and 10% of peak ionization density.

(the ionization will, in fact, help to determine the discharge-current distribution), the system clearly must be designed to operate with a discharge-current density well below 10 A/cm^2, and preferably below 3 A/cm^2.

Short-Pulse Energy Extraction Calculations

Theoretical results for the amplification of multiline and multiband Gaussian input pulses of various pulse widths, energies, and spectra have been obtained for two possible amplifier gas mixtures, 3:1/4:1::He:N_2:CO_2 and the 0:1/4:1::He:N_2:CO_2 mix. The relevant design parameters for these mixtures have been obtained from data developed at LASL. The gain coefficient of the 3:1/4:1 mix is taken as 3.5% cm^{-1}, whereas that of the 0:1/4:1 mix is 3.75% cm^{-1}. The energy available at the output aperture on the 10-μm band for a 2.8-m-long amplifier is 2.24 J/cm^2 and 3.10 J/cm^2 for the two mixtures, respectively. It should be stressed that the parameters for the two mixtures correspond to the <u>same</u> input electrical energy of 150 J/liter. Energy-extraction calculations have been performed for a two-pass geometry (2.8 m per pass) where population depletion on the first pass has been taken into account. The problem of 10- and 9-μm pulse separation arising from linear and nonlinear dispersion properties of the amplifying medium is not serious in this system.

Figures 19 and 20 present the results for 100- and 200-ps input pulses, respectively, containing up to five transitions in the 10.6-μm band. Figures 21 and 22 show the results for paths of the same length when the spectral content includes transitions in the 9.6-μm band.

The superiority of the 0:1/4:1 mixture is evident for all cases studied and the inclusion of transitions from the 9-μm branch increases the energy and intensity output substantially over the case in which only 10-μm transitions are present. Table VII summarizes these results.

Self-Focusing at 10.6 μm in NaCl Windows

The value of the second coefficient of the index of refraction, n_2, for NaCl at 10.6 μm has been inferred from third-harmonic-generation data. Using the value of 4.27 x 10^{-13} esu, the effects of the intensity-dependent nonlinear index of refraction upon beam propagation and focusability have been calculated as a function of laser power.

At intensities of 2 x 10^9 W/cm^2 the beam breakup distances so estimated, ~ 50 cm, are substantially greater than the window thickness, ~ 10 cm, so that damaging self-focusing does not appear to be a problem for our CO_2 lasers now under design or construction.

The calculations have been extended to determine the effect of this nonlinear phenomenon upon

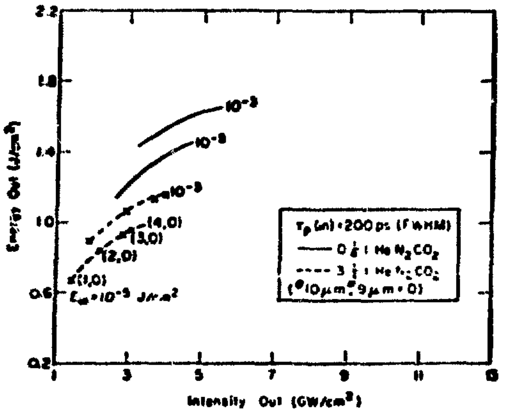

Fig. 19. Output energy vs output intensity for incident 100-ps pulse. The Gaussian pulse contains one to four lines at 10 μm.

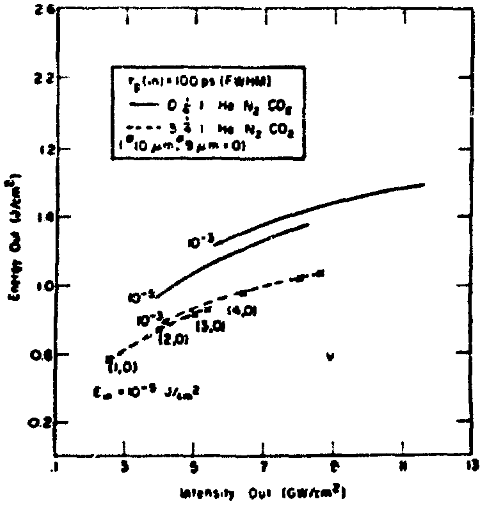

Fig. 20. Output energy vs output intensity for incident 200-ps pulse. The Gaussian pulse contains one to four lines at 10 μm.

beam quality and focusability. First results indicate that for a beam with Gaussian profile self-focusing effects at intensities of 4 x 10^9 W/cm^2 might reduce the focused intensity by ~ 20%. The codes used in this work are being modified to treat the HEGLF geometry, an annular beam of approximately uniform intensity.

Target Irradiation Optics

Two target irradiation geometries have been considered for the focusing chamber optics of the eight-beam, 10-kJ system. The irradiation may be two-sided, i.e., two sets of four beams each lie within the upper or lower design cones. Alternatively, the irradiation may be isotropic, in which the eight beams are arranged to achieve spherically symmetric illumination of a sphere. Present target design considerations call for the latter geometry; but the designs considered seek to satisfy both capabilities.

A design that uses the same set of mirrors for both irradiation possibilities is shown in Fig. 23.

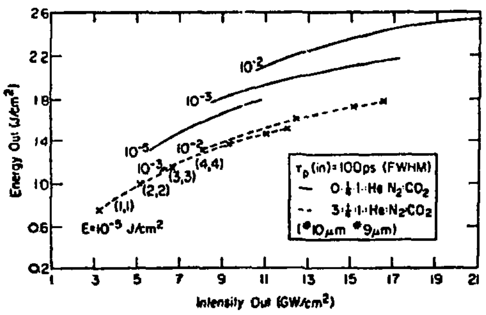

Fig. 21. Output energy vs output intensity for an incident 100-ps pulse. The Gaussian pulse contains lines at 10 and 9 μm.

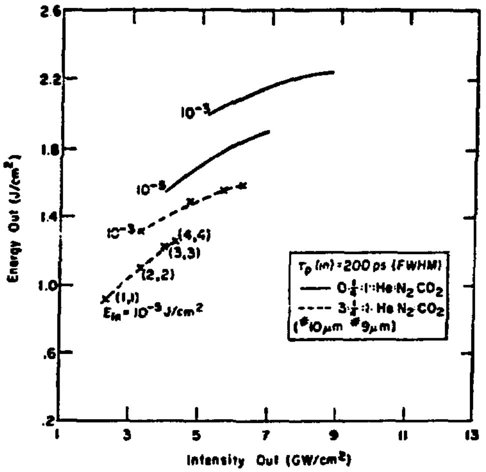

Fig. 22. Output energy vs output intensity for an incident 200-ps pulse. The Gaussian pulse contains lines at 10 and 9 μm.

TABLE VII

ENERGY EXTRACTION FROM A TWO-PASS AMPLIFIER (2.8 m PER PASS) FOR 100- AND 200-ps INPUT PULSES OF VARYING SPECTRAL CONTENT FOR TWO GAS MIXTURES

Lines/Band		3:1/4:1::He:N_2:CO_2		0:1/4:1::He:N_2:CO_2	
10-μm Band	9-μm Band	E_{out} (J/cm²)	I_{out} (GW/cm²)	E_{out} (J/cm²)	I_{out} (GW/cm²)
		Energy Flux, 10^{-5} J/cm²			
100-ps Input Pulse					
1	0	0.550	2.55	0.947	4.91
2	0	0.732	3.97	1.19	6.22
3	0	0.834	4.99	1.31	7.77
4	0	0.873	5.30	1.35	8.27
1	1	0.763	3.26	1.31	5.58
2	2	1.00	5.13	1.62	8.46
3	3	1.11	6.19	1.74	10.75
4	4	1.16	6.65	1.80	11.04
200-ps Input Pulse					
1	0	0.663	1.41	1.13	2.36
2	0	0.840	2.22	1.33	3.36
3	0	0.928	2.85	1.42	4.32
4	0	0.957	3.07	1.44	4.70
1	1	0.911	2.28	1.55	4.01
2	2	1.14	3.35	1.79	5.62
3	3	1.22	3.92	1.86	6.37
4	4	1.26	4.28	1.89	6.85
		Energy Flux, 10^{-3} J/cm²			
100-ps Input Pulse					
1	0	0.749	4.12	1.23	5.58
2	0	0.947	6.38	1.46	8.62
3	0	1.04	7.97	1.54	10.73
4	0	1.07	8.57	1.57	11.58
1	1	1.11	6.07	1.78	8.50
2	2	1.36	9.34	2.04	13.06
3	3	1.46	11.10	2.13	15.60
4	4	1.51	12.04	2.16	17.09
200-ps Input Pulse					
1	0	0.896	1.91	1.43	3.20
2	0	1.06	2.89	1.58	4.37
3	0	1.13	3.64	1.63	5.03
4	0	1.14	4.00	1.64	5.56
1	1	1.30	3.21	2.01	5.23
2	2	1.49	4.71	2.17	7.00
3	3	1.54	5.60	2.20	8.06
4	4	1.59	6.20	2.21	8.80

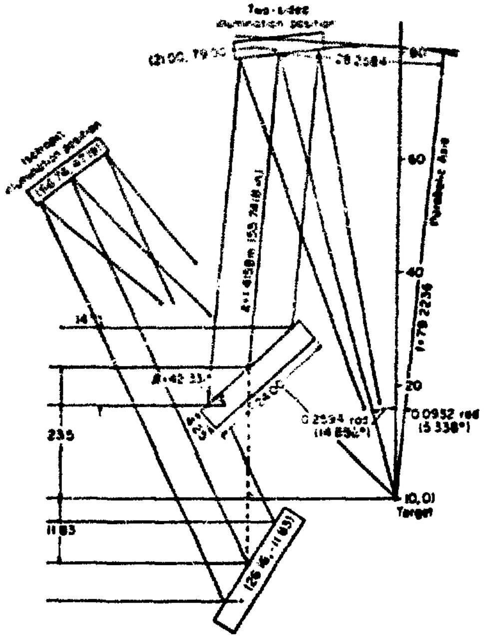

Fig. 23. Optical design for 10-kJ eight-beam CO_2 laser which uses the same set of mirrors for both a two-sided configuration and an isotropic configuration.

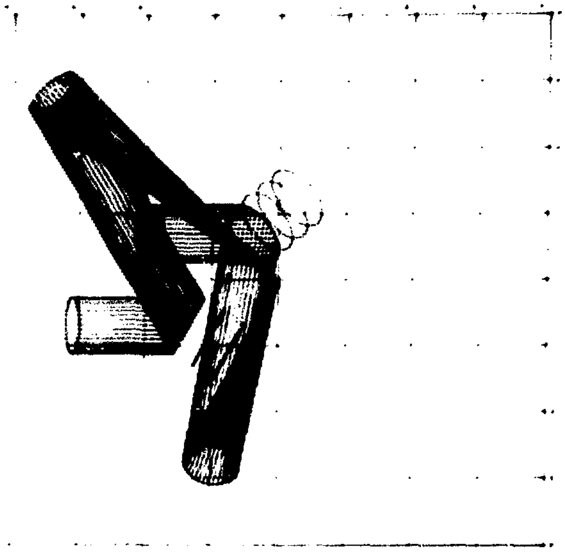

Fig. 24. Views of two neighboring beams based upon computer ray-tracing code.

The isotropic design is obtained by simply moving the center of the paraboloid mirror from Position (21.00,79.00) to a position roughly 30° farther from the vertical. The following should be clear from this drawing: First, the focusing chamber of the isotropic design will be lower and wider; second, the majority of the clearance for experimental diagnostics will be above and below the target rather than to the sides. What is not obvious is the question of clearance between the beams and the mounts.

Several views of two neighboring beams, based upon computer ray tracing, are seen in Fig. 24. For an isotropic scheme, the near-ideal design by almost any criterion[7] is obtained by placing the mirrors at the corners of a cube, with the bottom half of the cube rotated 45° relative to the top half (a cubic isosceles antiprism). The two neighboring beams, one illuminating from the upper half and the other from the lower half, could interfere with each other's mirror mounts. As seen in Fig. 24, three rings are drawn behind each of the turning mirrors, at 15.25, 30.50, and 45.75 cm (6, 12, and 18 in., respectively) from the flat. In the two views of Fig. 24, it may also be seen that a good clearance of 35.5 cm (14 in.) exists.

Isotropic designs of the type presented above may be characterized by two parameters: the focal length, f, and the distance, R_c, from the center of the focusing mirror to the axis of the paraboloid from which it was cut. Figure 25 shows the design space for possible isotropic designs. Two points, labeled P_1 and P_2, have been checked for adequate clearance for the servos. Point P_1 is obtained by using the mirrors of the two-sided design described above; however, the optical speed may be increased almost threefold by using the set of mirrors corresponding to Point P_2. Because of less interference between focusing mirrors in the isotropic design, there is more design flexibility and a smaller spot size on target may be achieved at the expense of a new set of focusing mirrors and possibly a new set of mirror mounts.

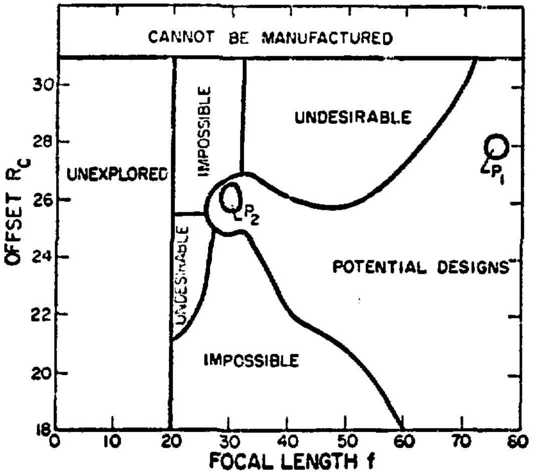

Fig. 25. Design space for potential isotropic design of 10-kJ eight-beam CO_2 system.

Laser-Target Isolation

To provide isolation against prepulsing, self-lasing, and target reflections in high-power CO_2 laser systems, the use of bleachable solid-state or gaseous absorbers has been considered. Although several materials have been considered, previous measurements of their absorption and saturation properties have been made only with CO_2 signals of lower power at durations longer than 200 ns. These data are not necessarily characteristic of the behavior of these materials at the intensities and durations of interest to our program (~ 1 J/cm^2 in ~ 1 ns). Consequently, we are conducting a systematic program, using both low-power cw probes and high-power short-pulse CO_2 lasers, to investigate the absorption and bleaching characteristics of several gases and solids in an attempt to identify those that have the required optical properties.

High-Intensity Absorption in Solids - Germanium

To develop new interstage isolation techniques for high-power CO_2 laser work, we have measured the absorption in p-type germanium at surface intensities up to 500 MW/cm^2.

Single pulses of 1-ns duration at 10.6 µm were generated in an oscillator- amplifier system capable of producing output energy of ~ 2 J. Spatial intensity variations were reduced to about ± 10% by the use of a Fourier-transform spatial filter. The spatial filter was needed to avoid 50% errors in the apparent transmission of the sample at intermediate and high intensities.

The material we used was 0.77-Ω·cm gallium-doped (p-type) germanium having an unsaturated absorption coefficient ($k_h = N_h\sigma_h$) of 2.85 cm^{-1}. Optical path length, L, in the sample was 0.59 cm. The sample was illuminated uniformly at Brewster's angle, with an illumination cross-section area of 1.24 cm^2 perpendicular to the internal propagation direction. Intensity was determined by calculating the peak intensity for a temporal Gaussian pulse, which would have the same energy and would be deconvolved full width at half height, as observed for the experimental incident pulse.

Figure 26 plots the results obtained. The initial small-signal transmission of 0.19 can be bleached to a value approaching 0.85 for input fluxes of 100 MW/cm^2.

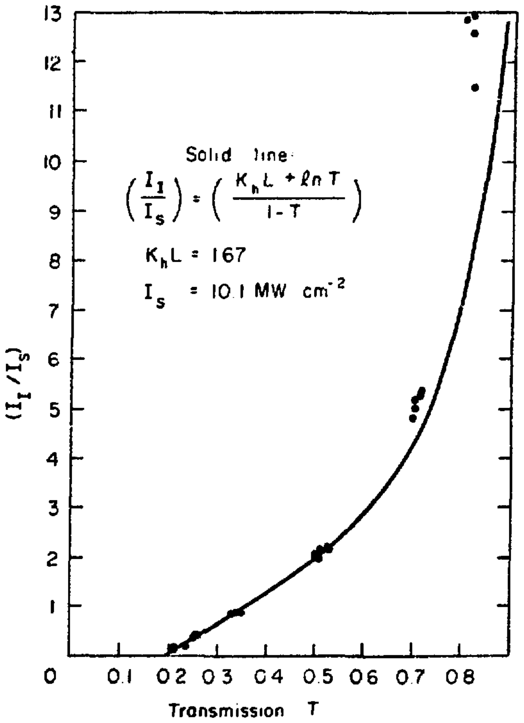

Fig. 26. Intensity-dependent bleaching of doped germanium at 10.59 µm. Solid line: trend of observed transmission (dots).

At intensities $I \gtrsim 11\ I_s$, we noted a uniform faint surface corona, but no optical damage, even after many shots. The right-most four points in Fig. 26 correspond to this condition. The anomalous saturation of the transmission may here include significant contributions both from absorption by the surface corona and from power-broadening.

Not shown on the plot is a single point at a surface intensity of 490 MW/cm^2, which produced irreversible optical damage in the test sample. This value corresponds to a beam intensity of ~ 2 GW/cm^2.

In summary, the utility of p-type germanium as a bleachable absorber has been confirmed. Our results demonstrate the feasibility of using p-type germanium as an interstage isolation device that provides a maximum transmission of 66% and a 30-db small-signal isolation level. Such an isolator could have a resistance of 1 Ω cm and could be 2.1 cm thick.

High-Intensity Absorption Saturation in Gases

We have made extensive high-power absorption measurements on several gases to explore the desirability of using bleachable gaseous absorbers for CO_2 laser isolation. Sulfur hexafluoride has been used previously as an external nonlinear gaseous absorber; NH_2D, C_2H_4, and hot CO_2 are being investigated.

The oscillator/preamplifier assembly of our DBS was used to provide a 1.2-ns infrared pulse with energies ranging from 0.01 to 100 mJ/cm^2. The output of the third-stage amplifier of the SBS was used to obtain similar pulses with energies from 100 to 800 mJ/cm^2. Thus far, absorption has been studied only on the CO_2 P-20 line at 10.6 μm. Because gaseous absorbers have long relaxation times, calorimeters provide adequate diagnostics for 1-ns absorption experiments. The input energy was monitored by means of a calibrated beam splitter of ~ 10% reflectivity.

Because SF_6, NH_2D (deuterated ammonia), and C_2H_4 are being considered as isolators in our CO_2 lasers, we studied these gases first. Experimental results for SF_6 and NH_2D are shown in Figs. 27 and 28, respectively. In these figures, the solid line shows the observed energy transmission versus input energy; whereas the broken line shows the transmission that would be predicted from an extrapolation of cw data.

Note that for 1-ns pulses complete saturation was not observed in SF_6. However, the 1-ns pulse transmission was significantly larger than the cw transmission and increased with input energy. An energy transmission of ~ 77% was measured for 10-torr cm SF_6 at an input flux of 500 mJ/cm^2.

Short low-intensity laser pulses gave an ab-

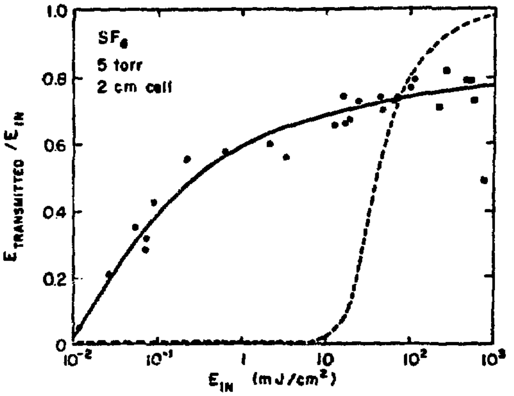

Fig. 27. Flux-dependent energy transmissivity of SF_6 at 10.59 μm. Solid line: trend of observed transmission (dots). Broken line: behavior expected from an ideal two-level saturable absorber with the cw saturation energy of SF_6.

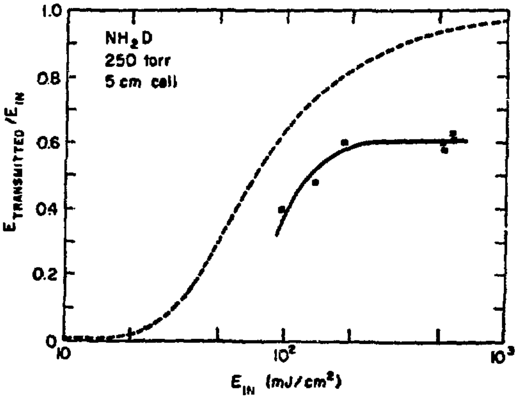

Fig. 28. Flux-dependent energy transmissivity of NH_2D at 10.59 μm. Solid line: trend of observed transmission (squares). Broken line: behavior expected from an ideal two-level saturable absorber with the cw saturation energy of NH_2D.

sorption equal to that obtained with a cw input. As the intensity of the short-pulse laser radiation increased, the molecular levels that were initially involved in the absorption process probably did "saturate."

Note that for the 10-torr·cm gas mixture studied, an absorption of 7 mJ/cm^2 would correspond to the absorption of a single 10.6-μm photon by each SF_6 molecule. Because the measured absorption is roughly 700 mJ/cm^2 a multiple-photon absorption process is indicated. This result is consistent with phenomena observed in our laser isotope separation program.[8]

Similar results are obtained with NH_2D (Fig. 28). No bleaching is evident at the highest energies employed and, at an input of 500 mJ/cm^2 about 60% transmission is observed for 1250 torr·cm of NH_2D.

Finally, absorption measurements have been performed on ethylene (C_2H_4) and helium/ethylene mixtures. Ethylene is known to absorb on both the P- and R-branches of the 10-μm CO_2 band. Preliminary results indicate that it is compatible with some CO_2 laser mixes.

Figure 29 shows the 10.6-μm transmission of pure C_2H_4 as a function of pressure. Although C_2H_4 does not exhibit a classical two-level saturation over the range measured, it can be seen that at high powers the transmission for 10.6-μm radiation is significantly increased. This behavior, which is typical of that observed for other absorbers such as SF_6 and NH_2D, suggests that such gases can be used for isolation, but with some loss in the transmitted high-power beam.

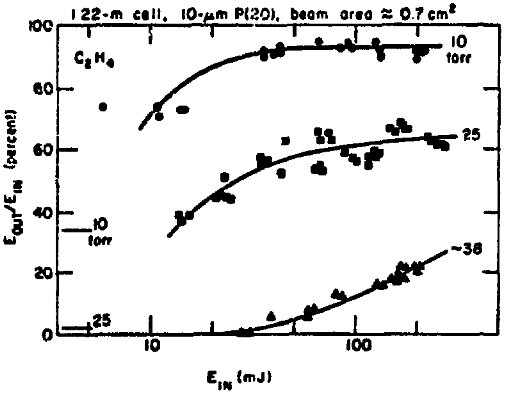

Fig. 29. Experimentally observed energy transmissivity of C_2H_4 at various pressures and 10.59 μm.

Figure 30 shows the effect of a helium buffer gas on the transmission of 10 torr of C_2H_4. We used the buffer gas to simulate the broadening effects of a high-pressure laser mixture on C_2H_4. At very low energy levels (cw limit), increasing the helium partial pressure resulted in increased absorption, due in part to pressure-broadening of the absorbing transition. At 600 torr the absorption cross section became constant. At high power levels the transmission increased with the laser flux, again exhibiting saturation effects. Analysis and modeling of these phenomena are still under way. However, for the 10-kJ prototype amplifier, the present data suggest that ~ 1 torr of C_2H_4 might provide the required isolation and still yield adequate transmission at the higher powers.

If power-broadening is the explanation for the lack of saturation in SF_6, NH_2D, and C_2H_4, then it is likely that similar polyatomic absorbing gases will also fail to saturate. However, it is possible that simpler (e.g., triatomic) molecules may still be bleachable. If a bleachable absorber cannot be found, then the desirable isolator will be the gas that has the highest ratio of small-signal to large-signal absorption.

Hot CO_2 for Prepulse Target Protection and Laser Gain Suppression in the Proposed 1/4-ns, Multiline, SBS Amplifier Chain

We have investigated the use of hot CO_2 absorbers as another approach to solving two difficult problems: low-pressure, narrowband hot CO_2 to suppress precursor gain, and high-pressure, broadband hot CO_2 to suppress amplified spontaneous emission. The combination of the two types of absorbers appears well-suited to solving both problems, with a maximum energy loss of less than 35% compared to amplifier operation without such absorbers. The proposed amplifier absorber arrangement is depicted in Fig. 31; the parameters of this system are listed in Table VIII. Figure 32 compares the output pulse of the system without absorbers and with absorbers.

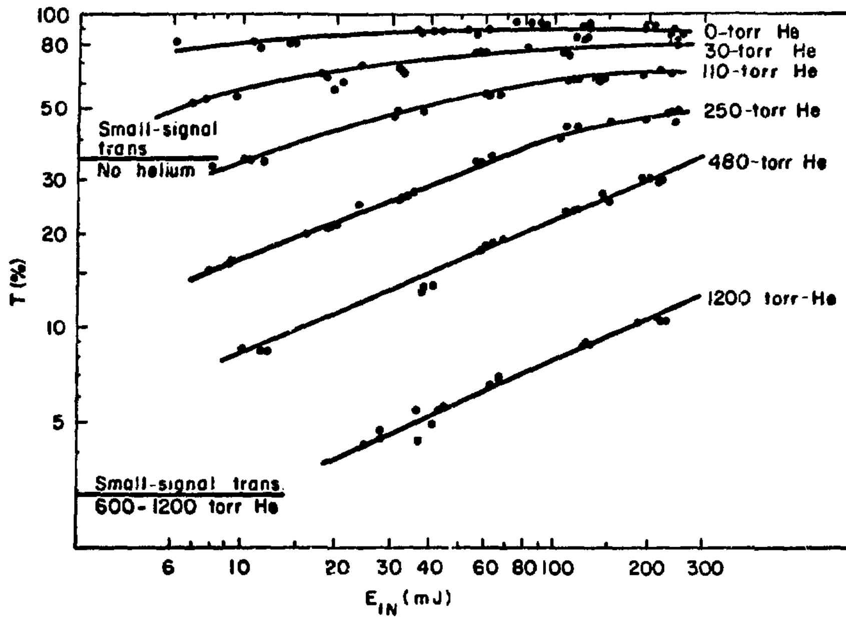

Fig. 30. Observed energy transmissivity of 10-torr C_2H_4 with various partial pressures of helium at 10.59 μm in a cell 122 cm long.

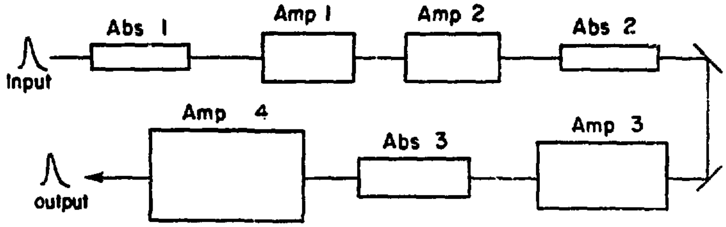

Fig. 31. Proposed amplifier chain for 0.25-ns, three-line operation of single-beam CO_2 laser.

TABLE VIII

PARAMETERS FOR SBS AMPLIFIER CHAIN FOR 0.25-ns, THREE-LINE OPERATION

Device	$g_o(\alpha_o)$ (cm^{-1})	*Length (cm)*	*Beam Area* (cm^2)	*Pressure (torr)*
Absorption cell 1	*0.018*	*333*	*0.4*	*30*
Amplifier 1	*0.04*	*100*	*15*	*600*
Amplifier 2	*0.04*	*100*	*15*	*600*
Absorption cell 2	*0.018*	*444*	*0.62*	*600*
Amplifier 3	*0.04*	*100*	*40*	*1800*
Absorption cell 3	*0.018*	*222*	*10*	*1500*
Amplifier 4	*0.3*	*200*	*400*	*1500*

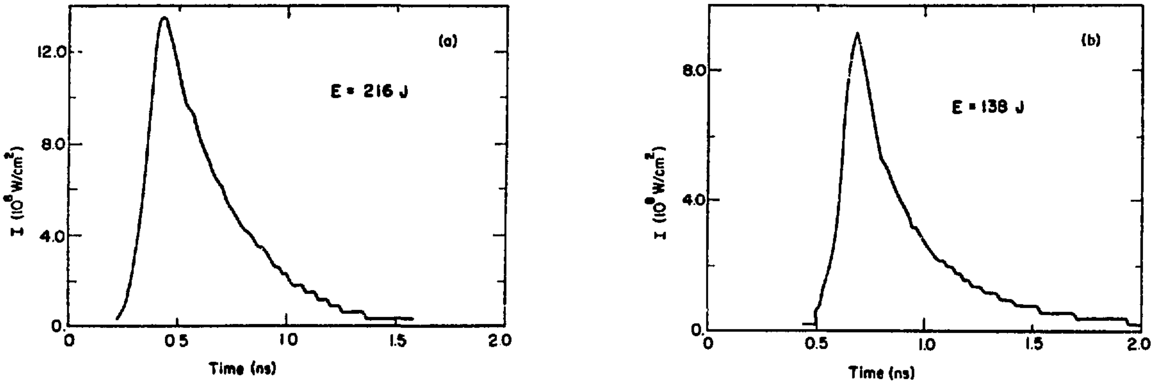

Fig. 32. Output pulse of system shown in Fig. 31; (a) without absorbers, (b) with absorbers.

Helium-Free Gas Mixtures for Short-Pulse CO_2 Amplifiers

Typically, CO_2 lasers have been operated with gas mixtures containing 50% or more helium. For large units, the amount of helium involved dictates the use of a costly and complicated gas-recovery system. We therefore conducted an experimental program to evaluate helium-free mixtures for use in our short-pulse amplifiers. Under proper discharge conditions a wide range of N_2-CO_2 mixtures gave superior performance relative to the 3:1/4:1:-:$He:N_2:CO_2$ mixture presently used. The best helium-free mixtures for electron-beam-stabilized discharges were those with $N_2:CO_2$ proportions around 1:4. When compared with the helium mixtures, several advantages appear in addition to the economics of eliminating helium. A quantitative comparison of this mixture with a 3:1/4:1 mixture of equal pressure and temperature shows the following:

- Pumping efficiency can be higher, by 40% or more.
- Energy stored for a given gain is 30% greater, alleviating the self-oscillation problem.
- Rotational relaxation[7,10,11] is 37% faster, giving improved short-pulse performance.
- Heat capacity is 39% larger, lowering both the temperature rise and the over pressure after pumping.
- The gas discharge requires 70% higher voltages for efficient operation. This is desirable in the sense that discharge currents are reduced, but is undesirable from a high-voltage design standpoint.

Table IX provides a comparison of 3:1/4:1 and 0:1/4:1 mixtures at 1800 torr and 300 K.

Figure 33 compares the measured values of small-signal gain for several mixtures as a function of electrical energy delivered to the electron-beam-sustained discharge.

TABLE IX

PHYSICAL CHARACTERISTICS OF 3:1/4:1 AND 0:1/4:1 MIXTURES AT 1800 TORR AND 300 K

Mixture $He:N_2:CO_2$	Gas Density (mg/cm^3)	Line Width[9] FWHM (GHz)	Optimum Field (kV/cm)	c_v (J/ℓ)	Rotational[7,10,11] Relaxation Time (ps)
3:1/4:1	1.43	10.0	10.5	1.44	69.4
0:1/4:1	3.93	13.0	18.0	2.0	43.4

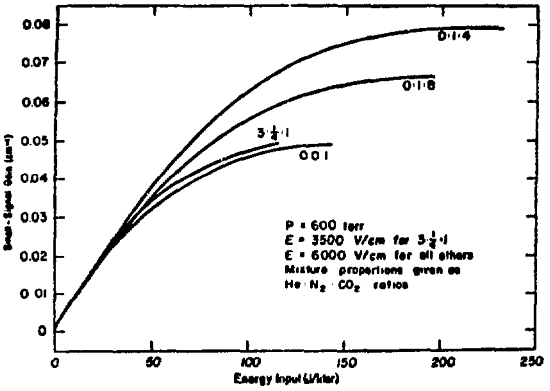

Fig. 33. Comparison of measured small-signal gain for various laser gas mixtures at 10.59 µm under given conditions.

The superiority of the 0:1/4:1 mixture is clearly evident at the high input energies. The increased line-broadening[9] in the helium-free mixtures implies a larger inversion for a given small-signal gain. As an example, Fig. 33 shows that the 3:1/4:1 and 0:1/4:1 gas mixtures have virtually identical gain for low electrical-energy inputs, but the energy stored in this inversion is 30% greater for the 0:1/4:1 mixture.

The performance obtained depends on the discharge electric field and on current density. For a 0:1/4:1 mix at a pressure of 600 torr, best performance is obtained with an electric field of ~ 6 kV/cm^2. Performance degrades progressively with decreasing discharge current density.

We performed some calculations to determine the dependence of excitation efficiency on E/N by using a code based on the work of Lockett.[12] Published values of electronic excitation cross sections[13] and molecular reaction rates[14,15] were used. Figure 34 shows some results of these calculations. The excitation efficiency for short-pulse amplifiers is, in effect, a figure of merit for the conversion of electrical to stored asymmetrical-mode vibrational energy in the CO_2 molecules. Although excitation efficiency has not been measured directly, the best overall performance is found at E/N values that correspond to the maxima shown in Fig. 34. Calculations of small-signal gain based on the excitation rates used to plot Fig. 34, result in an overestimate of gain for the 3:1/4:1 mix and a slight underestimate for the 0:1/4:1 mixture.

Because of the much higher density of CO_2 in the helium-free mixtures, less excitation is required for a given gain. This undoubtedly contributes to the improved performance we observed. Various gas additives were studied to identify those which might suppress gain without materially affecting the inversion, or which might improve overall laser performance. Small amounts of NH_3, NH_2D, or C_2H_4 additives do not seriously deplete the inversion, while providing gain suppression on many CO_2 lines. Unfortunately, these gases do not appear to bleach readily and thus inhibit energy extraction. We have studied hydrogen for its effect on laser performance and found no significant degradation at concentrations $\leq 5\%$. At higher concentrations, laser performance was progressively degraded.

Initiation of Glow Discharges in CO_2 Laser Gases With Volumetric Preionization by a Radioactive Gas

The reliability of self-sustained, high-pressure-discharge CO_2 lasers is strongly influenced by the density and uniformity of the preionization. In addition, the volume scalability of these discharges is limited by the dimensions over which uniform preionization of the required density can be achieved.

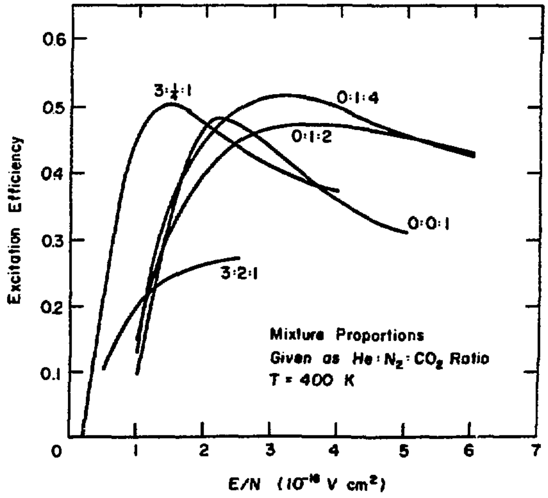

Fig. 34. Calculated fraction of input electrical energy feeding the upper CO_2 laser level (assumed in equilibrium with N_2 excitation) as a function of E/N.

Present techniques employ blades, pins, or flashboards to generate uv light at the boundaries of the discharge region. The uv light penetrates the discharge volume, creating a spatially nonuniform electron density that is adequate for the initiation of a glow discharge for some geometries and gas mixes. Because CO_2 attenuates the ionization uv radiation, these boundary techniques become less useful as the dimensions of the discharge or the partial pressure of CO_2 are increased.

Recently, we proved a technique which eliminates the problems inherent with boundary ionization sources.[16] Small quantities of tritium were added to the laser gas mix, providing a constant source of spatially uniform preionization. A voltage pulse of sufficient amplitude to produce breakdown was then applied to the preionized gas.

We succeeded in producing the discharge under a variety of conditions. Uniform glow discharges were obtained in helium-free laser gas mixes, with energy inputs of several hundred joules per liter. Although these are the most difficult discharge conditions, the amount of radioactive gas required for effective preionization was less than 100 $\mu Ci/cm^3$. Figure 35 illustrates discharge performance obtained with this preionization method.

These experiments employed somewhat crude electrode geometries. The electrodes were flat copper plates glued to the faces of a Plexiglas sheet spacer. No attempt was made to optimize the spatial profile of the electric field within the discharge, nor to inhibit electrical breakdown along the Plexiglas surface. Also, the electrical circuit which provided the discharge pulse was relatively slow. In spite of these difficulties, initial experiments were successful.

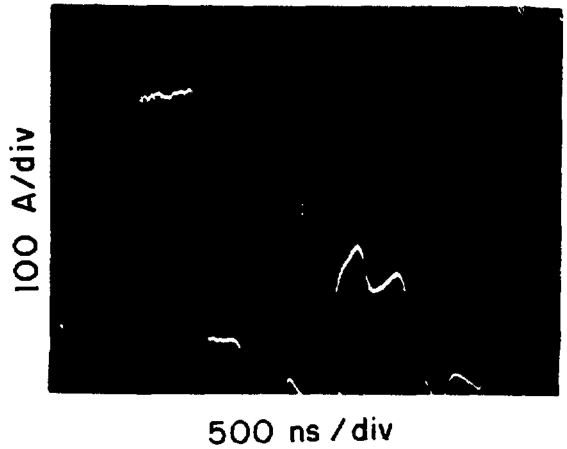

Fig. 35. Oscilloscope trace of voltage waveform of an operating tritium-preionized laser discharge. 550-torr 0:1:1::He:N_2:CO_2 mix; current density, 25 A/cm ; energy deposition, 294 J/liter atm.

Tritium radiates a beta spectrum with 6 keV average energy and 12-year half-life. Its selection as the radioactive source for these experiments was based mainly on convenience. The technology for handling tritium is well developed and presents no severe health problems in the quantities used, even in the event of an accident.

The technique we developed is not limited to the use of tritium. Many radioactive gases, with higher specific activity or different chemical behavior, are better suited for particular requirements.

Also, many other laser gases exist which might be used in such a discharge, e.g., high-pressure mercury vapor, which cannot be effectively preionized by uv light. Mercury has a low recombination coefficient, so that a very high level of preionization might be achieved with low concentration of the radioactive gas.

Other excimer lasers have been developed which require relativistic electron-beam excitation due to the absence of effective methods for producing glow discharges in these gases. Volume preionization by a radioactive gas may remove this difficulty.

Electron-Beam Preionization of Self-Sustained CO_2 Laser Glow Discharge

The construction of preionized self-sustained glow discharges in gases at atmospheric pressure has, in the past, involved mostly an adaptation of previously reported techniques. No serious efforts have been made to optimize the performance of these discharges with regard to efficiency, reliability, or scalability.

Recent experiments have attacked these problems in a fundamental way. In these studies, we used electron-beam rather than uv preionization to provide a spatially uniform level of initial ionization as well as to decouple self-sustained discharge operation from the photoionization cross sections of the laser gas mixture being studied. Also, this technique made it possible to vary the level of preionization over a wide range by controlling the delay between the termination of the preionizing pulse and the beginning of the main discharge pulse. For diagnostic work, these are significant advantages over the conventional uv preionization technique.

The laser chamber employed a 1.5-cm electrode spacing. The active medium had a cross-sectional area of 17.5 cm^2 and a length of 7 cm. The electron beam was generated in a small cold-cathode device operating at 150 kV, and delivered a primary current density of 50 mA/cm^2 in a 250-ns pulse. We found that the discharge would operate well in the self-sustained mode for most gases with a range of delay from 0 to 5 µs between the preionizing and the main discharge pulses.

The main discharge pulse was applied by discharging a length of high-voltage coaxial cable into the preionized gas. The cable impedance Z_0 was measured by charging the cable to a known potential V_c and monitoring the discharge current amplitude I_d with a short-circuit load. Once the impedance of the cable is known, the operating E/P (electric field vs pressure ratio) of the discharge can be determined directly according to the relation

$$\frac{E}{P} = \frac{V_c - Z_0 I}{LP} . \qquad (8)$$

Here, L is the discharge electrode separation and P is the gas pressure. The current waveform was integrated to give the energy input to the gas as a function of time. The latter procedure was important for determining the time history of both the small-signal gain and the specific energy deposition in a given gas mixture.

The experiments were organized in the following manner: first, we carefully measured the operating E/P for a standard 3:1/4:1::He:N_2:CO_2 gas mixture. Then we attempted to lower this value by appropriate choice of gas additives. Because self-sustained discharges operate at E/P values above the optimum for pumping laser levels, we anticipated that the presence of a gas component that lowered the E/P from its normal value would result in increased discharge efficiency.

More than a dozen additives of low ionization potential were studied. The most pronounced effects were noted with tri-propyl-amine (TPA), although xenon gave nearly equal improvement. The operating E/P of the 3:1/4:1 mixture is 11 V/cm·torr. The addition of TPA at its room-temperature vapor pressure reduced this value to 8 V/cm·torr. When 60 torr of xenon was added, the value was 8.9 V/cm·torr.

The second step in this series of experiments was to study the effects of the additives on laser pumping efficiency. For many additives studied, the quantities required to produce a measurable effect on E/P also decreased the pumping efficiency. However, both xenon and TPA improved the efficiency significantly. As expected from the E/P measurements, TPA had the most striking effect.

The third step was to find the ratio of major gas constituents which, with xenon and TPA, gave the highest pumping efficiency. We found that helium-free mixtures gave the best performance, although these mixtures have the disadvantage of operating at higher E/P.

Typical results for a variety of gas mixtures are shown in Fig. 36. Note that the optimum mixture is 60% CO_2 and 40% N_2, with TPA added. This mixture operates at an E/P of 18 V/cm·torr and has

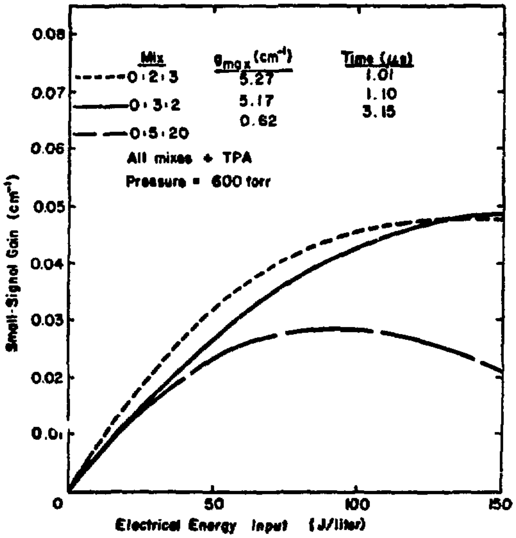

Fig. 36. Measured small-signal gain vs specific electrical energy input for various laser gas mixtures at 600 torr.

a pumping efficiency ~ 70% that of the 0:1/4:1 mixture in an electron-beam-stabilized discharge. The results achieved with fast pumping are shown in Fig. 37. Extremely high gains are possible with very good efficiency when the pumping time is kept short relative to the relaxation times of the relevant vibrational levels. Fast pumping is straightforward in a self-sustained discharge, whereas it can be accomplished in an electron-beam-stabilized discharge only at the expense of providing very high primary current densities.

In summary, the following statement can be made concerning self-sustained discharges with gas additives:

- The addition of TPA or xenon to CO_2 laser gas mixtures lowers the E/P significantly and increases the pumping efficiency correspondingly.
- The addition of TPA or xenon also improves the stability of the discharge for any gas mixture.
- The most efficient gas mixtures for self-sustained discharge operation are those without helium for pumping currents of 10 A/cm^2 or greater. However, discharges with helium are more stable and operate at significantly lower E/P.

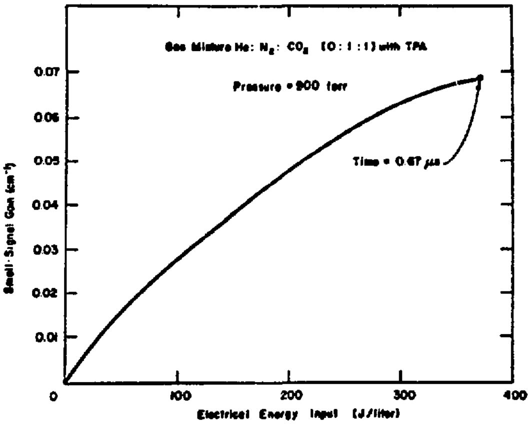

Fig. 37. Measured small-signal gain vs specific electrical energy input for a helium-free mixture with fast pumping.

- Efficiency comparable to that of electron-beam-stabilized discharges can be achieved with appropriate preionization in a self-sustained discharge.
- Fast pumping rates are readily achieved with self-sustained discharges. This is a fact of primary importance in the design of short-pulse oscillators and small-scale amplifiers.

REFERENCES

1. S. M. Hamadani, J. Goldhar, N. A. Kurnit, and A. Javan "Coherent Optical Pulse Reshaping in a Resonant Molecular Absorber," Appl. Phys. Lett. 25, 160 (1974).

2. E. Yablonovitch and J. Goldhar, "Short CO_2 Laser Pulse Generation by Optical Free Induction Decay," Appl. Phys. Lett. 25, 580 (1974).

3. A. Gondhalekar, E. Holzhauer, and N. R. Heckenberg, "Single Longitudinal Mode Operation of High Pressure Pulsed CO_2 Lasers," Appl. Phys. Lett. 46A, 229 (1973).

4. T. C. Owen, L. W. Coleman, and T. J. Burgess, "Ultrafast Optical Kerr Effect in CS_2 at 10.6 μm," Appl. Phys. Lett. 22, 272 (1973).

5. D. L. Smith and D. L. Davis, "Generation of Single, 1-ns Pulses at 10.6 μm Without Mode-locking," IEEE J. Quantum Electron. 10, 138 (1974).

6. J. F. Figueira and H. D. Sutphin, "Generation of Multiband 1-ns pulses in CO_2 Lasers," Appl. Phys. Lett. 25, 661 (1974).

7. R. L. Abrams and P. K. Cheo, "Collisional Relaxation of CO_2 Rotational Levels by N_2 and He," Appl. Phys. Lett. 15, 177 (1969).

8. J. L. Lyman, R. J. Jensen, J. Rink, C. P. Robinson, and S. D. Rockwood, "Isotopic Enrichment of SF_6 in S^{34} by Multiple Absorption of CO_2 Laser Radiation," Appl. Phys. Lett. 27, 87 (1975).

9. R. L. Abrams, "Broadening Coefficients for the P(20) CO_2 Laser Transition," Appl. Phys. Lett. 25, 609 (1974).

10. R. L. Abrams and P. K. Cheo, "Collisional Relaxation of CO_2 Rotational Levels by N_2 and He," Appl. Phys. Lett. 15, 177 (1969).

11. R. Jacobs, K. J. Pettipiece, and S. J. Thomas, "Rotational Relaxation Rate Constants for Ca," Appl. Phys. Lett. 24, 8 (1974).

12. Several codes exist at LASL and elsehere that solve the Boltzman equation for vibrational excitation rates for CO_2. See, for example, Los Alamos Scientific Laboratory Report LA-5562-MS (April 1974).

13. J. J. Lowke, T. V. Phelps, and B. W. Irwin, "Predicted Electron Transport Coefficients and Operating Characteristics of CO_2:N_2:He Laser Mixtures," J. Appl. Phys. 44, 4664 (1973).

14. C. J. S. M. Simpson and T. R. D. Chandler, "A Shock Tube Study of Vibrational Relaxation in Pure CO_2 and Mixtures of CO_2 with the Inert Gases, Nitrogen, Deuterium and Hydrogen," Proc. Roy. Soc. London A 317, 265 (1970).

15. W. A. Rosser, Jr., A. D. Wood, and E. T. Gerry, "Deactivation of Vibrationally Excited Carbon Dioxide ($_3$) by Collisions with Carbon Dioxide or with Nitrogen," J. of Chem. Physics 50, 4996 (1969).

16. J. T. Ganley, J. T. Verdeyen, and G. H. Miley, "Enhancement of CO_2 Laser Power and Efficiency in Neutron Irradiation," Appl. Phys. Lett. 18, 568 (1971).

II. NEW LASER RESEARCH AND DEVELOPMENT

New types of lasers must be developed to provide the desired energy per pulse, pulse length, pulse shape, wavelength, and efficiency for laser-fusion applications. Our advanced laser research has focused on rare-gas oxides, on Hg_2 excimers, and on the HF chemical laser. Because HF work at LASL has been discontinued as of January 1976, we report progress to date in this area as well as suggested approaches and techniques that should be valuable to those still active in HF laser research.

ADVANCED LASER RESEARCH

Introduction

Our goals in this effort are the identification and evaluation of promising lasers for fusion application both in the visible and uv spectral region and the development of a fundamental data base. Two systems seem to hold promise: the rare-gas oxides based on the $O(^1S) \rightarrow O(^1D)$ transition in oxygen at 557 nm and the excimer radiation at 335 nm in Hg_2. These systems have been discussed extensively in previous reports and represent the major emphasis of our effort. The search for other laser candidates continues.

The major experimental devices used in our investigation are the high-current relativistic electron-beam (REB) and the electrical-discharge systems. The REB represents a very useful tool to study atomic and molecular kinetic processes and related laser behavior. However, we believe that these laser systems can be excited more easily by electrical discharges. We are, therefore, concentrating on studying the physics and technology of this method of excitation. If these pumping techniques are proved to be useful in visible and uv laser systems, it may be possible to extend the existing capability in our high-energy CO_2 laser systems to operation at shorter wavelengths.

A major problem in fusion laser systems is optical damage. This is of particular importance for visible and uv lasers with respect to energy saturation and efficient operation. To minimize the zero-signal gain, the stimulated-emission cross section, σ_s, for a given amount of stored energy must be small. The saturation energy flux, E_s, for a laser transition is $h\nu/2\sigma_s$, with h being Planck's constant and ν the laser frequency. The saturation flux is correspondingly large for small σ_s. Note that the laser-saturation flux is also increased because of the higher value of photon energy, $h\nu$. In the case of the ArO laser operating at 557 nm, the effective value of $\sigma_s \approx 10^{-20}$ cm^2 and E_s = 16 J/cm^2. For efficient operation the laser energy flux, E, should be equal to, or larger than, E_s. However, because most reflective optics are damaged at a flux of $\gtrsim$ 5 J/cm^2, optical components must approach the damage levels defined by E_s. Reflective coatings exist that can withstand these flux levels.

We have conducted a series of laser-damage studies that are discussed later in this section. The experimental devices we used have been developed and are in an initial test phase. Further topics discussed in this section are the use of electron beams to study kinetic processes in rare-gas mixtures, our investigations of mercury lasers, as well as related theoretical work on the effects of electrons on excited-state kinetics for Hg_2 and argon.

Experimental Facilities

Several experimental test beds have been constructed to investigate the electrical-discharge pumping process, with the intent to provide flexible systems for general research use.

An electron-beam-controlled discharge system has been developed and is in an initial testing phase. The basic apparatus has been modified extensively for this research application. The discharge chamber will allow operation at gas pressures up to 20 atm at an applied voltage of 100 kV. The electron gun operates at 200 keV and will provide a gas-current density of 20 A/cm^2. All electrical circuits have been designed for fast-pulse excitation; the system may also be operated as a self-sustained discharge.

Several preionized self-sustained discharge systems have been fabricated that are compatible with corrosive gases. The technology of fast-pulsed excitation has been emphasized in these devices. For noncorrosive gases, we used a commercial fast-pulse electrical-discharge laser to evaluate several prospective lasers. This system is particularly convenient because it operates repetitively up to 60 Hz.

A valuable tool for the study of atomic and molecular kinetics and for initial laser investigations is the high-current relativistic electron beam (REB). Several of these devices have been acquired, the characteristics of which are summarized in Table X. The Febetron 706 is ideal for studying fast kinetic processes and will be discussed later. The POCO machine will be delivered soon and should be operational by April 1976. This device allows high-energy transverse electron-beam excitation of a gas over an active length of 100 cm with a 20- to 40-ns pulse. Risetime of the pulse is 11 ns. The POCO machine should be useful in evaluating large high-power lasers. It will be of particular use in our investigations of rare-gas-oxide systems.

Kinetic Measurements

Our studies of the kinetic processes in rare-gas atomic and molecular systems are continuing. Of particular interest are the durations of short processes and the effects of electron collisions on such processes.

TABLE X

RELATIVISTIC ELECTRON-BEAM MACHINES FOR INVESTIGATING LASER KINETIC PROCESSES

Machines	*Beam Energy (MeV)*	*Beam Current (kA)*	*Total Energy (J)*	*Pulse Duration (ns)*
Febetron 706	*0.5*	*7*	*10*	*2.5*
Febetron 705	*2.0*	*5*	*400*	*40*
PI 316	*2.0*	*50*	*2000*	*30*
POCO (Cassandra)	*2.0*	*300*	*15000*	*20-40*
Nereus	*0.4*	*30*	*400*	*30*

We have constructed an experimental system (now fully operational) to investigate fundamental kinetic processes in rare gases. The system uses a Febetron 706 for electron-beam excitation of high-pressure gas on a time scale of 2.5 ns (see Table X). Time-dependent spectral emission is monitored by a McPherson-218 monochromator in the beam direction and by a McPherson-216.5 monochromator in the transverse direction. The signal detected by fast photodiodes is recorded with a Tektronix automatic data-acquisition and processing system (ADAPS). This multichannel system is equipped with fast transient digitizers (Tektronix 7912) and a minicomputer with peripherals. Despite the severe environmental conditions, the noise level has been reduced to less than 1 mV. This allows data recovery and processing over a dynamic input range of 10^3 by simple control of gain in the equipment. Our ADAPS system provides on-line real-time data processing with the following features:

- Subtraction of base-line distortion and noise;
- Signal storage and display on a video output either as a linear or a log plot; and
- Signal integration over a specified interval.

The ADAPS is being programmed for curve-fitting routines.

A schematic of the apparatus is shown in Fig. 38. The gas to be studied can be excited either directly by the electron beam or optically by radiation from a second gas cell that is directly excited by the electron beam and optically connected to a test cell. The second method is particularly useful to clearly define kinetic processes in the absence of electron-induced collisional effects. In typical operation the electron beam excites argon at gas pressures up to 60 atm in the first cell. Optical radiation from the Ar_2^* excimer at 126 nm is generated with an isotropic power output up to 10 MW and is directed into a second test cell through a MgF_2 window. This radiation then optically pumps the $^1P_1$ level in xenon or the $^3P_1$ level in krypton in an electron-free environment. Because of the high gas pressures used in these experiments, the pump light is typically fully absorbed in the test chamber. Because a quantum ef-

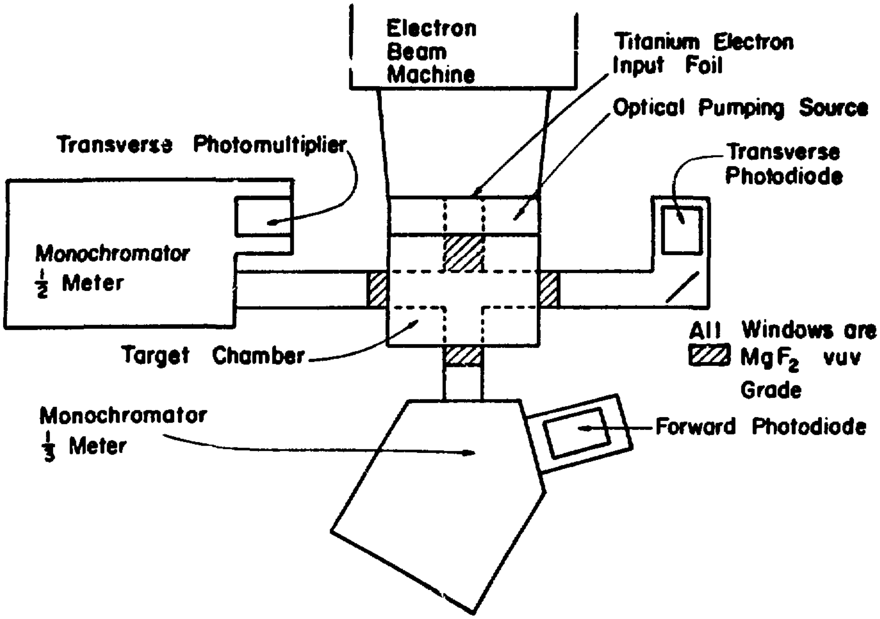

Fig. 38. Schematic of optical pumping apparatus.

ficiency near unity is realized, we obtain very intense emission from the test cell.

Time scales of interest in the kinetics of rare-gas molecules are 10 ns or less. To use the 2.5-ns impulse capability of the excitation source effectively, we have to generate an optical pumping pulse out of the Ar_2* excimer on a similarly short time scale. However, this is difficult to achieve, because the radiative lifetime of the 0_u^+ state in Ar_2* is relatively long, 4 ns. This decay time can be shortened by adding a background impurity that relaxes the argon excimer collisionally, with a decay time equal to or less than the duration of the electron-beam pulse. However, the number of such impurities is limited; not only must the additive collisionally relax Ar_2* but also must not absorb the argon excimer radiation. Molecular nitrogen, N_2, has been identified as suitable. Data obtained in 60 atm of argon with increasing N_2 pressure indicated a rate for the reaction

$$Ar_2^* + N_2 \rightarrow N_2^* + 2Ar \qquad (1)$$

of 3×10^{-11} cm^3s^{-1}. By using N_2 as a collisional deactivator, we have obtained optically pumped pulses from Ar_2* that are comparable to the electron-beam excitation pulse. However, this method was not entirely satisfactory, because of secondary optical pumping of the test gas by radiation emitted from excited N_2.

Other materials tried for this purpose were krypton, xenon, and H_2. Krypton and xenon yield relaxation rates for Ar_2* of 4×10^{-10} and 2×10^{-10} cm^3s^{-1}, respectively. For H_2, the transfer process is expected to be to dissociative states via the reaction

$$Ar_2^* + H_2 \rightarrow 2H + 2Ar + \Delta E \ . \qquad (2)$$

We also obtained a secondary relaxation process which is thought to be due to the reaction

$$Ar_2^* + H \rightarrow \text{products} \ . \qquad (3)$$

The rate constant determined for Eq. (2) was 8×10^{-11} cm^3s^{-1} and for Eq. (3) was 5×10^{-10} cm^3s^{-1}.

The use of H_2 and Ar_2* as a short-pulse optical-pump source appeared to be satisfactory. Optical-pump pulses at 125 nm can be obtained with a risetime of 3 ns, a FWHM of 2.5 ns, and a decay

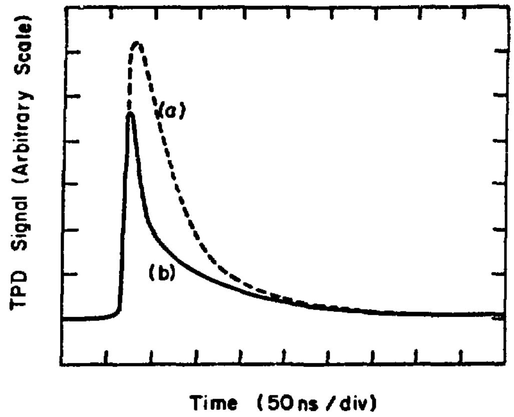

Fig. 39. Transverse photomultiplier detector signal from 1500-torr xenon when using an optical pumping source fillec to (a) 50 000-torr argon, (b) 50 000-torr argon + 233-torr mercury.

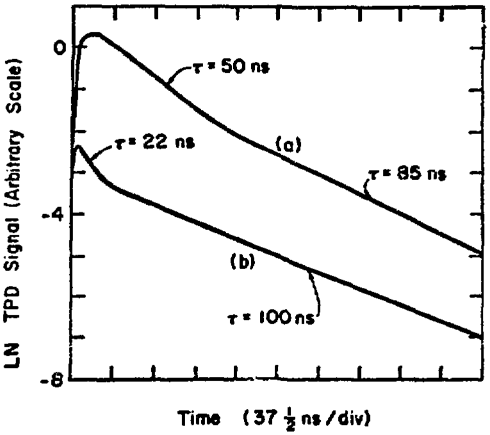

Fig. 40. Plot of natural log of signals shown in Fig. 39.

time of 1 ns. An example of the use of this technique to pump xenon is shown in Figs. 39 and 40. The test cell contains 2 atm of xenon and the pumping cell contains 60 atm argon either with no H_2 (Curve a) or with 235 torr H_2 (Curve b). Plotted is the 172-nm fluorescence from the Xe_2^* dimer. As indicated, the decay rate is considerably different depending on the temporal character of the optical pumping radiation. From Curve b, we can obtain a lower limit on the radiative lifetime of the state.

We have used similar optical pumping techniques previously to measure the stimulated-emission coefficient, radiative lifetime, and kinetic processes in ArO. This work has been summarized in LASL Report LA-6050-PR and has been published in the literature.[1]

Mercury Excimer Lasers

We are studying the Hg_2 excimer extensively because it holds promise of high-energy storage, high efficiency, and operation at a high repetition rate. Optical gain[2] has been demonstrated at three wavelengths in the 335-nm band, which is one of three Hg_2 excimer bands that cover a wavelength interval from the uv to the near ir.

In our program, we intend to demonstrate a uniform large-volume mercury discharge with good optical quality at a high neutral density (> $10^{19}/cm^3$). As reported previously (LA-6050-PR), we constructed a heat-pipe-cell apparatus to determine the discharge and optical quality of a dense mercury medium. Although this apparatus did not operate to design specification, we did obtain some preliminary information about high-pressure mercury that has provided a design-data base for our present efforts.

The medium uniformity in the heat pipe was measured by using a Foucault method, i.e., a pinhole and knife edge. Because the heat pipe is not a focusing element, two lenses had to be added to the basic apparatus, one to collimate the light from the pinhole and the second to refocus onto the knife edge. The rather crude apparatus, which had an instrumental width of 250 μrad with the heat pipe cold, proved adequate for the task at hand.

The measurements indicated good medium uniformity up to a density of 5 x 10^{18} /cm^3; when the density was increased, medium quality degraded rapidly. The amount of degradation was about proportional to the mercury density. The problem is thought to occur at the interface between the hot mercury and the cold argon used to protect the windows. At the highest pressure tested (~ 2000 torr), the aberration totaled about 6 mrad across the 15-mm clear aperture.

The heat-pipe cell was difficult to operate during these tests because of problems with wicks and with large mass transfer in the vertical arm (not a heat pipe) of the cell which was used to insert the high-voltage lead. It was very difficult to obtain uniform wetting of the wick structure and to maintain that wetting during operation. The only wick material we have been able to use with some success has been pure nickel. However, even these wicks show a strong tendency to dewet under operation unless extreme care is taken to avoid any contamination. In addition, the strong rate of attack by hot mercury on nickel limits the lifetime of such wicks to at most about 10 days. These problems, coupled with some ambiguity as to whether or not the wicks were actually pumping, may have contributed to the negative results concerning medium homogeneity.

We have made preliminary measurements of the discharge characteristics at mercury pressures up to ~ 2000 torr. The discharge appeared to be reasonably uniform for durations of up to ~ 1 μs over an area of ~ 20 cm^2. However, some uncertainty exists because the full discharge area could not be observed. A preliminary E/N of ~ 1.5×10^{-16} V cm^2 was measured, which is in the region of high efficiency of production of the $^3P_1$ and $^3P_2$ states of mercury; these are the source states (by three-body association) for the Hg_2^* excimer bands that are of interest for laser systems.

To circumvent the above difficulties, we have constructed a new 7.5-cm-diam heat pipe, with split heaters and coolers to provide greater control of the conditions in the interface zone. In addition, indications are good that stainless steel, after proper chemical treatment, may be a long-lasting wick material. The deletion of arms other than heat-pipe arms for discharge studies should allow us to conduct similar optical studies with less ambiguity than in the original device. These investigations should then reveal why mercury heat pipes are difficult to operate and what the temporal variations in the gas-vapor interface are.

Heat pipes are considered for metal-vapor laser systems because these systems require good homogeneity of the lasing medium. However, because of the many difficulties encountered in developing the heat-pipe approach, we have constructed a heated mercury cell to study the discharge behavior and the excited-state kinetics of this system. The cell incorporates all-metal seals, bakeable high-voltage feedthroughs, and sapphire windows for transverse discharge experiments in pure mercury at pressures up to 5 atm and temperatures to 775 K. The cell also contains a pair of parallel plate electrodes up to 50 cm long and a bakeable sliding spark preionizer. Because of the high flux losses due to the sapphire windows (~ 6%/window) operation of the cell as a laser oscillator is not feasible at the levels of gain anticipated. However, the apparatus is adequate for gain measurements by the probe technique and such measurements will be made. Future improvements include the replacement of the sapphire windows with quartz windows fused on at Brewster's angle and using a molybdenum-quartz seal. This cell is being baked and tested in vacuum. Some leaks in the metal seals after thermal cycling led to a redesign of the seals.

THEORETICAL CONSIDERATIONS AND STUDIES

Effect of Electron Collisions on Excited-State Kinetics

Most gas lasers of interest for fusion application use a gas mixture in which a rare gas constitutes a major fraction of the active medium. However, the use of an electrical discharge to pump electronic laser transitions can destroy the excited states of the rare gases by either a collision-induced decay to the ground state (superelastic collision) or by a second collision-induced transition from the excited state to higher lying electronic states or to ionization. These effects are particularly important at high excited-state and high electron densities, because they can cause large losses in excited-state population density with an attendant reduction in laser performance. To evaluate these effects quantitatively one must, first, evaluate the effect of the excited-state inelastic-loss process on the electron-distribution function and then convolve the resultant distribution function with the inelastic cross section to determine a rate for the process. This procedure has been carried out in argon and mercury for several values of the discharge parameter E/N.

In our calculations we used a version of LASL's computer code to solve the Boltzmann transport equation. (Details of this code have been given in several previous progress reports.) Fourteen individual cross sections for the electronic states in argon were used; only one inelastic process was included to account for ionization out of the lowest ^3P levels. The peak value of the cross section was 10^{-15} cm^2. The results indicated that for fractional population densities of excited electronic states less than 10^{-3} of the ground state, the electron-distribution function was insensitive to the excited-state population fraction over a wide range in E/N. This being the case, the rate for these processes can be calculated directly and the effects of electron collisions on excited-state kinetics can be inserted in the laser kinetic code in a simple manner.

We performed a similar calculation for mercury. Included were cross sections for the $^3P_0$, $^3P_1$, $^3P_2$, and $^1P_1$ electronic states as well as a value of 10^{-15} cm^2 for excitation from the $^3P_2$ state to the ionization continuum. The results were similar to those for argon, i.e., for fractional populations of excited electronic states less than 10^{-3}, the effect on the electron-distribution function was small.

Studies of this problem are continuing.

New Lasers - Theoretical Investigations

General -- Some attention has been devoted to uncovering other attractive lasers. A good example has been the HF laser, but we have also investigated the noble-gas excimer lasers, rare-gas-oxide molecules, mercury, and rare-gas dimers. To be specific, we have recently completed detailed calculations on the potential-energy curves for ArO and Zn_2 as a model of Hg_2 as well as on the transition moments connecting the various excited states in these molecules. The results are needed for the detailed modeling of laser systems involving these molecules.

Electron Energy Distribution in Electron-Beam-Initiated Xenon and Argon Plasmas -- We have performed calculations to determine the time evolution of electron energy distributions in electron-beam-initiated, unsustained, xenon and argon plasmas. These calculations were to provide the electron-impact excitation rates for excimer laser models and were performed to test the adequacy of the Maxwellian energy distribution, the distribution generally assumed for the electrons in these models. In our calculations we included electron-neutral elastic and inelastic collisions, electron-electron collisions, and electron-ion dissociative recombination.

A representative example of the results is shown in Fig. 41, which illustrates the evaluation of electron-electron distributions. The "normalized" distribution, $[\bar{n}(\epsilon) \equiv n(\epsilon)/(\epsilon^{1/2}\,\Sigma_\epsilon n(\epsilon))]$, in xenon at a pressure of 20 atm, for an electron-beam pulse of 2 ns is shown in this figure.

These results indicate that, in equilibrium, below the thresholds for inelastic electron-neutral processes, the distributions can be reasonably well approximated by a Maxwellian distribution. However, as the results for the 2-ns pulse in Fig. 41 indicate, above the inelastic thresholds the in-

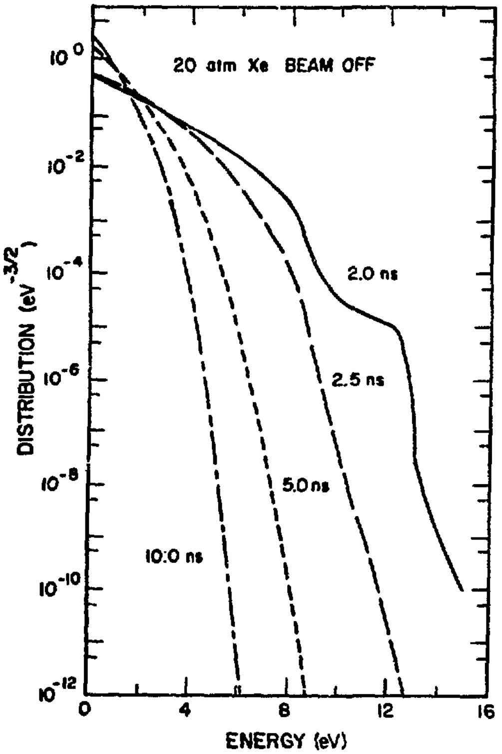

Fig. 41. "Normalized" electron-distribution function in xenon for a pressure of 20 atm and an electron-beam pulse of 2 ns.

elastic processes dominate so that the high-energy tails of the distributions are largely missing. As a result, a model that assumes a Maxwellian distribution everywhere must either underestimate the electron temperature or overestimate the ionization and direct-impact excitation rates.

Figure 41 also indicates that after removal of the electron beam the electrons will equilibrate with the gas on a time scale that is long compared to many other processes in noble-gas excimer laser systems. This result is certainly one of the most important to come from this study because in many laboratory determinations of rates for kinetic processes in these systems it has been assumed that the electron temperature equals the gas temperature immediately after removal of the electron beam.

The Electronic States of Argon Oxide -- The rare-gas-oxide molecules have recently attracted interest because they hold promise for laser fusion applications (visible wavelength, high saturation flux, and high efficiency) and because lasing has been demonstrated on the $O(^1S) \rightarrow O(^1D)$ transition in argon,[3,4] krypton, and xenon mixtures.[4] Of particular interest for the rare-gas-oxide systems are the electronic states of the rare-gas oxide,[5] the collision-induced emission of the $O(^1S) \rightarrow O(^1D)$ dipole-forbidden transition,[6] and the quenching of $O(^1D)$ to $O(^3P)$.[7]

To provide the data needed to model the above processes, we performed some ab initio configuration-interaction calculations on the electronic states of ArO arising from $Ar(^1S) + O(^3P, {}^1D, {}^1S)$. The resulting potential-energy curves are shown in Fig. 42. All the curves are basically repulsive, although the curve for the $1\ {}^1\Sigma^+$ state arising from $Ar + O(^1D)$ is extremely flat. The $1\ {}^1\Sigma^+$ state is crossed by the $^3\Sigma^-$ and $^3\Pi$ states at R = 2.10 and 1.87 Å, respectively. The curve crossings between these states, all of which have 0^+ symmetry components when spin-orbit coupling is included, support previous speculations[7] that such crossings are instrumental in the rapid quenching of $O(^1D)$ by the rare gases. At the respective crossings the $1\ {}^1\Sigma^+$ state lies 119 and 413 cm^{-1} above the $Ar + O(^1D)$ separated atom limit.

Figure 43 plots the calculated electronic transition moments for the $2\ {}^1\Sigma^+ \rightarrow 1\ {}^1\Sigma^+$ and $^1\Pi$ emissions. The argon strongly enhances the $2\ {}^1\Sigma^+ \rightarrow 1\ {}^1\Sigma^+$ transition moment. From these data we estimate the lifetime of the $2\ {}^1\Sigma^+$ state to be ~ 3 μs; this is to be compared with a lifetime of 0.8 s for the dipole forbidden $O(^1S) \rightarrow O(^1D)$ transition.[8] The $2\ {}^1\Sigma^+ \rightarrow {}^1\Pi$ transition is only slightly affected by the rare-gas atom.

The Electronic States of Zn_2 -- Promising systems for visible and uv lasers may be derived from

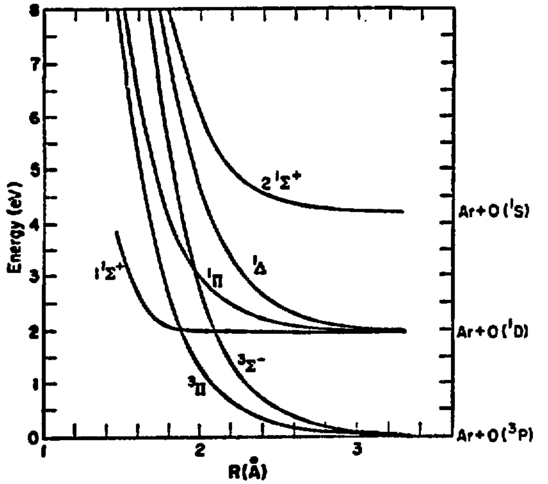

Fig. 42. Potential-energy curves for the low-lying electronic states of ArO, adjusted to give the correct atomic dissociation limits.

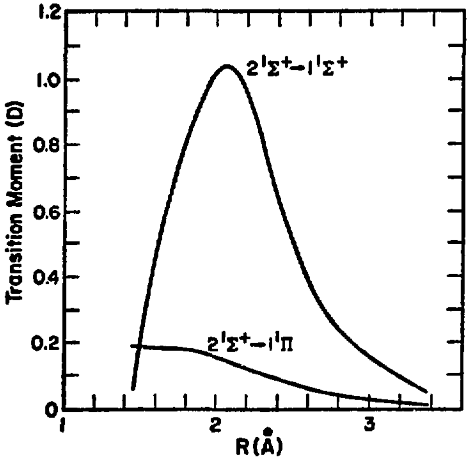

Fig. 43. Dipole transition moments (Debye) for the $2\,^1\Sigma^+$ state of ArO to the two optically allowed laser states as a function of internuclear distance.

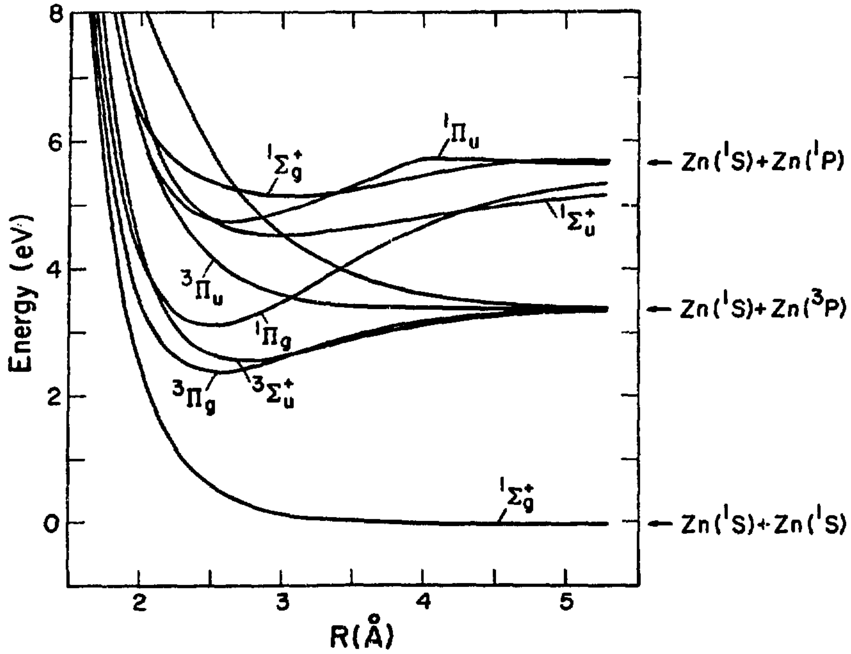

Fig. 44. Calculated potential-energy curves for Zn_2.

a class of molecules, such as Hg_2 or the rare-gas dimers, that has essentially dissociative ground states but bound electronic excited states. For Hg_2 and related systems, little experimental knowledge exists of the potential-energy curves involved. To provide a better understanding of Zn_2, Cd_2, and Hg_2, we have calculated the electronic states of Zn_2 arising from Zn(^{1}S) + Zn(^{1}S, ^{3}P, ^{1}P).

The calculated potential-energy curves of Zn_2 are shown in Fig. 44. As expected, the ground state and two of the triplet states (${}^3\Sigma_g^+$, ${}^3\Pi_u$) are essentially repulsive. The other triplet states (${}^3\Sigma_u^+$, ${}^3\Pi_g$) and all four singlet states are bound. The unexpected minima in the ${}^1\Pi_u$ and 2 ${}^1\Sigma_g^+$ states arise from interaction with states that have appreciable $Zn^+ Zn^-$ character. The spectroscopic constants for the bound states are given in Table XI.

The calculations on Zn_2 have been used as a model for the Hg_2 system. A preliminary analysis indicates that the 3350- and 4850-Å emissions in Hg_2 are not likely to arise from the 0_u^- and 1_u components of the ${}^3\Sigma_u^+$ manifold as previously assumed.[9] If the 3350-Å emission is assigned to the 1_u state, a likely long-wavelength emitter is the manifold of states deriving from the lower ${}^3\Pi_g$ state (such as 1_g) by three-body collisions.

The Rydberg States of F_2 -- In an attempt to understand the electronic structure of the excited states of F_2 and its ions, we have performed an extensive series of configuration-interaction (CI) calculations on F_2 and F_2^+. Results for the lowest valence states were reported in LA-6050-PR. Here we will present the results that include the Rydberg states. The primary motivation for this study was the desire to examine the role of excited electronic states in laser systems, such as H_2 - F_2 and rare-gas-F_2, which are initiated by high-energy electron beams. The calculational method used was basically that described in the previous report except that the atomic basis set was augmented by diffuse 3s(ζ = 0.036) and 3p(ζ = 0.034) functions optimized from the atomic Rydberg states.

For each many-electron symmetry, we determined a set of reference configurations by including all possible arrangements of the outer ten electrons in the $3\sigma_g$, $3\sigma_u$, $1\pi_u$, and $1\pi_g$ orbitals. All single and double excitations relative to this reference

TABLE XI

SPECTROSCOPIC CONSTANTS FOR THE BOUND STATES OF Zn_2 DISSOCIATING TO $Zn(^1S) + Zn(^1S, {}^3P, \text{and } {}^1P)$; UNITS ARE AS INDICATED

State	Absorption[a] T_e (eV)	Emission[a] T_v (eV)	Equilibrium Internuclear Distance R_e (Å)	Dissociation Energy D_e (eV)	ω_e (cm^{-1})
$^3\Pi_g$	3.02	2.49	2.56	1.05	175
$^3\Sigma_u$	3.20	2.86	2.74	0.87	150
$^1\Pi_g$	3.42	2.81	2.51	2.42	202
$^1\Sigma_u^+$	4.82	4.66	2.97	1.00	107
$^1\Pi_u$	5.04	4.61	2.64	0.83	166
$2^1\Sigma_g^+$	5.45	5.33	3.07	0.44	104

---

[a] Corrected for the errors in the atomic excitation energies.

set were included subject to the restrictions that (1) the $1\sigma_g$ and $1\sigma_u$ orbitals remain doubly occupied, and (2) no more than one electron occupy a virtual orbital. These restrictions resulted in 298 to 398 spin eigenfunctions for the various singlet states. We performed configuration-interaction (CI) calculations at 17 internuclear distances between 0.9 and 4.0 Å; the calculated total energy at 1.42 Å was 198.87 atomic units.

We determined the electronic transition moments connecting the ground and various excited states in the dipole length representation in a straightforward fashion, because the CI wavefunctions were expressed in terms of the same set of orthogonal orbitals described above.

Of the manifold of 12 molecular states arising from two ground-state $F(^2P)$ atoms, only the ground state ($^1\Sigma_g^+$) is attractive while the other states are strictly repulsive (with the exception of possible van der Waals minima). The calculated electron radius, R_e, of the ground state (1.423 Å) agrees well with the experimental value (1.4118 Å), while the calculated dissociation energy (D_e = 1.91 eV) is actually 0.25 eV greater than the most recently determined value (1.66 eV).

At the R_e of the ground state, the excited valence states extend from 3.35 eV ($^3\Pi_u$) to 10.76 eV ($^3\Sigma_u^+$) for triplet states and from 4.77 eV ($^1\Pi_u$) to 10.58 eV ($^1\Sigma_u^-$) for singlets. Results for the singlet states are given in Table XI. Vertical excitation energies for the other triplet states are

$^3\Pi_g$(7.03), $^3\Sigma_u^+$(7.48), $^3\Sigma_g^-$(8.66), and $^3\Sigma_u^-$(10.69).

The next higher experimental dissociation limits for F_2 singlets include the Rydberg states $F(^2P) + F(2p^4\ 3s,\ ^2P)$ at 12.98 eV, and $F(^2P) + F(2p^4\ 3p,\ ^2D)$ at 14.58 eV; and the ionic states $F^+(^1D) + F^-(^1S)$ at 16.42 eV and $F^+(^1S)$ at 19.40 eV. Our calculated values for these limits are 14.23, 15.78, 16.45, and 18.84 eV, respectively -- suggesting considerably more error (> 1.2 eV) for excitation energies to Rydberg states than to ionic states.

The potential-energy curves of the two lowest states of $^1\Pi_u$ and $^1\Sigma_u^+$ symmetries (i.e., the dipole-allowed symmetries from the ground state) are shown in Fig. 45. The potential-energy curves of these states have the following general characteristics:

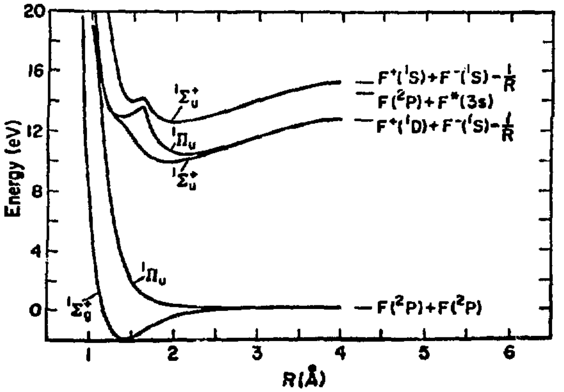

Fig. 45. Potential-energy curves for the ground state F_2 and the lowest two $^1\Sigma_u^+$ and $^1\Pi_u$ states.

- The Rydberg-like diabatic states have essentially flat curves at large R with shallow minima (1 to 2 eV) near R_e of the ground state for any of the bound states.

- The ionic diabatic states exhibit an attractive 1/R interaction for large R with wide and deep minima near 2.0 Å.

Interactions between these Rydberg and ionic states of the same symmetry prevent curve-crossings as evident in Fig. 45. The interactions are particularly strong for the lowest two $^1\Sigma_u^+$ states, which are separated by ~ 2 eV in the curve-crossing region. For smaller values of R the dominant excitations are $1\pi_g \rightarrow 2\pi_u$ (3p) and $3\sigma_g \rightarrow 3\sigma_u (F^+F^-)$, respectively, while for large R the curves correspond to ionic $F^+(^1D$ and $^1S) + F^-(^1S)$ states. The crossing in the upper $^1\Pi_u$ state (near 1.6 Å) in Fig. 45 is quite sharp by comparison, as the next state (not shown) is nearly tangential to the cusp in the lower curve. The curve for R > 1.6 Å corresponds to the $1\pi_g \rightarrow 3\sigma_u$ Rydberg state, and for R > 1.6 Å to the ionic state. Crossings between the repulsive valence states and the Rydberg states are also found, as in the $^1\Pi_u$ states, where the crossing occurs on the inner wall of the Rydberg-state potential well. For some of the other states ($^1\Sigma_g^+$, $^1\Delta_g$, and $^1\Sigma_u^-$) the crossing occurs farther out near the bottom of the well for the Rydberg states.

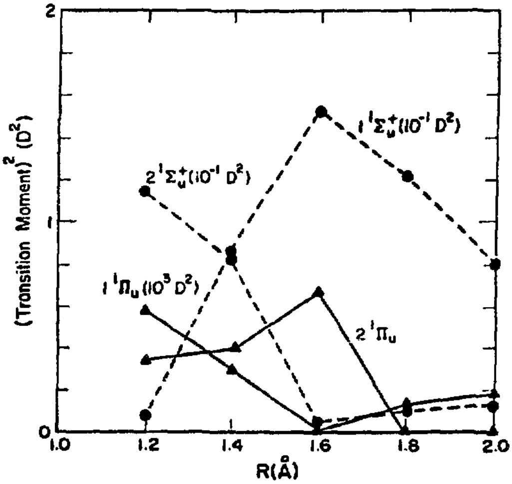

Fig. 46. Dipole transition moments (squared) between the ground state of F_2 and the lowest two $^1\Sigma_u^+$ and $^1\Pi_u$ states.

The change in character in the excited states is also reflected in the optical transition moments from the ground state (Fig. 46). Beyond the avoided curve-crossings (R > 1.6 Å), the transition moments generally drop precipitously. The transition moment for the $1\,^1\Pi_u \rightarrow {}^1\Sigma_g^+$ excitation (the square of which appears in the figure) changes sign near 1.6 Å, but in this case is not a consequence of any curve-crossing. Similar interactions between valence and Rydberg states have also been observed in other systems.

Laser-Damage Studies of Dielectric Coatings

Introduction -- Damage studies have been carried out on several dielectric thin films in an attempt to find damage-resistant materials for use in high-power laser-fusion application. Our initial studies were carried out at 1.06 μm. These results are reported below. Similar damage trends are expected in the visible wavelength region. Studies at 0.53 μm are in progress.

Damage to Dielectric Films by Standing-Wave Fields[10] -- We have evaluated the effect of damage to dielectric films by standing-wave (SW) electric fields for the case of 30-ps laser pulses at 1.06 μm. Single-layer films of TiO_2, ZrO_2, SiO_2, and MgF_2 were deposited by state-of-the-art electron-gun evaporation on BK-7 glass substrates with uniform surface preparation. The film thicknesses ranged from one to five quarter-wave (QW) increments.

The thresholds for TiO_2 films of odd QW thickness were greater than for even multiples (Fig. 47), which correlated well with the calculated internal maximum electric fields (Fig. 48). Threshold variations for ZrO_2 films were apparent but not as distinctly periodic with film thickness. Variations for SiO_2 films were negligible, again correlating with electric-field calculations.

Additional tests allowed comparisons of thresholds for (1) back- and front-surface films for normal incidence; (2) S- and P-polarized radiation at an incidence angle of 60°; and (3) circular and linear polarizations for normal incidence. We compared the thresholds with calculated SW field patterns at various locations in the films and generally found a definite correlation between the internal field maxima and the thresholds, but coating defects in a few instances apparently decreased or prevented any correlation. Specific findings were:

- Damage thresholds of TiO_2 films showed a strong dependence on the internal SW electric-field maxima.
- The higher end of the damage-threshold range for a given coating of ZrO_2 correlated well with the internal SW field maxima, but some evidence suggests that the lower end of the threshold range was restricted by film defects.
- Damage thresholds of MgF_2 coatings were affected slightly by SW field maxima. This influence was due to the low refractive index, to film defects, or to both.
- Damage thresholds of SiO_2 coatings on glass were not influenced by SW fields because the refractive index is nearly equal to that of the substrate. Random variations of the lower thresholds were presumably due to film defects.

RF-Sputter Coating Development

High damage-resistant films of TiO_2 to be used in coatings of laser optics for visible and near-ir wavelengths have been produced for us by Battelle Pacific Northwest Laboratories who used rf-sputtering techniques.[11] The laser-damage resistance of these films was remarkably superior to that of coatings deposited by other methods. Until the present, the best method of producing such coatings has been by electron-gun deposition. The damage thresholds of QW (at 1.06 μm) TiO_2 coatings produced by rf-sputtering were compared to those of coatings produced by the electron-gun method by a

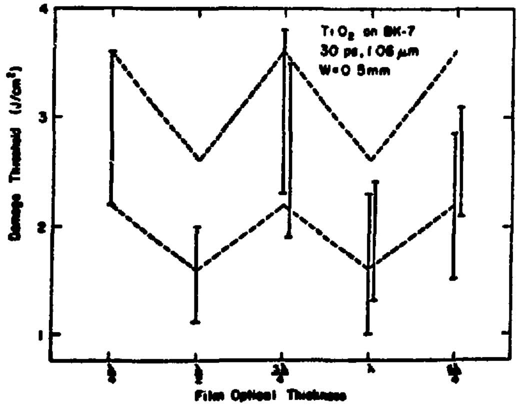

Fig. 47. Damage thresholds vs film optical thickness for TiO_2; 1.06-μm, 30-ps pulses.

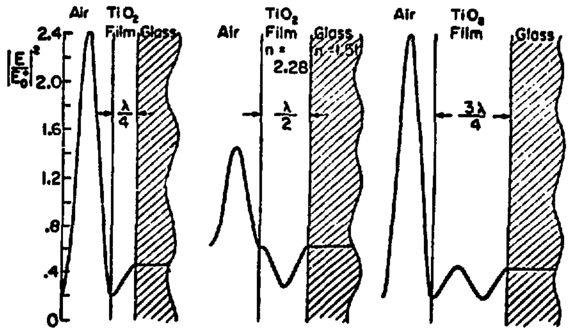

Fig. 48. Standing-wave electric field intensity distributions for λ/4, λ/2, and 3λ/4 films of TiO_2. The distributions are normalized to the incident electric field squared in air, $|E_o^+|$.

TABLE XII

DAMAGE THRESHOLDS OF SINGLE-LAYER QUARTER-WAVE THICK TiO_2 FILMS[a]

Deposition Technique	*Sample No.*	*Peak Energy Density (J/cm^2)*[b]
RF-sputtered	*B-22*	*8.0 - 11.3*
	B-33	*6.3 - 10.1*
	B-31	*5.1 - 9.8*
	B-27	*6.2 - 9.6*
	B-32	*5.5 - 9.2*
Electron-gun deposition	*C-1a*	*3.3 - 6.8*
	C-A1	*4.1 - 4.5*
	C-13	*2.2 - 3.6*

---

[a] *Test Conditions: single, 30-ps pulses at 1.06 μm, beam spot size of 0.50 mm; 40 shots to determine threshold range.*

[b] *Range of damage threshold observed.*

reputable commercial vendor. Single 30-ps pulses of 1.06-μm radiation were used in the measurements. Seventeen sputtered coatings were deposited with varied parameters on three types of substrates. The damage thresholds of the rf-sputtered coatings were about twice as high as those of coatings produced by electron-gun deposition. Several coatings had thresholds as high as 10 J/cm^2 as shown in Table XII.

Coatings of SiO_2 have also been prepared by Battelle, but the deposition parameters were not optimized for high-damage resistance. These films had damage thresholds of 4 to 8 J/cm^2, comparable to those of similar films produced by electron-gun deposition.

The next phase of contract work will be concentrated on improving the thickness uniformity of the films, optimizing the deposition parameters of SiO_2, and producing multilayer reflectors and antireflection coatings for damage tests at 0.53 and 1.06 μm.

Damage Resistance of Antireflection Coatings for Picosecond Pulses

The state of the art of producing damage-resistant dielectric antireflection coatings for use at 1.06 μm has been evaluated. Nine commercial coating companies, experienced in depositing refractory-oxide coatings with electron guns, suplied bilayer ZrO_2/SiO_2 coatings of the "vee" design on low-scatter BK-7P glass substrates prepared by Itek Corp. Each sample was irradiated at 40 different areas with single 30-ps pulses from a Nd:YAG laser. The irradiation spot-size radius of 0.5 mm was large enough to average over microscopic film defects. The damage thresholds (Table XIII) for the strongest coatings ranged from 5 to 7 J/cm^2; whereas the range for the weakest coatings was 2.5 to 4.5 J/cm^2. Because the design, materials, and substrates for these coatings were identical for each evaluation, the range of thresholds appears to be due to the various coating techniques used.

In addition, no correlation was found between the magnitude of scattering of a low-power 1.06-μm laser beam from these coatings and the high-power damage thresholds.

Hydrogen-Fluoride Laser Development

Introduction -- Our hydrogen-fluoride chemical-laser development program is being discontinued as of January 1976. In its final phases we concentrated on defining and testing minimum features that would make it possible to use the HF laser system in multiline irradiation tests at 2.7 μm of flat targets evaluated previously with Nd:glass

TABLE XIII

DAMAGE THRESHOLDS OF COMMERCIAL ZrO_2/SiO_2 ANTIREFLECTION COATINGS[a]

Coating Designation	Peak Energy Density (J/cm^2)
C-1	4.3 - 7.5
C-2	4.9 - 6.7
E-1	5.5 - 6.4
E-2	4.6 - 5.3
B-1	3.9 - 5.3
B-2	4.5 - 6.1
A-1	4.1 - 5.8
A-2	3.8 - 5.8
I-1	3.2 - 6.2
I-2	3.4 - 5.5
I-3	3.1 - 5.4
F-1	4.3 - 5.8
F-2	3.1 - 4.3
G-1	3.8 - 5.2
G-2	3.2 - 5.1
D-1	4.1 - 4.6
D-2	2.6 - 4.6
J-1	2.8 - 4.5
J-2	2.0 - 4.2

---

[a] *Vee-coat design:* GH'L'A, *where* G = BK-7P *glass*, $H' \triangleq 0.4$ QW *of* ZrO_2, *and* $L' \triangleq 1.2$ QW *of* SiO_2.

lasers at 1.06 µm and with CO_2 lasers at 10.6 µm. Criteria for the HF laser pulse were an output energy of at least 10 J in 1 ns or less, focused to 10^{-3} cm^2, with energy and intensity at the target not exceeding 1 mJ and 1 GW/cm^2, respectively, before the ≥ 10-GW main pulse arrives.

To meet these criteria in a MOPA (Master Oscillator Power-Amplifier) laser system using readily available resources, we laid out a direct approach as outlined in subsequent paragraphs. Salient features of our approach are the application of established methods in the long-pulse oscillator, electro-optic switching element, and electron-beam-energized F_2-H_2 final amplifier. We found that methods to suppress the amplification and transmission of laser energy aimed at the target ahead of the required 1-ns pulse required further development.

We used our three-stage experimental MOPA setup to test ways of suppressing the amplification of leakage radiation by saturating the amplifier with an independent pilot beam before and after the gated pulse. When this was done by switching the polarization of a 4-ns segment of the oscillator beam, we successfully extracted the amplified segment by reflection of S-polarization from a Brewster plate after two stages of amplification.

Pulse Generation Methods -- Simultaneous pumping and stimulated-emission powers exceeding the 10^{10} W needed for flat-target experiments have already been demonstrated at Sandia Laboratories with pulsed HF laser systems energized by a REBA electron-beam source. The pulses generating such powers occur over times of ≥ 20 ns FWHM. The intent of our effort was to extract cleanly a 1-ns segment of such a power pulse by the gated-MOPA method; this would generate a collimated pulse for delivery to the target and would discard amplifier energy developed before and after the gated delivery.

The most favorable system for electron-beam delivery and optical extraction demonstrated with REBA uses gas mixtures of F_2 and H_2 plus additives, at pressures near atmospheric, in a lambda geometry.[12] The ~ 2-MV electron beam is guided magnetically around a ~ 45° corner from an inlet tube and along the axis of the main laser channel, which has windows at both ends. We can replicate such a system by using our Pulserad-316 (2.8 MV, 20 kA, 35 ns) electron-beam sources to energize the main HF laser amplifier for the ≥ 10-J target pulse. Such an amplifier can serve as its own testbed for methods of prepulse control and gated extraction.

During 1975 we had been able to operate a multiline HF oscillator in TEM_{00} mode,[13] to amplify an HF oscillator beam to $> 10^7$ W over a 3-cm^2 beam area by a TEA preamplifier,[14] to control electro-optically the gating of the output of such an oscillator-preamplifier system with ~ 2-ns risetime,[14] and to conduct preliminary experiments in matching the multiline HF laser spectra of the F_2-H_2 and SF_6-HI systems.[15] Based on this experience we attempted the MOPA extraction of a target-quality beam of sufficient peak power from an electron-beam-energized F_2-H_2 amplifying medium.

Our prototype oscillator and electro-optic gate are described below. The best contrast achieved was ~ 100; however, by upgrading the electro-optic rotator one could expect to achieve a contrast of ~ 10^3. By improving the lasers for routine operation with SF_6-HI mixtures, we could also match their output spectrum to that of the H_2-F_2 amplifier. Other areas of improvements are oscillator operation on each line for sufficient time to establish mode quality and a low-enough output energy to avoid damage to the electro-optic gating element.

The fact that HF lasers do not accumulate inverted populations, but rather are pumped at a rate that supports their laser output power directly, opens a fresh approach to the controlled generation of a short pulse. First, amplifiers not involved in controlling the laser-beam divergence can be energized to develop their required operating power at the last possible instant. This leaves only a few tens of nanoseconds for prelasing to occur, which is too short a time for retroreflection from a target to interfere. Second, stimulated bleeding of the amplifier system to saturation prior to the full-power pulse may be accomplished deliberately by a pilot beam or a cavity, provided that the bleeding radiation is aimed away from the main-pulse target and that the bleeding beam is terminated or overcome at the very instant the target pulse is switched on. Finally, the rapid transformation of HF media from strong amplification to strong absorption provides a ready means of protection against energy retroreflected from a target.

Basic Scheme - Polarization Switching and Protective Absorber -- The scheme we envision is based upon amplifying a linearly polarized oscillator pulse, in which the polarization is briefly rotated 90°. If the amplified beam follows this rotation, the two polarizations can be separated downstream into pilot and target beams with a Brewster plate (a silicon plate will reflect 73% of the S-polarization and will pass all the P-polarization). A segment from the amplified pulse is thus obtained, with a contrast equal to the reciprocal of the impurity of the polarization. The state of the art in polarization purity is ~ 10^3.

The second element of the scheme is an absorber with narrow spectral lines which improves the contrast by absorbing the prepulse caused by incomplete polarization. The target pulse will be less affected by the absorber due to saturation and the wider bandwidth of the various wavelengths in the short target pulse.

Our time-dependent gain data for a 20-torr (2.67 kPa) H_2-F_2 mixture ignited with a flashlamp[16] showed that the $P_2(3)$ and $P_2(4)$ lines developed an absorption of ~ 0.15 cm^{-1} within ~ 1 μs after lasing stopped. These limited data show that a burnt-out laser can serve as a resonant absorber. To ensure applicability to an H_2-F_2 amplifier system, early attention should be given to the SF_6-HI system.

Our scheme offers several significant advantages over those conventionally used with slowly pumped amplifiers. Putting the polarization analyzer after the amplifier circumvents the problem of amplifying a short, high-contrast pulse in a high-gain amplifier.[17] In this scheme the amplifier is always saturated by power extraction. Unwanted energy contributes nothing to amplified spontaneous emission and is directed harmlessly through the Brewster plate. The scheme can be extended from a single pulse to a timed sequence of such pulses, with compensated flight paths, for increased utilization of the amplifier energy.

The demands on the absorber are less than in alternative schemes. It does not have to absorb as much prepulse power, because only the polarization impurity is reflected off the Brewster plate to the absorber. The absorber can thus be made to saturate more when the switched pulse arrives. Also, transmission of the main pulse through the absorber does not depend on saturation only. Broadening of the lines in the main pulse allows additional passage in the wings of the lines.

Supplementary Pulse Methods -- We have also briefly examined the prospects of other measures for producing single or sequenced short pulses in a hydrogen-fluoride MOPA system.

Free-induction decay[18] offers an alternative approach for isolating a subnanosecond slice from a longer laser pulse. It requires a suitable plasma switch to interrupt the laser beam on a ~ 30-ps time scale, and a spectrally narrow filter for each of the HF laser lines to be switched. A volume of vibrationally excited HF quite similar to the gain medium in an HF chemical laser is the most obvious choice just as it is for a conventionally saturable filter.

The fast increase in the gain of an HF laser amplifier pumped over a time of ~ 20 ns produces much faster changes in the response of this amplifier to spontaneous and externally introduced radiation. Analysis has shown that the rising gain produces a contrast in amplifying a switched beam that is somewhat greater than if the amplifier gain were not rising. However, the contrast will still be significantly less than in the input beam if the gain is substantially reduced during extraction, i.e., if the amplifier energy is extracted efficiently.

The rate of rise in gain, in relation to the time necessary to develop amplified spontaneous emission over the length of an amplifier, has also been analyzed. This gain is such that storage of HF laser inversion over times of ~ 1 ns, for efficient extraction in a sequence of much shorter pulses separated by ~ 1 ns, would merit further exploration. This analysis considered a 30-cm-deep medium pumped at a rate to develop gain coefficient of 4 cm^{-1} over 20 ns, and assumed a reduction of the reflectivity of surfaces surrounding the medium to ≤ 0.01.

Oscillator-Amplifier Coupling Experiments

Pilot Beam Development -- The pin-discharge HF laser oscillator, 300-cm TEA preamplifier, and laser-triggered electro-optic switch[14] which make up the pilot-beam train have been coupled together and successfully tested under a variety of conditions. Electro-optically gated temporal slices from the 4-mm-diam pin-oscillator output, having a 2.5-ns risetime and 4-ns FWHM, were expanded to a diameter of 20 mm and were directed through the TEA preamplifier. Amplification of the peak-pulse intensity by a factor of 75 is accompanied by deterioration in the contrast ratio from ~ 80 at the entrance to the preamplifier to 30-50 at the exit. Peak pilot-pulse energy-release rates are estimated to be ~ 15 mJ/ns. Film burn patterns taken with various apertures downstream of the preamplifier have shown distributions of Fresnel rings consistent with high beam quality. All measurements were made with the $LiNbO_3$ electro-optic crystal. Earlier preliminary experiments with CdTe indicated similar behavior.

Still other experiments carried out without the electro-optic switch have yielded evidence that the TEA preamplifier is not being saturated by the full 200-ns pin-oscillator pulse. We obtained these data by employing calibrated neutral-density filters entering the preamplifier by a factor of 100. The results indicate that, if desirable, it should be possible to obtain two to four times higher powers in the output pilot beam by using a more energetic oscillator. This lack of saturation also explains the observation that contrast in the gated pulse decreased only from ~ 80 before amplification to ~ 40 afterward.

We conducted another series of experiments with the pilot-beam train to show that prepulse leakage can be reduced, and hence the final gated pilot-pulse contrast ratio increased, by using the electro-optic switch as a means of changing the direction of main beam propagation through the TEA preamplifier. This was accomplished by guiding the two physically separated beams carrying the vertical (V) and horizontal (H) components of polarization emerging from the pin-oscillator electro-optic switch configuration through the preamplifier from nearly opposite directions. The H-beam was expanded, directed down the TEA axis, and used to fire the laser-triggered Blumlein portion of the electro-optic switch. The V-beam was maintained at a diameter of 4 mm and, while inside the preamplifier, remained entirely within the gas volume bathed by the expanded H-beam. During the few nanoseconds the electro-optic shutter was open, the pin-oscillator output appeared in the V-beam, which then carried the main flow of energy through the preamplifier.

The results of these experiments were informative despite the fact that, as a result of the different beam diameters, the energy density of the leakage beam during the prepulse period was only one-third that of the expanded main beam. Nevertheless, the contrast ratio of the 4-ns pulse was restored from ~ 4 ± 1, observed previously for the unexpanded beam alone, to ~ 80, the original gated-oscillator pulse contrast. Thus we achieved substantial suppression of the amplification of the prepulse leakage signal in the preamplifier.

With this success, we implemented a geometrically simpler modification of the pilot-beam optical train to isolate shuttered, vertically polarized pulses after amplification. The analyzing Rochon prism was removed from the electro-optic switch so that the oscillator beam, with its polarization subject to gated rotation, was fed directly to the preamplifier. A CaF_2 flat positioned at the Brewster angle with respect to the incoming beam provided discrimination at any desired location in the beam path. The horizontally polarized beam suppressed the amplification of leaked vertical polarization before the pulse, and was transmitted through this splitter to trigger the electro-optic switch. Tests with the Brewster splitter positioned just downstream of the TEA preamplifier confirmed $\leq 10^{-4}$ reflection of the horizontally polarized component of the incident beam and demonstrated that 4-ns pulses with a contrast ratio of up to 90 could be switched out in this manner.

MOPA Control of Electron-Beam HF Amplifier--The pilot-beam system described above has been coupled with SF_6-C_2H_6 gain medium excited by our Pulserad Model-316 electron beam. A magnetic field guided the electron beam axially through a 50-cm laser cell having a sapphire or quartz window on one end and a flat aluminized Mylar mirror in front of the electron-beam anode at the other. After recent reductions in Model-316 jitter, we consistently achieved time overlap between the periods of active laser-cell gain and ungated pilot-beam pulse (~ 100 ns FWHM).

Pilot pulses consisting of the fully amplified pin-oscillator output with an estimated power density of 6 MW/cm^2 in a 2-cm-diam beam swept out some 32% of the electron-beam-irradiated gas medium and were amplified about 20-fold. We achieved 400-fold amplification when the pilot beam was attenuated by a factor of ~ 30 before entering the test cell. Clearly, saturation effects must be taken into consideration in interpreting these results. Also, the energy extracted from the beam volume was less than the energy obtained from the same volume by amplified spontaneous emission (ASE) when no pilot beam was used. The extracted energy was lower because some of the energy in the beam volume was entrained by ASE developed in the amplifying medium outside the beam volume.

This problem has been solved by saturating the whole gain volume with the extracting beam. The oscillator beam was expanded to the 60-mm diameter of the gain region in the amplifier. The degree of saturation necessary to eliminate troublesome ASE was reduced by reducing the reflectivity of the amplifier walls. The expanded oscillator beam was directed into the amplifier with a splitter outside the sapphire window. A high degree of saturation was achieved by passing the beam through the whole gain volume twice, using the beam doubled back on itself by reflection from the plane mirror at the end of the amplifier. Most of the beam energy then passed through the external splitter for analysis.

This scheme extracted 11.6 J in a 30-ns pulse from a medium that produced an ASE output of 7.7 J. We believe that the extracted energy represents the energy available from the medium and that significant energy is lost to the walls by off-axis rays developed in the ASE output. Burn patterns showed that the extracted beam was of much better quality than the ASE beam, as would be expected. Power amplification was considerable. The oscillator beam from the splitter had an energy of ~ 0.1 J over 120 ns. The output of 11 J in 30 ns represents a power amplification of ~ 400.

The magnitude of the energy thus extracted varied with the time in the pilot-beam pulse when the amplifier gain became positive. Maximum extracted energies correlated with interaction at the beginning of the pilot pulse, and occurred when the reflecting aluminized Mylar mirror and the sapphire coupling window were parallel. If the coupling window was canted by ~ 3.6°, the ASE energy fell by more than 90%, and the corresponding extracted energy was 4.9 J. Thus, reflection from the amplifier window is an influential factor in the competition between MOPA extraction and ASE.

These results show that no fundamental problem exists in extracting energy from an electron-beam-pumped HF amplifier, and they suggest that in previous experiments even more energy might have been extracted with a more suitable oscillator-beam power and geometric coupling.

The culmination of our effort to develop a gated MOPA for the HF laser system was the demonstration of clean, 4-ns gated pulses extracted from the electron-beam-energized SF_6-C_2H_6 laser amplifier by switching the polarization of the pilot beam. The setup used the 2-cm-diam pilot beam from the TEA preamplifier, as described in the final paragraph of the preceding topic (Pilot-Beam Development) above, but with the CaF_2 Brewster splitter placed in the beam after it emerged from its traversal of ~ 32% of the amplifier volume. Also, because sapphire is birefringent we used a quartz window on the amplifier cell.

Because these experiments were performed only to demonstrate this pulse-gating principle, some 97% of the intensity contained in the initially horizontally polarized preamplifier output was used to trigger the electro-optic switch. The remaining 3%, split off with a near-normal CaF_2 flat, drove the amplifier. Success in these experiments depended upon overlap in time between the shuttered 4-ns vertically polarized pulse and the ~ 25-ns period of positive amplifier gain produced by the independently triggered Pulserad 316. Overlap was obtained in three of eleven coupling experiments attempted. From the limited data available we can estimate that the contrast ratio in the final, amplified, switched-out pulse is at least 15.

Control of Diffraction Effects -- The radial intensity profile of the beam produced downstream by an HF laser oscillator-amplifier has been improved as a result of two important properties. The first is attributed to the fact that large Fresnel numbers are produced in an optical system whenever the image of an aperture is formed, and the second one results from the characteristics of the gain-saturated amplifier. Because the Fresnel number, F, is in general large only near the aperture image plane, it is necessary to examine the development of observable Fresnel rings in the neighborhood of $F = \infty$. At odd integral values of F, intensity peaking occurs at the pattern center. Sharp-edged apertures produce peaking by a factor of four, even at large Fresnel numbers,[19] and could damage optical components. Reduced but substantial peaking is also observed when Gaussian beams are passed through apertures. Such peaking can be considerably reduced by the use of an apodized or soft-edged aperture.[20] We have found that peaking is similarly reduced by passing the beam through a gain-saturated amplifier after a sharp-edged aperture. This reduction occurs because the gain in the intensity valleys and shadow regions of the Fresnel pattern is greater than at the peaks. When the last significant aperture in the HF system is placed in front of the TEA amplifier and this aperture is imaged to a diameter of 3 mm, it is found experimentally that no diffraction rings or peaking can be seen over an axial range of ~ 5 cm around the image plane.

Electron-Beam and Fluorine Methods

Pulserad 316 Electron-Beam Development -- Installation of externally controlled switches at five points, instead of the original one, in the Pulserad 316 Marx circuit has reduced firing jitter of this electron-beam generator from ± 50 ns to ± 12 ns. This reduction has enabled us to reliably synchronize the ~ 25-ns laser amplifier pulse with the ~ 100-ns pilot-beam burst from the TEA preamplifier, and to conduct the systematic tests of beam amplification and its competition with amplified spontaneous emission described above. Experiments with the ~ 4-ns pilot pulse generated with the electro-optic gate were complicated, but not prohibitively, by the residual jitter.

We are concluding the checkout of a high-pressure gas switch installed in place of the oil Blumlein switch on one of the Pulserad 316 units. This new switch should reduce overall time jitter to less than 3 ns. Jitter as low as 0.5 ns has been measured for a Blumlein voltage of 1.2 MV. The coaxial cable for triggering the Blumlein switch is being replaced with a cable of larger diameter because the original cable failed after about every 100 shots.

Two problems were isolated on the Pulserad 316, which limited useful propagation of the electron beam for initiation of the SF_6-C_2H_6 laser volume: (1) the large prepulse voltage of 10 to 20% of the main Blumlein voltage seen by the diode during the Marx erection time and (2) the absence of a guiding magnetic field (B_z) in the diode gap. To reduce the prepulse voltage, we installed a peaking switch within the cathode shank which holds off 380 kV; and to allow better magnetic-field penetration into the diode gap we replaced the 25-mm-thick stainless steel anode end-plate with a Lucite plate having a ~ 1-mm-thick plating of copper on the inner surface. This combination of changes allowed us to operate the machine with the diode gap set at 20 mm, to produce the normal impedance-matched condition of 50 Ω while maintaining anode-foil integrity. However, only ~ 1200 J of electron-beam energy emerged from the anode because the resistance of the vacuum peaking switch nearly matches that of the diode gap. This condition led to a 17-J superradiant laser emission from the SF_6-C_2H_6 mixture. With the concomitant improvement in system integrity, this output was quite adequate for executing the final gated pulse-extraction experiments.

<u>Disappearance of F_2 in Nereus-Initiated H_2-F_2 System</u> -- Ninety-six shots have been fired by using the Nereus electron-beam machine to initiate the H_2-F_2 reaction in the Nereus cell and monitoring the F_2 concentration with a He-Cd laser at 325 nm. These measurements show an increase in absorption that is essentially synchronous with the arrival of the electron beam. This increase is followed by restoration of the original transmission if only F_2 is present in the system, and by substantial increases in transmission when H_2 is also present and the chain reaction consumes F_2.

All four windows of the Nereus cell were probed perpendicular to the electron-beam axis, both at the nominal center of the electron beam and at a location vertically displaced from it, that is, at the center and at the top of each window. This probing occurred at the conditions for maximum laser output, i.e., a $4:1::F_2:H_2$ mix at 80 kPa and an anode spacing of 3.2 mm. A second group of experiments probed the beam axis at different windows in 1:1, 2:1, and $1:2::F_2:H_2$ mixes. A third group of experiments explored the effects of different electron-beam dosages by varying the anode-to-cathode spacing. In some experiments we attempted to better define the measurement and the dosage region by using modified windows which limited the uv-absorption path length. In miscellaneous experiments we measured any influence on the absorption due to the H_2 or the buffer gases, O_2 and SF_6.

The main conclusions from our observations are:

- The decrease in transmission while the electron beam is present at the pro-beam position may be due to F^-, which also absorbs at 325 nm.

- At a time corresponding approximately to the peak current, and for heavy dosage, the transmission increases at a time scale inversely related to the amplitude of the current, increasing to a value related to the amplitude of the current and then remaining nearly constant for hundreds of nanoseconds.

- In a mixture nominally stoichiometric for the production of HF, the constant transmission level is less than that expected for removal of all the F_2. This suggests that some F_2, perhaps near the windows, has not reacted and may not have been dosed sufficiently.

- In a mixture having excess F_2, the constant transmission level is higher than that expected for depletion of F_2 solely by one-to-one reaction with H_2. This result may imply some thermal dissociation of F_2. Computer calculations using as a model an equilibrium-state Chapman-Jouguet detonation show essentially no F_2 present.

- Various tests indicate that the presence of H_2 and O_2 does not affect the measurements, but that SF_6, under some conditions, might. Changes in the absorption coefficient of F_2 due to temperature variations were not identified but may be present.

<u>F_2-H_2 Laser Line Gain Measurements</u> -- We have conducted a series of single-line, time-resolved oscillator-amplifier gain measurements in which the oscillator probed the Nereus/H_2-F_2 laser cell transversely at two locations simultaneously. These measurements extended the multiline transverse measurements completed earlier.[21]

The oscillator beam was divided into three components: one was used as a reference, whereas the other two were directed through the centers of the first and third windows of the H_2-F_2 laser cell, transverse to the axis of propagation of the Nereus beam and reflected from a gold-coated mirror in the opposite window mount. The two oscillator beams were then each passed through an ir monochromator which selected a specific HF laser line. In each experiment the two monochromators were set for the same wavelength. The amplified oscillator pulses were monitored with gold-doped-germanium fast-response detectors. Our experiments were performed with both a laser cavity set up in the H_2-F_2

cell using the 45° turning mirror and with no laser cavity (the 45° turning mirror removed from the H_2-F_2 cell). These experiments were difficult; especially obtaining optical alignment was quite tedious. Firing jitter of both the Nereus and the oscillator laser caused variations in the timing of the amplifier pulse relative to the oscillator pulse. About 25 cursory experiments were conducted, which examined gain characteristics of five of the strongest HF laser lines, $P_1(6)$, $P_1(7)$, $P_1(8)$, $P_2(7)$, and $P_3(5)$.

Several interesting observations were made. Laser amplification of up to seventyfold over the ~ 10-cm folded path was attained in this system on the $P_1(8)$ line. The several HF lines behaved differently in time over the ~30-ns event and exhibted markedly varying gain behavior. Following the gain pulse in many of these experiments the medium being probed by the oscillator was highly absorbing. This postgain absorption, which occurs at different times at different locations in the Nereus H_2-F_2 cell, supports a plausible explanation of the somewhat unique "burn patterns" of output laser energy that have been characteristic of the Nereus HF laser system.[22] A systematic line-by-line study similar to the one begun here might yield valuable information concerning the lasing kinetics of the HF system.

Nereus Electron-Beam Calorimetry -- Results of F_2-H_2 laser experiments energized by the ~ 300-kV Nereus electron-beam generator raised questions of the spatial distribution of electron-beam dose inside the laser cell. Earlier calorimetric measurements[23] of dose distribution at several axial positions had been made with a segmented calorimeter positioned in place of the cell, or beyond its open end. These measurements had shown that the dose at the end plane was dependent upon whether the cell was present or removed, indicating that the cell channeled the beam. Also, uv transmission measurements of F_2 disappearance indicated possibly very small electron-beam dosages near the cell walls. To explore these matters, we conducted a calorimetric study of Nereus electron-beam propagation with a circular segmented calorimeter inside the 51-mm-diam cell. The calorimeter assembly consisted of a central 22.2-mm-diam disk and of the quadrants of the surrounding annulus with inner and outer diameters of 25.4 and 47.8 mm, respectively. The results verified that the electron-beam dose at each axial position was greatest near the cell axis and was not systematically distorted azimuthally. Presence or absence of entrance-window hardware had no discernible effect at the resolution of these measurements.

REFERENCES

1. W. M. Hughes, N. T. Olson, and R. Hunter, "Experiments on 558-nm Argon Oxide Laser System," Appl. Phys. Lett. 28, 81 (1976).

2. LaVern Schlie, AFWL, private communication, 1975.

3. H. T. Powell, J. R. Murray, and C. K. Rhodes, "Collision-Induced Auroral Line Lasers," Conference on Laser Engineering and Applications, Washington, D.C., May 1975, Paper 7.8. See also W. M. Hughes, N. T. Olson, and R. Hunter, "Experiments on 558-ns Argon Oxide Laser System," Appl. Phys. Lett. 28, 81 (1975).

4. H. T. Powell, J. R. Murray, and C. K. Rhodes, "Laser Oscillation on the Green Bands of XeO and KrO," Appl. Phys. Lett. 25, 730 (1974). See also R. L. Huestis, R. A. Gutcheck, R. M. Hill, M. V. McCusker, and D. C. Lorents, "Studies of Electron-Beam Pumped Molecular Lasers," Stanford Research Institute, Technical Report No. 4 (SRI No. MP 75-18).

5. C. Dewey Cooper, G. C. Cobb, and E. L. Tolnas, "Visible Spectra of XeO and KrO." J. Molec. Spectros. 7, 223 (1961).

6. R. F. Hampson, Jr., and H. Okabe, "Collisional Stimulation of the $O(^1S)$ - $O(^1D)$ Emission of Oxygen Atoms Formed in Vacuum-Ultraviolet Photolysis of Nitrous Oxides," J. Chem. Phys. 52, 1930 (1970); D. L. Cunningham and K. C. Clark, "Rates of Collision-Induced Emission from Metastable $O(^1S)$," J. Chem. Phys. 61, 1118 (1974).

7. S. V. Filseth, F. Stuhl, and K. H. Welge, "Collisional Deactivation of $O(^1S)$," J. Chem. Phys. 52, 239 (1970); R. J. Donovau and D. Husain, "Recent Advances in the Chemistry of Electrically Excited Atoms," Chem. Rev. 70, 489 (1970).

8. C. Nicolaides, O. Sinanoglu, and P. Westhaus, "Theory of Atomic Structure Including Electron Correlation. IV. Method for Forbidden-Transi-

tion Probabilities with Results for [OI], [OII], [OIII], [NI], [NII], and [CI]," Phys. Rev. A4, 1400 (1971); A. Corney and O. M. Williams, "Measurement of the Radiative Lifetime of the $^1S_0$ Metastable Level of Atomic Oxygen," J. Phys. B. 5, 686 (1972).

9. W. Finkelnberg and Th. Peters, Handbuch der Physik, Vol. XXVIII, S. Flugge, ed., (Springer-Verlag, Berlin, 1957); S. Morzowski, "Forbidden Lines in the Laboratory," Rev. Mod. Phys. 16, 153 (1944).

10. B. E. Newnam, D. H. Gill, and G. Faulkner, "Influence of Standing-Wave Fields on the Laser Damage Resistance of Dielectric Films," presented at NBS-ASTM Symposium on Damage in Laser Materials, July 30 and 31, 1975, at Boulder, Colorado; to appear in proceedings to be published, 1976.

11. D. H. Gill, B. E. Newnam, J. S. Hartman, and W. J. Coleman, "Super-High Damage Thresholds for RF-Sputtered TiO_2 Films," presented at Fall Meeting of Optical Society of America, October 21-24, 1975, Boston MA.

12. SAND 75-0262, Laser-Fusion and Electron-Beam-Fusion Progress Report for July-December, 1974, Directorate of Physical Research 5200, Sandia Laboratories, Albuquerque, NM, June 1975, Sec. 2.1.1.1, pp. 9-13.

13. F. Skoberne, "Laser Program at LASL, July 1 - December 31, 1974," Los Alamos Scientific Laboratory report LA-5919-PR, Sec. III.A.2.a, p. 59 (April 1975).

14. F. Skoberne, "Laser Program at LASL, January 1 - June 30, 1975," Los Alamos Scientific Laboratory report LA-6050-PR, Sec. III.A.3.b, p. 60-62.

15. F. Skoberne, "Laser Program at LASL, July 1 - December 31, 1974," Los Alamos Scientific Laboratory report LA-5919, Sec. III.A.2.c. and Fig. 43, p. 60; also N. R. Greiner, "Time-Resolved Output Spectrum from a Hydrogen Fluoride Laser Using Mixtures of SF_6 and HI," IEEE J. Quantum Electron. QE-11, 844 (1975).

16. N. R. Greiner, "Submicrosecond Pulses from a Hydrogen-Fluorine Laser with High Energy Density and Quantum Efficiency," IEEE J. Quantum Electron. QE-8, 872 (1972).

17. K. R. Manes, D. L. Smith, R. A. Haas, and S. S. Glaros, "Prepulse Extinction-Ratio Measurements on a CO_2-Laser System," IEEE J. Quantum Electron. QE-11, 635 (1975).

18. E. Yablonovitch, "Generation of a Short Optical Pulse of Arbitrary Shape and Phase Variation," IEEE J. Quantum Electron. QE-11, 789 (1975).

19. A. J. Campillo, J. E. Pearson, S. L. Shapiro, and N. J. Terrell, Jr., "Fresnel Diffraction Effects in the Design of High-Power Laser Systems," Appl. Phys. Lett. 23, 85 (1973).

20. A. J. Campillo, D. H. Gill, B. E. Newnam, S. L. Shapiro, and J. Terrell, "Reduction of Fresnel Diffraction Effects by Soft Apertures," IEEE J. Quantum Electron. QE-10, 767 (1974).

21. F. Skoberne, "Laser Program at LASL, January 1 - June 30, 1975," Los Alamos Scientific Laboratory report LA-6050-PR, Sec. III.A.2.d., pp. 58-59.

22. F. Skoberne, "Laser Program at LASL, January 1 - June 30, 1975," Los Alamos Scientific Laboratory report LA-6050-PR, Sec. III.A.2.c., and Fig. 52, p. 58.

23. F. Skoberne, "Laser Program at LASL, January 1 - June 30, 1975," Los Alamos Scientific Laboratory report LA-6050-PR, Sec. III.A.4.b., pp. 65-66.

c1735

III. TARGET EXPERIMENTS

Our target experiments with Nd:glass and CO_2 lasers provide the physical measurements that, with the help of theoretical analyses, are establishing a fundamental understanding of laser-target interaction, particularly of plasma physics and target compression.

INTRODUCTION

Well-conceived target-interaction experiments are the keystone to unified progress in laser design, to the understanding of laser-plasma interactions, and to computer-assisted target design.

Target chambers, focusing optics, and diagnostics exist in various stages of development, from conceptual design to routine use. We are conducting experiments with a single-beam 150-J, 1-ns CO_2 laser; a single-beam 10-J, 50-ps glass laser; and a four-beam glass laser of variable energy and pulse length (now being used in a two-beam configuration). Experiments will begin in FY 76 with the dual-beam CO_2 system at higher energy.

The laser oscillator, amplifiers, focusing optics, and the target must be considered as one experimental system. This is particularly true for the CO_2 laser, where convenient optical switches and isolators are still under development. Thus, an important part of our experimental program concentrates on diagnostics of the laser and target behavior with respect to pulse contrast ratio, target reflectivity, and the effects of prepulses (diagnostics are discussed in Sec. V.)

Carbon-dioxide experiments are under way to clarify the dependence of target absorption, thermal transport, and hydrodynamic behavior of different laser targets on laser power and wavelength. We will investigate the effects of reduced pulse lengths and multiwavelength laser operation on target interaction, as well as the effect of symmetry of illumination, in the near future. These investigations may have important implications for both laser and target design.

Our glass lasers are used for important control experiments: to learn more about the wavelength-dependence of laser-plasma interactions and to provide information useful to the design of high-energy CO_2 lasers and laser-fusion targets. They are not prototypes for laser development -- Lawrence Livermore Laboratory is responsible for research and development in this area. No further development, as such, is being done on the glass lasers. They are maintained and operated as research tools. Improvements are limited to those needed to achieve the experimental schedule. Many important experiments remain to be conducted before the higher energy lasers are put into operation, and the glass lasers will play an important role in this effort. The frequency conversion of the ir 1.06-μm light to 0.53 μm to gain more information on the crucial question of wavelength scaling of laser-target interactions is an important example.

NUCLEAR REACTION PRODUCTS - ALPHA AND PROTON MEASUREMENTS

Detector

We have designed and built a time-of-flight thin-film detector for the study of charged particles produced in laser fusion.[1] The basic components of this nonmagnetic detector assembly are illustrated in Fig. 49. Three important features are incorporated: (1) by coupling a large-aperture off-axis parabolic reflector, E, to a 5-cm-diam photomultiplier, we can obtain a very large solid angle of acceptance; (2) by using thin-film scintillators, S, and appropriate filter foils, the enormous amount of x-ray background can be reduced effectively; and (3) the acceptance of the detector is independent of particle type and energy. This latter feature is particularly important because a complete description of the energy spectrum of the

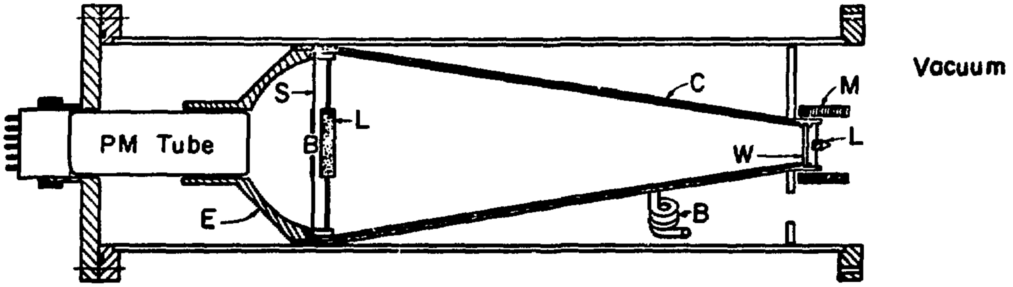

Fig. 49. Schematic of detector: magnet (M); window (W); shielding cone (C); lead plug (L); thin scintillator (S); light collector (E); and photomultiplier tube (PMT).

alpha particles and the protons may reveal many relevant laser-fusion parameters.

This detector will remain well-suited for target compression measurements for several generations of laser-fusion developments. As the value of ρR (density times radius) of targets becomes higher, the alpha particles will not escape readily from the burn region. The protons from either d-d or d-^{3}He reactions will still have a substantial range.

With this detector we are also able to detect ions in the hundred-keV region. The detector functions well as an x-ray monitor and may become an effective instrument in determining the laser focusing quality and energy absorption on a shot-to-shot basis.

Measurement

We used the detector described above to observe the high-energy ions from targets during some tests with our high-energy Nd:glass laser. However, a more extensive measurement of alpha particles from d-t reactions, and protons from d-d reactions was carried out[2] at KMSF, Ann Arbor MI, on their experimental setup.[3] This work was performed under an ERDA contract. The laser energy was delivered to the target in two beams, and the laser pulse was composed of a train of one to six pulses from the KMSF pulse stacker.[3] The nominal duration of each component pulse was 30 ps, and the peak-to-peak separation was 40 ps, with an energy of 5 to 7 J per pulse per beam. The peak intensity on target was estimated at ~ 3×10^{15} W/cm^2. The targets were glass microballoons ~50 μm in diameter with a wall thickness of 0.7 μm, filled to 10 atm with a 60:40 at.% D_2T_2 mixture.

Figure 50(a) shows an oscilloscope trace from an alpha-particle measurement. The signal at the left is the x-ray pulse, which was used as a zero-time fiducial mark in time-of-flight calculations. The reproducibility of the x-ray pulse was such that an accurate quadratic fit could be made to the falling edge and the x-ray signal could be subtracted from the data. Figure 50(b) shows the data after subtraction of such a fit. The large peak at late time is caused by high-energy hydrogen ions emitted from the corona of the plasma. Experiments with empty microballoons and polyethylene spheres, and shots having no neutron yield, showed that this proton background had a sharp high-energy cutoff at a velocity of 9.8×10^8 cm/s. Therefore, there was no interference with the alpha-particle measurement at energies above 2 MeV. Figure 50(c) is an oscilloscope trace of a d-d proton measurement. A thicker foil reduced the x-ray signal substantially.

The oscilloscope traces were digitized, the x-ray background was subtracted, and the particle distribution function as a function of energy was calculated with appropriate corrections for energy loss in the window. We also applied a correction for the energy dependence of the scintillator response. A typical alpha-particle spectrum showing

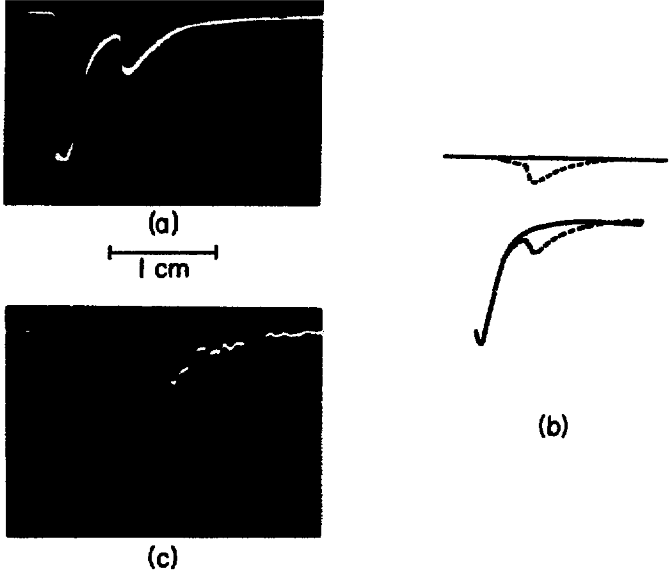

Fig. 50. Alpha spectroscopy measurements. (a) Oscilloscope trace of an alpha-particle measurement; unit scale, 200 ns or 20 V. (b) Data of (a) showing fit to x-ray pulse and result of subtraction of x-ray background. (c) Oscilloscope trace showing d-d proton signal and x-ray background. Unit scale, 40 ns or 0.2 V.

the background below 2 MeV is given in Fig. 51(a), and a linear plot of the distribution function above 2 MeV is shown in Fig. 51(b). The solid lines in Fig. 51(a) indicate the different slopes of the alpha-particle and background distributions. The alpha-particle distribution was, in general, independent of neutron yield for yields between 10^6 and 10^7 neutrons. The alpha spectrum and neutron yield were both independent of the number of pulses in the pulse train. The number of alpha particles with energy above 2 MeV detected on each shot was 0.25 to 0.5 of the neutron number.

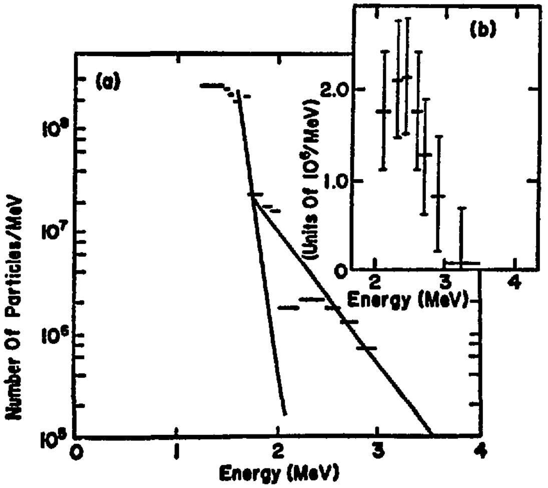

Fig. 51. Alpha-particle distribution. (a) Distribution function of alpha particles from a (D-T)-filled glass microballoon including hydrogen ion background. (b) Portion of (a) above 2 MeV in linear scale.

The maximum ρR can be estimated from the energy shift of the alpha particles and protons. The stopping power of a plasma containing ions with bound electrons is uncertain, but for silicon at temperatures below 500 eV it is reasonable to use the stopping power of the un-ionized material.[4] At 1 keV, substituting the stopping power of a fully ionized plasma[5] increases ρR twofold. An energy shift of 1.5 MeV for the alpha particles gives a ρR of 1.4×10^{-3} g/cm^2. By using the measured shift in the proton energy (160 keV), we obtained a ρR of $(2 \pm 1) \times 10^{-3}$ g/cm^2. The initial ρR of the glass shell was 1.8×10^{-4} g/cm^2. Therefore, convergence of the shell occurred, and ρR increased tenfold, but the peak density is undetermined.

This result can be compared with the one-dimensional calculation[6] for a similar experiment where a varying fraction of the absorbed energy was assumed to be deposited in high-energy electrons and photons. For a thermal plasma we found a ρR of 1.5×10^{-2} g/cm^2, which is outside the error of the experiment. Radiative preheat alone gave 7.0×10^{-3} g/cm^2, but the addition of a superthermal electron component containing 4 to 7% of the absorbed energy gave a ρR of 2.5×10^{-3} g/cm^2, which agrees with our experiment. Also, the reduced collapse time in the preheat case agrees with the independence of yield and number of pulses. The experiment then indicates a degradation of target performance compared to the most optimistic calculation. Fuel densities of 0.6 to 2.0 g/cm^3 are implied by this comparison. The ion temperature calculated was 0.7 keV, which would give a neutron-yield dependence of $\sim T^5$, and the variation in neutron yield from shot to shot can be explained by small temperature changes rather than by changes in density. The ratio of d-t reactions to d-d reactions determined from the proton measurement was 60:70. The fuel ion temperature implied by this ratio is 2 to 3 keV.

Our experiment indicates that convergence of a spherical shell occurred, and that some compression of the D-T fuel can be deduced. The experiment also indicates that optimum conditions are not achieved in these targets, perhaps because of the presence of high-energy electrons and photons.

Calculated Alpha-Particle Spectra

The primary purpose of this work is to provide information on the distribution of alpha particles emitted from small microballoon laser targets. A secondary purpose is to see what information on target compression can readily be extracted from measured alpha energy spectra alone. We achieved these goals by carrying out a parameter study to identify the effects of various characteristics of the imploding fuel and pusher.

Because an extensive region of parameter space needs to be explored, but only in a heuristic manner, a fairly simple fast-running code is desired. We formulated such a code by using a simple nonhydrodynamic model of the compressed target at the instant of alpha emission along with an analytical algorithm of spectral degradation.[7] This algorithm is based on the Fokker-Planck equation and is valid for a spectral width large enough for stopping-power divergence to dominate over statistical energy straggling. By stopping- power divergence we mean the process by which particles of different energies become further separated in energy as they traverse the same amounts of absorber because slower particles lose energy faster than do faster particles. As has been shown,[7] it is surprising how narrow a spectrum must be so that stochastic straggling would dominate stopping-power divergence. However, in any case, the alpha-particle spectrum generated by a thermonuclear plasma is broad enough initially that the subsequent broadening is almost entirely caused by stopping-power divergence.

As expected, the calculated results show that the greatest sources of uncertainty in the emitted alpha spectra stem from plasma-temperature uncertainty (in both fuel and pusher) and from ignorance of plasma stopping powers at a specified temperature. However, it was also shown that ignorance of the density of the imploding pusher contributes a surprisingly large uncertainty, quite comparable to that contributed by ignorance of the remnant pusher mass at the instant of alpha emission.

The results also clearly show that practically all the spectral broadening is caused by the fuel, whereas most of the shift in peak energy is caused by the pusher. Thus, because these two measurable aspects of spectral degradation are caused nearly independently by different regions of the target, an accurate measurement of the alpha spectrum could, in principle, give information on each. Particularly intriguing is the possibility of determining fuel compression from an independent determination of fuel temperature and a measurement of the shape of the alpha spectrum, assuming that the target is small enough so that the diameter of the compressed fuel is smaller than the range of the alpha particles in the fuel. For larger targets, in which this criterion is not met, the spectral shape becomes nearly independent of the compression. Of course, such a large target could be measured in the same way by using the spectrum of protons, for which the fuel has much less stopping power at comparable energy.

The characteristic of spectral degradation that can be presently measured is the shift in peak energy from 3.5 MeV to some lower value. These data, limited by the uncertainties mentioned previously, provide information on the mass thickness of the converging pusher shell. And, assuming spherical symmetry, this information, in turn, allows us to deduce the compression of the fuel.

However, because of incertainties in our knowledge of the imploding pusher, this inference only provides a lower limit on fuel compression. For example, we have recently measured[8] a peak shift of 1.3 MeV for a small glass microballoon target. From our calculated spectra, we infer that the fuel-density compression factor at the time of alpha emission is at least 70, but we cannot determine the value precisely. Nevertheless, this method shows strong promise, particularly as we gain information on the converging pusher plasma.

SPECTRA AND ANGULAR DISTRIBUTIONS OF ELECTRONS EMITTED FROM LASER-PRODUCED PLASMAS

We have demonstrated the existence of nonthermal particle distributions in plasmas created by high-intensity laser pulses incident on solid targets, by measuring the high-energy x-radiation,[9] and the so-called "fast" ions[10] emitted from the plasmas. We also reported some initial electron spectral measurements.[11] The determination of the spectra and of the number of high- energy electrons is important because preheat due to electrons is crucial in computer simulations used for target design.

Here we report time-integrated measurements of the high-energy electrons emitted from plasmas created by both Nd:glass and CO_2 laser pulses incident on flat polyethylene (CH_2) targets. Both the spectra and the angular distributions were measured.

The spectral measurements were made with two magnetic spectrometers. One is a 180° focusing device similar to that designed by Paolini et al.[12] We used this instrument for electrons whose energies ranged from 75 keV to 1 MeV. The low-energy end of this range was determined by the decreasing sensitivity of the detecting film for low-energy electrons. For energies greater than 75 keV the thin windows of the device had a negligible effect.

The photographic film used in the spectrometers was calibrated at various exposures. The sensitivity of this film was assumed to be determined by the energy loss to electrons passing through a thin absorber. To test these procedures we measured the electron emission spectrum of ^{137}Cs and compared the data with published curves.[13] The comparison indicated excellent agreement.

A typical spectrum obtained with the Nd:glass laser is shown in Fig. 52. The intensity in the focal spot reached ~ 5 x 10^{15} W/cm^2. The solid

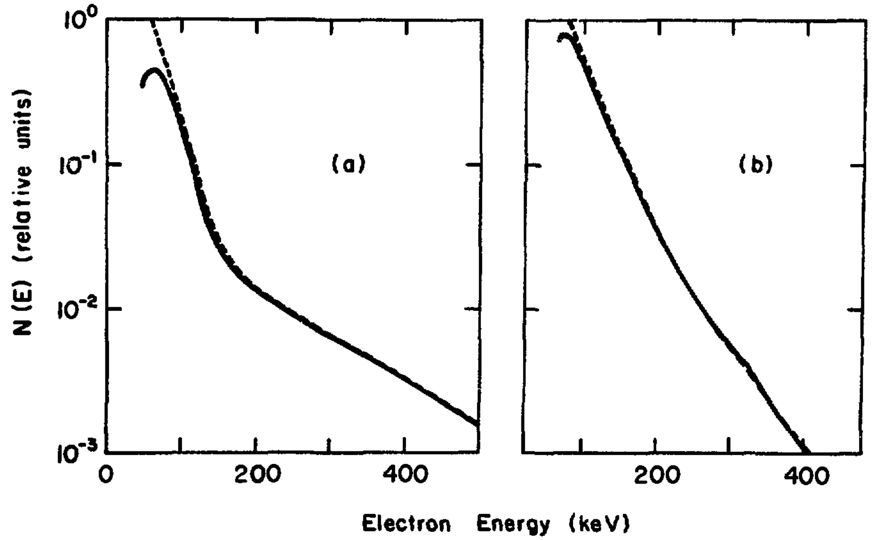

Fig. 52. Spectra of electrons emitted from plasmas created by 100-J, 0.3-ns FWHM Nd:glass laser pulses. These two plots show the extremes in the measured spectra. Each is fitted to two Maxwellian curves at different temperatures, shown as dashed curves. The temperatures, T_1 and T_2, used for the fitted curves in the two cases are (a) T_1 = 20 keV, T_2 = 120 keV; and (b) T_1 = 30 keV, T_2 = 70 keV.

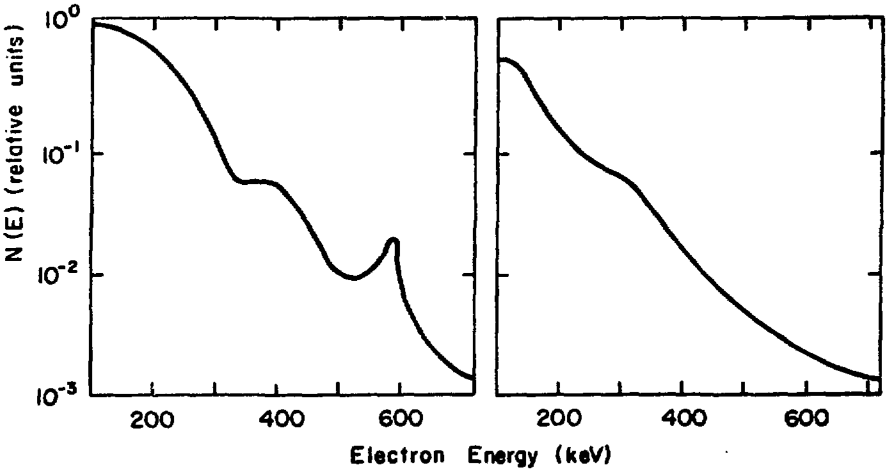

Fig. 53. Spectra of electrons emitted from plasmas created by 100-J, 1.2-ns FWHM CO_2 laser pulses. Considerable structure can be seen, which precludes fitting the detailed spectra to two temperatures as in the Nd:glass cases (Fig. 52).

curve is the measured spectrum from 80 to 500 keV. The dashed curve is the sum of two Maxwellians with the form

$$N = C\left[\frac{N_1}{T_1}\sqrt{\frac{E}{T_1}}\cdot \exp -E/T_1 + \frac{N_2}{T_2}\sqrt{\frac{E}{T_2}}\cdot \exp -E/T_2\right], \quad (1)$$

where T_1 = 20 keV, T_2 = 120 keV, N_2/N_1 = 0.027, and E = electron energy. A second spectrum taken under similar conditions is shown in Fig. 52(b). These two spectra are near the extremes of the range of spectra observed with the Nd:glass laser. To fit all the spectral data obtained with this laser to functions of the form of Eq. (1) requires $18 < T_1 <$ 30 keV and $70 < T_2 < 120$ keV.

Spectra obtained with a CO_2 laser are shown in Fig. 53. The intensity in the focal spot reached ~ 3 x 10^{14} W/cm^2, ~ 7% of that obtained with the Nd:glass laser. Much structure can be seen in these spectra. The energies and widths of the spectral features were not reproducible from experiment to experiment. Although the added structure does not allow detailed fitting to simple functions such as Eq. (1), a set of single temperatures ranging from 70 to 120 keV covers all the spectra adequately. This range of temperatures is identical to that of the high-energy portion of the Nd:glass data.

A composite of data taken with both lasers is shown in Fig. 54. Data from the two lasers are

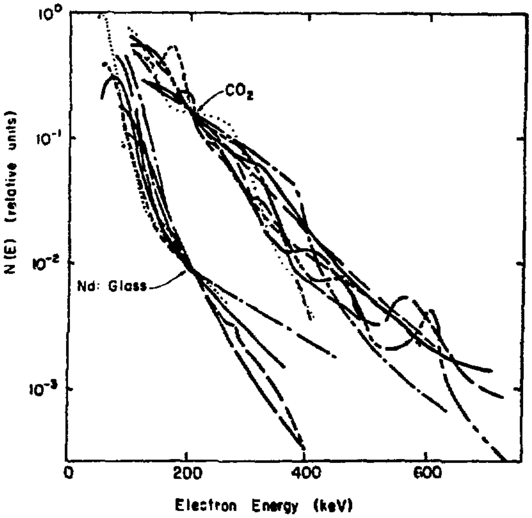

Fig. 54. Composite of spectra taken with both the Nd:glass (intensity, ~ 5 x 10^{15} W/cm^2) and CO_2 (intensity ~ 3 x 10^{14} W/cm^2) lasers. Seven spectra taken with the Nd:glass laser and nine spectra from the CO_2 laser are normalized to their average value, at 200-keV energy. In both cases the standard deviation of the ratios of normalization constants was ~ 4. The relative intensity between the averages for the two lasers is preserved.

normalized separately to their average values at an electron energy of 200 keV. The ratio of the average number of electrons between the CO_2 and the Nd:glass is ~ 18. Statistically we assign an error of ~ 2 to this ratio. This 18-fold increase with the CO_2 laser occurs only for the high-temperature portion of the spectrum. (The lower temperature portion of the spectrum for CO_2 illumination, if it exists, is masked by the higher temperature portion.)

The second magnetic spectrometer deviates from the design of a conventional semicircular focusing system. In this device the detecting emulsion is carried on a cylindrical surface with the entrance slit located on the cylinder and the magnetic field parallel to the axis. The spectrometer possesses no focusing property, and consequently does not have good resolution. Its principal virtue is its greatly reduced dispersion at higher electron energies, which results in increased film densities at high energies. The device provides a broad spectral response and small size allowing it to be placed close to the target without interfering with other diagnostics. A spectrum obtained with this device from a CO_2 laser-produced plasma is shown in Fig. 55. Electrons with energies up to 2 MeV were observed. The poorer resolution of this instrument masks the details of the spectral structure. Apparently, for electron energies greater than 1 MeV the two-temperature fit of Eq. (1) is inadequate -- not surprising for a distribution that is obviously nonthermal.

The angular distribution of the energetic electrons emitted from the plasma we observed by using stacks of photographic emulsions enclosed in a light-tight envelope allowing electrons with energies greater than 75 keV to enter.

The angular distribution of the electron emission from flat targets was strongly peaked along the target normal, similar to angular distributions observed for electrostatically accelerated fast ions.[2] The 6th, 7th, 8th, and 9th layers of a stack of film are shown in Fig. 56. These emulsions were at depths in the stack which required the electrons to pass through material thicknesses that are the end ranges for electron energies of 560, 695, and 760 keV. The full angular width (left to right) is ~ 40° with the direction of the target normal slightly above and to the right of each emulsion. The heavily exposed region in the upper right corner of each emulsion defines the preferred emission cone about the target normal. The unexposed shapes are shadows of objects in the target chamber.

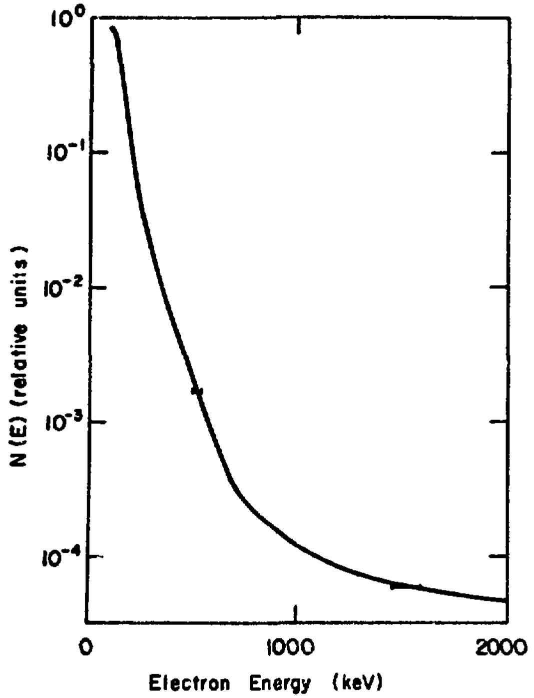

Fig. 55. Spectrum of electrons emitted from a plasma created by a 100-J, 1.2-ns FWHM CO_2 laser, as obtained by a film spectrometer. The horizontal bars at 500 and 1500 keV indicate the energy resolution of the instrument.

In addition to the general peaking of the emission in the direction of the target normal, a great deal of structure can be seen both within and far from the primary emission cone. Structure with angular widths from 10° to less than 1° can be seen in Fig. 56. We shall not speculate as to the mechanisms for the generation of such spatial anisotropies. However, we may conclude that quite complicated field distributions exist between the absorption region and the low-density "outer edge" of these plasmas.

When comparing the electron emission from the laser side and from the back side of 150-μm-thick CH_2 targets, we observed much lower emission on the

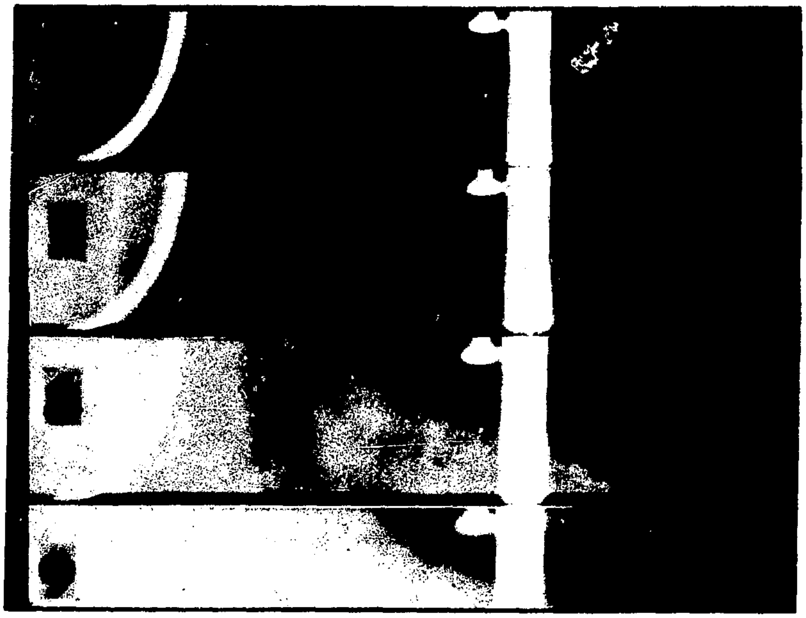

Fig. 56. Sixth through ninth emulsions in a film stack exposed for one shot from the CO_2 laser. The full angular width shown is 40° and the direction of the target normal is slightly above and to the right of each emulsion. The general feature of emission, preferentially along the target normal, is evident as is fine-scale structure with angular widths down to less than 1°.

back side; however, to within a factor of 3, this asymmetry could be explained by the loss in passing through the massive target.

We estimated the total energy emitted by these plasmas in the form of high-energy electrons, by using the observed angular distributions and spectra. In the case of CO_2 illuminations we find $\sim 1\%$ of the incident laser energy emitted as electrons with energies greater than 75 keV. This corresponds to $\geq 10^{13}$ electrons emitted with 100-J incident on a thin, flat target. For Nd:glass illumination the fraction of the incident energy emitted as electrons is only 10^{-3} to 10^{-4}.

LOW-ENERGY X-RAY MEASUREMENTS

Spectroscopy

Crystal Bragg spectrometers, as discussed in earlier progress reports, have proven to be one of our most versatile plasma diagnostics. We improved the quality of silicon line data considerably by the use of an EDDT diffraction crystal. The processing of film data has been largely automated making data rapidly available in a useful form. Figure 57 is a sample of a spectrum obtained with an EDDT crystal from a glass microballoon irradiated with our Nd:glass laser. The ordinate is x-ray intensity and the abscissa is photon energy in keV. Wavelengths in angstroms appear above prominent silicon lines. A Joyce-Loebel densitometer is tied directly to the NOVA computer linked to our glass laser, which allows us to digitize and store the film density automatically as a function of position. The data are then displayed on a Tektronix graphics terminal. Two prominent lines are tentatively identified and the graphics terminal cursor is used to enter the wavelength cues. A

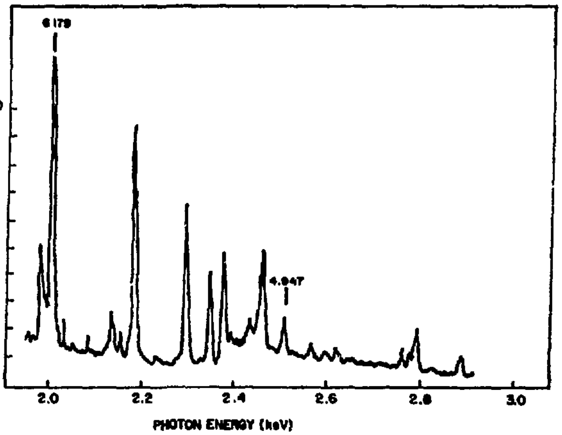

Fig. 57. Silicon line spectrum obtained with an EDDT crystal from a glass microballoon irradiated with the Nd:glass laser.

program then sets the wavelength scale for the entire spectrum. Its validity is checked by comparing the wavelengths yielded for various lines with tabulated values and by comparing the predicted source coordinates with those measured in the experiment. In practice this procedure rapidly yields an unambiguous wavelength calibration. By calibrating the film density as a function of exposure and mass-absorption coefficients for window materials stored in the computer, the data can be processed to show intensity as a function of energy. Figure 57 is a reproduction of the terminal display.

This interactive procedure can be used to analyze much more complex spectra than the silicon lines of Fig. 57. For instance, Fig. 58 shows film density as a function of photon energy from a nickel target irradiated with ~ 10 J in 70 ps from our Nd:glass laser. The dispersive element was a KAP crystal. The plethora of lines are L-transitions of highly ionized nickel. Fluorine-like and neon-like states (9 and 10 remaining electrons, respectively) seem to dominate. The spectrum has not been convoluted with the transmission of the 10-μm beryllium spectrograph window, and the low-energy portion of the spectrum is therefore highly attenuated.

We have measured the x-ray continuum and line intensity from plasmas produced by focusing 10.6-μm laser light on low-Z targets. The irradiance on target in these experiments was 3×10^{14} W/cm^2. The data on the soft x-ray continuum from plasmas produced by irradiation of flat polyethylene targets with 10.6- and 1.06-μm laser light, respectively, are compared in Fig. 59. Plasma temperatures of 300 eV were deduced from continuum measurements at energies less than 2 keV.

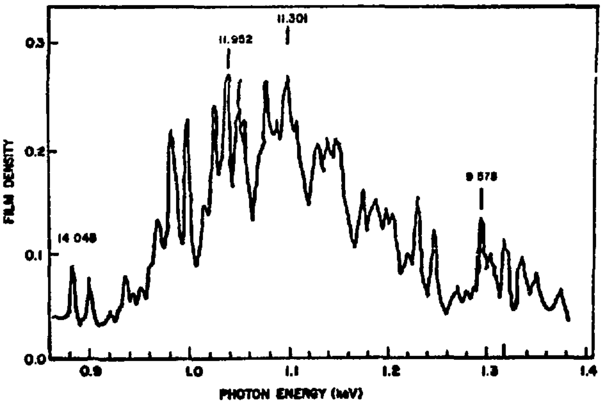

Fig. 58. L-lines from a nickel target irradiated with the Nd:glass laser. The low-energy portion is highly attenuated by the window. A KAP diffracting crystal was used.

X-ray lines characteristic of helium-like transitions were observed, from flat targets ranging from sodium to silicon (see Fig. 60), by using a KAP diffracting crystal. We observed the hydrogen-like transitions only from the sodium target. Temperatures deduced from line ratios using the coronal model are in agreement with those from the continuum measurements, suggesting low plasma densities in the radiating region -- recognizing, of course, limitations imposed by spatial and temporal inhomogeneities in the plasma.

The cold K_α line of silicon, aluminum, and magnesium has been observed in the spectra. These lines are undoubtedly excited by high-energy electrons and may therefore be a diagnostic for the

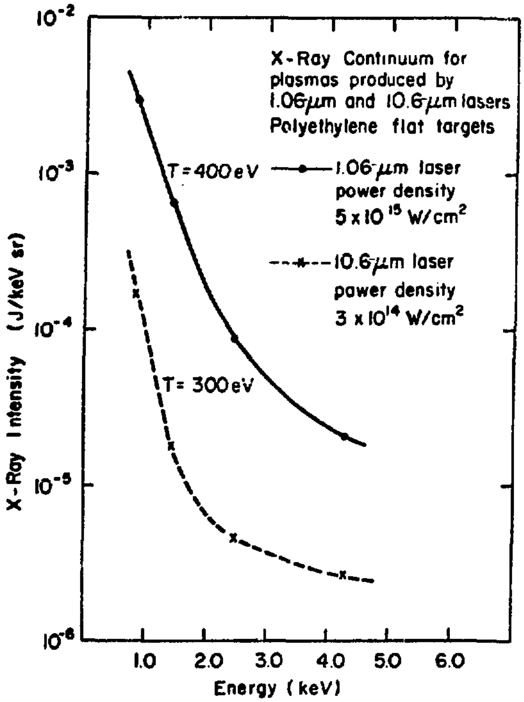

Fig. 59. X-ray continuum produced by plasmas created by irradiating polyethylene targets with 1.06- and 10.6-μm lasers.

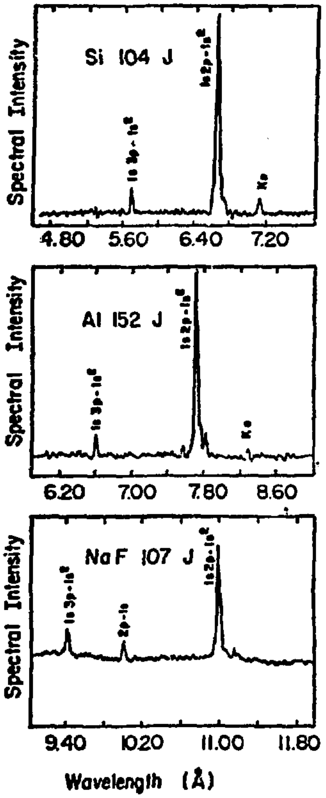

Fig. 60. X-ray line spectra obtained from various targets irradiated with a CO_2 laser. Note the cold K lines.

study of target preheat by suprathermal electrons. (The spectra of suprathermal electrons emitted from laser-produced plasmas were discussed earlier in this section.) The K_α emissions are not normally observed from plasmas produced by 1.06-μm laser light.

The x-ray continuum intensity in the $\sim$ 0.6- to 2-keV region, assuming a temperature of 300 eV and isotropy, is (4 ± 2) x 10^{-3} J for 100 J of incident 10.6-μm laser light. The x-ray conversion to discrete lines is $\sim$ 30% less. The x-ray conversion efficiency depends on the energy absorbed by flat targets, which is less than 20%.

X-Ray Pinhole Camera

X-ray pinhole cameras were used successfully in our CO_2 laser-target experiments. Images were recorded from plastic and glass targets.

The cameras were similar to those used for over two years in experiments with 1.06-μm light. The cameras' characteristics are:

Target-to-pinhole	1 cm
Magnification	7.2
Resolution	40 μm for single pinhole 25 μm for three pinhole
Filtration	25 μm for Be & selected greater filtration
Film	RAR 2490 or No-Screen medical x-ray film or Film stack consisting of above two types.

We observed an interesting phenomenon in these experiments at the 100-J level of CO_2 laser irradiation. The soft x-ray flux ($\sim$ 1 to 4 keV) was $\sim$ 100 times lower than in Nd:glass laser experiments. Because the soft x-ray emission is believed to emanate from the vicinity of the critical surface, this difference may be due to the lower critical density for 10.6-μm radiation (critical density, n_c, is 10^{19} cm^{-3}) as compared to 1.06-μm radiation ($n_c = 10^{21}$ cm^{-3}).

The difference in flux may also be explained by the laser-power dependence. Because 1.06-μm experiments involved a 0.3-ns pulse whereas the 10.6-μm experiments used 1.2 ns, the CO_2 irradiation at 10.6 μm was four times lower in power at the same energy. The x-ray flux measurements of the pinhole camera are consistent with other x-ray spectroscopic data.

Another phenomenon detected by the camera is shown in Fig. 61. Here the target was a cross made of glass fibers mounted in an 8-mm-diam hole in a molybdenum holder. X-ray emission is seen to a distance of 1 mm from the $\leq$ 0.2-mm focal region. Possible explanation for this observation are (1) a high lateral thermal conductivity, and (2) a large "return current" to the interaction region to replace the emitted electrons. Both explanations will be considered in future target designs.

A third phenomenon, which occurred on only a few experiments, involved a heavy exposure of the entire frame of the No-Screen film. We suspect that a narrow, intense beam of electrons struck the platinum foil in which the pinholes are drilled, thereby emitting a high bremsstrahlung flux that easily penetrates the 13-μm-thick beryllium window over the film pack. The existence of intense, narrow "pencil beams" of electrons was observed

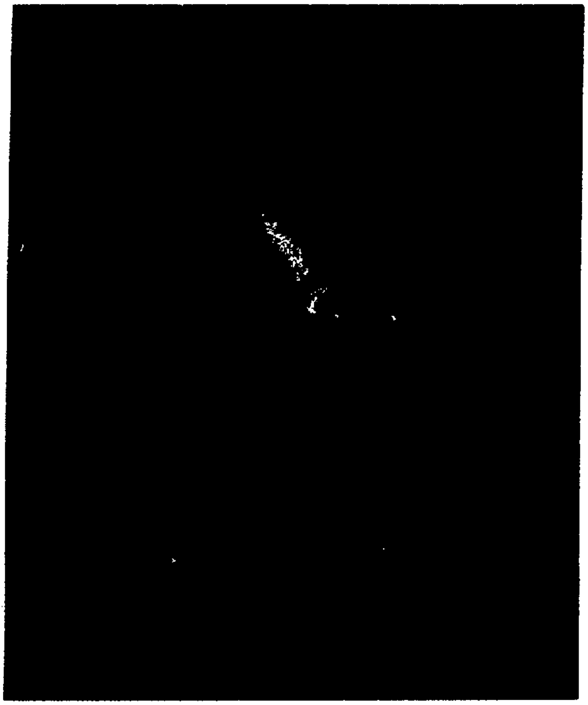

Fig. 61. X-ray pinhole image of crossed glass fibers irradiated with a CO_2 laser. The bright region is ~ 1 mm wide.

previously[1] in CO_2 experiments. This "problem" for x-ray photography is ameliorated by using a film less sensitive to x rays exceeding 4 keV.

REFERENCES

1. T. H. Tan, A. H. Williams, and G. H. McCall, "A Thin-Film Detector System for Laser-Fusion Studies," Nucl. Instr. and Methods 131, 425 (1975).
2. G. H. McCall, T. H. Tan, and A. W. Williams, "Measurement of Alpha Particles and Protons from a Laser-Imploded Target," submitted for publication.
3. G. Charatis, J. Downward, R. Goforth, B. Guscott, T. Henderson, S. Hildenn, R. Johnson K. Moncur, T. Leonard, F. Mayer, S. Segall, L. Siebert, D. Solomon, and C. Thomas, "Experimental Study of Laser-Driven Compression of Spherical Glass Shells," Fifth IAWA Conference on Plasma Physics, Tokyo, Japan, Paper IAWA-CN-33/F1, IAEA (Vienna), 1975).
4. L. C. Northcliffe, "Energy Loss and Ranges of Charged Particles," Publication 1133, p. 353, Nat. Acad. of Science, Nat. Res. Council, Washington, D.C., 1964.
5. D. J. Sigmar and G. Joyce, "Plasma Heating by Energetic Particles," Nucl. Fusion 11, 447 (1971).
6. G. S. Fraley and R. J. Mason, "Preheat Effects on Microballoon Laser-Fusion Implosions," Phys. Rev. Lett. 35, 520 (1975).
7. M. G. Payne, "Energy Straggling of Heavy Charged Particles in Thick Absorbers," Phys. Rev. 185, 611 (1969).
8. G. H. McCall, T. H. Tan, and A. W. Williams, "Measurement of Alpha Particles and Protons from a Laser-Imploded Target," submitted for publication.
9. J. F. Kephart, R. P. Godwin, and G. H. McCall, "Bremstrahlung Emission from Laser-Produced Plasmas," Appl. Phys. Lett. 25, 108 (1974); J. F. Cuderman and K. M. Gilbert, in Advances in X-Ray Analysis, Vol. 18 (Plenum Press, 1975) p. 159; B. H. Ripin, P. G. Burkhalter, F. C. Young, J. M. McMahon, D. G. Colombant, S. E. Bodner, R. R. Whitlock, D. J. Nagel, D. J. Johnson, N. K. Winsor, C. M. Dozier, R. D. Bleach, J. A. Stamper, and E. A. McLean, "X-Ray Emission Spectra from High Power Laser-Produced Plasmas," Phys. Rev. Lett. 34, 1313 (1975).
10. A. W. Ehler, "High-Energy Ions from a CO_2 Laser-Produced Plasma," J. Appl. Phys. 46, 2464 (1975); J. Martineau, P. Paranthoen, M. Rabeau, and C. Patou, "Nanosecond CO_2 Laser Interaction Experiments," Bull. Am. Phys. Soc. 20, 1265 (1975); J. S. Pearlman and J. P. Anthes, "Interaction of High-Power Laser Radiation with Thin Polystyrene Films," ibid; H. Pepin, H. A. Baldis, T. W. Johnston, K. Parbhakar, and B. Grek, "X-Ray Emission and Ion Energy Measurements in ns CO_2 Laser-Produced Plasmas," ibid, p. 1303; E. Fabre, C. Popovics, and C. Stenz, "Experiments on CO_2 Laser Interaction with Polyethylene Slabs," 7th European Conf. on Controlled Fusion and Plasma Phys., Lausanne (1975).
11. G. L. Cano, P. J. Brannon, and J. E. Powell, "Spectral Measurements of Hot Electrons from Laser-Produced Plasmas," Bull. Am. Phys. Soc 19, 886 (1974); J. F. Kephart and D. V. Giovanielli, "Spatially Resolved Observation of the Energetic Electrons from a Laser-Produced Plasma," ibid; K. G. Tirsell, R. A. Haas, H. C. Catron, and V. W. Slivinsky, "Spectral Measurements of Electrons Emitted from 1.06 m Laser-Produced Plasmas," Bull. Am. Phys. Soc. 20, 1246 (1975); D. V. Giovanielli, J. F. Kephart, and A. Williams, "Emitted Electron Spectra from Plasmas Produced with Nd and CO_2 Lasers," ibid, p. 1318.
12. F. R. Paolini, G. C. Theordoridis, and W. F. Welsh, "Satellite Instrumentation for Charged Particle Measurements II. Magnetic Analyzes for 0.1 to 1.0 MeV Electrons," IEEE Trans. Nucl. Sci. NS-15, 1974 (1968).
13. K. Siegbahn, ed., Alpha-, Beta- and Gamma-Ray Spectroscopy (North Holland Publishing Co., Amsterdam, 1965), p. 496.

51,740

IV. LASER-FUSION TARGET DESIGN AND FABRICATION

Our pellet fabrication effort, supported by extensive theoretical investigations, supplies the thermonuclear fuel in packaged form suitable for laser-driven compressional heating experiments. These targets range from simple deuterated-tritiated plastic films to frozen DT pellets to complex DT gas-filled hollow microballoons, mounted on ultrathin supports and coated with various metals and/or plastics. Numerous quality-control and nondestructive testing techniques for characterizing the finished pellets are being developed.

TARGET DESIGN AND FABRICATION

General High-Pressure DT Gas-Filled Targets

Introduction -- We have continued the development of techniques and methods to fabricate hollow, multilayered spherical targets to be filled with high-pressure DT fuel gas. These targets generally consist of a high-Z, high-density, metal pusher shell overcoated with a low-Z, low-density absorber-ablator layer. This outer layer absorbs energy from the incident laser beam, is heated, vaporizes, and streams away from the pusher shell (i.e., ablates) causing the shell to implode via the rocket reaction forces. The pusher shell can be deposited onto a nonremovable mandrel (e.g., a glass or metal microballoon) or, alternately, improved performance may be obtained if the pusher shell is fabricated directly as a free-standing metal microballoon. High-strength pusher shells are desired in either case so that as high a DT pressure (i.e., high density) as possible can be used, minimizing the additional compression required to attain a fusion burn.

Nonremovable Mandrels

General -- Many of our current targets use bare glass microballoons as pusher shells, filled with high-pressure DT gas as the fuel. Therefore, we continued our development of methods for quality selection and characterization of these bare glass microballoons. These techniques should be applicable to metal microballoons as well, and also be useful in the selection and characterization of the microballoons used as mandrels for structured, multilayered targets.

Crunch Test -- We have previously described the crunch test in which sized and density-separated microballoons are subjected to an external gas pressurization to preferentially crush the aspherical or nonuniform-wall-thickness microballoons, thereby increasing the fraction of high-quality microballoons in the survivors.[1,2] During the past six months, we have collected data to quantify the effects of this crunch test so that we could optimize our procedures.

Crushing curves (number of balls broken per pressure increment) for glass microballoons (GMBs) that had been preprocessed to varying degrees are shown in Fig. 62. The data were obtained by using

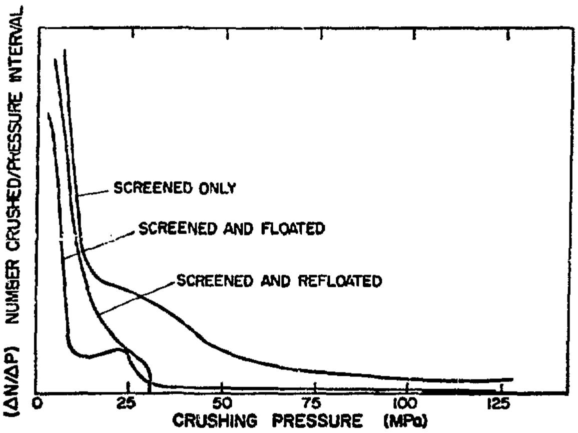

Fig. 62. Typical crunch-test results for glass microballoons processed in various ways.

pressurized nitrogen gas to crush the GMBs and our acoustic transducer technique[3] to measure the breaking rate as a function of pressure. We think the large initial breaking rate common to all the curves in Fig. 62 reflects the crushing of the many very-low-quality, thinner-walled GMBs in the as-received material. The breaking rate then tends to level off.

The uppermost curve in Fig. 62 is for GMBs that were only size-separated by screening before the crush so that the sample contained a wide range of wall thicknesses. This can be seen in Fig. 63 where we show wall-thickness distributions of this material as-screened, and after being crushed at one of several pressures. This crushing curve in Fig. 62 (after the first steep decrease) essentially reflects the wall-thickness distribution of the sample, the GMBs with thicker walls being crushed at the higher pressures. Therefore, the primary effect of the crush in this case is to increase the average wall thickness of the survivors, as shown by the data in Fig. 63. Thus, if only thick-walled microballoons are required, a crush prior to density separation can be used to remove the thinner walled GMBs, reducing the amount of material that must be density-separated.

The left-most curve in Fig. 62, and the wall-thickness distributions in Fig. 64 are for GMBs that were both size- and density-separated before the crush (i.e., screened and floated). The crushing curve drops sharply to near zero at ~ 27 MPa because at that point we have crushed almost all the GMBs in the sample, both good and bad. A few thicker walled GMBs are present in the sample because our density separation is not perfect. These break above 27 MPa and continue to break out to the maximum pressure used (136 MPa). If we refloat these density-separated GMBs (i.e., repeat the density separation), we can remove almost all these thicker walled GMBs, as illustrated by the third curve in Fig. 62 (refloated) where the breaking rate drops to zero at ~ 30 MPa.

The wall-thickness distributions for the screened and floated GMBs in Fig. 64 illustrate

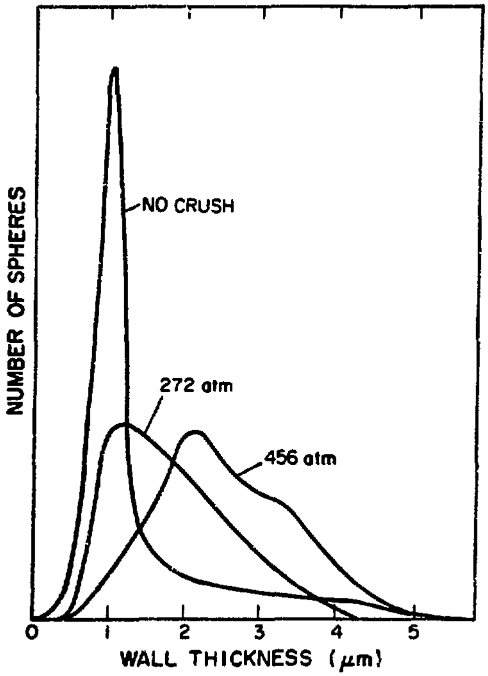

Fig. 63. Wall-thickness distributions of as-screened glass microballoons before and after crushing at several pressures.

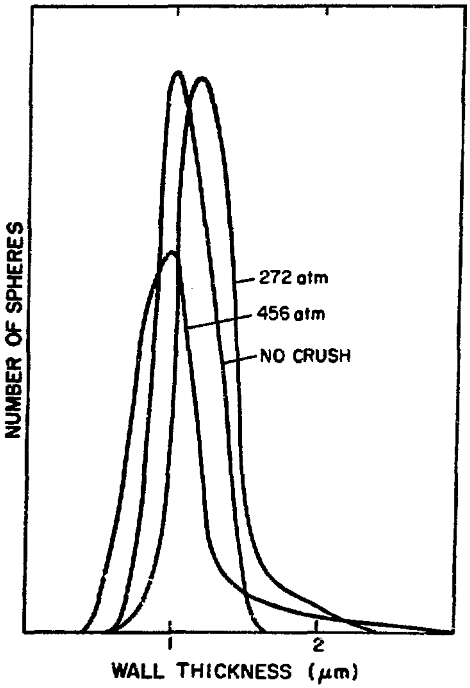

Fig. 64. Wall-thickness distributions of size- and density-separated glass microballoons before and after crushing at several pressures.

TABLE XIV

COMPARISON OF QUALITY OF MICROBALLOONS PROCESSED BY VARIOUS TECHNIQUES

Processing[a]	*Amount of Product That Is Of High Quality (%)*[b]
Screened only	< 0.2
Screened and crushed at ~ 16 MPa (2.4 kpsi)	~ 0.2
Screened and floated to give $0.13 <$ density < 0.16 g/cm^3	1.6
Screened, floated (0.13 to 0.16 g/cm^3) and crushed (under liquid) at ~ 26 MPa (3.8 kpsi)	~ 50

---

[a] *All microballoons 3M-type B18A, screened to between 96- and 113-µm diameter (FWHM) (90- to 115-µm extreme limits).*

[b] *As determined by optical interferometry (see below).*

that the crush test has little effect on the wall-thickness distribution of these GMBs, primarily because of the narrow distribution in the starting material (i.e., no thick-walled tail).

The effect of these processing steps on the quality of the resultant product is summarized in Table XIV, as determined by examining the surviving GMBs by optical interferometry with a Jamin-Lebedeff interferometer attachment on an optical microscope. Initially we generated a comprehensive set of data for Table XIV by using high-pressure gas to crush the GMBs and were surprised to find that many good-looking GMBs (~ 1-µm wall by 100-µm diameter) survived crushing pressures of 135 MPa (20 kpsi). However, when further examination disclosed that none of these survivors would hold gas, we concluded that some of the GMBs fail under crushing pressures by cracking in such a way as to be undetectable by optical interferometry (or microradiography). As a result, we now crush under liquid so that any GMB that is cracked will be filled with the crushing liquid. These liquid-filled GMBs are then removed from the good survivors via density separation.

These data clearly illustrate the value of our screen-float-crush processing for the quality of the end product. However, because all the preprocessing is batchwise and the final selection and characterization are done one at a time, even modest increases in batch quality markedly improve the total output of the selection process.

Measurement of Microballoons -- Previously we relied on microradiographic inspection for final quality selection and measurement of bare and coated microballoons to be used as laser-fusion targets. However, for glass microballoons (GMBs) we recently began to use optical interferometry because it is more sensitive, faster, and easier to use. At the same time, we have continued our development and evaluation of microradiographic techniques for the inspection of opaque microballoons.

For interferometry we use a Jamin-Lebedeff attachment on a commercial optical microscope. Microballoons are selected for quality by operator assessment of the circularity and concentricity of the interference fringes superimposed on the microballoon image as illustrated in Fig. 65, similar to the technique first reported by Stone and Souers.[4] With this technique, wall-thickness variations of ~ 0.04 µm are easily detectable. To measure the wall thickness of the GMBs, we developed a technique similar to the one reported by Weinstein[5] in which we measure the interference-fringe shift at the center of the ball relative to the background. This is accomplished by first setting the center of the ball to the black, zero-order fringe condition and then measuring the optical path-length change necessary to move the black fringe out to the back-

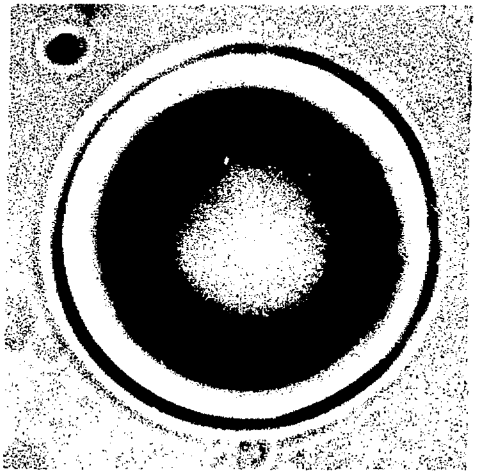

Fig. 65. Interference pattern of a high-quality glass microballoon.

ground by adjusting the optical wedge in the sample beam. This optical path difference can be related to the geometric path difference of the two beams, and thus to the GMB wall thickness, by using the refractive indices of the glass in the microballoon walls and of the DT gas contained within the GMB (if any). The estimated error in our wall-thickness measurements is ± 0.06 μm.

Diameter measurements for the GMBs are obtained by using an optical microscope with a filar micrometer, obtaining a precision of about ± 0.5%. However, the accuracy of our measurements is in question because of calibration problems, but it appears to be no worse than 1 to 2%. A comparison of Lawrence Livermore Laboratory and Los Alamos wall-thickness and diameter measurements for five GMBs is shown in Table XV, including both optical-microscopic and microradiographic data. The agreement of the two sets of interferometric wall-thickness measurements is excellent, and the agreement of these with the microradiographic data is well within the lower resolution limit of this latter technique (± 0.25 μm). Similarly, the diameter measurements all agree to within our current estimated accuracy.

In our microradiographic technique, we are obtaining the size data directly from the geometry of the microballoon image on the microradiograph by means of an optical microscope, and it is this latter instrument that limits the resolution of our process to ± 0.25 μm. To evaluate the effectiveness of the microradiographic technique for wall-thickness measurements on thin-walled GMBs, we have measured a series of such GMBs by both radiography and by optical interferometry. The data are plot-

TABLE XV

COMPARISON OF GLASS MICROBALLOON (GMB) MEASUREMENTS

	Outside Diameter (μm)			Wall Thickness (μm)		
	Optical Microscopy		Microradiography[c]	Optical Interferometry		Microradiography[c]
GMB No.	LLL[a]	LASL[b]	LASL	LLL[d]	LASL[e]	LASL
1	82.4	83.4	81.4	0.54	0.56 0.51[f] 0.66[g]	0.8 0.5 1.1
2	82.9	83.8	82.7	0.61 0.59 0.62	0.67 0.62 0.69	0.8
3	84.9	83.4	83.6	0.56 0.54 0.57	0.54 0.52 0.56	0.7
4	84.9	85.8	85.0	0.70 0.67 0.72	0.67 0.63 0.70	0.8
5	87.3	88.0	86.5	0.59	0.59 0.58 0.60	0.6

---

[a] LLL diameters measured with Vickers shearing eyepiece.

[b] LASL diameters measured with filar-micrometer eyepiece.

[c] Microradiographic data obtained by reading geometry of microradiographs in an optical microscope.

[d] LLL wall thickness by Weinstein's method.[5]

[e] LASL wall thickness by method described here.

[f] Minimum value observed.

[g] Maximum value observed.

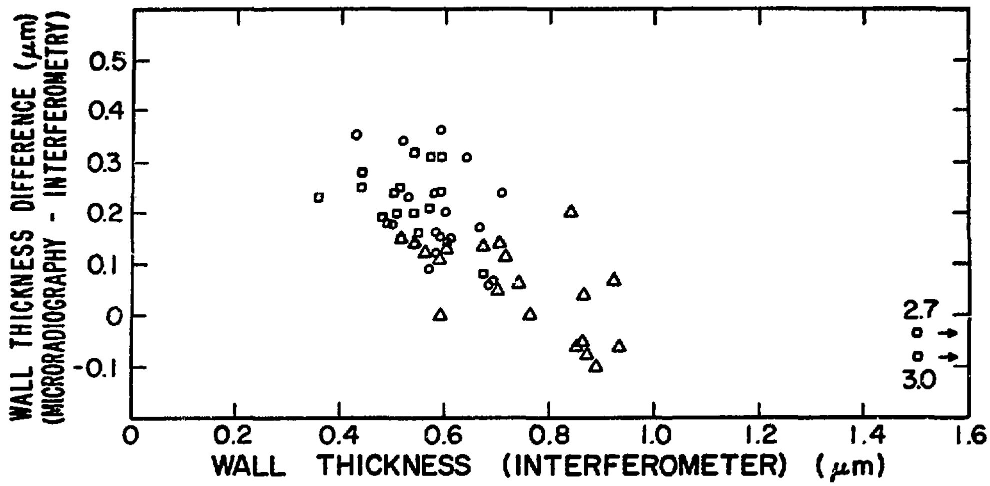

Fig. 66. Differences in wall thickness of glass microballoons measured microradiographically and interferometrically.

ted in Fig. 66 as the difference between the two measurements vs the interferometric value. At a wall thickness of 0.7 to 0.8 μm the results of the two methods clearly begin to diverge and the differences get larger as the thicknesses decrease. We are developing a technique to analyze the microradiographs photometrically, which is based on a method developed at KMSF[6] but employs an image-analysis system that will allow us to analyze the entire circumference of the microballoon at a glance. This technique should provide improved resolution and extend the usefulness to thinner walled GMBs.

Pusher Shell Deposition

General -- We have continued the development of methods to deposit uniform layers of high-Z metals onto various types of mandrels for use as pusher shells. The primary objective is the attainment of high-strength coatings with useful deuterium-tritium permeability.

Chemical Vapor Deposition -- Chemical vapor deposition (CVD) has been very useful for coating microballoon substrates because we can use a gas-fluidized-bed coating apparatus that provides generally good mixing of the substrates and allows the application of useful metal coatings to these otherwise difficult-to-handle substrates. We have concentrated on the deposition of molybdenum from $Mo(CO)_6$ and have used this material to further develop our apparatus and techniques. An improved fluid-bed reactor, Fig. 67, was designed and built incorporating a water-cooled orifice inlet to the fluid bed, precise metering of carrier-gas flow, and uniform temperature control of the $Mo(CO)_6$ bed via a water (or oil) jacket. With this improved apparatus we can plate at least 10-μm-thick layers of "molybdenum" onto glass or metal substrates in a single, continuous coating run with good inter- and intra-particle coating uniformity and only minimal agglomeration. However, we have determined that at deposition temperatures from 625 to 775 K the coatings obtained are actually dimolybdenum carbide (Mo_2C) rather than molybdenum metal. With an inert carrier gas we obtain coatings with very smooth surfaces, which, however, are highly stressed and exhibit many radial cracks. With a hydrogen carrier gas we obtain unstressed coatings, but the surfaces are very rough, presumably due to gas-phase nucleation. Heat treatment of the former coatings in hydrogen at 1025 K anneals the stresses but results in unacceptable degradation of the (Solacell) mandrels.

We have completed preliminary experiments to investigate hydrogen permeation into, and out of, several batches of Mo_2C-coated Solacells. The data indicate that we can load such microballoons with

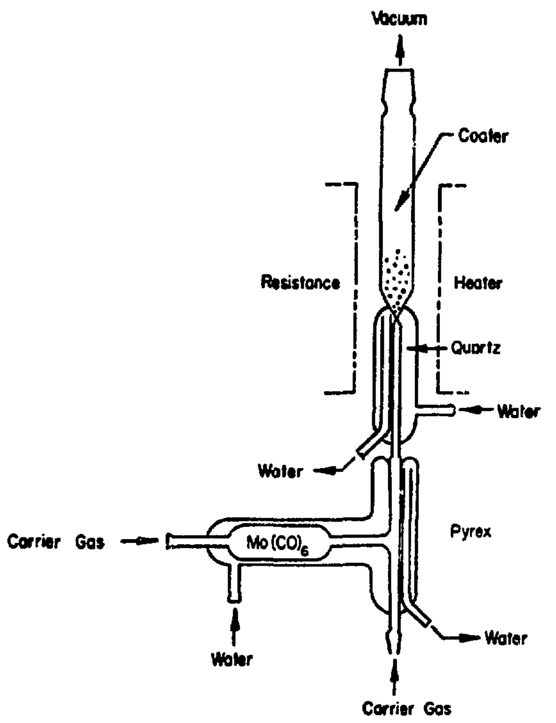

Fig. 67. Schematic of improved fluidized-bed apparatus used for chemical vapor-deposition coating.

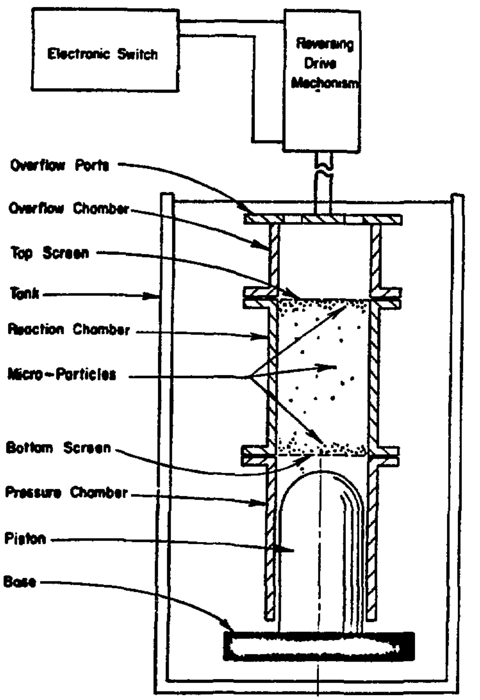

Fig. 68. Schematic of apparatus for electroless plating of discrete microparticles.

DT fuel gas by permeation through the walls at 675 K and that, at room temperature, the gas will be retained for many months.

Electroless Plating -- In electroless plating the metal is generated by chemical reduction in an aqueous solution. In the past we dispersed the microballoon mandrels in the vortex of a vigorously stirred plating solution until the desired thickness of the deposit was obtained. This method resulted in useful coatings, but particle agglomeration was a serious problem, coating uniformity from sphere to sphere in a given coating run was poor (i.e., thicknesses often varied by more than 100%), and it was difficult to obtain good surfaces on coatings thicker than 5 μm. In addition, different stirring techniques were required for buoyant and for nonbuoyant microballoons.

These difficulties prompted us to develop a new technique for electroless plating in which the plating solution is pumped in such a way as to disperse the particles in the solution. This apparatus is shown schematically in Fig. 68. The microballoons to be coated are contained in a cylindrical chamber between two end screens. The cylinder is immersed in plating solution and is driven up and down over a solid piston to pump the solution effectively through the particle-containing chamber. This pumping imparts a random stirring motion to the microballoons regardless of their relative density. When the cylinder moves downward, plating solution is forced through the bottom screen into the reaction cavity, which lifts, rotates, and disperses any sinking particles. Conversely, when the cylinder moves upward, solution flows into the reaction cavity by suction through the top screen, thus rotating and dispersing the floating particles throughout the liquid solution. In addition, if any gas is being evolved, it is forced out through the top screen during the downward stroke of the cylinder, keeping the reaction chamber filled with liquid.

With this new apparatus, we can routinely plate uniform, smooth-surfaced, agglomeration-free coatings at high rates (e.g., ~15 μm/h for nickel) regardless of substrate density. We have applied layers from 1 to 35 μm thick with this technique.

Electroplating -- Electroplating is of considerable interest to us because a good, basic electroplating technique will give us the capability of depositing a very wide range of metals and alloys, including some having rather high strengths. However, electroplating onto microballoon substrates is a considerable challenge because the microballoons must make contact with a metallic, current-carrying cathode without plating the microballoons to the cathode or to each other.

We have tried many different schemes before finally arriving at the successful apparatus shown in Fig. 69. Here again, we contain the microballoons to be coated in a cylindrical reaction cavity that is closed off at each end with a plastic screen. A cathode wire is mounted adjacent to each screen inside the reaction chamber. Plating solution is pumped through this chamber first downward and then upward, which forces the particles alternately against each end of the chamber. A switching system is used so that only the cathode against which the particles are being pumped is activated, the one at the inlet end being inert. Finally, most of the volume of the cavity is filled with large (3-mm) plastic spheres. As the much smaller micro-

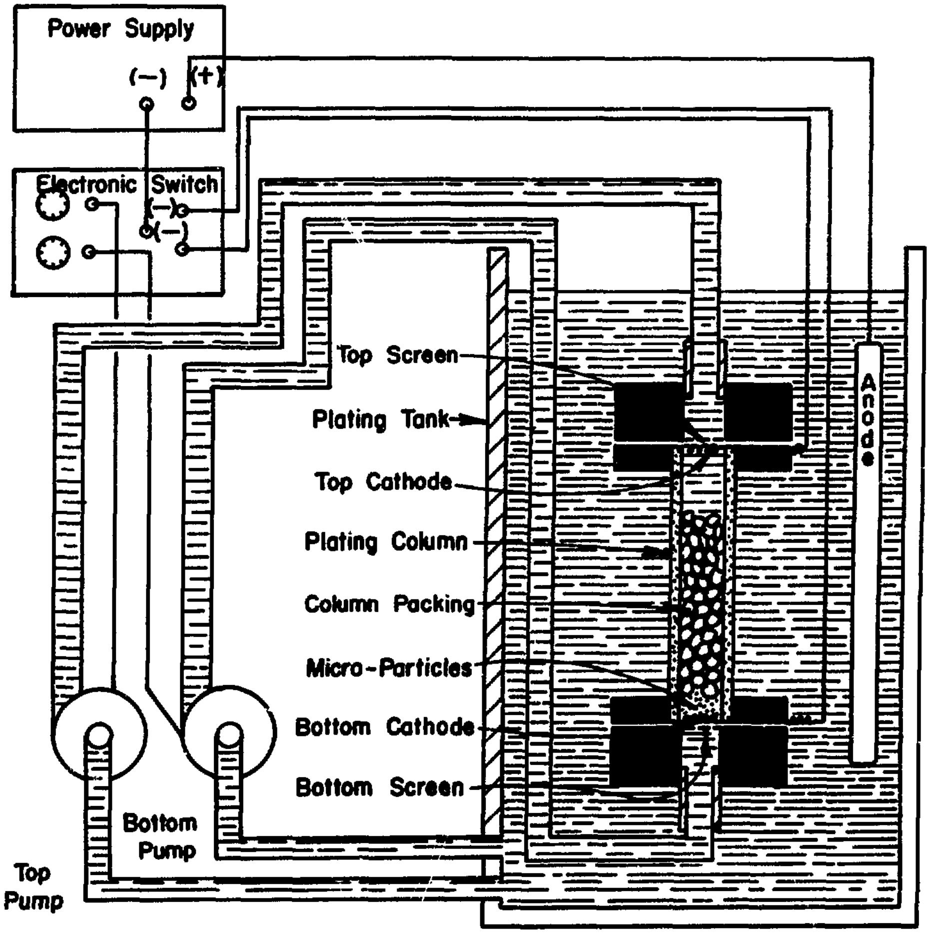

Fig. 69. Schematic of apparatus for electrolytic plating of discrete microparticles.

balloons are pumped from one end of the chamber to the other, they tumble against these larger particles many times, thus breaking up any agglomerates that are forming.

This apparatus is very effective. We can plate thick, high-quality layers of metal onto any microballoon substrates regardless of their density relative to the plating solution with yields of uniformly plated, discrete (unagglomerated) particles in excess of 80%. We have plated bright nickel, copper, and gold-copper alloys and we are now working on a high-strength nickel-iron alloy.

Cryogenic Targets

General -- Laser-fusion targets fueled with cryogenic liquid or solid DT offer the advantage of high initial fuel density without the disadvantage of the diluent atoms (e.g., carbon or lithium) which are present in the room-temperature solids that have a high hydrogen density [e.g., Li(D,T) or $(\text{-CDT})_n$]. However, significant experimental complications are encountered in the fabrication of these cryogenic targets and in their use in the laser-target interaction experiments. Nonetheless, the cryogenic targets are sufficiently promising for us to pursue their development.

Spherical Geometries -- The cryogenic target receiving the most attention is a uniform, hollow shell of solid DT ice, frozen onto the inside surface of a glass or metal microballoon container that serves as the pusher shell. We are concentrating our efforts on glass microballoons, simultaneously developing the techniques to (a) freeze the DT into a uniformly thick layer on the inside surface of the glass and (b) to measure the thickness uniformity of the DT ice shell. Two general approaches are being examined. In one, the DT is frozen either by conduction through the support system or by a low pressure of cryogenic helium or hydrogen gas; in the second approach, we employ a directed jet of cryogenic hydrogen or helium to quick-freeze the target.

The Dewar system used in the former (nonflow) approach has been modified to reduce temperature gradients and to allow the use of a heat-exchange gas for cooling the DT-filled targets. We have studied the condensation and freezing in DT-filled glass microballoons (GMBs) that were supported in the center of a 3-mm-diam aperture by sandwiching the GMB between two 20-nm-thick cellulose acetate films.

In initial experiments we first froze the DT into a single blob and then held the pellet in an isothermal environment to determine if the heat input from the radioactive decay of the tritium would cause sublimation and recondensation to redistribute the DT to a uniform solid layer on the inside of the GMB. We were not able to observe any change in the initially formed solid blob, even after several hours in an isothermal environment.

When the DT-filled GMBs are cooled entirely in an isothermal manner, we see signs of solidification in all parts of the pellet every time solid forms, and the solid layers are much more uniform than the single blob observed previously.[7] The detailed nature of the solid layer appears to be determined by the length of time the sample has been held at 20 K and below. These observations suggest that a programmed cooling cycle might be useful in obtaining and preserving uniform DT ice layers.

We have developed a spot-reflection technique of interferometry that is more sensitive than the shearing-plate interferometer discussed previously[7] but that provides information for only two small spots on the surface of the sphere. In this application we make use of the familiar interference of light reflected from an oil film on water or from the wall of a soap bubble. If the spherical shell is viewed normal to an incident monochromatic light beam, two bright spots are seen where the surface of the ball is at the proper angle for specular reflection. At each of these spots reflections from the inner and outer surfaces interfere according to the thickness of the layer traversed. We monitor the intensity of one of these spots with a photomultiplier as a DT layer forms and grows in the microballoon and observe a sinusoidal variation in intensity, from which the DT layer thickness can be calculated. Variations in intensity have been observed that seem to be fairly consistent with the expected layer thickness, but interference from other surfaces in the cryostat has made the results difficult to interpret.

To continue these approaches, we have designed a new cryostat system that will again improve the temperature uniformity in the vicinity of the sample (to ~ 10 mK) and will allow programmed cooling rates from 10^{-3} K/s to ~10 K/s. This system will also allow the use of very low illumination levels for pellet observation to minimize this perturbation of the temperature environment of the pellet.

Interesting results were also obtained in our flow-cooling experiments. In this case, a stream of cold helium was directed downward onto a deuterium-filled GMB that was glued to a glass fiber and was contained in a vacuum chamber most of whose walls were at room temperature. The pellet behavior was observed either by transmitted-light microscopy or by shearing-plate interferometry. Starting with a warm pellet we observed, as we increased the cold helium flow rate, liquid deuterium to form on the inside of the GMB in a layer that was thickest at the top (where the helium impinged), thinning out to approximately zero at the bottom. If the helium flow was increased further, all the condensate suddenly collected at the top of the pellet and finally formed a single blob of solid. These results are very promising. We are adding a second cooling jet, as well as better shielding of the pellet from room-temperature radiation, to determine if relatively uniform liquid layers can then be generated and maintained.

Theoretical Support and Direction

Introduction -- Areas that have received major emphasis in our theoretical studies are:

- The acquisition of a two-dimensional design tool for current and future targets; the continuation of one-dimensional target designs and hydrodynamic modeling of laser-target experiments; hydrodynamic stability calculations that include self-generated magnetic fields.

- The continuation of plasma studies of stability and profile modification in light of recent CO_2 data with development of more efficient codes and theoretical tools to study the phenomena; and a continued effort to understand the important problem of limited heat conduction.

Hydrodynamics, Target Design, and Modeling -- Because of programmatic importance, there has been a continuing effort to develop two-dimensional tools for design studies. To facilitate this development, we took two steps: (1) to acquire from Lawrence Livermore Laboratory the two-dimensional laser-fusion design code, LASNEX, and (2) to select from four of our two-dimensional codes, one (MCRAD) which our design effort will principally support -- although one of the other three codes could occasionally be used for particular physics problems.

We acquired LASNEX in October 1975. Before starting an extended set of design calculations with it, it seemed advisable to compare the predictions of a LASNEX run in its one-dimensional mode with the predictions of our one-dimensional codes CLYDE and CERES. These studies are still in progress. Some calculations agree well, such as those for DT microballoon targets run in a three-dimensional mode with radiation off. Differences existing in some comparison calculations are being screened.

Efforts to upgrade MCRAD -- a two-dimensional hydroradiation-transport code we used in the past for radiation studies -- are under way. It is an interactive code, employing our high-speed SANDERS graphics facility. Bowties and boomerangs, which form in the Lagrangian mesh during the running of a problem, are readily repaired by means of a light pen, allowing for operationally efficient and speedy simulation of complex laser-target designs.

MCRAD has been augmented with the addition of: (1) a DT burn option, by which the reaction alpha-particle energy is either deposited locally or discarded; (2) an electron conduction option, which allows for the diffusion of energy through the target by electron conduction; and (3) a laser deposition option, which delivers laser energy to the target surfaces by the Monte Carlo transport of photons. A portion of the light is selected and the remainder absorbed upon each interaction of a photon bundle with the target.

We have also continued our work on hydrodynamic modeling. The hydrodynamic equations of steady-state ablative flow have been solved in spherical geometry. Heat conduction couples the laser flux to the flow. The problem is reduced to the solution of two coupled ordinary nonlinear differential equations for the flow velocity $v(r)$ and the temperature $T(r)$, which are integrated numerically. In the planar ablation problem, the solutions are such that the sonic transition point and the critical point for the laser light are coincident if one imposes the Chapman-Jouguet condition. Without this condition, there is no transsonic point; planar flow is then never supersonic. In contrast, in our spherical model we find a two-parameter family of solutions in which the flow passes from subsonic at radii inside of the ablation surface to supersonic further from the spherical center. The critical radius, r_c, i.e., the radius at which the laser energy deposition occurs, may be inside the adiabatic sonic radius but not inside the isothermal sonic radius, r_s. The solutions depend upon the two dimensionless parameters $M = \rho_s v_s{}^3 r_s/T_s\kappa_s$ and ρ_c/ρ_s, where ρ_s, v_s, r_s, T_s, and κ_s are, respectively, the mass density, flow velocity, radius, temperature, and thermal conductivity at the isothermal sonic transition point and ρ_c is the critical mass density at which the laser energy is deposited. From the computed solutions, we find that the laser power, W, required to generate a given ablation profile scales as $W \sim \rho_c{}^{-1/2} \sim \lambda$, the laser wavelength. Using this result, we derive a thermal coupling efficiency relating laser power to ablation pressure at the target surface. The efficiency scales as $\lambda^{-1/2}$ favoring lasers of shorter wavelength to irradiate spherically symmetric fusion targets. Scaling laws of the solutions further indicate that the ablation pressure scales as $P_a \sim \kappa_o T^3$ where thermal conductivity is $\kappa = \kappa_o T^{5/2}$ and that, for a given fractional burnthrough of a thin shell, the ablation pressure scales with atomic number, $P_a \sim Z^{1/2}$.

Plasma Physics Studies Associated with Laser-Target Interactions

General -- We continued our microscopic plasma-physics research with particular emphasis on coupling more macroscopic hydrodynamic physics, including self-consistent profile modification, with our stability codes. Recent target data suggested a reinvestigation of stimulated Brillouin scattering. Limited electron thermal conduction has continued to be an important area of research. A detailed investigation of ion acoustic anomalous resistance and classical resistance is presented. And finally, we continued our efforts to understand self-generated magnetic fields in a collisionless plasma.

Stability and Absorption in Self-Consistent Plasma Profiles -- Our studies of the plasma instabilities induced when laser light is incident on a target plasma continued. In our last report (LA-6050-PR) we described comparisons of two-dimensional simulations of obliquely incident radiation on an inhomogeneous plasma with a much simpler stability calculation of the step-like equilibrium that was formed. The radiation was polarized in the plane of incidence and the effect of equilibrium flow on the stability of the excited plasma waves was shown to be negligible. We have now extended these calculations to include arbitrary polarization and a self-consistent flowing equilibrium.

Because of recent experimental target data obtained at LASL and at Limeil, which suggest that the absorption fraction at high laser intensities is low (10% at 10 μm and 30% at 1 μm), we have reinvestigated the possibility that stimulated Brillouin scattering over a wide angular range might be responsible for a large part of the scattered energy. To reasonably assess this possibility, we need more self-consistent theoretical calculations. Three approaches have been taken. First, the hybrid code described in LA-5739-PR has been used to study the long-term development of Brillouin scattering in one dimension. Second, the stability code described in LA-5919-PR, p. 100, has been improved by allowing for an arbitrary laser electric-field polarization and an arbitrary plasma-flow field. Thirdly, in an effort to bridge the gap between more detailed plasma codes and larger hydrodynamics codes, we have completed the development of a code, PHASE, which performs a two-dimensional time-dependent stability analysis on the time-varying equilibrium determined by a simple one-dimensional Eulerian hydrodynamics model including the effects of the laser ponderomotive force. We have also been able to derive an analytic model for the one-dimensional quasi-steady equilibrium produced by obliquely incident radiation polarized out of the plane of incidence.

To determine self-consistently the conditions for onset of stimulated Brillouin scattering and to obtain information on its saturation level with the first approach, we have simulated with the hybrid code the idealized situation of an isothermally expanding plasma with a high-intensity laser impinging on it. We find that if the plasma is not allowed to expand significantly before the laser reaches maximum power (corresponding to the absence of a prepulse), the onset of stimulated Brillouin scattering is delayed predominantly by velocity-gradient stabilization until a time t(ps) > 120 $T_e^{1/2} n_c/\lambda_0 P_1 r$, where P_1 is the laser intensity in units of 10^{14} W/cm^2; T_e is the electron temperature in keV; λ_0 is the wavelength in microns; and n/n_c is the square of the ratio of the local plasma frequency to the laser frequency. If $eE/m\, v_e > 1$, the subcritical plasma density is low, as is discussed below, and stimulated Brillouin scattering is small. If there is a prepulse, the extended corona can give rise to large scattering initially, followed by a period of reduced scattering before the prepulse plasma is blown away, at which point the scattering level slowly increases as in the case of no prepulse. This may explain some experimental differences between target interactions with and without a prepulse. The time dependence of the scattering for cases with and without a prepulse are shown in Fig. 70, illustrating the two effects just described. The instability is generally observed to be in a regime of convective instability due to the weak trapping of ions in the excited ion waves. It is then the increase in the thickness of the region of instability and in the gradient length that gives rise to an increase in the scattering level with time. In general, the scattering is not expected to be one-dimensional, but to be two-dimensional as described below. Qualitatively, however, the scattering in two dimensions should begin at about the same time. Filamentation may become more important at late time due to the ion heating.

Using the second approach, we performed a number of theoretical calculations on Brillouin scattering, in which an inhomogeneous flow in the underdense plasma is present. The stability calculations are as described in LA-5919-PR, p. 100, except that there is a component of the electric field out of the plane of incidence, i.e., there exists an electric field in the z-direction, E_z, and in the low-frequency ion equation there appears an inhomogeneous flow in the x-direction. The numerical procedure we developed finds conditions for which absolute instability will occur, as described below.

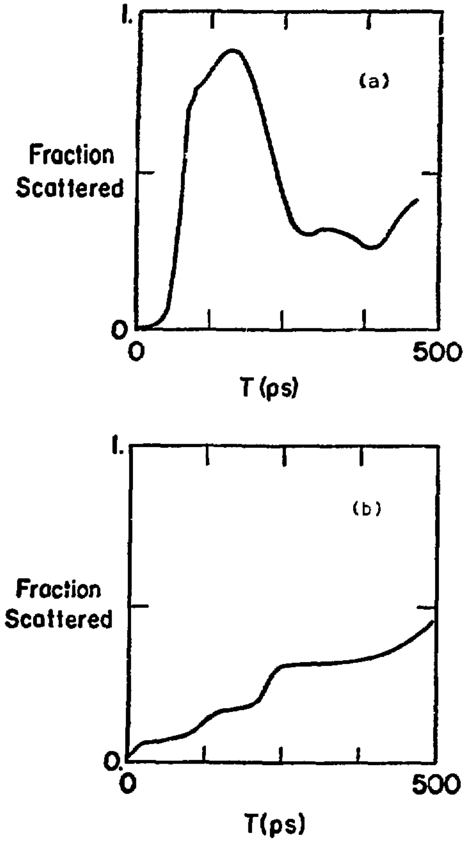

Fig. 70. Fraction of light scattered vs time (a) with and (b) without a prepulse for $eE_0/m\omega v_e = 0.5$.

Typical results for a case in which laser light is incident normal to a stationary underdense plasma density profile are shown in Fig. 71. The amplitude of the scattered light-wave's electric field and the amplitude of the ion density fluctuation are also shown. The peak ion-fluctuation amplitude occurs over the region where there is wave-number matching between the pump and the excited waves. Note that absolute instability exists, i.e., at any given point in space scattering will increase in time until nonlinearities saturate the instability. The growth rates increase slightly as the excited wave propagates more obliquely to the gradient and then rapidly increases near 90° to the gradient.

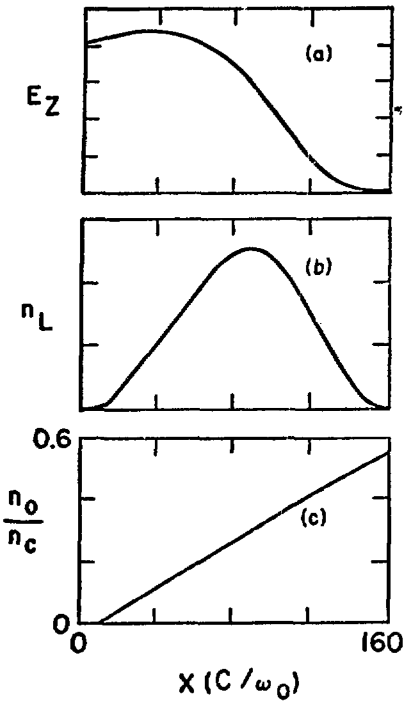

Fig. 71. Laser light impinging normal to a stationary underdense plasma; (a) unstable electric field in z-direction and (b) ion-density eigenfunctions for (c) indicated stationary density profile. The units of E_z and n_L are arbitrary. Density is in units of the critical density. The incident laser has a free-space electric field $eE_o/m_e\omega_o c = 0.05$, where definitions are standard. The electron thermal velocity, ion-to-electron mass ratio, and electron-to-ion temperature ratio are, respectively, $v_e/c = 0.1$, $M_i/m_e = 100$, and $T_e/T_i >> 1$. The unstable waves are taken to propagate along the density gradient.

The electric-field and ion wave density eigenfunctions for the same case as above (Fig. 71) are plotted in Fig. 72, except that we now allow the plasma to rarefact out with a zero-order flow given by $v_{xo}(x)/c_s = x/600-1.35$. In this equation $v_{xo}(x)$ is the inhomogeneous flow velocity and c_s is the ion acoustic velocity. Clearly, the eigenfunctions are narrower -- implying that gain occurs over a smaller region. Correspondingly, the flow has reduced both the real frequency and the growth rate by a large factor. A large number of calculations suggests stabilization consistent both with previous theoretical calculations and with the hybrid simulations described above.

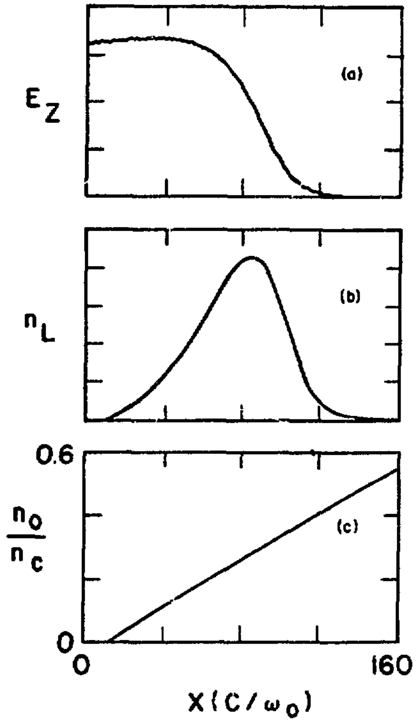

Fig. 72. Same parameters as in Fig. 71 except that there is a zero-order flow velocity $v_{xo} = c_s(\frac{x}{600} - 1.35)$, where $c_s \equiv (T_e/M_i)^{1/2}$.

The two-dimensional simulations reported in LA-5919-PR showed the formation of a step-like density profile near the critical density ($\omega = \omega_{pe}$) for obliquely incident radiation polarized in the plane of incidence. The same step-like equilibrium is observed to form for radiation polarized out of the plane of incidence. The basic idea of this quasi-steady equilibrium can be obtained by writing the combined fluid equations and wave equation in a frame moving with the density jump

$$\frac{dv}{d\xi} = \frac{-\frac{1}{4}\frac{d|\underset{\sim}{E}|^2}{d\xi}}{\underset{\sim}{v} - 1/\underset{\sim}{v}} \quad . \tag{1}$$

$$\frac{d^2\underset{\sim}{E}}{d\xi^2} + \left\{1 - \frac{N_2\underset{\sim}{v}_2}{\underset{\sim}{v}}\right\}\underset{\sim}{E} = 0 \; , \tag{2}$$

where $\underset{\sim}{E} = eE/\omega(T_e m_e)^{1/2}$, $\underset{\sim}{v} = v/(T_e/M_i)^{1/2}$, $\xi = x\omega\cos\theta/c$, and $\underset{\sim}{N}_2 = N_2/N_c\cos^2\theta$ is the normalized density on the upper density shelf. Equation (1) requires that $d|E|^2/d\xi = 0$ at $\underset{\sim}{v} = 1$ for continuity of $d\underset{\sim}{v}/d\xi$. We also require that $\underset{\sim}{E}$ go to zero in the overdense region. An integration of Eq. (1) and Eq. (2) yields an equation which is equivalent to that of a particle in a two-dimensional symmetric potential well. Because the force is always central, we have an additional constraint which determines a solution in terms of the electric field at the sonic point. The field at the sonic point, in turn, can be related by the WKB approximation to the field outside the plasma. The resulting equilibrium structure is shown in Fig. 73. For small $\underset{\sim}{E}$ we can show that the density jump and the velocity in the lower density region scale as $\underset{\sim}{E}_0$. For large $\underset{\sim}{E}_0$ we also find that the lower density velocity scales as $\underset{\sim}{E}_0$.

Agreement of this equilibrium with the time-dependent Eulerian hydrodynamics portion of PHASE is extremely good and, in cases where the ion wave dispersion is small, the agreement with the hybrid-code results is within the error of measurement.

With PHASE we have studied the stability of this self-consistent flowing equilibrium to perturbations with a finite wavenumber perpendicular both to the density gradient and to the polarization vector. We find that the equilibrium is most unstable to a mode with a density perturbation localized about the critical density but with transverse wavenumber $k_y c/\omega_0 < 1$. That is, the critical density surface begins to wrinkle at very long wavelengths, giving rise to stimulated scattered radiation with $k_y = (k_y \pm k_{y0})\, c/\omega$ where k_{y0} is the incident wavenumber perpendicular to the gradient. The growth rate appears to be proportional to the incident electric-field amplitude including the effects of the change of the equilibrium with incident power. Typical eigenfunctions of the instability are shown in Fig. 74. We also find that the flow has a substantial effect on the instability. If an initial density profile like that shown in Fig. 73 is chosen with no flow, we find much larger growth rates than in the actual equilibrium with flow. The eigenfunctions, nevertheless, are very similar in both cases.

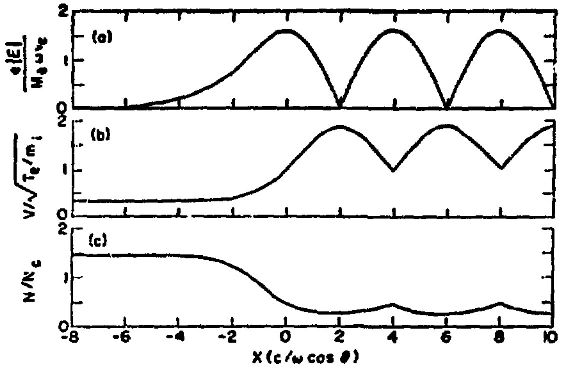

Fig. 73. Step-like equilibrium structure showing (a) $\underset{\sim}{E}$, (b) $\underset{\sim}{v}$, and (c) n as a function of ξ for E = 0.7.

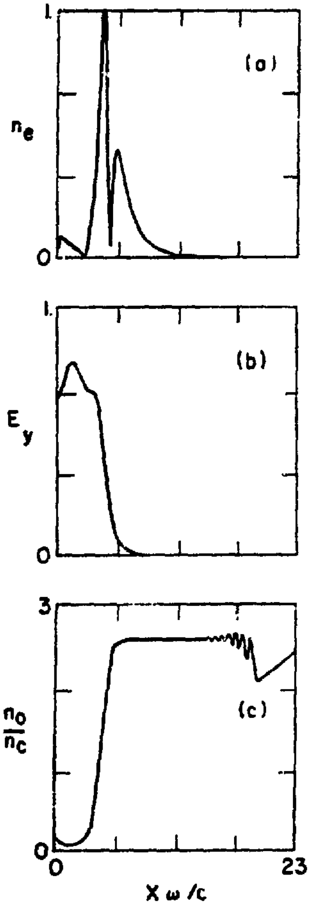

Fig. 74. Typical eigenfunctions of (a) perturbed density and (b) electric field for E_0 = 1.5, m_i/m_e = 100, and k_y c/ω = 0.1, with the equilibrium density profile (c) given for reference.

An important conclusion from these calculations is that the sharp interface that tends to be produced by the laser impinging on the plasma is quite unstable and may result in its complete breakup. Work is under way to determine the saturation mechanism of this instability.

We have continued to study the nonlinear evolution of parametric instabilities -- especially those that may provide anomalous absorption in laser-plasma interactions. Emphasis has been directed towards understanding the effects of coupling-saturation, a new nonlinear turbulence effect reported one year ago.[8] The "$2\omega_{pe}$" parametric decay instability of a photon into two Langmuir plasmons is known in linear theory to be an absolute instability localized in the density profile at one-quarter critical density. We have found that in a homogeneous plasma, coupling saturation greatly reduces the conversion of photons into plasmons compared with earlier estimates carried out in the U.S.S.R.[9] A similar study of the electron-ion decay instability for electrons hot compared to ions has again shown that coupling saturation is a strong effect limiting the conversion of photons into plasmons. Recently,[10] we have found a simplified description of coupling saturation which is universally applicable to parametric instabilities.

<u>Effects of Induced Ion Wave Turbulence on Transport</u> --Earlier work[11] has suggested that in certain high-power-laser interaction experiments there is a substantial reduction in thermal conductivity below not only the Spitzer value but also below the "classical flux-limit" value. One proposed mechanism for this reduction is the scattering of electrons by ion acoustic fluctuations excited by the relative streaming of the cold electron component and the ions.[12] Numerical simulations of this instability have been reported by many authors. However, the calculations suffer from being either one-dimensional or in a regime where the ratio of electron drift velocity, v_D, to electron thermal velocity, v_e, is not small. We have completed calculations in two dimensions for the instability in the weak or so-called ion acoustic regime for a variety of electron-to-ion mass ratios and a few electron-to-ion temperature ratios. Rather than include the hot electrons, which set up the cold return current, we specify the problem by requiring that the net electric current be constant and are doing it by adjusting the component of the electric field in the direction of the current. We then compute the resistivity from the size of the induced electric field.

We find that the instability saturates due to nonlinearities on the ion waves that are excited. That is, local regions of large ion density are set up, which, besides causing rapid small-angle scattering of the bulk of electrons, also cause large-angle scattering of a small number of ions. The local value of n/n_c is typically of order 1, while any given Fourier mode of the perturbed density rarely exceeds 0.1. The scattering of electrons by these fluctuations gives rise to a collision frequency substantially in agreement with calculations reported earlier (LA-5739-PR). The collision frequency as observed in the two-dimensional simulations is shown in Fig. 75 for the initial v_D/v_e =

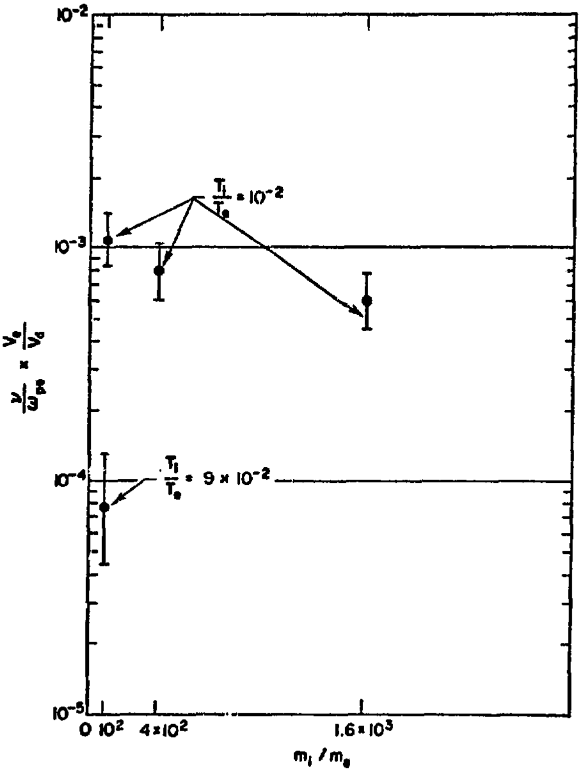

Fig. 75. Effective collision frequency vs ion-electron mass ratio for different initial electron vs ion temperature ratios.

0.5 and for a variety of electron-to-ion mass ratios and two different temperature ratios. Note that the effective collision frequency seems to scale with $(m_e/M_i)^{1/4}$ and with T_e/T_i. The former dependence has been reported before. Most significantly, however, and distinct from earlier simulations by other authors is the fact that the effective collision frequency is essentially constant after saturation over a considerable length of time. That is, the resistance appears to be a quasi-steady phenomenon. This is due, in part, at least, to the fact that the anomalous resistance is only one-tenth as large at these lower drift velocities, which correspondingly reduces the ohmic heating rate and substantially increases the time scale for change of the equilibrium.

Because the deceleration of hot electrons by the electric field dominates that caused by small-angle scattering, we can compute the reflection distance for hot electrons from the effective collision frequency, ν_{eff}, obtained in these simulations: $L \sim n_c v_h/n_h \nu_{eff}$, where v_h is both the characteristic thermal speed and the drift speed of the hot-electron component with density n_h assumed much less than the cold-background component n_c. Because the observed effective collision frequency is $\sim 0.001\ \omega_{pe}$, near densities of 10^{21} cm^{-3} (only for $n_h \sim n_c$ and $T_h < 10$ eV), the reflection distance would be as small as 1 to 3 μm, as seems to be required by hydrodynamic modeling.[11] Therefore, to inhibit the heat flow in a few microns by means of current-driven ion fluctuations, a compact election distribution and a cold return drift velocity as large as the electron thermal velocity are required.

Effect of Ambipolar Electric Field on Hot-Electron Transport -- Based on a cursory examination of the problem we reported earlier (LA-5739-PR), the ambipolar electric field plays an insignificant role in the transport of energetic electrons. In light of a recent paper,[13] we have reexamined the problem more carefully with the aid of a Monte Carlo electron-transport code. Although the effect of the electric field typically dominates the effect of direct scattering on hot electrons, results of this new investigation reaffirm our earlier conclusion that the hot electrons are only weakly affected by the ambipolar field when the collision frequencies are not significantly above classical.

In the Monte Carlo electron-transport code, energetic electrons are transported through a fixed planar background, which can have arbitrary spatial-density variation and Z composition. By making the quasi-neutrality approximation, $j_h = -j_c$, where j_h is the current due to energetic electrons and j_c is the neutralizing current of the cold background plasma, the ambipolar electric field E is given by $E = -j_h/\sigma_c$, where σ_c is the electrical conductivity of the background plasma. In this approximation the electric field scales as $j_h T_c^{3/2}/Z$, independent of the cold background density, where T_c is the background electron temperature. The energetic electrons lose energy primarily to the background electrons and heat them at the rate $dT_c/dt = \nu_{ee} n_h T_h/n_c$. The background electron heating rate scales as $n_h/T_h^{1/2}$, independent of the background density n_c. Here, ν_{ee} is the collision rate between the energetic and background electrons. Neglected in the model is joule heating of the background electrons, which dominates when $Z n_h T_h^{3/2} > n_c T_c^{3/2}$. Because $E \sim T_c^{3/2}$, the neglect of this additional heating implies that our model overestimates the magnitude of the ambipolar electric field.

Some results obtained by the Monte Carlo code can be anticipated by simple estimates. Assuming a constant electric field, $E = -j_h/\sigma_c$, where $j_h = e n_h (T_h/2\pi m_e)^{1/2}$ and m_e is the electron mass, the distance D over which the energetic electrons travel before they are turned around by the electric field can be calculated. The quantities n_h and T_h are not independent variables, but are related by $Q = n_h T_h (9T_h/8\pi m_e)^{1/2}$, where Q is the absorbed laser-light energy flux to be transported by the energetic electrons. Thus, $D = 2.9\ T_h^2 T_c^{3/2}/QZ$, for T in eV and Q in W/cm^2. For $T_c = 500$ eV, $T_h = 20$ keV, and an absorbed flux of $Q = 5 \times 10^{13}$ W/cm^2 corresponding to current CO_2 laser experiments, $D = 0.26/Z$ μm, which is much too large to explain the acceleration of fast ions in current experiments. For $Q = 5 \times 10^{15}$ W/cm^2 corresponding to current Nd:glass laser experiments, $D = 26/Z$ μm. It must be remembered that these values are underestimates of the turning distance D, due to the approximations used in the formula for D.

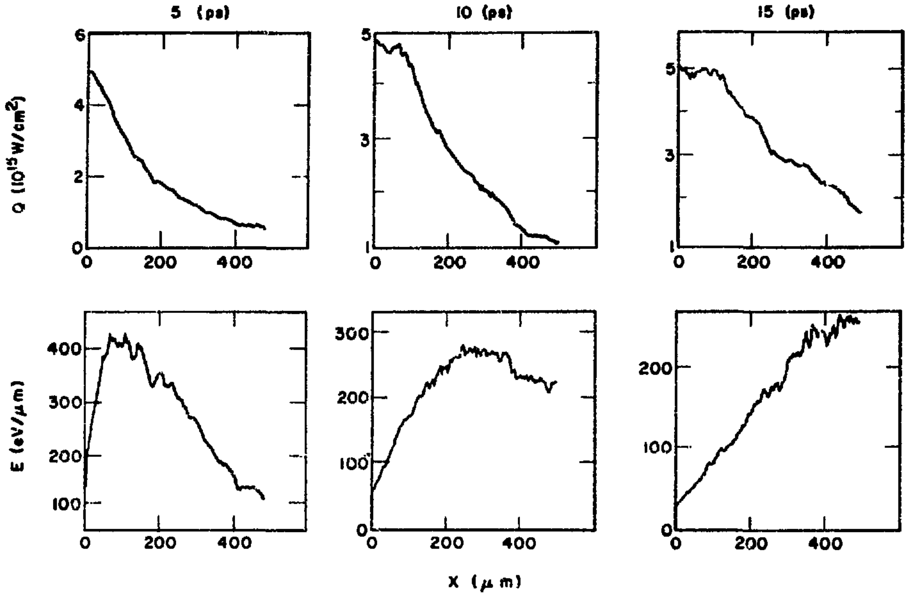

Fig. 76. For the three different times indicated, the top row shows the spatial distribution of heat flux carried by 20-keV isotropic Maxwellian distribution from the left boundary and transported through a uniform plasma with $Z = 6$ and density of 10^{21} cm^{-3}. The bottom row shows the corresponding spatial distribution of the ambipolar electric field.

As an example of the Monte Carlo results, we consider the case of a one-sided isotropic Maxwellian distribution with a temperature of 20 keV and carrying an energy flux of 5×10^{15} W/cm^2 from the left boundary transported through a uniform background density of 10^{21} cm^{-3} with $Z = 6$ and an initial temperature of 50 eV. Figure 76 shows for three different times the spatial variation of the heat flux transported by energetic electrons and the spatial variation of the ambipolar electric field. The top row of Fig. 76 shows that the thermal front propagates into the high-density materials at roughly 1/5th the energetic electron thermal speed, justifying the neglect of hydrodynamic motion in the model. The bottom row shows the decrease in electric-field magnitude due to the heating of the background.

Figure 77 compares the spatial variation of the heat flux and the spatial variation of the background temperature at 9 ps for two cases with and without the ambipolar electric field and with the heat flux carried by an initial 40-keV Maxwellian distribution of energetic electrons. Because of the ambipolar electric field, the heat flux at

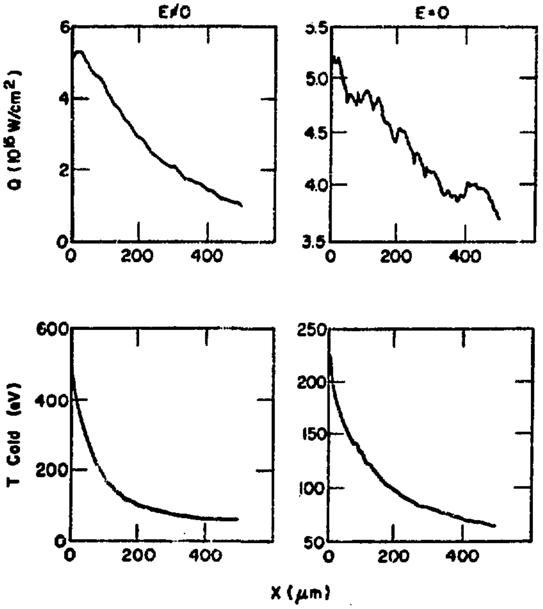

Fig. 77. Spatial distribution of heat flux carried by 40-keV isotropic Maxwellian distribution transported through a uniform plasma with $Z = 6$ and density of 10^{21} cm^{-3} is compared at 9 ps for two cases with and without the ambipolar electric field. The bottom row compares the spatial background temperature distribution for the two cases.

200 μm is only reduced by 33%. At 500 μm the heat flux is reduced to 1/3 of its former value. The temperature profile shows that the slowing-down of the energetic electrons by the electric field contributes to a greater coupling between the energetic electrons and the cold background, which causes an increased heating of the background.

Consequently, we see that the ambipolar electric field due to classical collisions between the background electrons and the ions has only an insignificant effect on the transport of energetic electrons for our current experiment at both 10 and 1 μm. Although the results shown in Figs. 76 and 77 assume that the background density is uniform, we have shown analytically that the results should be independent of the background density profile if joule heating were neglected. We have verified this conclusion with the Monte Carlo case by comparing the results obtained in a background density varying linearly from 10^{21} to 10^{22} cm^{-3} across the simulation box to that obtained with a uniform density of 10^{21} cm^{-3}. There is no significant difference between the two cases.

Self-Generated Magnetic Fields -- It has been pointed out that megagauss magnetic fields, B_z, can develop during resonance absorption.[14,15] The main effort has been to calculate the time rate of change of B_z through $\Delta x E_1$, where E_{1y} is essentially a slowly varying (on the time scale of the incident field) electric field arising from the time-averaged stress $<T_{xy}>$ induced by the beats of the high-frequency incident electric field. We find that these earlier calculations lead to the paradoxical result that $B_z = 0$ as long as the laser is on, in contradiction to computer simulations. We show that this result is a consequence of the fact that $<T_{xy}>$ includes contributions from wave-particle interactions P_{xy}, which must be included to allow finally for $E_{1y} = 0$ and therefore $B_z = 0$. These terms have been included by using a form of kinetic theory introduced to analyze electron heating and Landau damping in intense electric fields.[16] The kinetic theory has been generalized to allow for two-dimensional heating, and it has been shown that the theory rigorously satisfies momentum balance. We can evaluate from computer simulations the pressure contribution to $<T_{xy}>$ due to the electric fields. This direct information on two-dimensional heating may lead to a phenomenological representation of the hot-electron velocity tail associated with laser heating.

Plasma-simulation studies of self-generated magnetic fields in a collisionless plasma have continued. In LA-6050-PR we have shown that, if at some boundary in the plasma we had a finite spot where electrons are accelerated outwards as in resonant absorption, large self-generated magnetic fields develop in front of such a spot. More recently we have considered a finite region within a plasma in which some fractions of the electrons are stochastically heated. Typically, we have a density comparable to, or higher than, the density of the accelerated electrons on one side of the heating region and a decreasing density on the other side. When the density of the accelerated particles is comparable to the background density, large magnetic fields develop, which maximize at the accelerating region. As fewer particles are accelerated, the magnetic fields maximize in the lower density regions. At densities above the density of the accelerated electrons, the plasma is always able to shield out any magnetic fields that would develop from the current patterns of the hot electrons. The results thus far tell us that any self-generated magnetic fields in collisionless plasmas reside at critical or lower density.

REFERENCES

1. F. Skoberne, "Laser Program at LASL, July 1 - December 31, 1974," Los Alamos Scientific Laboratory report LA-5919-PR, p. 73.
2. R. J. Fries and E. H. Farnum, "Laser Target Fabrication - A Status Report," Los Alamos Scientific Laboratory report LA-5703-SR (30 April 1974). Rev. Feb. 1975, p. 12.
3. H. R. Maltrud, E. H. Farnum, and R. J. Fries, "An Acoustic Measuring System for Determining the Breaking Strength of Microballoons," Bull. Am. Phys. Soc. 20, 1247 (1975); also, F. Skoberne, "Laser Program at LASL, January 1 - June 30, 1975," Los Alamos Scientific Laboratory report LA-6050-PR.

4. R. R. Stone, D. W. Gregg, and P. C. Souers, "Nondestructive Inspection of Transparent Microtargets for Laser Fusion," J. Appl. Phys. 46, 2693 (1975).

5. B. W. Weinstein, "White Light Interferometric Measurements of the Wall Thickness of Hollow Glass Microspheres," Lawrence Livermore Laboratory report UCRL 76968 (June 1975).

6. T. M. Henderson, KMS Fusion, Ann Arbor, MI, private communication (March 1975).

7. F. Skoberne, "Laser Program at LASL, January 1 - June 30, 1975," Los Alamos Scientific Laboratory report LA-6050-PR (January 1976).

8. D. F. Dubois and B. Bezzerides, submitted for publication.

9. V. V. Pustovalov, V. P. Silin, and V. T. Tikhonchuk, "Nonlinear Conversion of Radiation Into Plasma Waves," Sov. Phys. JETP, 938 (1974).

10. B. Bezzerides and D. F. DuBois, submitted for publication.

11. R. C. Malone, R. L. McCrory, and R. L. Morse, "Indications of Strongly Flux-Limited Electron Thermal Conduction in Laser-Target Experiments," Phys. Rev. Lett. 34, 721 (1975).

12. D. W. Forslund, "Instabilities Associated with Heat Conduction in the Solar Wind and Their Consequences," J. of Geophys. Res. 75, 17 (1970).

13. E. J. Valeo and I. B. Bernstein, "Fast-Ion Generation in Laser-Plasma Interactions," 5th Annual Symposium on Anomalous Absorption (1975).

14. J. A. Stamper and D. A. Tidman, "Magnetic Field Generation Due to Radiation Pressure in a Laser-Produced Plasma," Phys. Fluids 16, 2024 (1973).

15. J. J. Thompson, C. E. Max, and K. Estabrook, "Magnetic Fields Due to Resonance Absorption of Laser Light," Lawrence Livermore Laboratory report UCRL 766690.

16. B. Bezzerides and D. F. Dubois, "Electron Heating and Landau Damping in Intense Localized Electric Fields," Phys. Rev. Lett. 34, 1381 (1975).

17. W. A. Beyer, R. J. Ryan, and F. T. Adler, "Efficient Illumination of a Sphere," Los Alamos Scientific Laboratory report LA-5318 (September 1973).

18. S. A. Goldstein, R. C. Davidson, J. G. Siambis, and Roswell Lee, "Focused-Flow Model of Relativistic Diodes," Phys. Rev. Lett. 33, 1471 (1974).

-) 741

V. LASER AND TARGET DIAGNOSTICS DEVELOPMENT

The tiny volume and brief duration involved in the laser-fusion process create needs for new diagnostic techniques having spatial and temporal resolutions in the submicrometer and 1- to 100-ps regime, respectively. These needs are being met with a vigorous program of diagnostics in such areas as laser calorimetry, charged-particle and neutron detection, x-ray spectrometry, and subnanosecond streak-camera development.

INTRODUCTION

Improving the state of the art in laser and target diagnostics is a critical pacing item for the laser-fusion program. Diagnostics equipment and techniques are now only marginally adequate for understanding laser-target interactions and energy-coupling in laser-produced plasmas. Calorimetry and the spatial and temporal imaging of subkilovolt x rays are a major part of this effort. Encouraging developments are in progress, particularly with respect to x-ray streak cameras.

PRESENT AND FUTURE COMPUTER CAPABILITY FOR DATA RECORDING AND PROCESSING

The laser-fusion program has reached the point where the acquisition and analysis of the data after a laser-target test is a bottleneck. Although the data are recorded in microseconds, it requires man-hours to digitize, tabulate, graphically display, and parameterize the information contained in the data. A computer-controlled data-acquisition system provides a highly effective method to expand and supplement present data-acquisition and reduction methods. Such a system also provides new possibilities in data acquisition and reduction if the amount of data increases, without the need to increase the manpower in direct proportion to the amount of new data.

A NOVA-840 minicomputer, used to control the operation of the Nd:glass laser, has been modified both at the hardware and software level to test the feasibility of computer-based data acquisition and reduction. To accommodate the size and number of data-analysis programs now in use, we have expanded the capacity of the NOVA computer to 56k words of memory. CAMAC crates have been installed in the glass-laser target room to house modules that digitize signals from target-chamber detectors and transmit the signals to the computer. One crate contains ten channels of 10-MHz transient-signal digitizers and 12 channels of peak-sensing analog-to-digital converters. A second crate will hold 50-MHz transient-signal digitizers. This expansion has enhanced data acquisition, but the requirement that the computer control the laser and the inherent growth limitation of the NOVA in its second role emphasize the need to establish a computer capability dedicated exclusively to data acquisition (from several remote sites) and data reduction capable of future growth.

The primary method of interfacing the computer with the diagnostic instruments is through the CAMAC system. Many companies supply digital and analog signal interfaces for use with their minicomputer systems. Such units are often not sufficiently fast (analog-to-digital conversion rates of > 40 kHz) and require long signal lines as well as extensive signal preconditioning for laser-type applications. Our CAMAC system was designed to handle fast nuclear signals remotely and to provide a standardized method of interfacing these signals with the minicomputer. CAMAC systems are well suited to the type of signals produced by laser-target diagnostics, and are inherently more flexible than the single-computer self-integrated systems on the market.

Calorimeters are used extensively as a laser and plasma diagnostic tool. The relative shortness of a laser-related signal results in a calorimeter signal that is essentially an impulse response with an exponential decay time that may range up to minutes. The maximum height of the transient curve yields the energy deposited. Originally, we used a pen-recorder trace of the calorimeter signal to obtain the height of the leading edge of the transient record; but faster calorimeters require faster recorders and in the extreme case of microsecond signals, we use oscilloscopes. The recording hardware for a single calorimeter may cost up to $5000.00. An array of ~ 50 calorimeters might be needed which would cost more than ~ $250 000 and would require extensive manual analysis. In contrast, CAMAC peak-holding and digitizing units can produce the same data from the leading-edge information or from a repeating digitization of the exponential decay curve with ~ $6500 of CAMAC hardware to replace the recorders in less than 5 min of computer time.

X-ray and charged-reaction product monitors are used as diagnostic tools to provide temperature and reaction yield information from laser/target interactions. These data are usually recorded by means of fast oscilloscopes costing $5000, and the data, in the form of Polaroid oscillographs, must be reduced manually after being recorded and processed. Again, CAMAC units (at $125 per channel) can substantially reduce both hardware cost and the data-processing time. Similar cost and time savings can be attained in the recording and processing of ion currents.

For signals with risetimes of ~ 300 ps, fast-digitizing oscilloscopes exist that have CAMAC interfacing units. Although these units cost $10 000, the reduction in data-analysis time may justify the investment.

For certain types of data, commercially available digitizers are either not fast enough or do not offer sufficient spatial resolution to allow direct connection to a computer system. These diagnostic devices generally produce film recordings that must be digitized before computer reduction is possible. The film recording may be scanned on a microdensitometer whose normal form of output is a pen recording. We have connected a densitometer directly to the NOVA computer via CAMAC, and the resulting savings in time has expedited the reduction of film-recorded data.

ULTRAFAST DIAGNOSTICS

Proximity-Focused Streak Tube

Our proximity-focused streak tube,[1] employing a microchannel plate for transverse photoelectron velocity selection, has been built in two basic configurations. The design shown in Fig. 78 uses a transmission-type photocathode structure. X-rays enter 10° off the axis of symmetry to minimize direct feedthrough to the tube's phosphor, because it has been shown that microchannel plates make excellent collimators of x rays as well as electrons.[2] X rays enter the tube by passing first through a thin beryllium vacuum window and then through a thin beryllium support foil for the gold photocathode. Photoelectrons generated by the photocathode fall through an intense electric field that is generated when a 10-kV pulse momentarily applies an overvoltage to the photocathode channel - plate gap. The electrons then pass through a long microchannel plate into a field-free region where deflection

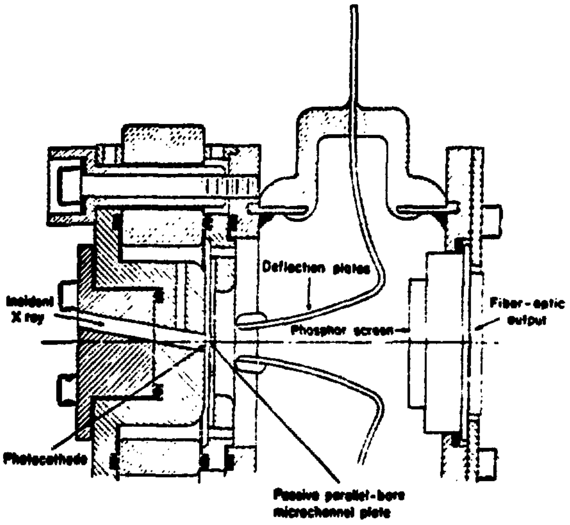

Fig. 78. Sectional view of transmission photocathode proximity-focused x-ray streak tube.

plates apply the streaking field. The beam is registered on a conventional phosphor cup with a fiber-optic output. The overall distance from photocathode to phosphor is 3 cm, to minimize longitudinal velocity dispersion through the tube. This direct-illumination geometry is similar to that we will use for visible streak-tube application. The prototype is shown in Fig. 79 which indicates the scale of the device. We built the prototypes for both designs from glass to enable the study of tube function. Production versions built by industry will be smaller and permanently sealed.

Oblique-incidence illumination is used in the second configuration. This design provides an "infinitely thick" photocathode, thereby enabling the tube to respond to higher photon energies without photocathode modification. Because the device has very low capacitance, its limit can probably be extended to subpicosecond resolution, assuming a 25-eV photoelectron spread. Should this spread be 8 eV, as has been suggested,[3] we are already close to this resolution. It will be of interest to compare photocathode efficiencies of the two geometries. Our second design uses a strip microchannel plate (MCP) for both velocity selection and as the knife-edge collimator of the streak tube, thereby simplifying optics. Final versions will probably draw upon both designs.

Fig. 79. Prototype proximity-focused x-ray streak tube.

Success of this x-ray streak tube rests on the deflection efficiency of the streak electrodes and on the ability of the power supply to drive them. We have studied the electrode design extensively by using a plasma-simulation code.[4] Recent results obtained with the laser-triggered solid dielectric spark gap, discussed elsewhere in this report, have shown sufficient risetime to attain the specifications listed in Table XVI. The first prototype has been installed in the glass-laser chamber and has produced an x-ray image from the irradiation of a 150-μm nickel ball by two 9-J beams. Because we obtained this image without a follow-on image intensifier of 10^5 to 10^6 gain, we are optimistic about the efficiency of the system.

Figure 80 shows a deflected image for our proximity-focused tube with a 100-μm slit irradiated by an x-ray pulse from a 150-μm-diam nickel ball iluminated with a 1-J Nd:glass laser pulse. For this test, a prelude to actual streaking, we added an image intensifier of 100-fold gain. The MCP used in these tests has an aspect ratio of only 90, primarily because it had been used in previous measurements, and its properties are well documented. If the MCP acts as a nearly perfect geometric collimator, its image of the slit should be ~ 0.3 mm wide. Without transverse-velocity selection, assuming 8-eV photoelectron spread, the image should be ~ 1.7 mm wide. The image width is nearly that predicted theoretically and scattering is unimportant. Note that the sensitivity of the tube is impressive, because this image was formed by a rather weak laser shot. The image is curved in this extremely off-centered position because the width of the entrance slit exceeds the width of the deflection plates, which leads to fringing effects.

Future tubes will use MCP aspect ratios of 400 and will yield correspondingly better resolution. Thus, we feel that the theoretical predictions for this device will be exceeded. We are presently measuring actual temporal resolutions -- a difficult task for a device of this speed. In November 1975 ERDA awarded a contract for the production of several visible and x-ray versions of this device to I.T.T., Ft. Wayne IN. This contract should lead to production versions of the tube.

TABLE XVI

PROXIMITY-FOCUSED STREAK-TUBE SPECIFICATIONS

Tube	
Length	3 cm (photocathode to phosphor)
Diameter	2 cm
Acceleration voltage	10 kV (photocathode to MCP)
Photocathode extraction field	400 kV/cm (pulsed)
Photocathode material	100- to 200-Å gold
Phosphor output	P-20
Voltage MCP	0
Aspect ratio MCP	300:1
Streak rate	6 ps/mm (150 ps/25 mm)
Resolution	10 ℓp/mm (static and dynamic)
Initial spatial resolution	10 μm referenced to target
Initial temporal resolution	< 2 ps (assuming 25 eV P.E. spread)
Design temporal resolution	0.9 ps
Record length	18 mm prototype, 25 mm production
Trigger	
Laser-triggered solid dielectric	
Jitter	< 70 ps
Risetime	oscilloscope-limited
Delay	2.3 ns
Energy required	1 to 3 mJ

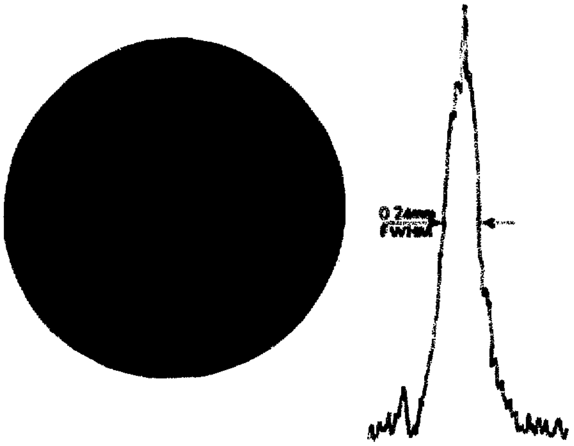

Fig. 80. Test image from prototype streak tube obtained with x-rays from a 150-μm-diam nickel ball irradiated with a 1-J pulse from a Nd:glass laser.

Laser-Initiated Krytron-Switched Blumlein Structure for Pulse Selection

A new technique has been developed which permits us to reliably select a single pulse from a modelocked glass-laser oscillator.[4] This technique replaces the laser-triggered spark gap previously used with a krytron-switched Blumlein pulse-forming network driving a dual-crystal longitudinal-mode KD*P Pockels cell.

Solid Dielectric Laser-Triggered Spark Gap

We have tested a spark gap using a thin sheet of dielectric material in the interelectrode space. The gap, shown in Fig. 81, is triggered by focusing a ≤ 10-mJ laser pulse from a glass laser through a 1-mm-diam hole in one of the electrodes onto the interelectrode dielectric sheet.

By using 25-μm-thick Mylar for the dielectric stressed to 10 kV, the shot-to-shot jitter has been measured to be less than ± 70 ps. The delay from trigger-beam arrival at the gap to electrical-pulse

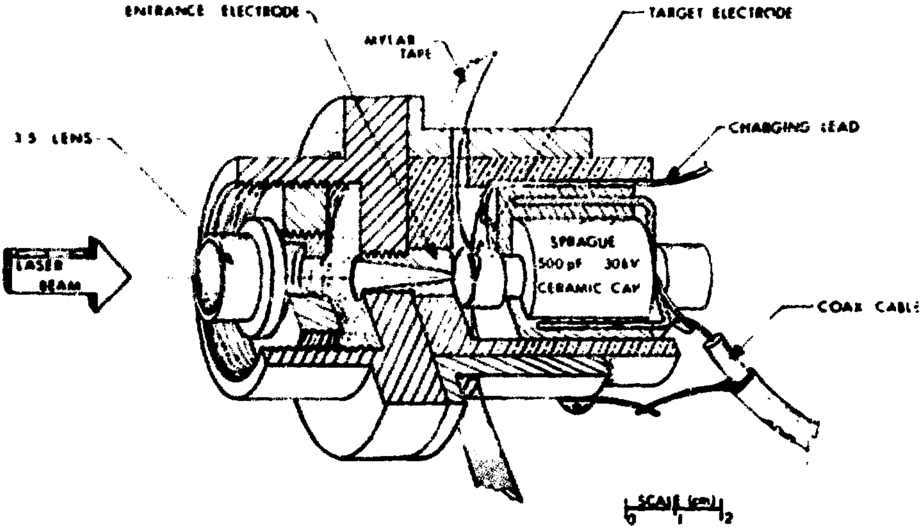

Fig. [illegible]. Sectional view of solid dielectric laser-triggered spark gap.

initiation was less than the width of the laser pulse used (50 ps).

Streak-Tube Pulser

A Blumlein pulse-forming network (PFN) and a high-purity alumina-filled delay line have been constructed which both use the dielectric gap described above. The spark gap is an integral part of the pulse networks and is initiated by a focused laser beam that ionizes the Mylar between the molybdenum electrodes.

The Blumlein PFN applies a -10-kV, 3-ns-wide pulse to the photocathode of the streak tube. The alumina-filled transmission line delays the -10-kV subnanosecond streak pulse, which is developed when the gap is initiated, and ensures that the pulses are applied in proper phase to the streak tube. We have tested the pulser successfully in the target-chamber vacuum system where the streak tube will operate.

Calorimeters

Calorimeters with a minimum of mass using chromel-constantan thermocouple sensing elements for ion calorimetry of laser-produced plasmas have been described previously (LA-6050-PR). Many of these calorimeters have been put into use for ion as well as light calorimetry in both 1.06- and 10.6-μm laser experiments. The calorimeters have been calibrated and their characteristics studied by using a pulsed CO_2 laser beam. As presently used, the calorimeters provide a signal of ~ 0.4 μV/μJ incident. The calibration varies remarkably little from detector to detector. Because noise levels in laser experiments with these devices are ~ 1 μV, useful signals are obtained with energies of only a few microjoules incident on the calorimeters.

Because of the success of these devices and because of their versatility, we are investigating methods of further decreasing the detector mass (thus increasing the μV/μJ sensitivity) and are planning to construct thermopile arrays of similar detectors. Subkilovolt x-ray calorimetry would, for example, profit from such an array. In addition, electronics have been developed and tested successfully, which allow calorimeter signals to be digitized and stored automatically in our NOVA computer. This eliminates the costly and time-consuming use of strip-chart recorders.

Ion-Current Collectors

Because of their small size and simple construction, ion-current collectors have become a standard diagnostic device for laser-produced plasmas.

A design we use extensively is constructed from a standard feedthrough with a collector disk on the center conductor. The ion energy per unit charge is typically > 100 keV in our 100-J, 1-ns CO_2 experiments. At these high ion energies, many secondary electrons are produced for each incident ion, which amplifies the ion signal. To measure the number of ions emanating from the target plasma, we used a charge collector with two grids. The outer grid was at ground potential, whereas the inner grid (that nearest the collector) was at a high negative potential. Electrons flowing along with the ions are rejected if the mesh spacing is less than the Debye length of the plasma. In addition, the negative grid reflects electrons from the collector back to the collector so that only ion current is measured. Two identical collectors were used; the inner grid of one was at -300 V and the corresponding grid of the other was at ground. The current difference provided an estimate of γ, the number of secondary electrons per incident ion. For a brass collector, the value of γ for carbon ions as a function of energy is plotted in Fig. 82. The solid curve is an estimate of γ extrapolated from measurements on elements of lower mass number.

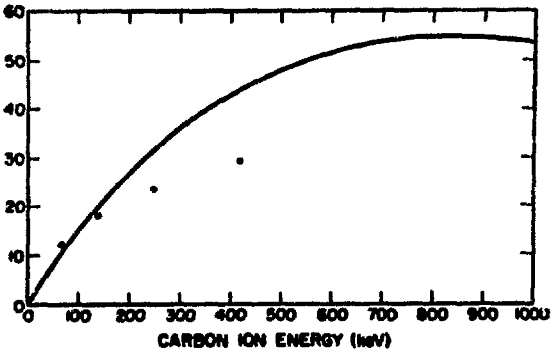

Fig. 82. Secondary electrons per incident ion, γ, as a function of carbon ion energy. Solid curve is an estimate based upon measurements on elements of lower mass number.

X-Ray Diagnostics

We have initiated film calibrations at subkilovolt x-ray energies. Results for three films at an x-ray energy of 525 eV (oxygen K-radiation) are shown in Fig. 83. The film we use for the x-ray pinhole camera and for the lower energy x-ray Bragg spectrometer, Kodak RAR 2490, is 3.6 times less sensitive at 0.53 keV than at 1.0 keV at a diffuse optical density of 0.5. If this film lacks the sensitivity for measurements at subkilovolt energies, we will use Kodak 101-01, which is ten times more sensitive but much more difficult to handle and process.

Our cooperation with the Field-Testing Division at LASL has been expanded. Joint studies of film calibration, diffraction crystals, ultrafast scintillators, and other x-ray problems (with emphasis on the subkilovolt range) are being pursued.

X-ray pinhole images and preliminary spatially resolved line spectra, collected by means of a crystal spectrograph with an entrance slit, indicate that spectra such as those discussed in the target-experiments section must be interpreted with caution. Microballoon spectra consist of helium-like and hydrogen-like silicon lines, which apparently originate from different portions of the target (and presumably also have a strong temporal dependence) -- the hydrogen-like from a much smaller region than the helium-like as shown in Fig. 84. Thus, analyses based upon line-intensity ratios to determine temperature or density must be suspect.

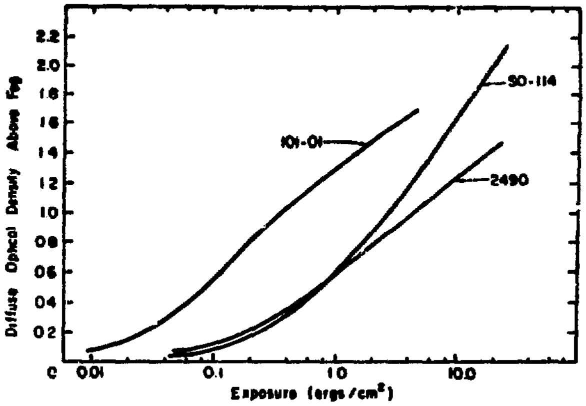

Fig. 83. X-ray film density as a function of exposure for oxygen K radiation. Characteristic curves for three films at 525 eV are shown.

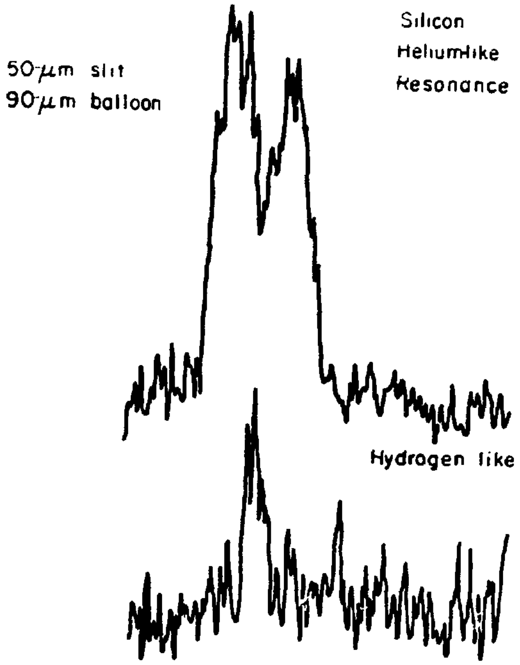

Fig. 84. Spatially resolved helium-like and hydrogen-like lines of silicon from a glass microballoon obtained with a slit oriented at right angles to the KAP diffracting crystal.

Our "rectangular"-crystal spectrographs have been used for a variety of energy regions by changing both the source position and the dispersive crystals. Nevertheless, an instrument with a new geometry, a 40° isosceles triangle with the crystal on the hypotenuse, has been put into use. The advantages of the triangle over the rectangle are easier use of the crystals for wavelengths approaching the crystal lattice spacing and a more nearly linear dispersion on the film. With an EDDT crystal and a convenient source position the hydrogen-like Lyman alpha line of silicon falls in the middle of the recording film with the triangle, whereas with the rectangle precise alignment is required to record this line at all.

We are conducting an in-depth study of soft x-ray reflection devices of various forms. Designs are evolving for a variety of diagnostics ranging from broad-band x-ray calorimetry to a high-resolution Wolter-type grazing-incidence microscope.

REFERENCES

1. A. Lieber, H. Sutphin, R. Benjamin, S. Gitomer, and W. Hall, "Proximity-Focused Ultra-Fast Streak Tube," Bull. Am. Phys. Soc. 20, 1286 (1975).
2. A. Lieber, R. Benjamin, P. Lyons, and C. Webb, "Microchannel Plate as a Parallel-Bore Collimator for Soft X-Ray Imaging," Nucl. Instrum. & Meth. 127, 553 (1975).
3. L. Coleman and D. Attwood, "Time Resolved X-Ray Spectral and Spatial Studies in Laser-Fusion Experiments," Bull. Am. Phys. Soc. 20, 1267 (1975).
4. R. Hyer, H. Stuphin, and K. Winn, "Laser-Initiated Krytron-Switched Blumlein Structure for Pulse Selection," Rev. Sci. Instrum. 46, 1333 (1975).

VI. APPLICATIONS OF LASER FUSION -- FEASIBILTY AND SYSTEMS STUDIES

Our feasibility and systems studies are being performed to analyze the technical feasibility and economic incentives of various commercial and military applications of laser fusion. The direct production of electricity in central-station power plants is of major concern. The general objectives of these studies are: the conceptualization and preliminary engineering assessment of laser-fusion reactors and generating stations; the development of parametric computer models of power-plant subsystems for economic and technology tradeoff and comparison studies; and the identification of problems requiring long-term development. Alternative commercial applications of laser fusion to produce fuel for fission reactors and as sources of high-temperature process heat are also being investigated.

POWER-PLANT ENGINEERING ANALYSES

Magnetically Protected Reactor Concept

The computer program for simulation of fusion-pellet microexplosions in magnetic fields[1] is one of the principal investigative tools for use in engineering feasibility studies of the magnetically protected laser-fusion reactor (MPLFR) concept. We are expanding the capabilities of this code to permit detailed design of the solenoids and energy sinks. This increased capability will permit the following:

- The modeling of energy-sink regions with generalized conical shapes.
- The modeling of solenoids of arbitrary design, exterior to the blanket region.
- The inclusion of as many as 100 types of charged particles in the expanding plasma.
- The determination of both the angle of incidence and the energy of each simulation particle that strikes the cavity wall or energy sinks and the maintenance of records of these events.

Supplementary computer programs are being developed to calculate the rate of spall, erosion, and evaporation of the energy-sink surfaces due to energy deposition by the charged particles from fusion-pellet microexplosions.

The freedom to model energy sinks and solenoid designs will permit us to include fringing magnetic fields and tailored energy-sink designs to obtain minimal erosion of the energy-sink surfaces. We also expect to determine tradeoff relationships between capital investment and component lifetimes. The large number of types of charged particles that can be considered in the expanding plasma will permit calculations for structured fusion pellets.

Enhancement of Tritium Breeding Ratios

First-generation laser-fusion reactors (LFRs) will utilize the deuterium-tritium fuel cycle, and tritium must be produced, as required,by neutron reactions with lithium. Tritium breeding ratios greater than unity are easily obtained in conceptual LFRs with natural lithium in the blanket regions; however, it may be advantageous to restrict tritium breeding to as few reactors as possible in a multireactor generating station or energy park, permitting alternative designs of the remaining reactors that may not be compatible with the inclusion of lithium blankets around the reactor cavities. Examples of such alternative designs are high-temperature gas-cooled reactors and reactors designed to produce process heat from radiating sources.

We have investigated how the tritium breeding ratio in the wetted-wall reactor concept is affected if different structural materials are used, if beryllium is used as a neutron-moderating and -multiplying material, and if the lithium is enriched in the ^{6}Li isotope. The reactor model used in the study is summarized in Table XVII.

Calculated tritium breeding ratios for the basic reactor model including natural lithium (7.56 at.% ^{6}Li) are given in Table XVIII for several potential structural materials.

We have performed calculations to determine the effects of including a region consisting of 90 vol% beryllium and 10 vol% lithium in the outer lithium coolant region of the basic reactor model. For a reactor with niobium structure containing natural lithium we found that the breeding ratio increases monotonically from 1.40 to 1.87 as the thickness of the beryllium region is increased from 10 to 50 cm.

The effects of enriching the lithium to 45 at.% ^{6}Li outside a 30-cm-thick beryllium region in the outer lithium coolant region of the basic reactor model were also determined. At the optimum position of the beryllium region, the breeding ratio increased from 1.78 to 1.83 for a reactor with niobium structure. These calculations were repeated for reactors with molybdenum or vanadium -- 20 wt% titanium structural material. The breeding ratios for these two cases are 1.76 and 2.03, respectively.

Although optimum reactor designs, corresponding to maximum tritium breeding ratios, were not determined in this study, our results indicate that adequate tritium breeding ratios can probably be obtained to permit freeing half the LFRs in a large generating station or energy park from the necessity of breeding tritium.

TABLE XVII

WETTED-WALL REACTOR CONCEPT

Region	Outside radius (m)
Cavity	1.70
Wetted wall	1.7025
Li plenum	1.7075
Structural wall[a]	1.7426
Li coolant	2.4426
Structural wall	2.4761
Li coolant	2.6761
Outer wall	2.6982

---

[a] Interior structural walls are 90 vol% structure and 10% lithium.

Radiation Damage to Optical Surfaces in Laser-Fusion Generating Stations

Radiation damage to the mirrors that direct and focus the laser beams into reactor cavities is one of the most serious potential radiation-damage problems that LFR designers have to contend with. These mirrors may be exposed to high-energy neutrons, x rays, gamma rays, energetic charged particles, and, possibly, to cavity materials such as lithium vapor.

We have estimated the surface-temperature increases due to energy deposition by x rays on typical metallic mirrors and have found that for the conceptual designs now being evaluated, surface damage to the mirrors will probably not occur from this source if the mirrors are cooled. Satisfactory engineering designs can apparently also be devised to accommodate energy desposition by gamma rays. The MPLFR concept provides protection of the mirrors from charged particles. However, no feasible method seems to exist to protect these mirrors from neutron irradiation.

The effects of neutron irradiation on mirror surfaces are unknown. Atomic dislocations will occur and transmutation products will be formed. Among the transmutation products that may result in damage are gases such as helium.

We are calculating the rates at which atomic dislocations and transmutation products will form

TABLE XVIII

DEPENDENCE OF TRITIUM BREEDING RATIO ON STRUCTURAL MATERIAL

Structural Material	Breeding Ratio
Niobium	1.31
Molybdenum	1.40
Vanadium - 20 wt% titanium	1.47
Sintered aluminum product	1.33
Stainless steel	1.33

in typical metallic mirrors for various beam-transport geometries in conceptual LFRs. The results should enable us to estimate the magnitude of the problem. Calculations are being made for three-dimensional models of reactor concepts by using multigroup Monte Carlo codes. Metallic detectors are placed at various positions in the beam-transport tubes to evaluate the effects of different mirror placements.

Electric Generating-Station Concepts

We have previously performed detailed studies of electric generating-station concepts based on the wetted-wall reactor design.[2] Because of potentially higher microexplosion repetition rates in the magnetically protected reactor design, the power level of magnetically protected reactors is projected to be about ten times greater than that of wetted-wall reactors and will result in significantly different generating-station concepts.

We have completed the specification of components for a generating-station concept based on the MPLFR and CO_2 laser technology. Four reactors with a thermal power output of ~ 1250 MW each are included in the station (compared with the wetted-wall-reactor generating-station concept which includes 20 reactors with a thermal power output of ~150 MW each). The major differences between this concept and the one based on the wetted-wall-reactor design are differences in the degree of modularization which lead to differences in the optimum number of redundant components and the potential advantages of centralizing components.

The incentive to centralize the laser system with laser beams directed from one set of laser power amplifiers sequentially to respective reactors is diminished as the number of reactors in the plant decreases. Two potentially attractive arrangements of laser-system components have emerged from our economic studies of generating stations that utilize MPLFRs. For the first case, each reactor is provided with a complete laser power-amplifier system, but the pulse-forming networks (including capacitive energy storage) for the lasers are centralized. Redundant capacitors are provided to prevent plant shutdown from failure of these components; however, redundant laser power amplifiers are not included and individual reactors would have to be shut down if any of the laser power amplifiers failed. For the second case, both the laser power amplifiers and the pulse-forming networks are centralized, and 100% redundancy of main laser power amplifiers is included. For this case a rotating mirror is required to direct laser beams to successive reactor cavities. We estimate that the total costs of generating electric power will be ~10% less for the second plant concept than for the first, and the generating station that we have studied in detail is based on this approach. Layouts of major plant components are shown in Figs. 85-87.

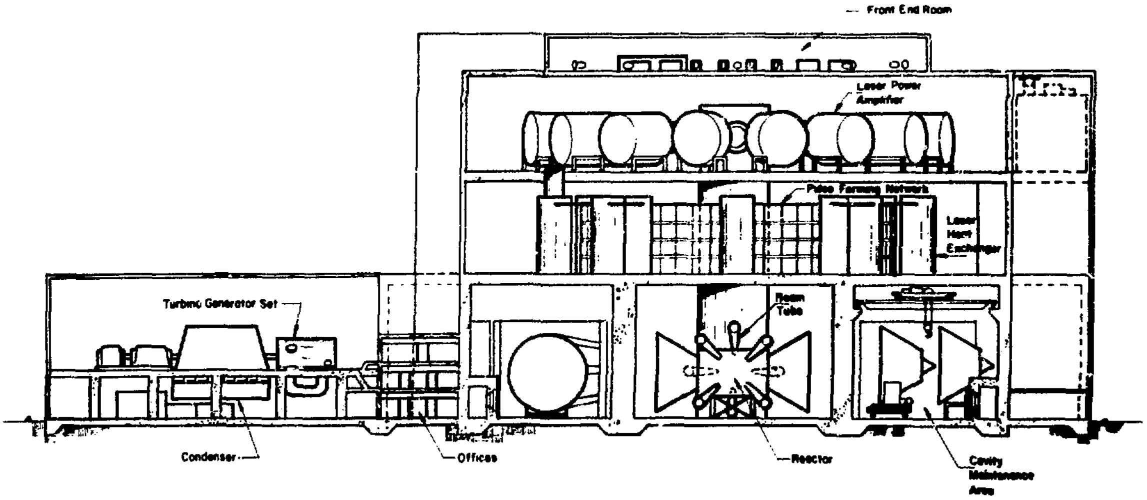

Fig. 85. Electric generating station utilizing magnetically protected laser-fusion reactors and CO_2 laser technology, cross-section elevation as indicated in Figs. 86 and 87.

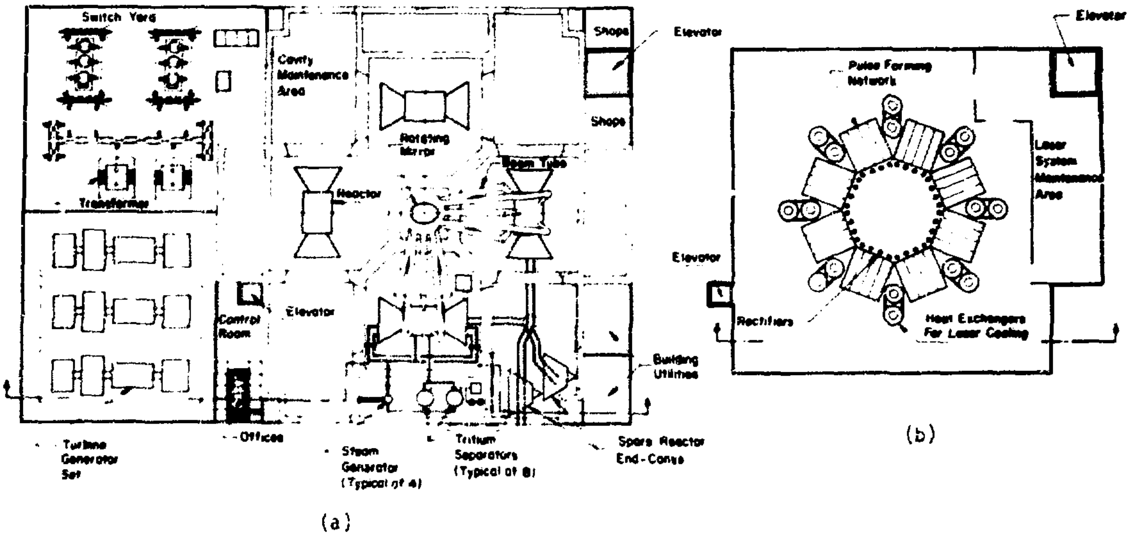

Fig. 86. Electric generating station utilizing magnetically protected laser-fusion reactors: (a) first-level, reactor and energy-conversion systems area, plan view; (b) second-level, power-supply room, plan view.

The reactors, heat exchangers, lithium-tritium separators, control room, and energy-conversion equipment are located on the first level of the station. Hot-cell maintenance areas for periodic servicing of the MPLFR energy-sink cones and other radioactive components are also on this level. Tracks are provided for movement of energy-sink cones between reactors and maintenance areas. Single-loop lithium heat-transfer systems are used between the reactors and the steam generators, and semipermeable membrane lithium-tritium separators are included in the lithium loops. Separate heat-exchanger and lithium-tritium separator systems are provided for each reactor.

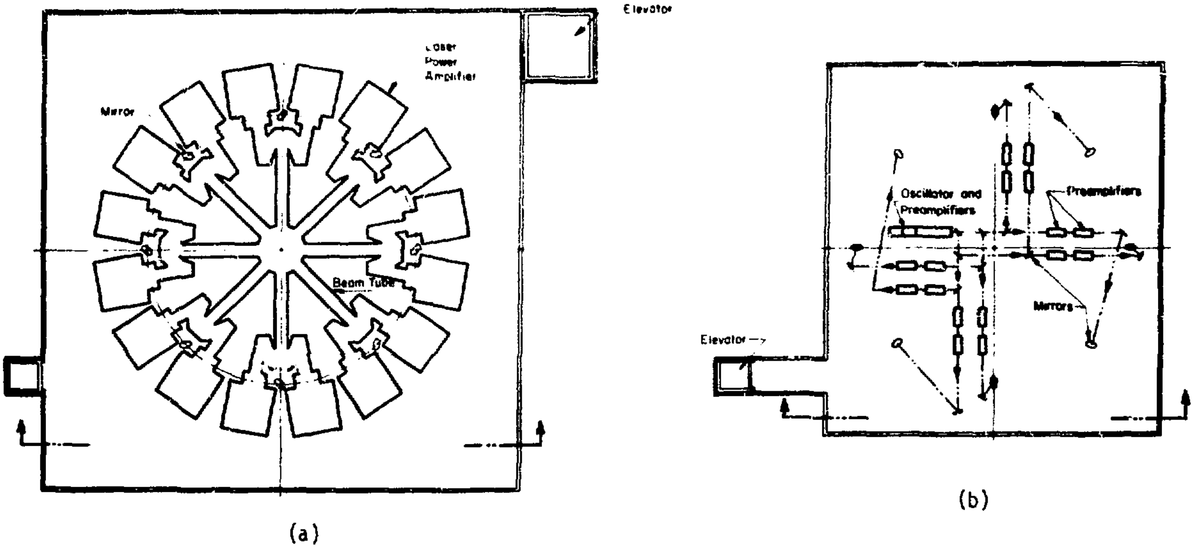

Fig. 87. Electric generating station utilizing magnetically protected laser-fusion reactors: (a) third-level, laser-power-amplifier room, plan view; (b) fourth level, front-end room, plan view.

The pulse-forming networks are located on the second level and the main laser power amplifiers on the third level. There are 16 laser power amplifiers, eight of which would be operated at one time to provide eight laser beams for quasi-symmetric illumination of fusion pellets. Selector mirrors direct the laser beams from operating laser power amplifiers to the rotating mirror, also located on the third level. The required rotational velocity of the mirror is 10 rps. For the design laser-beam length, the laser-beam focal spot travels only ~ 1 x 10^{-4} mm during a 1.0-ns pulse; thus, the focused beam will not move significantly off a millimeter-size target during the arrival time of a laser pulse. A laser-power-amplifier and pulse-forming-network maintenance area is located on the third level, which is serviced from ground level by a freight elevator.

The front-end system, i.e., the oscillator and preamplifiers, is located on the top level. Differences in beam path length from the laser power amplifiers to the reactor cavity centers are compensated by corresponding differences in path lengths in the front-end system so that amplified laser pulses arrive at the cavity centers simultaneously.

All levels are serviced by a personnel and small-component elevator. Shielding of the reactor enclosures and hot-cell maintenance areas is provided by thick concrete walls. Each reactor can be isolated from the system for service without affecting the operation of the remainder.

Some generating-station operating characteristics are given in Table XIX. Three types of conversion systems have been evaluated: (1) a low-

TABLE XIX

OPERATING CHARACTERISTICS OF LASER-FUSION GENERATING STATION
BASED ON MAGNETICALLY PROTECTED REACTORS

Reactor Cavities		
Fusion-pellet yield, MJ		*100*
Microexplosion repetition rate per cavity, s^{-1}		*10*
Thermal power per cavity, MW		*1249*
Reactor dimensions:	*cavity radius, m*	*2.51*
	blanket thickness, m	*0.90*
Reactor materials:	*cavity wall*	*Nb*
	structure	*Nb, SS*
Tritium breeding ratio		*1.31*
Laser beams per cavity		*8*
Lasers and Beam Transport		
Number of laser-power amplifiers		*8 (with 100% redundancy)*
Beam energy per laser power amplifier, MJ		*0.135*
Laser efficiency, %		*6.3*
Pulse rate, Hz		*40*
Number of mirrors per beam		*9*
Beam transport efficiency, %		*92.7*

Overall Plant	*Low-Temperature Steam Turbines*	*High-Temperature Steam Turbines*	*High-Temperature Steam Turbines w/Potassium Topping Cycle*
Number of reactor cavities	*4*	*4*	*4*
Total thermal power, MW	*5000*	*5000*	*5000*
Net electrical power, MW	*1165*	*1500*	*1900*
Generating plant efficiency, %	*38*	*45*	*54*
Net plant efficiency, %	*23*	*30*	*38*
Relative power production cost	*1.0*	*0.92*	*0.81*

temperature (turbine inlet, 723 K) steam cycle; (2) a high-temperature (turbine inlet, 839 K) steam cycle; and (3) a high-temperature steam cycle with a potassium-vapor topping cycle (potassium vapor, 1100 K). The net electric power output using the potassium vapor-steam cycle is more than 60% greater than for the low-temperature steam cycle and the cost of producing power is significantly less for this conversion system than for others. However, the topping cycle is not illustrated in the figures.

In the conceptual electrical generating stations, the laser type is optional and may be either a CO_2, chemical HF, or some other high-efficiency gas laser. If chemical HF lasers were used, part of the space occupied by pulse-forming networks for a CO_2 system would be used for HF electrolysis systems.

ALTERNATIVE APPLICATIONS OF LASER-FUSION REACTORS

Laser-Fusion Hybrid Reactor Studies

Our investigation of the ^{239}Pu-burner/^{233}U-breeder hybrid concept is continuing. Reactor blanket designs that we have investigated in recent studies have incorporated concentric spherical shells with the following material compositions: (1) a lithium-cooled region of stainless steel-clad rods of $^{238}UO_2$ and $^{239}PuO_2$ adjacent to the reactor cavity; and (2) a region of stainless steel-clad ^{232}ThC rods, also cooled by lithium. A schematic illustrating the concept is shown in Fig. 88.

The mixed-oxide region contains the equilibrium concentration of $^{239}PuO_2$. The plutonium is continuously recycled in the fuel fabrication and processing cycles and serves only to amplify the neutron population and to produce thermal power. Leakage neutrons from the oxide region are captured in the ThC region for breeding ^{233}U. The ^{233}U concentration will increase until it either reaches equilibrium or the blanket is processed. We anticipate that economic considerations will require that the ^{233}U breeding region be processed much earlier than equilibrium concentration is achieved. Tritium breeding occurs in both regions of the reactor blanket.

The overall reactor design is based on the wetted-wall reactor concept (3.4-m minimum cavity

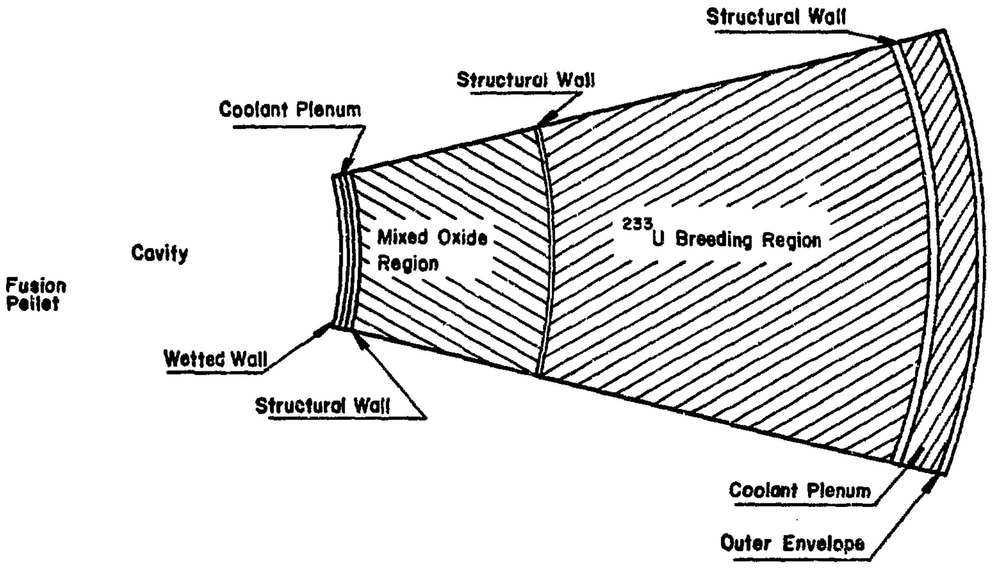

Fig. 88. Conceptual design of ^{239}Pu-barrier/^{233}U-burner hybrid reactor.

diameter for 100-MJ pellet microexplosions) with outward radial flow of the coolant from the cavity wall. Because leakage neutrons from the mixed-oxide region are utilized for breeding ^{233}U, designs that maximize thermal output also have maximum ^{233}U breeding rates. The breeding rates of ^{233}U and tritium, and the thermal power output of the system, increase as the fuel volume fraction in the mixed-oxide region is increased. Essentially all the fusion power is deposited in the mixed-oxide region and essentially all the fission power is produced in this region, especially immediately after processing of the ThC breeding region (i.e., when the ^{233}U concentration is zero). Thus, the coolant temperature would increase mainly in the mixed-oxide region. We optimized the design of the mixed-oxide region for maximum reactor power output and ^{233}U breeding rate, consistent with the following constraints and values of design parameters:

- The fuel rods are contained as bundles in conical cans with hexagonal cross sections made of 2.5-mm-thick stainless steel. Each bundle contains 37 fuel rods.
- The fuel rods are cylinders of constant diameter, so that the coolant volume fraction increases with radial distance from the reactor cavity. The minimum pitch-to-diameter ratio of the fuel rods is 1.05.
- Center-line fuel temperatures are constrained to less than 2700 K, and the thermal stresses in the fuel cladding shall not exceed the fatigue-stress limit of stainless steel (~ 2 x 10^8 N/m^2 at 800 K).
- The neutron multiplication factor of the system is constrained to less than 0.95, with or without coolant.
- The stainless steel cladding is 0.38-mm thick for fuel rods 13 mm in diameter or less.
- The lithium coolant temperature is 673 K at the inlet to the mixed-oxide region and is 973 K at the outlet.

Optimization of the mixed-oxide region involves an iterative feedback loop between neutronics, energy production, and heat-transfer calculations. The effects of pulsed operation were taken into account with two-dimensional, time-dependent heat-transfer calculations for fuel rods in a flowing liquid-lithium coolant with energy production distributions determined from neutronics calculations. The constraints and values of design parameters listed above are satisfied only for certain limiting values of fuel-rod diameter and length, coolant volume fraction and velocity, and fusion-pellet microexplosion yield and repetition rate.

The resulting geometry and composition of the various regions in the reactor are given in Table XX, and the performance is described in Table XXI. For the assumed fusion-pellet microexplosion repetition rate and yield, this reactor and associated auxilliary equipment would produce ~ 700 MW of electric power, and the ^{233}U production rate would be ~ 14 kg per day. The ^{233}U production rate would decrease and the power level would increase as the concentration of ^{233}U increases in the ThC region.

TABLE XX

GEOMETRY AND COMPOSITION OF HYBRID REACTOR

Region	*Outside radius (m)*
Cavity	*1.9925*
Wetted wall *60 vol% niobium* *40 vol% lithium*	*1.9950*
Lithium plenum	*2.0000*
Structural wall *90 vol% SS* *10 vol% lithium*	*2.0050*
Mixed-oxide region *57 vol% fuel* *16.3 vol% SS* *26.7 vol% lithium*	*2.305*
Structural wall *90 vol% SS* *10 vol% lithium*	*2.3100*
^{238}U breeding region *60 vol% ThC* *11.2 vol% SS* *28.8 vol% lithium*	*2.7100*
Structural wall *90 vol% SS* *10 vol% lithium*	*2.7150*
Lithium plenum	*2.8150*
Outer containment	*2.8250*

TABLE XXI

PERFORMANCE OF HYBRID REACTOR IMMEDIATELY AFTER PROCESSING OF ^{233}U BREEDING REGION

Fusion-pellet microexplosion repetition rate, s^{-1}		1
Fusion-pellet microexplosion yield, MJ		100
^{233}U production per fusion neutron, atom		1.18
Tritium breeding ratio		1.19
Equilibrium PuO_2 concentration in mixed-oxide region, %		9.
Maximum transient center-line fuel temperature, K		2700
Maximum transient thermal stress in fuel cladding, $N/m^2 \times 10^{-8}$		0.69
Neutron multiplication factor:	with coolant	0.78
	without coolant	0.83
Thermal power output, MW		3040

Additional investigations of this concept will include studies of end-of-cycle conditions. The ThC breeding region will be optimized after end-of-cycle power densities and coolant flow requirements are determined.

We plan to design a ^{239}Pu-burner/^{233}U-breeder reactor based on the magnetically protected reactor concept as the next major step in our hybrid reactor study. This concept should lend itself to more conventional liquid-metal breeder-reactor engineering designs than the wetted-wall reactor concept.

Utilization of Fusion Energy

Although the primary, long-range goal of the laser-fusion program is the production of economically competitive electric power, there are other potential applications of laser-fusion energy. We presented the results of a preliminary analysis of the use of laser fusion for radiolytic decomposition of reactants for the production of synthetic fuel in a previous report.[3] During this reporting period we have begun an investigation of the use of laser-fusion reactors as sources of process heat.

The primary energy forms of laser-fusion reactors using the (D+T)-fuel cycle are x rays, gamma rays, hot ionized plasmas, and high-energy neutrons. It is conceptually possible to convert all of these energy forms into high-temperature heat; however, the most straightforward engineering designs are based on the utilization of the neutron and gamma-ray energy, and our initial investigations have been restricted to such concepts.

Fusion neutrons pass through cavity walls with essentially no energy loss and can be utilized in blanket regions. In addition, there are exoergic reactions between neutrons and appropriately chosen blanket constituents that result in increased energy deposition in blanket regions. About 80% of the total energy produced in typical laser-fusion reactor designs is available for use free of cavity restraints. This is a unique characteristic of fusion reactors.

A significant potential advantage of laser-fusion reactors for process-heat applications, compared to fission reactors, is the absence of high-temperature limitations due to fuel-element distortion or melting and of fission-product release. The highest fission-reactor temperatures that have been proposed for use as process-heat sources (from high-temperature gas-cooled reactors) are in the range of 1550 to 1650 K. Temperatures in this range are adequate for many industrial processes; however, there are also many processes that require higher temperatures that are currently provided either by such inefficient sources as electric arcs or are not now economically competitive. About 28% of the nation's energy consumption is used directly for process heat and another 9% is used in industrial applications in the form of electricity.[4] The utilization of process heat would be even greater if an economical high-temperature heat source were available. Laser-fusion reactors could provide process heat up to temperature limits that are imposed only by the properties of refractory materials.

A variation of process-heat sources that utilizes the neutron and gamma-ray energy produced in a laser-fusion reactor by (n,γ) reactions between neutrons and structural materials would be based on the use of high-temperature radiation. For this concept, the blanket region is replaced by a refractory material in which neutron and gamma-ray energy is deposited, and energy transfer from this region to an adjacent region of process fluid or chemical reactants is accomplished by radiation.

We are investigating the feasibility of conceptual radiation sources that include carbon and a material with a high absorption cross section for thermal neutrons as the principal energy-deposition materials. The 14-MeV fusion neutrons give up their kinetic energy to the carbon by elastic collisions and are finally captured by the thermal-neutron absorber. We have performed initial calculations for systems with two regions in the blanket, a pure carbon region next to the reactor cavity followed by a 5-cm-thick region of 90 vol% carbon and 10 vol% boron carbide. Boron carbide was selected because of its high melting temperature (2625 K), its large thermal-neutron absorption cross section, and because thermal-neutron capture in boron is exoergic with 2.5 MeV deposited locally by charged particles. Some neutrons will inevitably leak from such a blanket and might affect a process stream adversely. We have found that neutron leakage is reduced to less than 0.2% for a blanket including a 1-m-thick carbon region surrounding a 4-m-diam cavity in spherical geometry. However, maximum total energy deposition in the blanket per fusion neutron occurs for a carbon thickness of ~ 0.75 m for which the fractional neutron leakage is 1.1%. Energy deposition in the blanket is 16.8 MeV per fusion neutron for the 0.80-m-thick blanket compared to 16.1 MeV per fusion neutron for the 1.05-m-thick blanket.

Calculated temperature distributions in the carbon and boron carbide for several cases of blanket thickness, type of carbon (graphite), and radiative power level are given in Table XXII. Maximum blanket temperatures are determined by the power level, the geometry, and the physical properties of the blanket. Systems with the best performance include pyrolytic graphite with thermal conduction along the crystal planes. Maximum blanket temperatures were limited to 4000 K, which is approximately the sublimation temperature of carbon. Analyses have also been made of the effects of pulsed operation on maximum blanket temperatures. Because of the extremely large heat capacities of such systems, fluctuations in temperature due to pulsed operation are trivially small.

TABLE XXII

OPERATING CONDITIONS AND PERFORMANCE OF SPHERICAL LASER-FUSION-REACTOR RADIATION HEAT SOURCES WITH 2000-K PROCESS STREAMS

Thermal Radiation Power (MW)	*Radiation Surface Temperature (K)*	*Blanket Thickness (m)[a]*	*Type of Graphite*	*Maximum Blanket Temperature (K)*
91.3	*2262*	*1.05*	*Pyrolytic, conduction along crystal planes.*	*3210*
23.9	*2087*	*0.76*	*AGOT, conduction normal to axis of extrusion.*	*4000*
22.8	*2075*	*1.05*	*AGOT, conduction parallel to axis of extrusion.*	*3970*
46.7	*2171*	*0.58*	*AGOT, conduction parallel to axis of extrusion.*	*4000*

---

[a] *Reactor cavity radius is 4 m.*

Energy deposition by plasma debris has been ignored in these preliminary calculations. The most attractive concept for using high-temperature radiation is probably the magnetically protected cavity. For such a system, the radiating heat source would be cylindrical and the kinetic energy of the plasma debris would be deposited in the energy-sink regions. This energy could be used in conjunction with energy deposition in the blanket, e.g., in preheating the process stream, or for other purposes.

It may be possible to breed tritium by replacing the boron carbide with a high-melting-point lithium compound, e.g., lithium oxide; however, it is doubtful that a breeding ratio as large as unity could be obtained, and the inclusion of lithium oxide may restrict permissible operating temperatures below those obtainable with other systems.

TEMPERATURE-DEPENDENT ORDINARY AND THERMAL DIFFUSION OF TRITIUM IN THERMONUCLEAR REACTORS

Our initial analyses of the potential radiological hazards of tritium leakage from laser-fusion generating stations indicate that leakage rates will have to be limited to 2 to 10 Ci per day for typical central-station plants. This requirement can apparently be satisfied by appropriate engineering design. Solutions to the problem include (1) maintaining the tritium concentrations in liquid-metal reactor blankets and heat-transfer loops at low enough levels to prevent excessive diffusion of tritium through containment walls and heat-exchanger interfaces, and (2) the use of special materials as diffusion barriers. Thus, the evaluation of tritium diffusion rates through hot metal barriers is very important and may affect the economics of laser-fusion power.

It has been the practice in analyses of tritium migration in thermonuclear generating-station concepts to include only ordinary diffusion and to neglect the detailed effects of the dependences on temperature of the physical properties of barrier materials and, more importantly, the effects of thermal diffusion. We have investigated these effects and find that they are significant, especially for the diffusion of tritium through metal barriers with large temperature gradients, e.g., heat-exchanger tubes.

The flux of a substance in dilute solution in a stationary solvent due to combined ordinary and thermal diffusion is given by[5]

$$\vec{J} = -\frac{D_0 C\, e^{-Q/RT}}{RT}\left[RT\left(1 - \frac{\partial\, \ln \gamma}{\partial\, \ln C}\right)\nabla\, \ln C + \frac{Q^*}{T}\nabla T\right],$$

where:

$\vec{J}$ = diffusion flux,

D_0 = preexponential factor in Arrhenius expression for mass diffusivity,

Q = activation energy for diffusion,

R = ideal-gas constant,

T = temperature,

C = concentration of diffusion substance,

γ = activity coefficient for dissolved diffusing substance, and

Q^* = heat of transport for diffusing substance in host material.

For sufficiently dilute solutions,

$$\frac{\partial\, \ln \gamma}{\partial\, \ln C_1} \approx 0$$

so that

$$\vec{J} = -D_0 e^{-Q/RT}\left(\nabla C + C\frac{Q^*}{RT^2}\nabla T\right).$$

The heat of transport can be either positive or negative in a given temperature range, depending on the host material. If the temperature gradient, the heat of transport Q^*, and the concentration gradient are all negative, the effect of thermal diffusion will be to oppose ordinary diffusion and to reduce the net transfer rate. If either the temperature gradient or Q^* (but not both) is positive, the total rate of diffusion will be greater than that due to ordinary diffusion. The temperature coefficient of the heat of transport for hydrogen isotopes in metals appears to be positive.[6] Therefore, for sufficiently high temperatures, the heat of transport will be positive for most cases of interest for thermonuclear reactors.

We have derived expressions for the diffusion of hydrogen isotopes through metal barriers in plane, cylindrical, and spherical geometries. In calculations made to assess the effects of including the temperature dependence of the diffusion coefficient and the effects of thermal diffusion separately, we have found that calculated diffusion rates of hydrogen isotopes through thin barriers based on the detailed dependence of the diffusion coefficient on temperature differ by only a few percent from diffusion rates based on the arithmetic average of the temperatures at the barrier surfaces. Thus, the common practice of using average temperatures for evaluating ordinary diffusion coefficients is probably sufficiently accurate for most calculations of tritium leakage rates in thermonuclear generating stations.

The effects of thermal diffusion compared to ordinary diffusion are illustrated in Fig. 89, which shows typical plots of the ratio of ordinary diffusion to thermal diffusion as functions of the absolute value of the heat of transport for different barrier temperatures and temperature gradients. The values of heat of transport are typical of stainless steels and refractory metals. Thermal diffusion is relatively more important at 500 K than at 1000 K.

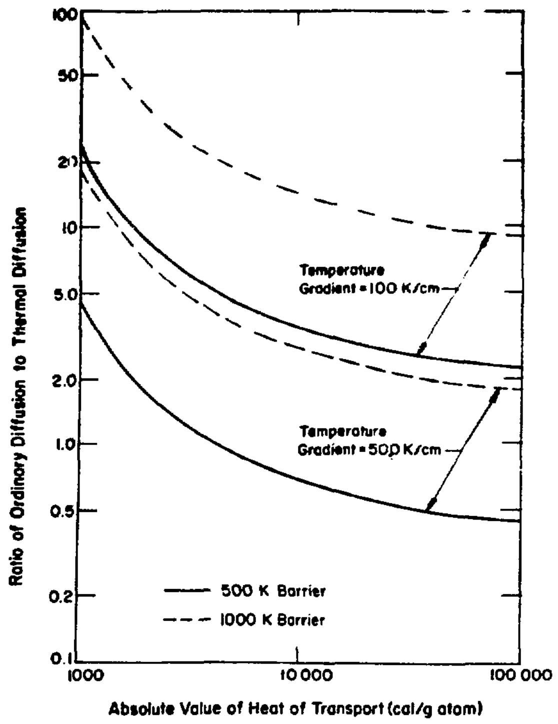

Fig. 89. Relative ordinary and thermal-diffusion rates as functions of heat of transport for a concentration gradient of 100 [(g-atom/cm^3)/cm].

We conclude from this study that thermal diffusion of hydrogen isotopes through metal barriers can be very significant in thermonuclear-reactor generating stations. Unfortunately, few heat-of-transport data for hydrogen isotopes in metals are available, which results in some doubt whether thermal-diffusion theory can now be applied to the analysis of tritium migration in thermonuclear reactors.

REFERENCES

1. "Laser Program at LASL, January 1 through June 30, 1975," Los Alamos Scientific Laboratory Report LA-6050-PR (January 1976).

2. J. Williams, T. Merson, F. Finch, F. Schilling, and T. Frank, "A Conceptual Laser Controlled Thermonuclear Reactor Power Plant," Proc. 1st Topical Meeting on Technology of Controlled Nuclear Fusion, Am. Nuc. Soc., San Diego, CA (April 1974).

3. "Laser Program at LASL, January 1 through July 30, 1975," Los Alamos Scientific Laboratory Report LA-6050-PR (January 1976).

4. G. L. Decker and E. A. Bonham, "Incentives for Nuclear Process Heat Applications in Industry," Proc. 1st National Topical Meeting on Nuclear Process Heat Applications, Los Alamos Scientific Laboratory October 1-3, 1974 .

5. R. E. Howard and A. B. Lidiard, "Matter Transport in Solids," Rep. Prog. Phys 27, 161 (1964).

6. O. D. Gonzales and R. A. Oriani, "Thermal Diffusion of Dissolved Hydrogen Isotopes in Iron and Nickel," Trans. Met. Soc. AIME 223, 1878 (1965).

VII. RESOURCES, FACILITIES, AND OPERATIONAL SAFETY

Construction of new laser laboratories continued. Safety policies and procedures are being formulated as needed to minimize the hazards of operating high-energy lasers. Biological threshold damage studies are under way to provide the necessary data for these regulations.

MANPOWER DISTRIBUTION

The distribution of employees assigned to the various categories of the ERDA-supported laser-induced fusion research program is shown in Table XXIII. Reexamination of main program requirements and available resources led to the termination of HF laser research and development; the effort involved has been transferred to the CO_2 program. After completion of this transition, the CO_2 development effort will increase by an additional ten people with a corresponding decrease in New Laser Systems R&D.

TABLE XXIII

APPROXIMATE STAFFING LEVEL OF LASER PROGRAM

December 31, 1975

Program	*Direct Employees*
Glass Laser Systems Development	*4*
CO_2 Laser System Development	*76*
New Laser Systems R & D	*29*
Pellet Design & Fabrication	*40*
Laser Target Experiments	*45*
Diagnostics Development	*20*
Systems Studies & Applications	*7*
Electron-Beam Target Design & Fabrication	*2*
TOTAL	*223*

FACILITIES

Laser-Fusion Laboratory

Two of the three buildings in this new Laser-Fusion Laboratory Complex are complete. The CO_2 Laser Laboratory (TSL-86), which will house the eight-beam CO_2 laser system, was occupied in August 1975 and the laser is in the early stages of assembly, as described in Sec. I. The laboratory which was to house the chemical laser work (TSL-85) has been reassigned to advanced laser experiments and to CO_2 laser development. Occupancy of this laboratory is beginning. Occupancy of the third building, the Laboratory-Office Building (TSL-87) is scheduled for February 1976.

High-Energy Gas Laser Facility

The High-Energy Gas Laser Facility (HEGLF), designed for operation in the 100- to 200-TW range at energies up to 100 kJ, represents a major building block in the ERDA laser-fusion program. This facility will extend our present CO_2 laser capabilities to power levels at which fusion experiments can be expected to release thermonuclear energies in the range of scientific breakeven. By investigating laser-fusion phenomena at these power levels, we will gain a more complete understanding of the physics involved, which we need to establish laser and target design parameter requirements with confidence. Preliminary design of the laser system is under way.

The HEGLF complex will consist of two main structures, a laser hall housing a six-beam 100- to 200-TW CO_2 laser and a shielded target-irradiation laboratory.

The shielding criteria call for protection of the public-at-large from a neutron source of 10^{20}

n/year produced by 200 full-energy (100-kJ) shots having an energy gain of ten. Because shielding is provided only for the target area, the separation of laser and target buildings leads to a substantial reduction in construction costs in comparison with a facility layout in which the laser and target are housed in a single laboratory.

The output of each of the six laser-power amplifiers will be transported via evacuated beam tubes, 6 in. (15.25 cm) in diameter, over an optical path length of ~ 300 ft (~ 91 m) from the laser output to the cylindrical target chamber, which will be 54 in. (137 cm) long and will have a diameter of 19.7 in. (49 cm).

Large metal mirrors, fabricated by micromachining techniques, will steer and focus the beams to the target position. The target will be illuminated either from two sides, by an array of three beams on each side grouped within a 40° cone, or symmetrically, by six beams arranged as if penetrating the faces of a cube.

A pre-Title I study, completed in June 1975 by Norman Engineering Co., Santa Monica CA, was used to develop design criteria and a detailed cost estimate. General facility descriptions were given in our progress report LA-6050-PR. Details of the laser specifications and features are given above, in Sec. II. Norman Engineering Co. is preparing a proposal for Title-I, -II, and -III work. Fee negotiations and contract signing should be completed in February 1976, with Title-I design commencing immediately thereafter. The total estimated cost of the facility is $54.5 M.

A contract has been signed with Mechanics Research, Inc. (MRI), Los Angeles, CA, for analysis of the various structures defined in the pre-Title I study to determine how these structures would contribute to optical pointing errors when excited by expected vibrations within and outside of the buildings. We have supplied MRI with soils data from both nearby and geologically similar sites, as well as with the results of related vibration analyses. At the start of Title-I design, we expect to know whether the current design criteria are adequate and, if not, which areas need special attention.

Dual-Beam System (DBS) Facility Modifications

Several modifications have been made to Bldg. TSL-29 which houses the DBS:

- The instrumentation screen room was removed from the main floor and is now housed in a trailer outside the north wall of the building.

- A mezzanine was installed in the southwest corner of TSL-29 to accommodate the master trigger generators for the DBS pulser. This move was necessary to provide access to the electrical power panel and to the rear of the building after installation of the new target screen room.

- The oil purifier for the main energy storage system has been installed in a small building adjacent to the oil storage tank. A considerable quantity of oil has been reclaimed and returned to the tank.

- Installation of the target chamber and its screen room is being completed.

OPERATIONAL SAFETY

General

No lost-time accidents have been reported (for 14 months continuous) and no incident involving biological damage from laser light occurred.

A Final Safety Analysis Report (FSAR) has been prepared for the new Laser-Fusion Laboratory Complex.

Biological Damage-Threshold Studies

Experiments on biological samples (rabbit corneas) with short-pulse (2-ns) ir lasers revealed that less energy than anticipated would cause permanent damage. Preliminary results indicate that for a 2-ns CO_2 pulse the damage threshold is as low as 20 mJ/cm^2 compared to 550 mJ/cm^2 with a pulse duration of 3.5 ms reported in the literature. A final report is being prepared.

Final results of the experimental eye-damage studies, conducted by the Jules Stein Eye Institute, UCLA, and by the University of Virginia, involving 1.060-µm radiation from a Nd:YAG laser using single 30-ps pulses on rhesus monkey corneas showed the following retinal damage-threshold values.

Spot Size on Retina (µm)	Energy Incident on Cornea for Threshold Retinal Damage (µJ)	Retinal Damage-Threshold Values	
		Energy (J/cm^2)	Power (10^{10} W/cm^2)
25	8.7 ± 4.8	2.7	9.0
25(0.532)[a]	18.2 ± 8.3	6.5	22.0
430	1521 ± 330	1.6	5.3
630	1017 ± 700	0.5	1.7
725	1184 ± 334	0.44	1.5

---

[a] Frequency-doubled wavelength of the Nd:YAG laser output.

VIII. PATENTS, PRESENTATIONS, AND PUBLICATIONS

APPLICATIONS FILED IN U.S. PATENT OFFICE

S.N. 608,379 - STREAK CAMERA TUBE - Albert J. Lieber. Filed August 27, 1975. (U)

S.N. 626,950 - METHOD FOR SIZING HOLLOW MICROSPHERES - Eugene H. Farnum and R. Jay Fries. Filed October 29, 1975. (U)

S.N. 626,953 - METHOD FOR SELECTING HOLLOW MICROSPHERES FOR USE IN LASER FUSION TARGETS - Eugene H. Farnum, R. Jay Fries, M. L. Smith, Jr., and D. L. Stoltz. Filed October 29, 1975. (U)

PRESENTATIONS

The following presentations were made at the Division of Plasma Physics Meeting of the American Physical Society, St. Petersburg, FL, November 10 - 14, 1975.

R. F. Benjamin, A. J. Lieber, P. B. Lyons, H. D. Sutphin, and C. B. Webb, "Micro-Channel Plate Collimators for Laser-Plasma Diagnostics."

A. J. Lieber, H. D. Sutphin, R. F. Benjamin, S. J. Gitomer, and W. S. Hall, "Proximity-Focused Ultra-Fast Streak Tube."

D. B. van Hulsteyn, R. F. Benjamin, A. J. Lieber, and G. H. McCall, "X-Ray Pinhole Cameras for Laser Plasma Experiments."

H. R. Maltrude, E. H. Farnum, and R. J. Fries, "An Acoustic Measuring System for Determining the Breaking Strength of Microballoons."

D. V. Giovanielli, J. F. Kephart, and A. H. Williams, "Emitted Electron Spectra from Plasmas Produced with Nd and CO_2 Lasers."

D. M. Stupin, E. H. Farnum, R. J. Fries, and M. A. Winkler, "Quality Selection of Laser-Fusion Target Microballoons."

M. M. Mueller, "Beta Absorption in Tritiated Targets and X-Ray Counting Corrections."

S. G. Sydoriak and D. R. Kohler, "Freezing and Melting Deuterium in Microballoons."

A. W. Ehler, "Effect of Secondary Electrons on Charge Collector Measurement of a Laser-Produced Plasma."

E. H. Farnum and R. J. Fries, "External Pressurization as a Means of Upgrading Glass Microballoons."

R. L. Carman, "Generation of Laser Pulses for Optimum Ablative Compressions."

T. H. Tan, G. H. McCall, and A. H. Williams, "Development of an Alpha Particle and Proton Detector for Laser-Fusion Studies."

T. H. Tan, G. H. McCall, and A. H. Williams, "Measurements of Alpha Particles and Protons Produced from Laser-Fusion."

D. S. Catlett, R. J. Fries, A. Mayer, W. McCreary, B. W. Powell, G. A. Simonsic, and D. Fossey, "Recent Developments in Laser-Fusion Target Coatings."

K. B. Mitchell and P. B. Lyons, "X-Ray Continuum and Line Radiation from Plasmas Produced by 10.6-μm Laser Focused on Flat Targets."

P. B. Weiss and G. Hopper, Standard Engineering Corp., "High-Speed Digitizing with CAMAC."

C. R. Phipps, Jr., "Measurement of Non-Maxwellian Electron Velocity Distributions in a Reflex Discharge."

The following papers were presented at the Amercian Nuclear Society Winter Meeting, San Francisco, CA, November 16 - 21, 1975.

F. T. Finch, T. G. Frank, L. A. Booth, and E. A. Kern, "Radioactive Waste Output from Laser-Fusion Generating Stations."

D. A. Freiwald, T. G. Frank, E. A. Kern, and L. A. Booth, "Laser-Fusion Electric Generating Stations Based on the Magnetically Protected Reactor Cavity."

E. A. Kern, T. G. Frank, and L. A. Booth, "Systems Analysis of Laser Fusion Power Plants."

J. H. Pendergrass and F. T. Finch, "Temperature-Dependent Ordinary and Thermal Diffusion of Tritium through Metal Barriers."

G. E. Bosler, "Energy Deposition in a Two-Dimensional LFR Model."

In addition, the following presentations were made at various institutions.

D. A. Freiwald and E. A. Kern, "Laser Fusion Sources for CTR Surface and Bulk Damage Testing," Int'l. Conf. on Radiation Test Facilities for CTR Surface and Materials Program, Argonne National Laboratory (July 15-18, 1975).

L. A. Booth, T. G. Frank, and F. T. Finch, "Engineering Concepts for Laser-Fusion Reactor Applications," 10th Intersociety Energy Conversion Eng. Conf., Newark,DE (August 18-22, 1975).

L. A. Booth, four invited lectures on electric power production from laser fusion presented at UCLA Short Course on Laser Fusion Power Applications, Los Angeles,CA (October 13-17, 1975).

J. V. Parker, "Chemical Lasers," invited paper, 2nd Nat'l. Quantum Electronics Conf., Oxford, England (September 2-4, 1975).

W. T. Leland, "Relation of Electric Discharge Parameters to Short-Pulse CO_2 Laser Efficiency," 2nd Nat'l. Symposium on Gas Laser Physics, Novosibirsk, USSR (June 16-19, 1975).

J. F. Figueira, "Instrumentation for High-Energy Infrared Laser Diagnostics," Soc. of Photo-Optical Instrumentation Engineers, Palos Verdes,CA (August 18-21, 1975).

W. H. Reichelt, "Optical Components in the LASL CO_2 Laser Program," invited talk, Air Force Weapons Laboratory (AFWL), Kirtland AFB, NM (September 18, 1975).

T. F. Stratton, "CO_2 Short-Pulse Laser Technology," summer course on High Power Lasers, Capri, Italy (September 22 - October 4, 1975).

P. B. Weiss and G. Hopper, Standard Engineering Corp., "High Speed Digitizing with CAMAC," 1975 Nucl. Sci. Symp. in conjunction with 1975 Nuclear Power Systems Symp., San Francisco CA (November 19-21, 1975).

K. B. Riepe, "Pulse Forming Networks for Fast Pumping of High Power Electron Beam Controlled CO_2 Lasers," Electro-Optics/Laser Int'l. Conf., Anaheim,CA (November 13, 1975).

PUBLICATIONS

(This list of publications is prepared by computer from a stored data base. It has been checked for accuracy, but there may be typographical inconsistencies.)

Henderson, Dale B.; "Ion Tail Filling in Laser Fusion Targets." LASL, 1975. 9P. (LA-5917-MS).

Skoberne, Frederick; "Laser Program at LASL, July 1 - December 31, 1974." LASL, 1975. 142P. (LA-5919-PR).

Mc Call, Gene H.; "Los Alamos Presentation on Laser Fusion to the Joint Committee on Atomic Energy, Washington, DC, March 13, 1975." LASL, 1975. 6P. (LA-5923MS).

Devaney, Joseph J.; Jackson, Douglas E.; "Optical Design of a Reaction Chamber for Weakly Absorbed Light. 1. Canted and Parallel Mirrors." LASL, 1975. 19P. (LA-5986-MS, Vol. I).

Devaney, Joseph J.; Finch, Francis T.; "Optical Design of a Reaction Chamber for Weakly Absorbed Light. 2. Parallel Mirrors, Multitravel." LASL, 1975. 9P. (LA-5986-MS,Vol.II).

Devaney, Joseph J.; "Optical Design of a Reaction Chamber for Weakly Absorbed Light. 3. Asymmetric Confocal Resonator." LASL, 1975. 15P. (LA-5986-MS, Vol.III).

Rink, John P.; "Cold Cathode Investigation." LASL, 1975. 5P. (LA-6009-MS).

Fraley, Gary S.; Mason, Rodney J.; "Preheat Effects on Microballoon Laser Fusion Implosions." LASL, 1975. 5P. (LA-6046-MS).

Gitomer, Steven J.; Morse, Richard L.; Newberger, Barry S.; "Structure and Scaling Laws of Laser Driven Ablative Implosions." LASL, 1975. 3P. (LA-6079-MS).

Devaney, Joseph J.; "Very High Intensity Reaction Chamber Design." LASL, 1975. 14P. (LA-6124-MS).

Forslund, David W.; Kindel, Joseph M.; Lindman, Erick L.; "Oblique Shocks in a Magnetized Plasma." Abstract published in: Atmospheric Effects. 1973. Symposium, San Diego, CA, Abstracts of Papers, P.17. Dna, 1973. (Dna-LA-10).

Forslund, David W.; Kindel, Joseph M.; Lindman, Erick L.; "Ion Coupling, Electron Heating, and Magnetic Turbulence from Plasma Instabilities." Abstract published in: Atmospheric Effects. 1973. Symposium, San Diego, CA, Abstracts of Papers, P.18. Dna, 1973. (Dna-LA-10).

Godfrey, Brendan B.; Newberger, Barry S.; "Collisional Damping of Langmuir Waves in One Dimensional Plasma Simulations." Plasma Phys., V.17, P.317-26. 1975.

Godfrey, Brendan B.; Newberger, Barry S.; Taggart, Keith A.; "Relativistic Plasma Dispersion Function." IEEE Trans. Plasma. Sci., V.Ps-3, P.60-7. 1975.

Godfrey, Brendan B.; Taggart, Keith A.; Newberger, Barry S.; "Relativistic Linear Theory in the Absence of External Fields." IEEE Trans. Plasma Sci., V.Ps-3, P.68-75. 1975.

Godfrey, Brendan B.; Thode, Lester E.; "Collective Ion Acceleration Via the Two Stream Instability." Ann. N. Y. Acad. Sci., V.251, P.582-9. 1975.

Stark, Eugene E.; Reichelt, Walter H.; "Damage Thresholds in Zinc Selenide, a/R Coated Sodium Chloride and Micromachined Mirrors by 10.6 Micron Multijoule, Nanosecond Pulses." Laser Induced Damage in Optical Materials. 1974. Symposium, Boulder, CO. Proc., P.53-8. Nbs, 1974.

Newnam, Brian E.; "Damage Resistance of Dielectric Reflectors for Picosecond Laser Pulses." TIC, 1974. 11P. MN (LA-UR-74-1053) Also published in: Laser Induced Damage in Optical Materials. 1974. Symposium, Boulder, CO. Proc., P.39-47. Nbs, 1974.

Gillespie, Claude M.; Freiwald, David A.; "Laser Fusion." Report of the Governor'S Task Force Committee On Nuclear Energy, P.II-29-34. Bureau of Engineering Research, Unm, 1975.

Suydam, Bergen R.; "Effect of Refractive Index Nonlinearity on the Optical Quality of High Power Laser Beams." IEEE J. Quantum Electron., V.Qe-11, P.225-30. 1975.

Mason, Rodney J.; Morse, Richard L.; "Hydrodynamics and Burn of Optimally Imploded Deuterium - Tritium Spheres." Phys. Fluids, V.18, P.814-28. 1975.

Dorr, Fred W.; "Direct Solution of the Discrete Poisson Equation in 0(N-Squared) Operations." SIAM Rev., V.17, P.412-5. 1975.

Schott, Garry L.; Rabideau, Sherman W.; Nowak, Andrew V.; Getzinger, Richard W.; "Can We Beat Fluorine and Hydrogen for Hydrogen Fluoride Lasers?" Abstract published in: IEEE J. Quantum Electron., V.Qe-11, P.690. 1975.

Rice, Walter W.; "Metal Atom Oxidation Lasers: A New Family of Chemical Lasers." Abstract published in: IEEE J. Quantum Electron., V.Qe-11, P.689-90. 1975.

Getzinger, Richard W.; Blair, Larry S.; Greiner, Norman R.; "Mixture Stability in High-Power Pulsed Hydrogen - Fluorine Chemical Lasers." Abstract published in: IEEE J. Quantum Electron., V.Qe-11, P.698. 1975.

Fisher, Robert A.; "Dispersive Temporal Compression of the Energy in Laser Pulses: A Review." TIC, 1975. 6P. MN (LA-UR-75-389).

Forslund, David W.; Kindel, Joseph M.; Lindman, Erick L.; "Theory of Stimulated Scattering Processes in Laser Irradiated Plasmas." Phys. Fluids, V.18, P.100216. 1975.

Forslund, David W.; Kindel, Joseph M.; Lindman, Erick L.; "Plasma Simulation Studies of Stimulated Scattering Processes in Laser Irradiated Plasmas." Phys. Fluids, V.18, P.1017-30. 1975.

Ehler, A. Wayne; "High Energy Ions from a Carbon Dioxide Laser Produced Plasma." J. Appl. Phys., V.46, P.2464-7. 1975.

Nowak, Andrew V.; Lyman, John L.; "Temperature Dependent Absorption Spectrum of the Nu(3) Band of Sulfur Hexafluoride at 10.6 Microns." J. Quant. Spectrosc. Radiat Transfer, V.15, P.945-61. 1975.

Giovanielli, Damon V.; Godwin, Robert P.; "Optics in Laser Produced Plasmas." Am. J. Phys., V.43, P.808-17. 1975.

Kirkpatrick, Ronald C.; Cremer, Charles C.; Madsen, Larry C.; Rogers, Harold H.; Cooper, Ralph S.; "Structured Fusion Target Designs." Nucl. Fusion, V.15, P.333-5. 1975.

Leland, Wallace T.; Kircher, Mary; Nutter, Murlin J.; Schappert, Gottfried T.; "Rotational Temperature in a High Pressure Pulsed Carbon Dioxide Laser." J. Appl. Phys., V.46, P.2174-6. 1975.

Carstens, Dean H. W.; Farnum, Eugene H.; Fries, Ralph Jay; Sheinberg, Haskell; "Fabrication of Lithium Deuterium (0.5) Tritium (0.5) Microspheres for use as Laser Fusion Targets." J. Nucl. Mater., V.57., P.1-10. 1975.

Loree, Thomas R.; Sherman, Lawrence M.; Thorne, James M.; "Amplification of the 1.32-Micron Line in Neodymium : Yag." IEEE J. Quantum Electron., V.Qe-11, P.371-2. 1975.

Reichelt, Walter H.; Landahl, Charles E.; Stark, Eugene E.; Stratton, Thomas F.; "Methods to Reduce the Effects of Self Lasing and Target Reflections in Carbon Dioxide Lasers." TIC, 1975. 6P. MN (LA-UR-74-1956).

Liberman, Irving; Bennett, Michael J.; Hayden, James J.; Singer, Sidney; "Measurement of Beam Quality from Short Pulse Carbon Dioxide Lasers." Abstract published in: IEEE J. Quantum Electron., V.Qe-11, P.D44, 1975.

Schappert, Gottfried T.; Ladish, Joseph S.; Leland, Wallace T.; Kircher, Mary; "Gain Recovery After Saturation in Short Pulse Carbon Dioxide Amplifiers." Abstract published in: IEEE J. Quantum Electron., V.Qe-11, P.D75-6. 1975.

Figueira, Joseph F.; Reichelt, Walter H.; Schappert, Gottfried T.; Feldman, Barry J.; "Multiline Operation of a Carbon Dioxide Oscillator/Amplifier System." Abstract published in: IEEE J. Quantum Electron., V.Qe-11, P.D74. 1975.

Figueira, Joseph F.; Schappert, Gottfried T.; Singer, Sidney; Thomas, Scott J.; "Parametric Study of a Multiband Carbon Dioxide Laser." Abstract published in: IEEE J. Quantum Electron., V.Qe-11, P.D74. 1975.

Goldstein, John C.; "Optical Quality Study of the LASL Carbon Dioxide Laser Amplifier System." TIC, 1975. 5P. MN (LA-UR-75-14).

Feldman, Barry J.; "Multiline Short Pulse Amplification and Compression in High Gain Carbon Dioxide Laser Amplifier." Opt. Commun., V.14, P.13-6. 1975.

Fisher, Robert A.; James, Larry T.; "Observations of Excited State Absorption in Ed-2 Neodymium Glass." Opt. Commun., V.13, P.402-4. 1975.

Carman, Robert L.; "Amplifiers Involving Two Photon Energy Extraction Schemes." Phys. Rev., V.a12, P.1048-61. 1975.

Jensen, Reed J.; "Hydrogen Fluoride Chemical Laser." TIC, 1975. 20P. MN (LA-UR-75-257).

Carbone, Robert J.; "Laser Application of Heat Pipe Technology in Energy Related Programs." TIC, 1975. 16P. MN (LA-UR-75-839).

Bosler, Gerald E.; Frank, Thurman G.; "Energy Deposition Rates in a Laser -Fusion Reactor." Abstract published in: Trans. Am. Nucl. Soc., V.21, P.16-7. 1975.

Mitchell, Kenneth B.; Stratton, Thomas F.; Weiss, Paul B.; "Backscatter Measurements from Laser Produced Plasmas at 10.6 Microns." Appl. Phys. Lett., V.27, P.11-3. 1975.

Cantrell, Cyrus D., III; Scully, Marlan O.; Et Al; "Review of Soft X Ray Lasers using Charge Exchange." TIC, 1975. 101P. MN (LA-UR-75-286).

Fries, Ralph Jay; Farnum, Eugene H.; "Nondestructive Fuel Assay of Laser Targets. 1. X Ray Method." Nucl. Instrum. Methods, V.126, P.285-91. 1975.

Caldwell, John T.; Atwater, Henry F.; Farnum, Eugene H.; Fries, Ralph Jay; Hyder, A. K.; "Nondestructive Fuel Assay of Laser Targets. 2. Photonuclear (Deuterium (Gamma,Neutron)) Method." Nucl. Instrum. Methods, V.126, P.293-7. 1975.

Jarmie, Nelson; Lovoi, Paul A.; Farnum, Eugene H.; Fries, Ralph Jay; Young, Frederick; "Nondestructive Fuel Assay of Laser Targets. 3. Elastic Scattering Method." Nucl. Instrum. Methods., V.126, P.299-302. 1975.

Taylor, David J.; "Spectral Acceptance for Second Harmonic Generation in CD*A (Cesium Dideuterium Arsenate)." J. Appl. Phys., V.46, P.3988-91. 1975.

Alfano, R. R.; Shapiro, Stanley L.; "Ultrashort Phenomena." Phys. Today, V.28, No.7, P.30-7. 1975.

Robinson, C. Paul; "Laser Isotope Separation." TIC, 1975. 20P. MN (LA-UR-75-642) abstract published in: J. Opt. Soc. Am., V.65, P.1173. 1975.

Boyer, Keith; "Laser Fusion: An Overview." TIC, 1975. 19P. MN (LA-UR-75-660).

Lyman, John L.; Jensen, Reed J.; Rink, John P.; Robinson, C. Paul; Rockwood, Stephen D.; "Isotopic Enrichment of Sulfur Hexafluoride in Sulfur -34 by Multiple Absorption of Carbon Dioxide Laser Radiation." Appl. Phys. Lett., V.27, P.87-9. 1975.

Booth, Lawrence A.; Frank, Thurman G.; Finch, Francis T.; "Engineering Concepts for Laser Fusion Reactor Applications." TIC, 1975. 18P. MN (LA-UR-75-736).

Lyman, John L.; Jensen, Reed J.; Rink, John P.; Robinson, C. Paul; Rockwood, Stephen D.; "Isotopic Enrichment by Multiple Absorption of Carbon Dioxide Laser Radiation." Abstract published in: IEEE J. Quantum Electron., V.Qe-11, P.D103. 1975.

Rockwood, Stephen D.; Hudson, Jerry W.; "Laser Driven Synthesis of Boron Hydrochloride from Boron Chloride and Hydrogen." Chem. Phys. Lett., V.34, P.542-5. 1975.

Fraley, Gary S.; Mason, Rodney J.; "Preheat Effects on Microballoon Laser Fusion Implosions." Phys. Rev. Lett., V.35, P.520-3. 1975. Abstract published in: Bull. Am. Phys. Soc., Ser.2, V.20, P.1231. 1975.

Hyer, Ronald C.; Sutphin, Howard D.; Winn, Kenneth R.; "Laser Initiated Krytron Switched Blumlein Structure for Pulse Selection." Rev. Sci. Instrum., V.46, P.1333-4. 1975.

Hughes, William M.; Olsen, T.; Hunter, Robert; "Determination of Argon Oxide 558 NM Laser Parameters." Abstract published in: IEEE J. Quantum Electron., V.Qe11, P.D88. 1975.

Piltch, Martin S.; Rink, John P.; Tallman, Charles R.; "Pulsed Infrared Difference Frequency Generation in Cadmium - Germanium -Arsenic(2)." Opt. Commun., V.15, P.112-4. 1975.

Singer, Sidney; "LASL 2.5 Kilojoule Carbon Dioxide Short Pulse Laser System." Abstract published in: IEEE J. Quantum Electron., V.Qe-11, P.D44-5. 1975.

Scott, J. F.; Sargent, M.; Cantrell, Cyrus D., III; "Laser Phase Transition Analogy: Application to First Order Transitions." Opt. Commun., V.15, P.13-6. 1975.

Moran, Michael J.; She, Chiao-Yao; Carman, Robert L.; "Interferometric Measurements of the Nonlinear Refractive Index Coefficient Relative to Carbon Disulfide in Laser System Related Materials." IEEE J. Quantum Electron, V.Qe-11, P.259-63. 1975.

Wada, J.; Lind, R. C.; Judd, O'Dean P.: "UV Photoionization Processes in Seeded High Pressure Laser Gases." Abstract published in: Bull. Am. Phys. Soc., Ser.2, V.19, P.149, 1973.

Freiwald, David A.; Frank, Thurman G.: "Introduction to Laser Fusion." LASL, 1975. 26P.

Robinson, C. Paul; "Isotope Separation." Abstract published in: J. Opt. Soc. Am., V.64, P.1356, 1974.

Campillo, Anthony J.; Kollman, Victor H.: "Ultrafast Streak Camera." Science, V.189, P.410, 1975.

☆U.S. GOVERNMENT PRINTING OFFICE: 1976-677-343/170